

**FIRST PRINCIPLE MODELING  
OF ALCOHOL FUEL CELL CATALYSIS**

**TRINH QUANG THANG**

**NATIONAL UNIVERSITY OF SINGAPORE**

**2014**

**FIRST PRINCIPLE MODELING  
OF ALCOHOL FUEL CELL CATALYSIS**

**TRINH QUANG THANG**

*(B. Eng. & M. Sc.,*

*Hanoi University of Science and Technology, Vietnam)*

**A THESIS SUBMITTED**

**FOR THE DEGREE OF DOCTOR OF PHILOSOPHY**

**DEPARTMENT OF CHEMICAL & BIOMOLECULAR**

**ENGINEERING**

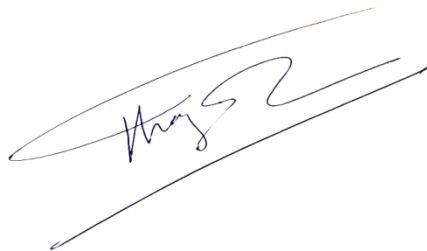
**NATIONAL UNIVERSITY OF SINGAPORE**

**2014**

## **Declaration**

I hereby declare that this thesis is my original work and it has been written by me in its entirety. I have duly acknowledged all the sources of information which have been used in this thesis.

This thesis has also not been submitted for any degree in any university previously.

A handwritten signature in blue ink, appearing to read 'Trinh Quang Thang', is written over a large, light-colored, stylized scribble or signature.

---

Trinh Quang Thang

09 December 2014

## ACKNOWLEDGEMENTS

I would like to take this opportunity to extend my gratitude and appreciation to my supervisor, *Dr. Karl Erik Birgersson* from NUS for his encouragement, support and guidance throughout the course of this research project. Without his supervision and help, I would not be able to complete my PhD studies.

I also wish to extend my sincere appreciation to *Dr. Mark Saeys*, who is now in Ghent University. Through him, I have learnt invaluable lessons in my research. He was pivotal in guiding me throughout my PhD research and willingness to share his knowledge. I still remember the first time I knocked on his door, which opened my grateful research journey.

I am also thankful to *Dr. Jinhua Yang* and *Prof. Lee Jim Yang* from NUS, and *Dr. Armando Borgna* from ICES, who are my collaborators. I appreciate their experimental works to support my theoretical results and their helpful discussions during my research.

To my senior, *Dr. Xu Jing* who mentored me in the usage of VASP and provided me with all the technical guidance, I thank you very much. To *Dr. Tan Kong Fei*, *Dr. Gavin Chua Yong Ping*, *Dr. Zhuo Mingkun*, *Dr. Ravi Kumar Tiwari*, *Dr. Hiroyo Kawai*, *Dr. Na Guo*, *Fan Xuexiang*, *Cui Luchao*, *Novi Wijaya*, *Arghya Banerjee* and *G. T. Kasun Kalhara Gunasooriya* who are my colleagues/lab mates, I thank you for your help, support, camaraderie and encouragement throughout my research work.

Finally, special thanks to my dear wife *Hoang Do Quyen*, for being there to support me as I pursue my doctorate degree. I am extremely grateful for her love, patience and especially her understanding, which have enabled my doctorate journey to be meaningful and successful. To my father, *Professor Trinh Quang Hoa*, I thank you for always standing beside me to support and encourage me to complete this journey. My PhD thesis is especially dedicated for you.

# TABLE OF CONTENTS

Acknowledgements .....	I
Table of contents .....	III
Summary .....	VII
List of tables .....	XI
List of figures .....	XIII
Symbols and abbreviations .....	XIX
Publications .....	XXII
Chapter 1. Introduction .....	1
1.1. Overview of Direct Alcohols fuel cells .....	1
1.2. Aim and structure of thesis .....	10
1.3. References .....	12
Chapter 2. Computational modeling .....	18
2.1. Computational Theory .....	19
2.2. DFT XPS Core-level binding calculations .....	20
2.3. Free Gibbs energy calculations for electro-chemical reactions .....	23
2.4. Describe the Hydrogen interaction by DFT: role of DFT-vdW functional .....	27
2.5. References .....	29

Chapter 3. Evaluating the Structure of Catalysts using First Principle calculated XPS Core-Level Binding Energies and guided characterize core- shell electro-catalyst .....	33
3.1. Introduction .....	33
3.2. Computational and Experimental Methods .....	37
3.2.1. Computational Methods .....	37
3.2.2. Core-level Binding Energy Calculations .....	44
3.2.3. Experimental Methods .....	46
3.3. Results and Discussion .....	47
3.3.1. C 1s core-level binding energies on Co(0001) .....	48
3.3.2. C 1s binding energies for species on Pt(111) .....	53
3.3.3. B 1s core-level binding energies .....	57
3.3.3. Identification of carbon and boron species on supported Co catalysts by core-level BE calculations .....	60
3.3.3. Structural study of Pd <sub>3</sub> M@Pd <sub>3</sub> Pt core-shell particles using Pt 4f <sub>7/2</sub> BE calculations .....	65
3.4. Conclusions .....	74
3.5. References .....	75

Chapter 4. Computational and Experimental Study of the Volcano Behavior of the Oxygen Reduction Activity of PdM@PdPt/C (M=Pt, Ni, Co, Fe and Cr) Core-Shell Electrocatalysts .....	81
4.1. Introduction .....	81
4.2. Computational and Experimental Methods .....	84
4.2.1. Computational Methods .....	84

4.2.3. Experimental Methods .....	87
4.3. Results and Discussion .....	88
4.3.1. Catalyst characterization .....	89
4.3.2. Volcano-like variation in the ORR activity .....	99
4.3.3. Methanol tolerance and stability .....	107
4.4. Conclusions .....	110
4.5. References .....	111
Chapter 5. DFT study on the reversal of the CH/OH selectivity in the activation of methanol over platinum by the presence of water .....	116
5.1. Introduction .....	116
5.2. Computational Methods .....	119
5.3. Results and Discussion .....	121
5.3.1. Adsorption of methanol, methoxy and hydroxyl groups on Pt(111) .....	121
5.3.2. Methanol activation on a clean surface .....	124
5.3.3. Effect of water on methanol activation .....	127
5.3.4. Effect of surface hydroxyl species on methanol activation .....	133
5.3.5. Activation of CH in CH <sub>3</sub> O on other transition metals: competition between direct dehydrogenation vs H-abstraction pathway .....	135
5.3.6. Energy Profile for the dehydrogenation of methanol .....	140
5.4. Conclusions .....	142
5.5. References .....	143



Chapter 6. Reaction path analysis to identify selectivity determining steps for the complete oxidation of Ethanol and guided design of an EOR catalyst:	
Preliminary results .....	148
6.1. Introduction .....	148
6.2. Computational Methods .....	154
6.3. Results and Discussion .....	155
6.3.1. Energy profile of the ethanol decomposition on Pt(111) .....	155
6.3.2. Study C-C cleavage in different intermediates on Pt(111) .....	157
6.3.3. Screening the selectivity of the initial deprotonation step on different transition metals .....	158
6.3.4. Screening the selectivity of the second deprotonation step .....	161
6.4. Conclusions .....	163
6.5. References .....	165
Chapter 7. Conclusion and Suggestion for Future works .....	168
7.1. Summary of major findings .....	168
7.2. Suggestion for future works .....	172
7.2.1. Study the C-C cleavage in the EOR via the decarboxylation pathways .....	172
7.2.2. Comprehensively evaluate EOR activity on alloys and core-shell catalysts .....	174
7.2.3. Study the water activation on metal oxide .....	175
7.3. References .....	176

## SUMMARY

Alcohols, which are easy to store and transport, can be generated from renewable sources and have high energy density. It has made Direct Alcohol Fuel Cells (DAFCs) a promising electrochemical device. DAFCs have features similar to current fuel cell devices such as Hydrogen fuel cells; hence, it can share many research achievements of those fuel cell technologies. However, there are still a lot of improvements to make the commercialization of DAFCs becomes feasible. DAFCs use catalyst to convert fuel (alcohols) to  $\text{CO}_2$  and produce electricity. Characterization of electrochemical catalysts, especial the structural study of nano-particle catalyst is difficult due to the small particle size and complicated composition. The development of more economical and more active oxygen electrode catalysts (anode catalyst) has also been identified as an important challenge for the introduction of fuel cell technology. Further more, there is a lack of comprehensive mechanistic understanding of the Alcohol electro-oxidation in realistic conditions (aqueous phase under applied potential). Finally, slow anode kinetics and poor activity in complete ethanol oxidation, which is caused by the difficulty of breaking the C-C bond in the ethanol molecule, has impeded the commercialization of DEFCs. Those are the objectives of this PhD study.

Density functional theory (DFT) has become an important tool for heterogeneous catalytic reaction analysis. Particularly in electrochemistry, DFT calculations can be used to predict and evaluate the behavior of electro-catalysts under electrochemical conditions, which is very difficult to obtain

from experiments due to the complexity of electrochemical systems. In this study, DFT calculations are performed to model electrochemical reactions and guide the design of catalysts in the DAFCs. Computational catalysis studies require a detailed atomic scale model of the catalyst structure. Firstly, to link the model structure with experimental multi-component catalyst nanostructures, we developed a procedure to accurately calculate XPS binding energies which can be compared with experimental catalyst characterization data. This procedure helps to identify the structure of carbon deposition and boron promoter during the Fischer-Tropsch synthesis and could be used to characterize the PdM@PdPt/C core-shell electro-catalyst.

A computational procedure was also developed to study electrochemical reactions. The procedure accounts for applied potential and pH, and can account for solvent effects. Using this approach, First principle calculations were used to screen the oxygen reduction activity of a series of Pd<sub>3</sub>M@Pd<sub>3</sub>Pt core-shell electrocatalysts for direct methanol fuel cells. Density functional theory (DFT) calculations indicate that the subsurface substitution of Pt by a 3d transition metal M improves the activity of the Pd<sub>3</sub>Pt catalysts by reducing the oxygen binding energy. Carbon-supported Pd<sub>3</sub>M@Pd<sub>3</sub>Pt (M=Ni, Co, Fe and Cr) core-shell electrocatalysts with similar particle size, a Pd<sub>3</sub>Pt rich surface, and a Pd<sub>3</sub>M alloy core were prepared by a galvanic replacement reaction between PdM alloy nanoparticles with a 70:30 Pt:M atomic ratio and an aqueous solution of PtCl<sub>4</sub><sup>2-</sup>. The predicted change in the surface Pt electronic structure was confirmed by comparing the calculated shift in the Pt 4f<sub>7/2</sub> core level binding energies with XPS data, and by comparing the change

in the calculated CO binding energies with the shift in the position of the CO stripping peak. Optimal activity close to the maximum of a volcano curve is predicted for Pd<sub>3</sub>Fe@Pd<sub>3</sub>Pt and Pd<sub>3</sub>Mn@Pd<sub>3</sub>Pt core-shell catalysts. In agreement with the DFT calculations, optimal activity and high methanol tolerance were observed for Pd<sub>3</sub>Fe@Pd<sub>3</sub>Pt. A lower activity is observed for the Pd<sub>3</sub>Cr@Pd<sub>3</sub>Pt catalyst with a lower CO binding energy and for the Pd<sub>3</sub>Co@Pd<sub>3</sub>Pt and Pd<sub>3</sub>Ni@Pd<sub>3</sub>Pt catalysts with higher CO binding energies. In the presence of 0.1 M methanol, the current density per Pt atom for the optimal Pd<sub>3</sub>Fe@Pd<sub>3</sub>Pt/C catalyst is 10 times higher than for commercial Pt/C catalysts. DFT calculations further indicate the CO and OH covered Pd<sub>3</sub>Fe@Pd<sub>3</sub>Pt electrocatalyst is stable towards Fe surface segregation.

Next, since water plays an important role in aqueous phase catalytic reactions, such as electro-oxidation in direct alcohol fuel cells, the effect of water on the activity and selectivity of the electro-oxidation of methanol and ethanol on Pt catalysts was also studied using the recently developed revPBE-vdW functional. Indeed, the presence of water increases the barriers for both C-H and O-H activation because water molecules stabilize the reactants more than the transition states. Hydrogen bonding has a larger effect for the C-H pathway than for the O-H pathway, and hence reverses the selectivity as compared to the gas-phase catalytic reaction. The presence of surface hydroxyl groups at certain applied potential gives rise to the competition between the H-abstraction assisted by surface OH versus the direct dehydrogenation catalyzed by surface metal sites. While the O-H activation by H-abstraction via the proton shuttling mechanism with very low barriers, C-H

activation is facilitated by surface hydroxyl only for surfaces that are less reactive than Pt, such as Ag and Au.

Finally, the reaction path analysis provided insight in the low CO<sub>2</sub> selectivity of Pt catalysts, identified activity and selectivity determining steps and provided suggestions to improve the EOR activity by changing the selectivity of the first two deprotonation steps. The low CO<sub>2</sub> selectivity during ethanol electro-oxidation on Pt catalysts was found to result from the selectivity of the first deprotonation steps, leading to CH<sub>3</sub>CHOH and CH<sub>3</sub>CHO. Screening proved computationally intensive, though some potential candidates with a different selectivity for the first deprotonation steps were identified: Rh, Ru and Ir. Unfortunately, their activity is calculated to be lower than Pt because of their higher C-H activation barriers, which is a challenge for all proposed non-Pt catalysts. The mechanistic knowledge and catalyst design guidance performed in this PhD thesis could be applied to study other fields of catalysis in the future, and few suggestions for future works are also proposed.

## LIST OF TABLES

Table 2.1.	Experimental measurement and computed energy (kJ/mol) with revPBE-vdW functional.	29
Table 3.1	Optimized structures for various well-characterized species on Co(0001) and Ni(100).	39
Table 3.2	Optimized structures and calculated C 1s binding energies for various well-characterized species on Pt(111).	40
Table 3.3	Optimized structures and calculated B 1s binding energies for various well-characterized boron species	41
Table 3.4	Calculated stability under Fischer-Tropsch conditions, $\Delta G_r$ (500 K, 20 bar), and C 1s and B 1s binding energy for various carbon and boron species on Co surfaces.	62
Table 3.5	Relative stability for different possible Pd <sub>3</sub> M@Pd <sub>3</sub> Pt core-shell structures..	66
Table 3.6	Average magnetic moments ( $\mu_B$ /atom) of the 3d transition metal atoms, M, and of the surface Pt atoms in a Pd <sub>3</sub> M@Pd <sub>3</sub> Pt core-shell slab with a four-layer core and a monolayer shell (Figure 3.1).	67
Table 4.1	PdM@PdPt/C sizes determined from the width of the (220) XRD peak (Figure 4.2b), the electrochemically active surface area (ECASA) and corresponding size and the Pd:Pt:M atomic ratios obtained from point-resolved EDX and XPS measurements. The lattice parameters were determined by DFT.	90
Table 4.2	Calculated surface segregation energies for M-Pt exchange (indicated by arrow) in the Pd <sub>3</sub> M@Pd <sub>3</sub> Pt core-shell structures for the clean surface, and with 0.25 ML CO*, OOH*, OH* and O*. Positive values correspond to a stable Pd <sub>3</sub> M@Pd <sub>3</sub> Pt core-shell configuration.	109
Table 5.1	Stabilization energy $E_{stab}$ of water towards the C-H and O-H activation from CH <sub>3</sub> OH and CH <sub>2</sub> OH on Pt(111)	130
Table 5.2	Activation barriers for two pathway of Methoxy decomposition on transition metals (kJ/mol)	138
Table 6.1	Chemical yield of main products in the EOR on different electrocatalyst	149

Table 6.2	Calculated activation barrier for the C-C cleavage in some intermediates on Pt(111)	157
Table 6.3	Calculated activation barriers for the first dehydrogenation steps in ethanol (eV)	158
Table 6.4	Structures of transition states of first dehydrogenation steps from ethanol on Rh and Ru	160

## LIST OF FIGURES

Figure 1.1	Power Generating Systems Efficiency Comparison.	1
Figure 1.2	Schematic of a direct-ethanol fuel cell.	4
Figure 2.1	(a) Initial and (b) final states of the photoemission process. Ejection of the core-electron from level $i$ results in a core-hole at this level. The effect of screening is shown by the increased occupation of the local valence band DOS in (b) compared to (a).	21
Figure 2.2	Top view (a) and side view (b) of ice-like water structure on $p(3 \times 3)$ Pt(111) surface (the dashed line is H-bonding).	24
Figure 2.3	Model used to calculate the Gibbs free energy for the electro-chemical reactions from DFT calculations.	25
Figure 3.1	Model structure to simulate $Pd_3M@Pd_3Pt$ core-shell electrocatalysts. The dark spheres represent Pd atoms, the large grey spheres are surface Pt atoms, and the small grey spheres correspond to core 3d transition metal atoms, M.	43
Figure 3.2	Calculated and experimental C 1s binding energies for various well-characterized carbon species on Co(0001) and Ni(100), using the final-state approximation (a) and the initial-state approximation (b). The adsorption site and the experimental reference are indicated.	48
Figure 3.3	Correlation between the net Bader charge on the carbon atom and the calculated C 1s binding energy.	50
Figure 3.4	(a) Calculated and experimental C 1s binding energies for various well-characterized carbon species on Pt(111). The adsorption site and the experimental reference are indicated. (b) Correlation between the net Bader charge on the carbon atom and the calculated C 1s binding energy	53
Figure 3.5	Calculated and experimental B 1s binding energies for various well-characterized bulk boride structure, using the final-state approximation (a) and the initial-state approximation (b). Experimental references are indicated.	57
Figure 3.6	Correlation between the net Bader charge on the boron atom and the calculated B 1s binding energy	58
Figure 3.7	C 1s XPS spectra for a 20 wt% Co/ $\gamma$ - $Al_2O_3$ catalyst after 200 hours of FTS at 20 bar and 240 °C	61



Figure 3.8	B 1s XPS spectra for a 20 wt% Co/ $\gamma$ -Al <sub>2</sub> O <sub>3</sub> catalyst promoted with 2 wt% boron, after reduction for 12 hours in 50 Nml/min H <sub>2</sub> at 500 °C and at atmospheric pressure.	64
Figure 3.9	Pt 4f XPS spectrum for Pd <sub>3</sub> Fe@Pd <sub>3</sub> Pt/C, as synthesized. The Pt 4f <sub>7/2</sub> peak is indicated.	65
Figure 3.10	(a) Calculated Pt 4f <sub>7/2</sub> surface core-level shift as a function of the core thickness in the model (Fig. 3.1), and for a shell thickness of one layer; (b) Calculated Pt 4f <sub>7/2</sub> surface core-level shift for the surface Pt atoms as a function of the shell thickness for a core thickness of four layers. Filled symbols represent calculated values, while open symbols represent measured Pt 4f <sub>7/2</sub> surface core-level shifts for the corresponding core-shell particles	68
Figure 3.11	Average calculated and experimental Pt 4f <sub>7/2</sub> surface core-level shifts (SCLS) for different shell thicknesses, using the final-state approximation (a), and the initial-state approximation (b).	69
Figure 3.12	(a) Correlation between the net Bader charge on the surface Pt atoms and the calculated Pt 4f <sub>7/2</sub> SCLS for the surface Pt atom for different shell thicknesses and (b) Correlation between the net Bader charge on the surface Pt atoms and the calculated Pt 4f <sub>7/2</sub> SCLS for a series of Pd <sub>3</sub> M@Pt core-shell catalysts with a monolayer Pt shell and a four-layer Pd <sub>3</sub> M core	71
Figure 3.13	Total density of states (DOS) projected on the d-band of the surface Pt atoms in Pd <sub>3</sub> Pt@Pd <sub>3</sub> M. The d-band centers are indicated. Note that a downward shift in d-band correlates with a stronger core-level BEs in Figure 6a. The occupancy of the Pt d-band is shown in the legend. The decreased occupancy, from 0.89 to 0.83, correlates roughly with an increased Pt Bader charge (Figure 3.12a).	73
Figure 4.1	XRD patterns for the PdM/C catalysts with a Pd:M ratio of 70:30 (a) and for the core-shell PdM@PdPt/C (M=Ni, Co, Fe and Cr) catalysts (b). The dotted lines indicate the fcc (111), (200) and (220) peaks positions for PdFe/C and PdFe@PdPt/C. The insert shows the (220) peak that was used to determine the average crystallite sizes in Table 4.1.	89
Figure 4.2	Cyclic voltammograms of core-shell catalyst PdM@PdPt/C (M=Pt, Ni, Co, Fe and Cr) in argon purged 0.1 M HClO <sub>4</sub> . Sweep rate 20 mV s <sup>-1</sup> ; room temperature.	91

Figure 4.3	Pt 4f XPS spectra of PdPt/C (a) and PdM@PdPt/C [M = Ni (b), Co(c), Fe (d) and Cr (e)]. Dot lines indicate the Pt 4f <sub>7/2</sub> peaks deconvoluted with Gaussian-Lorentzian peak fit using XPSpeak software.	92
Figure 4.4	(a) Parity diagram comparing the calculated Pt 4f <sub>7/2</sub> surface core-level shift for a slab with a monolayer Pd <sub>3</sub> Pt placed on four layers Pd <sub>3</sub> M (shown in insert), with the chemical shift measured by XPS for the PdM@PdPt/C catalysts. (b) Correlation between the calculated Pt 4f <sub>7/2</sub> surface core-level shift and the Pt d-band center projected on the surface Pt atoms relative to the Fermi level for this family of Pd <sub>3</sub> M@Pd <sub>3</sub> Pt core-shell structures.	93
Figure 4.5	CO-stripping voltammograms for the PdM@PdPt/C catalysts in 0.1 M HClO <sub>4</sub> after saturation with CO for 900 s. Scan rate: 20 mV/s.	96
Figure 4.6	(a) Correlation between the experimental CO stripping peak and the calculated CO adsorption energy at the Pt top site. (b) Correlation between the calculated CO adsorption energy and d-band center projected on the surface Pt atoms.	97
Figure 4.7	Free-energy diagram for the associative and the dissociative ORR mechanism, calculated on a p(2x2) Pd <sub>3</sub> Cr@Pd <sub>3</sub> Pt core-shell structure, for a potential U of 0.8 V, a pH of 1, 300 K and 1 atm O <sub>2</sub> . Inserts show the optimized O <sub>2</sub> dissociation transition state and the adsorbed OOH* geometry. All free energies were calculated relative to H <sub>2</sub> O(l).	99
Figure 4.8	Calculated Gibbs free reaction energy to form OOH* from O <sub>2</sub> (g) ( $\Delta G_{\text{OOH}}$ ), to protonate O* ( $\Delta G_{\text{O/OH}}$ ) and to dissociate O <sub>2</sub> ( $\Delta G^{\text{TS}}$ ), as illustrated in (a), for a potential U of 0.8 V and pH of 1, as a function of the oxygen affinity, $\Delta E_{\text{O}}$ (equation (3))	101
Figure 4.9	Oxygen binding energy, $\Delta E_{\text{O}}$ , as a function of center of the d-band projected on surface Pt atoms, $\epsilon_{\text{d}}$ .	103
Figure 4.10	ORR linear-sweep voltammograms for the PdM@PdPt/C (M=Pt, Ni, Co, Fe and Cr) electrocatalysts in an oxygen-saturated, 0.1M HClO <sub>4</sub> solution. Standard three-electrode cell with a sweep rate of 20 mV/s, rotation speed of 1600 rpm and at room temperature.	104
Figure 4.11	Kinetic mass activities at 0.8, 0.85 and 0.9 V RHE as a function of calculated oxygen binding energy.	105
Figure 4.12	(a) Kinetic mass activity at 0.8 V RHE as a function of CO stripping peak position and (b) Kinetic mass activity at 0.8 V RHE as a function of XPS Pt 4f <sub>7/2</sub> surface core-level shifts	106

- Figure 4.13 (a) ORR linear-sweep voltammograms for the PdM@PdPt/C (M=Pt, Ni, Co, Fe and Cr) electrocatalysts and for a commercial 3.0 nm Pt/C reference catalyst in an oxygen-saturated, 0.1M HClO<sub>4</sub> solution **in the presence of 0.1 M methanol**. Standard three-electrode cell with a sweep rate of 20 mV/s, rotation speed of 1600 rpm and at room temperature. (b) Kinetic mass activities at 0.9 V RHE without and with 0.1 M methanol as a function of calculated oxygen binding energy,  $\Delta E_{\text{O}}$ . The kinetic mass activity of a commercial 3.0 nm Pt/C catalyst without and with 0.1 M methanol (open symbols) is included for comparison. 107
- Figure 5.1 (a) Ice-like structure of water layer on Pt(111); (b) Adsorption of Methanol on pre-covered water layer on Pt(111); (c),(d) Two configurations of the adsorption of Methanol with 4 water on Pt(111). Adsorption energy  $E_{\text{ads}} = E_{\text{Methanol-water/Pt}} - E_{\text{water/Pt}} - E_{\text{Methanol(gas)}}$ . The reaction energy  $\Delta E_{\text{rxn}}$  is calculated for the reaction:  $\text{CH}_3\text{OH}_{(\text{l})} + 6 \text{H}_2\text{O}^* \rightarrow \text{CH}_3\text{OH-nH}_2\text{O}^* + (6-n) \text{H}_2\text{O}_{(\text{l})}$ ; (e),(f) two configurations of Methanol coadsorbed with a single water on Pt(111). 124
- Figure 5.2 Transition states of C-H (a) and O-H (b) activation from CH<sub>3</sub>OH, Transition states of C-H (c) and O-H (d) activation from CH<sub>2</sub>OH and C-H activation from CH<sub>3</sub>O (e) on clean Pt(111) surface. Reaction energy  $\Delta E$  is calculated for the reaction:  $\text{A-H}^* + * \rightarrow \text{A}^* + \text{H}^*$  (H\* and A\* are on separate unit cells). 127
- Figure 5.3 Two configurations of adsorbed CH<sub>2</sub>O on Pt(111): di- $\sigma$   $\eta(\text{C},\text{O})$  structure (a) and  $\eta(\text{O})$  atop structure (b) 128
- Figure 5.4 Transition states of C-H (a) and O-H (b) activation from CH<sub>3</sub>OH on surface with single water co-adsorbed. 129
- Figure 5.5 (a) OH activation in Methanol on Pt(111) with 5/9 ML coverage of water; (b) and (c) CH and O-H activation in Methanol on Pt(111) with 4/9 ML coverage of water. 131
- Figure 5.6 Adsorption of CH<sub>2</sub>OH (a); and the activation of C-H (b) and O-H (c) from CH<sub>2</sub>OH on water covered Pt(111) surface; 133
- Figure 5.7 Adsorption of CH<sub>3</sub>O (a) and the transition state of CH activation from CH<sub>3</sub>O (b) on water covered Pt(111) surface 134
- Figure 5.8 Replacement of one water by surface Hydroxyl group in (a) C-H activation and (b) O-H activation from CH<sub>3</sub>OH on water covered Pt(111) 135

Figure 5.9	Surface OH assistance reactions on Pt(111): (a) Activation of C-H and (b) activation of OH from CH <sub>3</sub> OH	136
Figure 5.10	Surface OH assistance reaction on Pt(111): (a) OH activation in CH <sub>2</sub> OH and (b) CH activation in CH <sub>3</sub> O	137
Figure 5.11	OH activation in CH <sub>3</sub> O assisted by surface Hydroxyl group on water covered Au(111)	138
Figure 5.12	Decomposition of Methoxy on Au(111): the direct dehydrogenation pathway (a), and the H-abstraction by surface Hydroxyl pathway (b)	139
Figure 5.13	Decomposition of Methoxy on Pd(111): the direct dehydrogenation pathway (a), and the H-abstraction by surface Hydroxyl pathway (b)	140
Figure 5.14	Correlation between the activation barriers difference of the two pathways versus the charge of transferred H atom in the H-abstraction pathway	141
Figure 5.15	The reaction Energy Profile for the Deprotonation of Methanol on Pt(111). (a) Reactions under UHV on clean surface; (b) Reactions in aqueous media on water covered surface. The reaction on clean surface and in water on Pt(111) can be expressed by the reaction: A-H → A + H, while the reaction in the surface OH assisted pathways can be expressed by the reaction: A-H + OH → A + H <sub>2</sub> O.	142
Figure 6.1	Mechanism of the electro-oxidation of ethanol on platinum electrodes	152
Figure 6.2	Reaction map for the ethanol decomposition on Rh(111)	153
Figure 6.3	Possible pathways for the C–C bond breaking of ethanol on the ternary RhPt/SnO <sub>2</sub> (110) catalyst.	154
Figure 6.4	Energy profile of ethanol decomposition on Pt(111)	157
Figure 6.5	Two first Deprotonation step of Ethanol decomposition on Ir(111)	163
Figure 6.6	Two first Deprotonation steps of Ethanol decomposition on Rh(111)	164
Figure 6.7	Two first Deprotonation step of Ethanol decomposition on Ru(0001)	165
Figure 7.1	Diagram of the Krebs cycle	175

Figure 7.2 Mechanisms operated in the WGS reaction over ceria- 177  
supported platinum catalysts, surface oxygen vacancy is  
indicated by the blank square

# SYMBOLS AND ABBREVIATIONS

## Symbols

$\psi(\vec{x}, \vec{R})$	Wave function
$\rho(\vec{r})$	Electronic density
$\varepsilon_C$	Core state
$\varepsilon_F$	Fermi level
$\varepsilon_{xc}$	Exchange-correlation energy per particle of the uniform electron gas
$E$	Total energy of the system
$E_b$	Binding energy
$E_{CL}$	Energy difference between two separate calculations
$E_{edge}$	Edge energy
$E_{ee}$	Electron-electron repulsion energy
$E_{\text{graphene}}$	Total energy per carbon atom for the graphene-covered surface
$E_{(nc)}$	Energy of core electrons at the unexcited stage
$E_{(nc-1)}$	Energy of core electrons at the valence/conduction band
$E_{ne}$	Nucleus-electron interaction energy
$E_{SCLS}$	Energy of the surface core level shift
$G$	Gibbs Free Energy
$H$	Enthalpy
$h$	Plank's constant
$k$	Boltzmann constant
$R$	Gas constant
$S$	Entropy
$T$	Temperature
$\nu_i$	Vibrational frequencies

## Abbreviations

AES	Atomic Emission Spectroscopy
ASAXS	Anomalous Small Angle X-ray Scattering
CPMD	Car–Parrinello molecular dynamics
CPO	Catalytic Partial Oxidation
CSTR	Continuously Stirred Tank Reactor
DFT	Density Functional Theory
DRIFTS	Diffused Reflectance Infrared Fourier Transform Spectroscopy
EXAFS	Extended X-ray Absorption
FBR	Fixed Bed Reactor
FFT	Fast Fourier Transformations
FID	Flame Ionization Detector
FLAPW	Full-Potential Linearised Augmented Plane-Wave-Method
FTIR	Fourier Transform Infra-Red spectroscopy
FTS	Fischer-Tropsch Synthesis
GGA	Generalized Gradient Approximation
HAADF	High Angle Angular Dark Filed
HREELS	High-Resolution Electron Energy Loss Spectroscopy
ICP-OES	Inductively Coupled Plasma-Optical Emission Spectrometry
LDA	Local Density Approximation
LEED	Low Energy Electron Diffraction
MC	Monte Carlo
MEP	Minimum Energy Path
NEB	Nudged Elastic Band
PAW	Projector-Augmented-Wave
PBE	Perdew-Burke-Ernzerhof functional
PDOS	Projected Density of States
PES	Potential Energy Surface
PW91	Perdew-Wang 91 functional
RPBE	Revised Perdew-Burke-Ernzerhof functional
RMM	Residual Minimization Method
SBCR	Slurry Bubble Column Reactor

SEM	Scanning Electron Microscopy
GHSV	Gas Hourly Space Velocity
SPARG	Sulfur Passivated Reforming
SR	Steam Reforming
STM	Scanning Tunneling Microscopy
TCD	Thermal Conductivity Detector
TEM	Transmission Electron Microscopy
TGA	Thermo-Gravimetric Analysis
TOF	Turnover Frequency
TPH	Temperature Programmed Hydrogenation
TPR	Temperature Programmed Reduction
TPO	Temperature Programmed Oxidation
UHV	Ultra High Vacuum
VASP	Vienna Ab-Initio Simulation Package
WGS	Water Gas Shift
XANES	X-ray Absorption Near Edge Spectroscopy
XRD	X-Ray Diffraction
XPS	X-ray Photoelectron Spectroscopy



## PUBLICATIONS

1. **Q.T. Trinh**, J.H. Yang, J.Y. Lee, M. Saeys, “Computational and experimental study of the Volcano behaviour of the oxygen reduction activity on PdM@PdPt/C (M = Pt, Ni, Co, Fe, and Cr) core-shell electrocatalysts”, *Journal of Catalysis*, 291 (2012), 26.
2. **Q.T. Trinh**, K.F. Tan, A. Borgna, M. Saeys, “Evaluating the Structure of Catalysts using First Principle calculated XPS Core-Level Binding Energies”, *Journal of Physical Chemistry C*, 117 (2013), 1684.
3. **Q.T. Trinh**, M. Saeys, “Role of water on the CH/OH selectivity reversal in the decomposition of methanol on Pt”, (to be submitted for publication)
4. **Q.T. Trinh**, M. Saeys, “Decomposition of Methoxy on transition metals: the competition between Direct Dehydrogenation versus surface Hydroxyl assistance pathways”, (in preparation, invited by Editor to submit to *AIChE Journal*)

## CONFERENCES

1. “*Design of a Core-shell Oxygen Reduction Catalysts: Theoretical and Experimental Volcano Curve*”, **Q.T. Trinh**, J.H. Yang, J.Y. Lee, M. Saeys, poster presentation, Gordon Research Conference – Catalysis, Colby-Sawyer College, New London, NH, UK, June 27 - July 2, 2010.

2. “*Volcano behavior of Pd<sub>3</sub>M@Pd<sub>3</sub>Pt core-shell oxygen reduction electrocatalysts by gradually changing the oxygen binding energies.*”, **Q.T. Trinh**, M. Saeys, oral presentation, the 2011 AIChE Annual Meeting, October 16-21, Minneapolis Convention Center, Minneapolis, MN, USA.
  
3. “*Describing High Surface Coverage Effects Under Reaction Conditions Using Van Der Waals Functionals: CO Adsorption and Aqueous Environments*”, G.T.K.K. Gunasooriya, **Q.T. Trinh**, M. Saeys, oral presentation, the 2013 AIChE Annual Meeting, November 03-08, San Francisco, California, USA.
  
4. “*Reaction Path Analysis of Ethanol Electro-Oxidation On Pt(111): Role of Water*”, **Q.T. Trinh**, M. Saeys, oral presentation, the 2013 AIChE Annual Meeting, November 03-08, San Francisco, California, United States. (**Best Presentation** in the session “*Reaction Path Analysis II*”, identified by Andrew J. Adamczyk (Massachusetts Institute of Technology)) with the invitation to submit a research article or AIChE letter to the AIChE Journal and will be published as “**Best Paper**” if accepted
  
5. “*Influence of water on the CH/OH selectivity in the decomposition of methanol on a Pt catalyst*”, **Q.T. Trinh**, M. Saeys, poster presentation, the 7<sup>th</sup> Singapore Catalysis Forum, Biopolis, Singapore, May 23, 2014.

# CHAPTER 1

## INTRODUCTION

### 1.1. Overview of Direct Alcohols fuel cells

Discovered in 1839 by Sir William Grove, the fuel cell is an electrochemical device which can convert chemical energy into electrical energy [1]. The oxidation of the fuel (e.g., hydrogen, methanol, ethanol, glycerol...) occurs at the anode whereas the reduction of oxidant (usually oxygen from air) occurs at the cathode. Nowadays, fuel cell systems are attracting lots of attention as promising technologies with less pollution and significantly higher thermodynamic efficiency than conventional heat engines (Figure 1.1) [2].

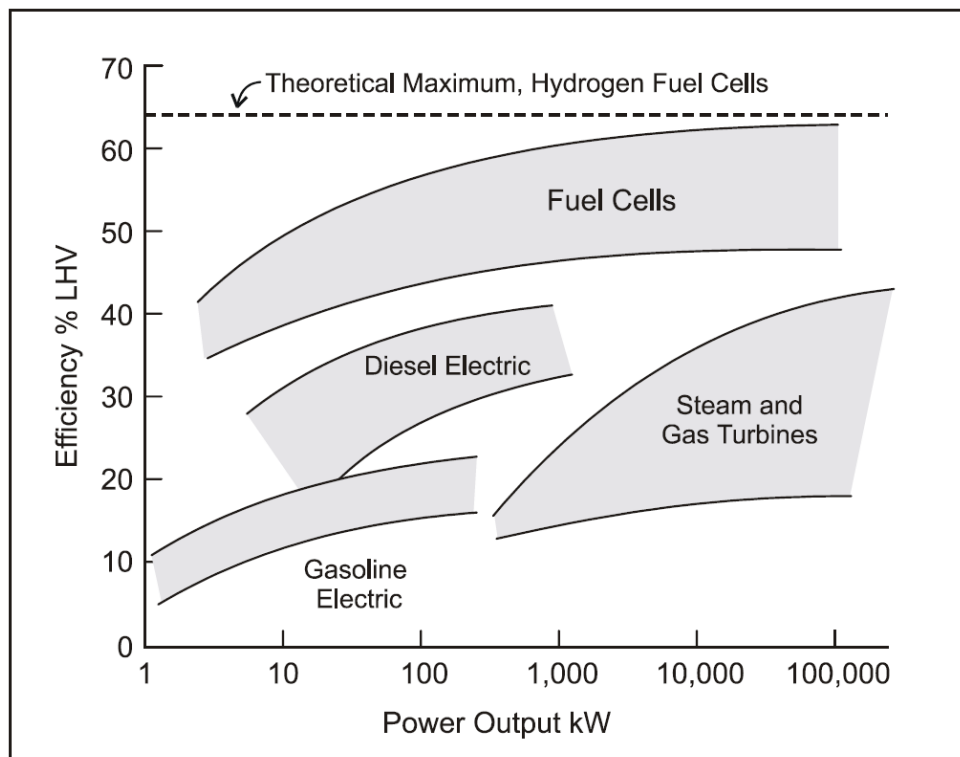


**Figure 1.1:** Power Generating Systems Efficiency Comparison [2]

Heat engines, which consume heat from the combustion of fuel to do useful work, have a maximum thermodynamic efficiency  $\varepsilon_{max}$  (Carnot limit) derived from equation (1) [3]:

$$\varepsilon_{max} = 1 - \frac{T_C}{T_H} \quad (1)$$

where  $T_C$  and  $T_H$  are the absolute temperature of the cold (outlet) and the hot (inlet) source, respectively. From this formula, in order to increase the thermodynamic efficiency of heat engines, we should increase the inlet temperature or decrease the outlet temperature. However the outlet temperature  $T_C$  cannot be lower than ambient temperature, and the inlet temperature is limited by material considerations, therefore the energy efficiency of heat engines cannot be as high as desired. It means even under ideal conditions, a heat engine is incapable of converting all heat energy supplied to it into mechanical energy and some of the heat is dissipated. In practical conditions, energy efficiencies of heat engines are much lower than the Carnot limit, e.g. the average efficiency of gasoline engine is less than 20% of the lower heating value (LHV) (Figure 1.1) [2]. As Carnot's theorem only applies to the conversion of heat into work, devices such as fuel cells that produce electrical energy converted from chemical energy in the fuel to do useful work can overcome the Carnot efficiency. This means that the maximum available work that the fuel cell could release is equal to the free energy change for the reaction, which is -229 kJ/mol for Hydrogen fuel cell [4]. Therefore, the advantage of fuel cell systems is that they have significantly higher energy efficiency [2,4-7]. The development of better polymer electrolyte membrane, which selectively allows the positively ion

(proton) to pass through it from anode to the cathode, makes the Proton exchange membrane fuel cells (PEMFCs) become a prime technology for small-to mid size applications such as portable devices [4-6].

Though widely applied commercially, Hydrogen-fed polymer electrolyte membrane fuel cells are weighed down by issues such as low volumetric energy density, non-renewability, and the supply, delivery and storage of hydrogen [4-7]. Many of these problems can be circumvented by replacing hydrogen with a liquid fuel. A liquid PEMFC also offers the convenience of “instant recharge” for portable electronic products through refueling [6,7]. Small hydrocarbon oxygenates such as methanol and ethanol are suitable liquid fuels from the viewpoint of energy density (24 MJ/L of ethanol and 15.6 MJ/L of methanol compare to 10.1 MJ/L of liquefied Hydrogen) [7-10]. Another advantage of alcohol fuel cells is that they are liquids at room temperature and can overcome the storage and transportation challenges in hydrogen fuel cells. They also can be electro-catalytically oxidized at relatively low temperatures although their reactivities are currently several orders of magnitude lower than that of hydrogen oxidation using standard Pt catalysts [10].

The DAFCs consist of the anode where the Alcohol electro-oxidation reaction occurs and the cathode where the oxygen reduction reaction (ORR) occurs. A proton exchange membrane (PEM) which serves as the electrolyte separates these two electrodes and selectively allows the protons to move from the anode to the cathode. The produced electrons flow through a circuit to the

cathode, forming an electric current to do useful work. The working principle of DAFCs is illustrated in Figure 2 [8]:

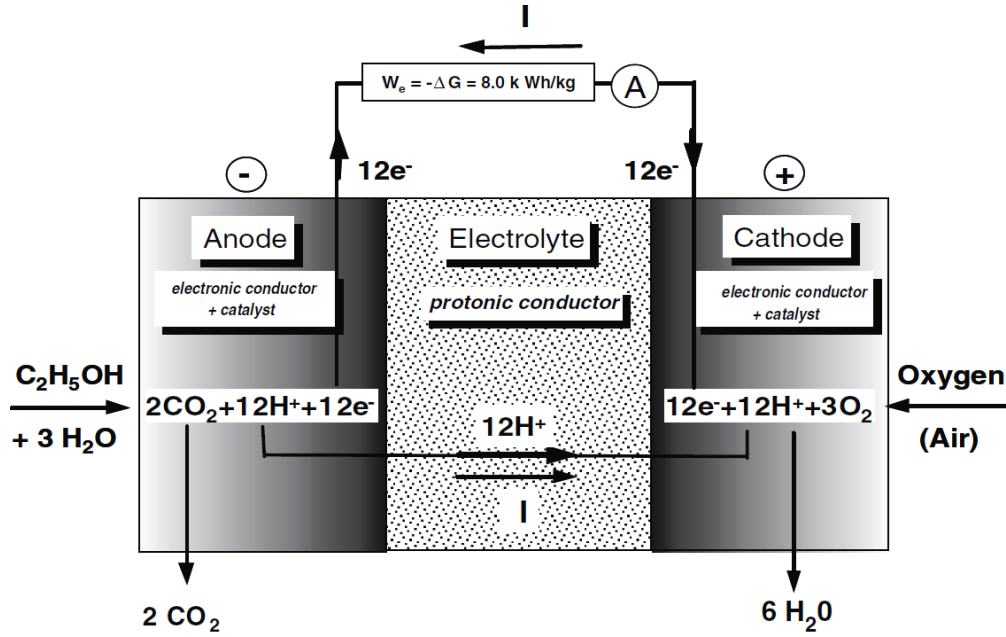
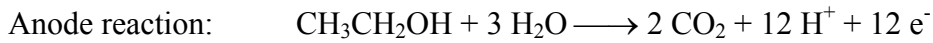


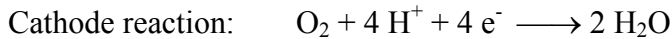
**Figure 1.2:** Schematic of a direct-ethanol fuel cell [8]

Using the Standard Gibbs free energy of formation  $\Delta G_f^0$  of individual compounds extracted from W.M. Haynes, CRC Handbook of Chemistry and Physics, [11] the change of Gibbs free energy for reactions at the anode and cathode and the standard electrode potentials  $E_1^0$  versus the standard hydrogen (reference) electrode (V vs SHE) calculated from Nernst equation [8] are:



$$\begin{aligned} \Delta G_1^0 &= 2 \times \Delta G_{\text{fCO}_2}^0 - (\Delta G_{\text{fCH}_3\text{CH}_2\text{OH}}^0 + 3 \times \Delta G_{\text{fH}_2\text{O}}^0) \\ &= 2 \times (-394.4) - (-178.4 + 3 \times (-237.1)) = -97.3 \frac{\text{kJ}}{\text{mol}} \end{aligned}$$

$$\Rightarrow E_1^0 = -\frac{\Delta G_1^0}{12F} = 0.085 \text{ V vs SHE} \quad (2)$$



$$\Delta G_2^0 = \Delta G_{\text{fH}_2\text{O}}^0 = 237.1 \frac{\text{kJ}}{\text{mol}} \Rightarrow E_2^0 = -\frac{\Delta G_2^0}{2F} = 1.23 \text{ V vs SHE} \quad (3)$$

Overall reaction:  $\text{CH}_3\text{CH}_2\text{OH} + 3 \text{O}_2 \longrightarrow 2 \text{CO}_2 + 3 \text{H}_2\text{O}$

The standard electromotive force (emf) at equilibrium  $E_{eq}^0$  is:

$$E_{eq}^0 = -\frac{\Delta G^0}{nF} = -\frac{6\Delta G_2^0 - \Delta G_1^0}{nF} = E_2^0 - E_1^0 = 1.145 \text{ V} \quad (4)$$

where  $F = 96485$  Coulomb is the Faraday constant.

From those thermodynamic data, DAFCs have quite high equilibrium electromotive force close to that of Hydrogen fuel cell (1.23 V). The energy efficiency for the above direct ethanol fuel cell in Figure 1.2 is the ratio between the electrical energy  $\Delta G$  and the heat of combustion energy  $\Delta H$ :

$$\varepsilon_{eq}^0 = \frac{\Delta G^0}{\Delta H^0} = \frac{1325}{1366} = 97\% \quad (5)$$

The generated electrons travel through an external circuit and produce electricity with the mass energy density  $W_e \approx 8 \text{ kWh/kg}$ .

On both two electrode sides of DAFCs, there are layers of catalysts to facilitate the electrochemical reactions, include the alcohol electro-oxidation reaction on anode side and Oxygen reduction reaction on cathode side. Pt is the most common catalyst component for electrochemical reactions such as electro-reduction of oxygen and electro-oxidation of alcohols, especially for fuel cell applications [10,12]. Until now, Pt is still the best pure catalyst for DAFCs [10,13]. However, the activity of Pt catalyst alone is not satisfied, and the catalytic activity of Pt could also be increased by modifying by other foreign atom adsorption (e.g. Sn, Rh and Os), or alloying Pt with another transition metals [14-16]. Alloying Pt electrocatalysts with 3d transition metals such as Ni, Co and Cr could enhances the ORR activity by a factor 2 to 3

[6,12], while alloying Pt with Y improves the ORR activity by a factor 6 to 10. [14] Recently, an 8-fold variation in ORR activity was reported when the submonolayer concentration of Cu in Pt(111) was changed for a series of model Cu/Pt(111) near-surface alloys with a varying subsurface Cu coverage. [19] Recently, the design of core-shell type electro-catalyst is receiving much attention as good electro-catalyst DAFCs, and core-shell catalysts have shown dramatically improvement in the activity for both oxygen reduction reaction and alcohol oxidation reaction [17-19]. However the structural study of those catalysts is very challenging. The nano-particle size in the catalysts is always less than 3 nm, which makes it very difficult for characterization, especially so for catalysts with core-shell structure due to the more complicated composition. Since the shell thickness is about 1 monolayer, it is nearly impossible to prove the core-shell structure via conventional technique such as XRD, TEM... [17,20] Therefore, the development of new characterization techniques becomes very important for the design of advanced DAFCs electro-catalyst.

Among alcohol fuel cells, direct methanol fuel cell (DMFC) has been most extensively developed since its first time explored by E. Muller in 1922. [21] DMFC has been applied in some small portable electronic devices such as cellular phones, music players, and notebooks... [7,22,23]. The developments in catalysts and technology have increased the energy efficiency of DMFCs to 40%, and made DMFC applicable not only in small to mid-sized applications, but also car engines [7,23]. However, despite extensively studied, the activities of anode and cathode electro-catalysts still need to be improved to achieve the



large-scale commercialization of DMFCs, beside to overcome other challenges include the high cost of electro-catalysts, high cost of the Nafion membrane, and the crossover problem... [9,17,24] Especially, the oxygen electrode problem is one of long term problems in research that are vital to the development of future technology [25]. For DMFC, one of materials-related issues is the low activity of Pt-based cathode catalysts in the oxygen reduction reaction (ORR), which is exacerbated by the presence of methanol crossover from the anode through the polymer electrolyte membrane (PEM), and the activity of some good methanol tolerance is still less than optimal [7,26]. Because of that, the investigation of more economical (by reducing the amount of Pt used) and more active oxygen electrode catalysts has been identified as an important challenge for the introduction of fuel cell technology [17,25].

The mechanism of Methanol electro-oxidation on a Pt surface has been studied extensively experimentally [27-30]. One of the pioneers is the methanol electro-oxidation kinetic study by Begotzky et al. which proposed a stepwise dehydrogenation scheme. [27] Later studies were conducted on well characterized monocrystalline Pt, polycrystalline Pt, thin film Pt and alloys of Pt [28-31]. However from experimental works, the complex 6-electron-transfer reaction mechanism is still not very comprehensively illustrated and the competitive between initial C-H versus O-H activation pathway is still confusing. The influence of water towards the initial activation steps was briefly mentioned in some studies, but the understanding of the role of water is missing. Theoretically studies could provide detailed mechanism for Methanol oxidation on Pt, but major of those studies were conducted on clean surface

under Ultra high vacuum (UHV) conditions [32-36]. Actually water plays an important role in aqueous phase catalytic reactions, such as electro-oxidation in direct alcohol fuel cells. Water can increase the activity and change the selectivity of the reaction [36-38]. Moreover, the mechanism of the methanol oxidation reaction was suggested to be different when changing from using a gas-fed electrode to the electrolyte-fed electrode [39]. In particular, water not only affects the activity and selectivity, it can also act as the source of active hydroxyl groups and open another reaction pathway [40-42]. However, the role of surface hydroxyl group, which has been claimed to play an important role in the activation of O-H bonds in alcohols [38,43-45], are not considered comprehensively when studying the decomposition of alcohols. Therefore understanding the detailed mechanism of the methanol oxidation in water media take into account the integration of surface hydroxyl is crucial to design better anode electro-catalyst for DMFC.

The Direct Ethanol Fuel Cell (DAFC) is a strong emerging alternative to the DMFC, which benefits from the non-toxicity and a higher energy density [6,8]. Therefore, in principle, DEFCs can power portable devices for a longer period of time with the same volume of fuel. Besides, the similarities between DEFC and DMFC could shorten the development of DEFCs since they can share many common features. Additionally, ethanol can be considered a “carbon neutral” fuel since it can be produced from renewable resources through fermentation of biomass. The use of ethanol would also be much more convenient than hydrogen for fuel cell applications, because it is easily stored and transported. The rising interest in DEFCs is evidenced by the escalating

number of research publications on this technology in recent years. Most of these publications are focused on the development of anode catalysts for ethanol electro-oxidation [8-10,46-48]. However, the activity of current catalysts for the ethanol oxidation reaction (EOR) is unsatisfactory, and until now there is still lacking good catalysts [8-10]. The difficulties in C-C cleavage at mild reaction conditions and the low selectivity towards CO<sub>2</sub> have limited the development of DEFCs. For most catalysts, the major products of EOR are acetaldehyde and acetic acid corresponding with two and four released electrons, respectively, while the complete oxidation to carbon dioxide release 12 electrons [8], and as a result, the efficiency of DEFCs is generally poor. For example, for DEFC working at 0.5 V, the energy efficiency is about 42.4% for complete oxidation to CO<sub>2</sub>, while it is only about 14% for the partial oxidation to acetic acid [8]. Until now the best catalyst is the ternary PtRhSnO<sub>2</sub>/C electro-catalyst was synthesized by the cation-adsorption-reduction-galvanic displacement method, and showed high activity in the ethanol oxidation [16]. However this catalyst is still far from commercialization, based on both stability and cost. Therefore, it is very important to find a better catalyst for the oxidation of ethanol to CO<sub>2</sub> to promote the development of DEFCs.

Currently, first principle calculations provide powerful tools to study and design heterogeneous catalysts, especially for complicated, multi-step reactions in electrochemical systems [13,17,18,36-38,47,48]. The typical scale to study catalytic reactions is the molecular scale - a scale which is difficult to access experimentally. First principles based molecular modelling on the other

hand is best placed to investigate molecular level effects and can greatly help to guide and validate the chemical intuition on the molecular scale [17,49,50]. Recent examples, e.g. the design of Ni catalysts with improved stability by promotion with Au [51], Sn [52] and B [53,54], understanding the deactivated mechanism and guide design of more stable Co Fischer-Tropsch Synthesis (FTS) catalyst [55,56], the design of more active hydro-desulphurisation catalysts, and the design of a BiPt electro-catalyst for the hydrogen evolution reaction [57], illustrate how first principles based modelling is beginning to guide the design of heterogeneous catalysts with improved activity, selectivity and stability. Recent advances in the theoretical description of electro-catalytic reactions [e.g. 13,36,58 and references therein] have opened the possibility to begin to use first principles based modelling to design improved electro-catalytic materials. Therefore, in this PhD study, first principle calculations will be used to model and guide design catalyst for electro-chemical reactions for DAFCs.

## **1.2. Aim and structure of thesis**

The aim of this PhD study therefore is to apply first principle calculations in modelling the electro-chemical reactions and developing active electro-catalysts for direct alcohol fuel cells (DMFC and DEFC) operating at ambient conditions. In essence, the thesis addresses modeling of heterogeneous catalyst for electrochemical reactions in Direct Alcohol fuel cells at four aspects include the structural evaluation, mechanistic study, catalytic activity and selectivity evaluation in realistic conditions.

The specific activities in this thesis study include the following topics:

1. Develop the model to evaluate the structure of nano-particle heterogeneous catalyst based on combining DFT core-level shift calculations and XPS measurement. Apply the developed model to evaluate the deactivation of the Co catalyst and the promotion effect of Boron on Co catalysts in Fischer-Tropsch synthesis (FTS), and expand this model in combine with point resolved to study the structure of core-shell electro catalysts.
2. Build the thermodynamic model to evaluate the activity of catalyst in electro-chemical reactions in realistic conditions include applied potential, room temperature and solvent pH. Apply this model to design an optimal catalyst for the oxygen reduction reaction (ORR), in which the activity is governed by the Sabatier principle and follows a Volcano curve.
3. Study the role of water towards the decomposition of Alcohol. As the electro-oxidation reaction of alcohol occurs in aqueous phase, the results of the influence of water will provide the comprehensive mechanistic understanding for the Alcohol electro-oxidation.
4. Identify the determining steps for the selectivity towards CO<sub>2</sub> (complete oxidation) of Ethanol oxidation reaction (EOR) and guided design catalyst for the EOR. This is done by analyzing all the elementary steps during the reaction on atomic level by Density functional theory calculations to identify the key determining steps for improvement suggestion.

The structure of this thesis will be organized as follow. In Chapter 2, the theory of first principle calculations will be briefly mentioned, follows by the description of applied computational modeling procedures in this study. Chapter 3 will present the structural evaluation of catalysts using first principle calculated XPS core-level binding energies and guided characterize core-shell electro-catalysts. A series of PdM@PdPt/C (M = Pt, Ni, Co, Fe, and Cr) core-shell electro-catalysts will be subject to the computational and experimental study of the Volcano behavior of the oxygen reduction activity to guide design of an optimal catalyst in Chapter 4. After that in Chapter 5, theoretical study on the oxidative mechanism of alcohol in aqueous environment and the role of water towards the alcohol decomposition will be conducted. Chapter 6 will show the preliminary results on designing catalyst for Ethanol oxidation reaction (EOR), wherein the detailed energy profile of EOR on Pt (111) surface is analyzed to identify selectivity determining steps and further research is carried out by calculating EOR on different transition metal surfaces (Pt, Pd, Rh, Co, Ir and Ru) in order to screen the best candidates for C-C bond cleavage. Finally, the conclusion and suggestions for future study are summarized in Chapter 7.

### **1.3. References.**

1. W. R. Grove, *Philosophical Magazine*, **14**, 127 (1839).
2. J. Dempsey (Edt), *Hydrogen Fuel Cell Engines and Related Technologies*, *College of the Desert*, Palm Desert, CA, USA, (2001).
3. M.J. Moran, H.N. Shapiro, *Fundamentals of Engineering Thermodynamics (6th Edition)*, John Wiley & Sons, Inc, New York, (2007).

4. I. Pilatowsky, R.J. Romero, C.A. Isaza, S.A. Gamboa, P.J. Sebastian, W. Rivera, *Cogeneration Fuel Cell-Sorption Air Conditioning Systems*, Springer-Verlag London, (2011).
5. R. Strobel, M. Oszcipok, M. Fasil, B. Rohland, L. Jorissen, J. Garche, *Journal of Power Sources*, **105**, 208 (2002).
6. W. Vielstich, H.A. Gasteiger, A. Lamm (Edt), *Handbook of Fuel Cells – Fundamentals, Technology and Applications*, John Wiley & Sons, Ltd, (2010).
7. A.S. Aricò, V. Baglio, and V. Antonucci, *Direct Methanol Fuel Cells: History, Status and Perspectives*, in H. Liu and J. Zhang (Edt), *Electrocatalysis of Direct Methanol Fuel Cells: From Fundamentals to Applications*, WILEY-VCH Verlag GmbH & Co. KGaA, Weinheim, pp. 1 – 78 (2009).
8. F. Vigier, S. Rousseau, C. Coutanceau, J.-M. Leger, C. Lamy, *Top. Catal.*, **40**, 111 (2006)
9. A. Rabis, P. Rodriguez, and T. J. Schmidt, *ACS Catal.*, **2**, 864 (2012).
10. E.H. Yu, X. Wang, X.T. Liu and L. Li, *Challenges and Perspectives of Nanocatalysts in Alcohol-Fuelled Direct Oxidation Fuel Cells*, in Z.-X. Liang and T.S. Zhao (Edts), *Catalysts for Alcohol-Fuelled Direct Oxidation Fuel Cells*, Royal Society of Chemistry, Cambridge, pp. 227-249 (2012).
11. W.M. Haynes, *CRC Handbook of Chemistry and Physics*, CRC Press/Taylor and Francis, Boca Raton, FL, (2010)
12. Q. Wang, G.Q. Sun, L.H. Jiang, Q. Xin, S.G. Sun, Y.X. Jiang, S.P. Chen, Z. Jusys, R. Behm, *Phys. Chem. Chem. Phys.*, **9**, 2686 (2007).

13. J.K. Nørskov, J. Rossmeisl, A. Logadottir, L. Lindqvist, J.R. Kitchin, T. Bligaard, H. Jónsson, *J. Phys. Chem. B*, **108**, 17886 (2004).
14. A. Kowal, M. Li, M. Shao, K. Sasaki, M.B. Vukmirovic, J. Zhang, N.S. Marinkovic, P. Liu, A.I. Frenkel, R.R. Adzic, *Nat. Mat.*, **8**, 325 (2009).
15. G. Wu, R. Swaidan, G.F. Cui, *J. Power Sources*, **172**, 180 (2007).
16. J. Melke, A. Schoekel, D. Dixon, C. Cremers, D.E. Ramaker, C. Roth, *J. Phys. Chem. C*, **114**, 5914 (2010).
17. Q.T. Trinh, J.H. Yang, J.Y. Lee, M. Saeys, *J. Catal.*, **291**, 26 (2012).
18. W.P. Zhou, X.F. Yang, M.B. Vukmirovic, B.E. Koel, J. Jiao, G. Peng, M. Mavrikakis, R.R. Adzic, *J. Am. Chem. Soc.*, **131**, 12755 (2009).
19. I.E.L. Stephens, A.S. Bondarenko, F.J. Perez-Alonso, F. Calle-Vallejo, L. Bech, T.P. Johansson, A.K. Jepsen, R. Frydendal, B.P. Knudsen, J. Rossmeisl, I. Chorkendorff, *J. Am. Chem. Soc.*, **133**, 5485 (2011).
20. C. Coutanceau, S. Brimaud, C. Lamy, J.-M. Leger, L. Dubau, S. Rousseau, F. Vigier, *Electrochimica Acta*, **53**, 6865 (2008).
21. E. Müller, *Z. Elektrochem.*, **28**, 101 (1922).
22. C. Lamy, E.M. Belgsir, J.-M. Leger, *J. Appl. Electrochem.*, **31**, 799 (2001).
23. J. Mergel, H. Janßen, M. Müller, J. Wilhelm, D. Stolten, *J. Fuel Cell Sci. Technol.*, **9**, 031011 (2012).
24. J. N. Tiwari, R. N. Tiwari, G. Singh, K. S. Kim, *Nano Energy*, **2**, 553 (2013).
25. G.M. Whitesides, G.W. Crabtree, *Science*, **315**, 796 (2007).
26. T. Lopes, E. Antolini, E.R. Gonzalez, *Int. J. Hydrogen Energy*, **33**, 5563 (2008).



27. V.S. Bagotzki and Yu. Vassileiv, *Electrochim. Acta*, **12**, 1323 (1967).
28. C. Lamy and C. Coutanceau, *Electrocatalysis of Alcohol Oxidation Reactions at Platinum Group Metals*, in Z.-X. Liang and T.S. Zhao (Edts), *Catalysts for Alcohol-Fuelled Direct Oxidation Fuel Cells*, Royal Society of Chemistry, Cambridge, pp. 1-70, (2012).
29. E. Gyenge, *Electrocatalytic Oxidation of Methanol, Ethanol and Formic Acid*, in H. Liu and J. Zhang (Edt), *Electrocatalysis of Direct Methanol Fuel Cells: From Fundamentals to Applications*, WILEY-VCH Verlag GmbH & Co. KGaA, Weinheim, pp. 165 – 287, (2009).
30. M.T.M. Koper, S.C.S. Lai, E. Herrero, *Mechanism of the oxidation of Carbon monoxide and small organic molecules at metal electrodes*, in M.T.M. Koper (Edt), *Fuel Cell Catalysis: A Surface Science Approach*, John Wiley & Sons, Inc., Hoboken, New Jersey, pp. 159 – 207, (2009).
31. A. Hamnett, *Catalysis Today*, **38**, 445 (1997).
32. J. Greeley, M. Mavrikakis, *J. Am. Chem. Soc.*, **124**, 7193 (2002).
33. J. Greeley, M. Mavrikakis, *J. Am. Chem. Soc.*, **126**, 3910 (2004).
34. S.K. Desai, M. Neurock, K. Kourtakis, *J. Phys. Chem. B*, **106**, 2559 (2002).
35. C.-Y. Niu, J. Jiao, B. Xing, G.-C. Wang and X.-H. Bu, *J. Comput. Chem.*, **31**, 2023 (2010).
36. D. Cao, G.-Q. Lu, A. Wieckowski, S. A. Wasileski and M. Neurock, *J. Phys. Chem. B*, **109**, 11622 (2005).
37. C. Michel, F. Auneau, F. Delbecq, and P. Sautet, *ACS Catal.*, **1**, 1430 (2011).

38. S. Chibani, C. Michel, F. Delbecq, C. Pinel and M. Besson, *Catal. Sci. Technol.*, **3**, 339 (2013).
39. A.S. Lin, A.D. Kowalak, W.E. O'Grady, *J. Power Sources*, **58**, 67 (1996).
40. X.H. Xia, T. Iwasita, *J. Electroanal. Chem.*, **411**, 95 (1996).
41. J. Rossmeisl, J.K. Nørskov, C.D. Taylor, M.J. Janik and M. Neurock, *J. Phys. Chem. B*, **110**, 21833 (2006).
42. C.D. Taylor, R.G. Kelly and M. Neurock, *J. Electrochem. Soc.*, **154**, F217 (2007).
43. B. N. Zope, D. D. Hibbitts, M. Neurock, R. J. Davis, *Science*, **330**, 74 (2010).
44. P. Rodriguez, Y. Kwon and M. T. M. Koper, *Nat. Chem.*, **4**, 177 (2012).
45. R. Kavanagh, X. Cao, W.-F. Lin, C. Hardacre and P. Hu, *J. Phys. Chem. C*, **116**, 7185 (2012).
46. S.C.S. Lai, M.T.M. Koper, *Faraday Discuss.*, **140**, 399 (2008).
47. A. Kowal, M. Li, M. Shao, K. Sasaki, M.B. Vukmirovic, J. Zhang, N.S. Marinkovic, P. Liu, A.I. Frenkel, R.R. Adzic, *Nat. Mat.*, **8**, 325 (2009).
48. H.F. Wang, Z.P. Liu, *J. Am. Chem. Soc.*, **130**, 10996 (2008).
49. R.A. van Santen, M. Neurock, *Molecular heterogeneous catalysis: a conceptual and computational approach*, VCH-Wiley, Weinheim, (2006).
50. J.K. Nørskov, T. Bligaard, J. Rossmeisl, C.H. Christensen, *Nat. Chem.*, **1**, 37 (2009).
51. F. Besenbacher, I. Chorkendorff, B. S. Clausen, B. Hammer, A. M. Molenbroek, J. K. Nørskov, I. Stensgaard, *Science*, **279**, 1913 (1998).
52. E. Nikolla, A. Holewinski, J. Schwank, S. Linic, *J. Am. Chem. Soc.*, **128**, 11354 (2006).

53. J. Xu, M. Saeys, *J. Catal.*, **242**, 217 (2006).
54. J. Xu, L. Chen, K.F. Tan, A. Borgna, M. Saeys, *J. Catal.*, **261**, 158, (2009).
55. K.F. Tan, J. Xu, J. Chang, A. Borgna, M Saeys, *J. Catal.*, **274**, 121, (2010).
56. K.F. Tan, J. Chang, A. Borgna, M. Saeys, *J. Catal.*, **280**, 50, (2011).
57. J. Greeley, T. F. Jaramillo, J. Bonde, I. Chorkendorff, J. K. Norskov, *Nat. Mat.*, **5**, 909 (2006)
58. M.J. Janik, C.D. Taylor, M. Neurock, *Top Catal.*, **46**, 306 (2007).

## CHAPTER 2

# COMPUTATIONAL MODELING

In 1998, the Nobel Prize in Chemistry was awarded for Walter Kohn "*for his development of the density-functional theory*" and John A. Pople "*for his development of computational methods in quantum chemistry*". [1] Nowadays, with the development of more and more powerful super-computer, first principle calculation based on Density Functional Theory (DFT) has become a very successful tool in catalyst design; include both heterogeneous catalysis and homogeneous catalysis [2-5]. The development of computational catalysis has facilitated the calculation on a molecular scale, and allowed understanding the detailed reaction mechanisms. In particular, the relative stability of various possible reaction intermediates and the activation barriers of surface reactions are calculated routinely, permitting the study of the thermodynamics and kinetics of these reactions [6-8]. Additionally, calculated vibration spectra can help identify the structure and the adsorption sites of surface species [9-11]. As reviewed by Norskov et al., this approach has been successful in guiding the computational design of optimal catalysts [3,8].

In this chapter, the theory of DFT and Vienna ab initio package (VASP), the software we used to do DFT calculations in the PhD study, will be briefly introduced. After that, the detailed description on the theory of DFT computed XPS core-level shift and the thermodynamic modeling of electro-chemical reactions will be presented, which are the base for the next research Chapters.

## 2.1. Computational Theory

First principle calculations, or ab initio calculations, are the methods to solve the governing quantum chemical equation of the system, which is well-known as the time-independent Schrodinger equation [12]. However, for a multi-particle system includes of  $M$  nuclei and  $n$  electrons, solving the Schrodinger equation with  $(3M + 4n)$  variables is very challenging [4,13]. Many approximation methods and theories are proposed to solve that equation with the good accuracy, and one of the most widely used is the Density Functional Theory (DFT) [13-15]. The DFT, which was developed by Hohenberg and Kohn [14] and Kohn and Sham [15] in 1965, replaces the  $4n$  dimensional electronic wave function by a three dimensional electron density and significantly simplified the Schrodinger equation. The computational cost to solve the Schrodinger equation by DFT is much lower compare to other methods [16], and the accuracy compare to experimental results for solid-state systems is converged within the range of 20 kJ/mol [17].

Many computer programs are being developed to solve the Schrodinger equation based on DFT with the target to give the solution faster and more accurate [13]. Some of the famous programs include GAUSSIAN, CPMD, VASP, DACAPO, SIESTA, TurboMole, Quantum-Expresso... Among of them, the Vienna Ab-Initio Simulation Package (VASP) is one of the most popular and widely used simulation software [18,19]. Been developed by Kresse, Hafner and collaborators, VASP is a computational code to do periodic DFT simulations. VASP could provide all the information of the systems; include the thermodynamic properties (enthalpy, entropy ...), kinetic

property of the reaction (activation barrier), electronic properties (density of state, Fermi level, band structure, core-level binding energy...) and other properties (magnetic momentum, charge ...). [20] Nowadays, VASP is widely applied to guide design of catalyst in heterogeneous catalysis [2,3,5], perform electron transport calculations, for example in oxide tunneling barrier for MTJs [21], and conduct many simulation in solid-state systems. The parallelized technique and numerical algorithm implemented in VASP made the DFT calculations could be converged very fast and accurate [20]. Due to those reasons, VASP will be the main computational software to perform DFT calculations in this PhD study.

## **2.2. DFT XPS Core-level binding calculations**

X-ray photoelectron spectroscopy (XPS) technique was originally discovered in 1958 by K.M. Siegbahn (Nobel prize in Physics in 1981) at the University of Uppsala, Sweden [22]. Nowadays, among surface analysis characterizations, X-ray photoelectron spectroscopy (XPS) is one of the most extensive, common and widely applicable techniques, and the outgrowth of research based on it made XPS become one of the most important chemical analytical tool both qualitatively and quantitatively [23-25]. In XPS, a core electron is excited by a beam of X-ray photons to create a core hole. The core-level binding energy (BE) measured by XPS is the difference of two total energies, namely, the energy before and after the core electron is removed, see Figure 2.1 below from the Olovson et al. paper [26]. In DFT, core-level BEs are obtained as the energy difference between an unexcited ground-state calculation and a calculation where a specified core electron excited. In the

final-state approximation, illustrated below, an electron is assumed to “instantaneously” screen the core hole created by the photons.

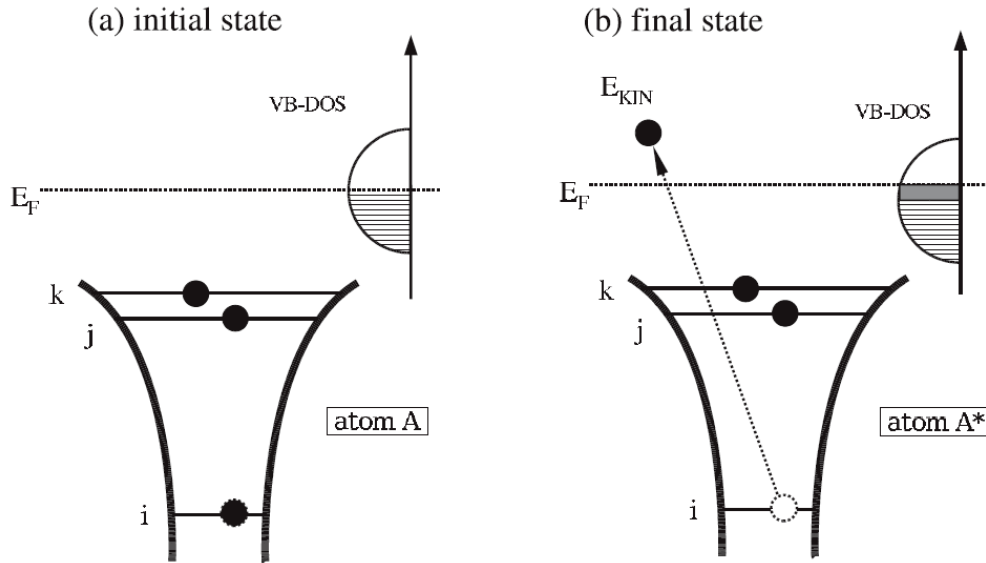


**Figure 2.1.** (a) Initial and (b) final states of the photoemission process. Ejection of the core-electron from level  $i$  results in a core-hole at this level. The effect of screening is shown by the increased occupation of the local valence band DOS in (b) compared to (a). [26]

In this work, core-level BEs will be calculated with the final-state approximation as implemented in VASP. For comparison, core-level BEs will also be computed with the computationally more efficient initial-state approximation. In the initial-state approximation, the core-level BE corresponds to the energy eigenvalue of the core orbital relative to the Fermi level. Practically, the Kohn-Sham equations are solved inside the PAW sphere for the core electrons, after self-consistency with a frozen core has been reached [27]. In the final-state approximation, core-level BEs are calculated as the energy difference between an unexcited ground-state calculation and a core-excited-state calculation in which a specified core electron is removed and an electron is added to the lowest unoccupied valence state to completely screen the localized core hole and preserve the charge neutrality of the system.

In the final-state approximation, the resulting core hole is hence completely screened, as indicated by the extra charge in the local valence density of states of the core-excited atom. It should be noted that in the complete-screening scheme, the core levels can also shift to screen the core hole.

Different implementations exist for the complete-screening final-state approximation [26]. In the original “Z+1” implementation, the core potential of the ionized atom Z is replaced by the core potential of the next atom in the periodic table, (Z+1), and an additional valence electron is added to screen the extra charge [28]. A second, more accurate approach is the modified PAW method, as implemented in VASP [27]. Here, the corresponding core-excited PAW potential is generated on-the-fly, and complete screening of the localized core hole is taken into account by allowing the valence electrons to relax after shifting the core electron to the valence [27]. Screening by the core electrons is neglected, i.e., the other core electrons are kept frozen in the configuration for which the PAW potential was generated, and the core hole is spherically symmetrized to keep the core density spherically symmetric. Recently, Marsman and Kresse introduced the relaxed-core PAW method which also accounts for core-relaxation effects in the complete-screening approximation [29]. The modified PAW method resembles the “Z+1” approximation, but is more accurate, in particular for lighter atoms. We have tested the modified PAW method resembles the “Z+1” approximation by performing “Z+1” calculations for Pt 4f<sub>7/2</sub> SCLS for Pt(111) and for the C 1s binding energy for CH on Co(0001). The “Z+1” method works well for Pt 4f<sub>7/2</sub>, but is somewhat problematic for C 1s binding energies. The Pt 4f<sub>7/2</sub>



surface core-level shift (SCLS) for Pt(111) of  $-0.42$  eV is calculated with the modified PAW method, while the “Z+1” method predicts  $-0.43$  eV. However, for CH on Co(0001), the “Z+1” method predicts a C 1s BE of 284.1 eV, compared with a C 1s BE of 283.6 eV obtained with the modified PAW method.

For systems with periodic 3D boundary conditions (bulk systems) it is not possible to determine the energy-zero, i.e., all the Kohn-Sham level energies are only determined within a constant offset in  $E_0$  [30,31]. Therefore, if we compare the KS levels of two different systems, we first have to correct for these offsets for both systems to have a common energy scale. E.g., in slab calculations with a sufficiently thick vacuum layer, one can assume that vacuum energy can be set to  $E_0$ , after having reached a constant value in the vacuum. Therefore relative energies are more accurate than absolute BEs due to error cancellation, chemical shifts are calculated rather than absolute core-level BEs. Core-level BEs are then obtained using an experimental reference value [31].

### **2.3. Free Gibbs energy calculations for electro-chemical reactions**

Since the electro-chemical reactions occur in the conditions include the aqueous environment, room temperature, applied potential, pH of solvent..., therefore to evaluate the activity of the catalyst in those reactions, all of the mentioned factors need to be take into account.

To include the effect of the water environment on the stability of surface species, one layer of water with an ice-like structure will be constructed [32,33], as illustrated in Figure 2.2. Six molecules of water are organized on the catalyst surfaces forming the hexagonal H-bonding network. The ice-like structure of water is commensurate with the p(3x3) slab modeling the catalyst surface and optimization of the adsorbed intermediates within this structure of water allowed to determine the configuration and stability of that species in aqueous media.

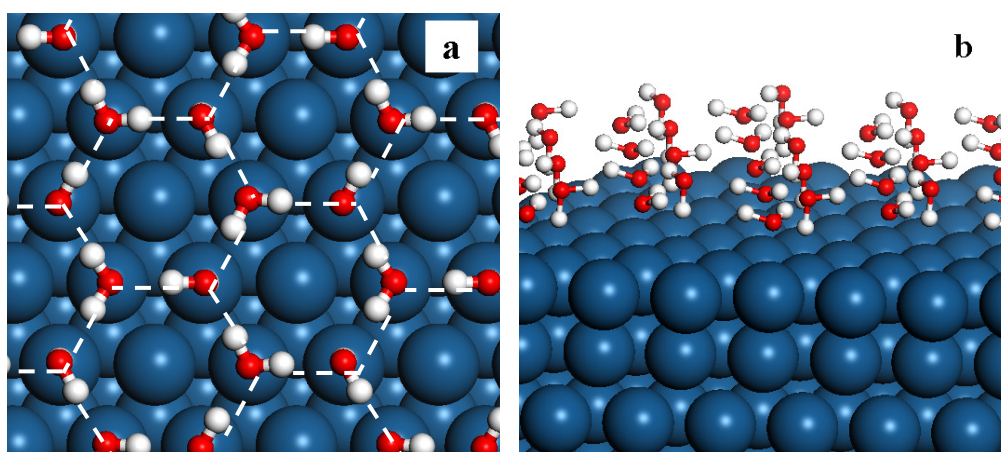
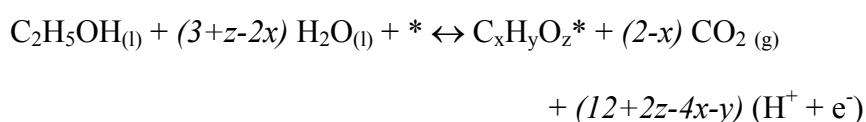


**Figure 2.2:** Top view (a) and side view (b) of ice-like water structure on p(3x3) Pt(111) surface (the dashed line is H-bonding)

The model of electrochemical reactions under fuel cell working conditions is built based on the approach proposed by Norskov et al. [34], in which the stability of reaction intermediates is computed as a function of applied potential  $U$  and pH of media at room temperature. For the electro-oxidation of alcohol (ethanol), the Gibbs free energy for forming the reaction intermediate  $M$  with the formula  $C_xH_yO_z^*$  will be calculated relative to liquid  $H_2O$  and ethanol at temperature  $T$ , for a potential  $U$  and a pH:





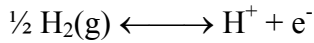
Zero point energies (ZPE) is calculated for all species. For the adsorbed species, the ZPE will be determined using calculated vibration frequencies on Pt(111), and assumed to be similar on the other surfaces. Entropy and enthalpy corrections were obtained from the NIST-JANAF tables [35] for the gas-phase species and calculated on a Pt(111) slab for the adsorbed species [36]. In detail, the vibrational frequencies of the specie will be computed by VASP. Next, the zero-point energy ZPE, entropy S and enthalpy  $H_{\text{correction}}$  can be calculated from the equation (2.3), (2.4) and (2.5) using the vibrational partition function [37]:

$$ZPE = \frac{1}{2} \sum_{i=1}^n h\nu_i \quad (2.3)$$

$$S_{\text{vib}} = -R \sum_i \ln \left( 1 - e^{-\frac{h\nu_i}{kT}} \right) + R \sum_i \left( \frac{h\nu_i}{kT} \right) \left( \frac{e^{-h\nu_i/kT}}{1 - e^{-h\nu_i/kT}} \right) \quad (2.4)$$

$$H_{\text{correction}} = [H(T) - H(0)] = RT \sum_i \left( \frac{h\nu_i}{kT} \right) \left( \frac{e^{-h\nu_i/kT}}{1 - e^{-h\nu_i/kT}} \right) \quad (2.5)$$

The effect of pH and potential U will be included using the Gibbs free energy of the following reaction, as described by Norskov et al. [34]:



$$\Delta G_{\text{H}^+} = -eU + k_B T \ln 10 \cdot (\text{pH}) \quad (2.6)$$

The  $\Delta G_1$  and  $\Delta G_2$  are included to correct the Gibbs free energy relative to Ethanol and water in liquid state:

$$\Delta G_1 = RT \ln p^*(\text{C}_2\text{H}_5\text{OH})_T \quad (2.7)$$

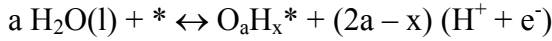
$$\Delta G_2 = RT \ln p^*(\text{H}_2\text{O})_T \quad (2.8)$$

where  $p^*(\text{C}_2\text{H}_5\text{OH})_T$  and  $p^*(\text{H}_2\text{O})_T$  are saturated vapor pressure for ethanol and water at temperature T, and could be extracted from the standard thermodynamic tables for all the gas-phase molecules [35].

Substitute all the equation from (2.2) to (2.8) into the equation (2.1), the stability of intermediate M will then be converted to free Gibbs energy at applied potential U, pH and temperature T by this equation:

$$\begin{aligned}\Delta G_M &= \Delta G_{\text{DFT}}^{\circ} + \Delta G_{\text{H}^+} + \Delta G_1 + \Delta G_2 \\ &= (\Delta E_w + \Delta \text{ZPE} + \Delta H_{\text{correction}} - T\Delta S) + (12+2z-4x-y)(-eU + k_B T \ln 10 \cdot (\text{pH})) \\ &\quad + RT \ln p^*(\text{C}_2\text{H}_5\text{OH})_T + (3+z-2x) \ln p^*(\text{H}_2\text{O})_T\end{aligned}\quad (2.9)$$

Equation (2.9) is applied for anode side reaction (alcohol oxidation). The same approach also could be used for the cathode reaction (oxygen reduction):



where a is 1 or 2 and x is 0 or 1. In Chapter 4, we will use this approach to study the volcano behavior of PdM@PdPt (M=Cr, Fe, Co, Ni and Pt) core-shell oxygen reduction electrocatalysts and guided design the optimal candidates. After that, the theoretical DFT prediction will be validated by experiments.

#### **2.4. Describe the Hydrogen interaction by DFT: role of DFT-vdW functional**

The conventional Perdew-Burke-Ernzerhof functional (DFT-PBE), [38] which implemented in the Vienna Ab initio Simulation Package (VASP), works very well in almost DFT calculations on metallic surfaces. However, to better describe the Hydrogen interaction between alcohol in an aqueous environment in Chapter 5, some improvement will need to be applied.

The important role of van der Waals (vdW) forces in the weak interaction between water molecules with metal surfaces has been reinforced [39,40] when evaluating the relative stability, adsorption sites, and adsorption geometries of competing water ad-structures. To describe the hydrogen interaction in our studied systems which include a co-adsorbed system of an alcohol with surrounding water molecules, the recent developed revPBE-vdW functional implemented in VASP will be used [41,42]. To evaluate how this functional describes the hydrogen-bond interactions, we conduct some calculations in comparison with calorimetric measurements, include the decomposition of water on Pt(111) [43], the formation of OH group on water covered Pt(111) [44], the UHV adsorption of Methanol and the reaction of Methanol with preadsorbed O on Pt(111) [45]. The results are shown in Table 2.1

The Reaction enthalpy for the decomposition of water on Pt(111) calculated by revPBE-vdW functional is 48 kJ/mol, in good agreement with experimental result of 50 kJ/mol [43]. The similar agreement is found in the formation of OH group on oxygen-covered Pt(111). DFT revPBE-vdW calculation gives the formation energy of -54 kJ/mol, agrees well with calorimetric measurement of -60 kJ/mol from Campbell's group [44], while DFT-PBE gives the formation energy of -32 kJ/mol, quite far from experimental measurement. These results show that revPBE-vdW functional describes quite well the hydrogen-bond interactions. Finally, revPBE-vdW also gives accurate adsorption energy and reaction energy. Our computed adsorption energy of Methanol on Pt(111) surfaces with revPBE-vdW functional is -44 kJ/mol, which match quite well with experimental measurement values of  $-58.6 \pm 0.8$

kJ/mol [45]. The computed reaction energy of -69 kJ/mol was calculated for the reaction  $\text{CH}_3\text{OH}(\text{g}) + \text{O}^* \rightarrow \text{CH}_3\text{O}^* + \text{OH}^*_{\text{coadsorbed}}$ , close to the measured  $\Delta H_{\text{rxn}}$  of  $-76.4 \pm 2.9$  kJ/mol [45].

**Table 2.1.** Experimental measurement and computed energy (kJ/mol) with revPBE-vdW functional

Reaction	Experimental measurement	Computed by revPBE-vdW
<b>Decomposition of water on Pt(111)</b> $\text{H}_2\text{O}^*_{\sqrt{3}\times\sqrt{3}} \rightarrow \text{OH}^* + \text{H}^*$	51 <sup>a</sup>	48
<b>Formation of Hydroxyl group on water-covered Pt(111)</b> $2\text{H}_2\text{O}(\text{g}) + \text{O}^*_{2\times 2} \rightarrow (\text{H}_2\text{O}\dots\text{OH}^*)_{\sqrt{3}\times\sqrt{3}} + \text{OH}^*_{1\times 1}$	-60 <sup>b</sup>	-54
<b>Adsorption of Methanol on Pt(111)</b> $\text{CH}_3\text{OH}(\text{g}) + \text{Pt}(111)_{3\times 3} \rightarrow \text{CH}_3\text{OH}^*-\text{Pt}(111)$	-59 <sup>c</sup>	-44
<b>Reaction energy of Methanol on Pt(111) predosed with Oxygen</b> $\text{CH}_3\text{OH}(\text{g}) + \text{O}^*_{3\times 3} \rightarrow \text{CH}_3\text{O}^* + \text{OH}^*_{\text{coadsorbed}}$	-76 <sup>c</sup>	-69

*Experimental data are obtained from literature:* <sup>a</sup> Karp et al. [43]; <sup>b</sup> Lew et al. [44] and <sup>c</sup> Karp et al. [45]

## 2.5. References.

1. "The Nobel Prize in Chemistry 1998", Press Release on 13 October 1998, The Royal Swedish Academy of Sciences, (1998).
2. R.A. van Santen, M. Neurock, *Molecular heterogeneous catalysis: a conceptual and computational approach*, VCH-Wiley, Weinheim, (2006).
3. J.K. Nørskov, T. Bligaard, J. Rossmeisl, C.H. Christensen, *Nat. Chem.*, **1**, 37 (2009).

4. P.R. Schleyer (Edt), *Encyclopedia of Computational Chemistry*, John Wiley & Sons, New York, (1998).
5. F. Besenbacher, I. Chorkendorff, B. S. Clausen, B. Hammer, A. M. Molenbroek, J. K. Nørskov, I. Stensgaard, *Science*, **279**, 1913 (1998).
6. R.R. Chianelli, G. Berhault, P. Raybaud, S. Kasztelan, J. Hafner, H. Toulhoat, *Appl. Catal. A Gen.*, **227**, 83 (2002).
7. S. Dahl, A. Logadottir, C.J.H. Jacobsen, J.K. Nørskov, *Appl. Catal. A Gen.*, **222**, 19 (2001).
8. J.K. Nørskov, F. Abild-Pedersen, F. Studt, T. Bligaard, *Proc. Natl. Acad. Sci. USA.*, **108**, 937 (2011).
9. F. Tielens, M. Saeys, E. Tourwe, G.B. Marin, A. Hubin, P. Geerlings, *J. Phys. Chem. A*, **106**, 1450 (2002).
10. M. Saeys, M.F. Reyniers, G.B. Marin, M. Neurock, *J. Phys. Chem. B*, **106**, 7489 (2002).
11. C. Morin, D. Simon, P. Sautet, *J. Phys. Chem. B*, **107**, 2995 (2003).
12. E. Schrödinger, *Phys. Rev.*, **28**, 1049 (1926).
13. W. Koch, M.C. Holthausen, *A Chemist's Guide to Density Functional Theory*, Wiley-VCH Verlag GmbH, Weinheim (2001).
14. H. Hohenberg, W. Kohn, *Phys. Rev.*, **163B**, 864 (1965).
15. W. Kohn, L.J. Sham, *Phys. Rev.*, **140A**, 1133 (1965).
16. R.G. Parr, W. Yang, *Density-Functional Theory of Atoms and Molecules*, Oxford University Press, New York (1989).
17. W. Kohn, *Rev. Mod. Phys.*, **71**, 1253 (1999).
18. G. Kresse, J. Hafner, *Phys. Rev. B*, **47**, 558 (1993).
19. G. Kresse, J. Futhmuller, *Comput. Mater. Sci.*, **6**, 15 (1996).



20. G. Kresse and J. Furthmüller, *VASP the Guide*, Vienna, (2007).  
(<http://cms.mpi.univie.ac.at/VASP>)
21. A.M. Sahadevan, R.K. Tiwari, G. Kalon, C.S. Bhatia, M. Saeys, H. Yang, *Appl. Phys. Lett.*, **101**, 042407 (2012).
22. E. Sokolowski, C. Nordling, K. Siegbahn, *Phys. Rev.*, **110**, 776 (1958).
23. A. Knop-Gericke, E. Kleimenov, M. Havecker, R. Blume, D. Teschner, S. Zafeiratos, R. Schlogl, V.I. Bukhtiyarov, V.V. Kaichev, I.P. Prosvirin, A.I. Nizovskii, H. Bluhm, A. Barinov, P. Dudin, M. Kiskinova, *Adv. Catal.*, **52**, 213 (2009).
24. A.M. Venezia, *Catal. Today*, **77**, 359 (2003).
25. S. Tougaard, *X-Ray Photoelectron Spectroscopy*, in P. Worsfold, A. Townshend, C. Poole (eds.), *Encyclopedia of Analytical Science*, 2<sup>nd</sup> edition, Elsevier Ltd, pp. 446-456 (2005).
26. W. Olovsson, C. Göransson, T. Marten, I.A. Abrikosov, *Phys. Stat. Sol. (b)*, **243**, 2447 (2006).
27. L. Kohler, G. Kresse, *Phys. Rev. B*, **70**, 165405 (2004).
28. B. Johansson, N. Martensson, *Phys. Rev. B*, **21**, 4427 (1980).
29. M. Marsman, G. Kresse, *J. Chem. Phys.*, **125**, 104101 (2006).
30. N.W. Ashcroft, N.D. Mermin, *Solid State Physics*, Saunders College, Philadelphia, (1976).
31. Q.T. Trinh, K.F. Tan, A. Borgna, M. Saeys, *J. Phys. Chem. C*, **117**, 1684 (2012).
32. Y. Gohda, S. Schnur, A. Groß, *Faraday Diss.*, **140**, 233 (2009).
33. C.D. Taylor, M.J. Janik, M. Neurock, R.G. Kelly, *Molecular Simulation*, **33**, 429 (2007).

34. J.K. Nørskov, J. Rossmeisl, A. Logadottir, L. Lindqvist, J.R. Kitchin, T. Bligaard, H. Jónsson, *J. Phys. Chem. B*, **108**, 17886 (2004).
35. M.W. Chase, *NIST-JANAF Thermodynamical Tables*, Fourth Edition, J. Phys. Chem. Ref. Data, Monograph 9, (1998).
36. D.A. McQuarrie, *Statistical Mechanics*, University Science Books, (2000).
37. K.K. Irikura, *Appendix B: Essential Statistical Thermodynamics*, in K.K. Irikura and D.J. Frurip (Eds), *Computational Thermochemistry: Prediction and Estimation of Molecular Thermodynamics*, Washington, DC: American Chemical Society, pp. 402-418 (1998).
38. J.P. Perdew, K. Burke, M. Ernzerhof, *Phys. Rev. Lett.*, **77**, 3865 (1996).
39. J. Carrasco, J. Klimes, A. Michaelides, *J. Chem. Phys.*, **138**, 024708 (2013)
40. I. Hamada, K. Lee and Y. Morikawa, *Phys. Rev. B*, **81**, 115452 (2010)
41. M. Dion, H. Rydberg, E. Schröder, D. C. Langreth, and B. I. Lundqvist, *Phys. Rev. Lett.*, **92**, 246401 (2004).
42. J. Klimes, D.R. Bowler, A. Michaelides, *Phys. Rev. B*, **83**, 195131 (2011).
43. E. M. Karp, C. T. Campbell, F. Studt, F. Abild-Pedersen and J. K. Nørskov, *J. Phys. Chem. C*, **116**, 25772 (2012).
44. W. Lew, M.C. Crowe, C.T. Campbell, J. Carrasco, A. Michaelides, *J. Phys. Chem. C*, **115**, 23008 (2011).
45. E.M. Karp, T.L. Silbaugh, M.C. Crowe, C.T. Campbell, *J. Am. Chem. Soc.*, **134**, 20388 (2012).

## CHAPTER 3

# **Evaluating the Structure of Catalysts using First Principle calculated XPS Core-Level Binding Energies and guided characterize core-shell electro-catalyst**

### **3.1. Introduction**

Since its introduction in 1958 [1], X-ray Photoelectron Spectroscopy (XPS) or Electron Spectroscopy for Chemical Analysis (ESCA) has become a popular surface characterization technique in heterogeneous catalysis [2,3]. In XPS, a core-level electron is excited by X-rays, and the kinetic energy of the collected electrons is measured. From an energy balance, the binding energy (BE) of the core-level electrons can be determined. It has been found that core-level BEs are highly sensitive to the chemical state and the environment of the surface species, and the chemical shifts in the BEs can be used to identify the structure and the binding site of the surface species. Moreover, the small penetration depth of the photoelectrons makes XPS surface sensitive [4,5]. The introduction of synchrotron-based XPS has reduced acquisition times to a few ms per spectrum, and enhanced the energy resolution to better than 0.1 eV [6]. In addition, depth-profile measurements [7,8], and *in situ* studies [9,10] have recently appeared. With those improved measurement techniques, modeling based analysis tools become important to help interpret the spectra.

Chemical shifts in the core-level BEs have been interpreted as initial-state effects originating from changes in the electrostatic interactions between the

core electrons and the valence electrons, and final-state effects arising from charge rearrangement and relaxation occurring in response to the core hole [11-13]. Initial-state effects dominate the chemical shifts in many cases [14,15], however, final-state effects are not always negligible and may contribute positively or negatively. [11,13,16] Various factors that contribute to initial-state chemical shifts were discussed in by Methfessel and Fiorentini [16] and by Weinert and Watson [17], and include inter-atomic charge transfer, changes in the reference Fermi-energy level, intra-atomic charge transfer, charge transfer from the local environment to the atom, and redistribution of charge due to bonding and hybridization. Charge transfer is hence often invoked to interpret shifts in the core-level BEs [12-14,16-20]. Chemical shifts are found to correlate quite well with charges for gas-phase molecules [12] and for some bimetallic systems [16,18,19], but the correlation has been debated for bulk alloys and for adlayer systems [17]. In practice, chemical shifts result from a complex combination of various factors, which often partially cancel [13,16-18,19]. This makes it challenging to quantitatively interpret chemical shifts.

Density functional theory (DFT) has become an important tool to analyze heterogeneous catalytic reactions [21,22]. In particular the relative stability of various possible reaction intermediates and the activation barriers of surface reactions are calculated routinely. In addition, calculated vibration spectra can help identify the structure and the adsorption site of surface species [e.g., 23-25]. Chemical shifts have also been calculated from first principles [e.g., 11,13-16,18,26-32]. For example, Takahata and Chong [28] calculated core-

level BEs for a test set of 59 small gas-phase molecules with an average deviation of 160 meV. Core-level BE calculations have been used to analyze the surface structure and the nature of the surface species in catalysis. For example, Todorova et al. [29] identified the structure of a strained PdO(101) layer on Pd(100) using DFT calculations in combination with calculated O 1s BEs and scanning tunneling microscopy images. Bianchettin et al. [30] combined synchrotron-based XPS with calculated Rh 3d<sub>5/2</sub> surface core-level shifts to investigate the Rh(100) surface reconstruction induced by oxygen. Kresse and Kohler [11] compared calculated vibration frequencies and Rh 3d<sub>5/2</sub> surface core-level shifts with experimental values to confirm the preferred top adsorption site of CO on Rh(111). Gandubert et al. [31] combined Co 2p<sub>3/2</sub> XPS with DFT core-level shift calculations to analyze the effect of promoter edge-decoration in CoMoS<sub>2</sub> catalysts on the toluene hydrogenation activity, while Todorova et al. [32] analyzed the structure of thin crystalline SiO<sub>2</sub> film on a Mo(112) substrate by a combination of DFT-based scanning tunneling microscopy image simulations, O 1s core-level shift calculations, and infrared reflection absorption spectroscopy. With the development of fast and high-resolution synchrotron-based XPS techniques, calculated chemical shifts are expected to become an important tool to analyze surface species and surface structures.

The motivation for this chapter was raised from the challenge of characterization of multi-component nano-size electrocatalyst. Until now, Pt is still the best pure catalyst for DAFCs, however, the activity of Pt catalyst alone is not satisfied, and the catalytic activity of Pt could also be increased by

modifying by other foreign atom adsorption, or alloying Pt with another transition metals such as the design of core-shell type electro-catalyst. However the structural study of those catalysts is very challenging. The nanoparticle size in the catalysts is always less than 3 nm, which makes it very difficult for characterization, especially so for catalysts with core-shell structure due to the more complicated composition. Since the shell thickness is about 1 monolayer, it is nearly impossible to prove the core-shell structure via conventional technique such as XRD, TEM... Therefore, the development of new characterization techniques becomes very important for the design of advanced DAFCs electro-catalyst. To address this issue, we developed the procedure to evaluate the structure of catalysts using Core-Level Binding Energies calculated from First-Principles. Firstly, we developed a procedure to accurately calculate XPS binding energies which can be compared with experimental catalyst characterization data. Next, we developed the procedure using experimental XPS and core-level BE calculations combining with DFT thermodynamics calculations to provide a powerful technique to analyze the structure of surface species and to help identify the nature and the chemical state of the catalyst. We tested our procedure in the Fisher-Tropsch process (FTS) since the FTS and the fuel cell reactions share many same intermediates. Indeed, the oxidative reactions of alcohol towards CO/CO<sub>2</sub> and proton (H<sub>2</sub>) occur in DAFCs are exactly the reverse processes of the synthesis of alcohols from the mixture of CO and H<sub>2</sub> occur in the Fisher-Tropsch process. Besides, XPS measurements were conducted under the vacuum atmosphere; therefore it is much more convenient to measure the XPS core-level binding energy of the structure in the gas-phase condition of the FTS

rather than in aqueous environment of DAFCs operation conditions. Rather than that, there are much more available data of XPS core-level binding energy from FTS in the literature so it is easy to detect the chemical state of the structure, while the data of XPS core-level binding energy for structure in DAFCs is very scarce.

In summary, in this chapter, we demonstrate that C 1s and B 1s chemical shifts can be calculated accurately using DFT with the final-state approximation. Next, we illustrate how such calculations, in combination with thermodynamic stability calculations, can help identify the nature of the resilient carbon species that are formed on a Co/ $\gamma$ -Al<sub>2</sub>O<sub>3</sub> catalyst during Fischer-Tropsch Synthesis (FTS) [33], and help elucidate the location of the boron promoter that was found to enhance the stability of Co catalysts [34,35]. Finally, we show how Pt 4f<sub>7/2</sub> surface core-level shift calculations can be used to characterize the structure of a series of Pd<sub>3</sub>M@Pd<sub>3</sub>Pt (M=Co, Ni, Fe and Cr) core-shell catalysts, developed to maximize the activity of the electrocatalytic oxygen reduction reaction [18,36].

## **3.2. Computational and Experimental Methods.**

### *3.2.1. Computational Methods.*

All structures were optimized using periodic spin-polarized DFT with the Perdew-Burke-Ernzerhof functional (DFT-PBE) [37] as implemented in the Vienna ab initio simulation package (VASP) [38,39]. Convergence tests were done to choose the appropriate cutoff energy and smearing width. Plane waves with a converged kinetic energy up to 450 eV were used, and the electron-ion

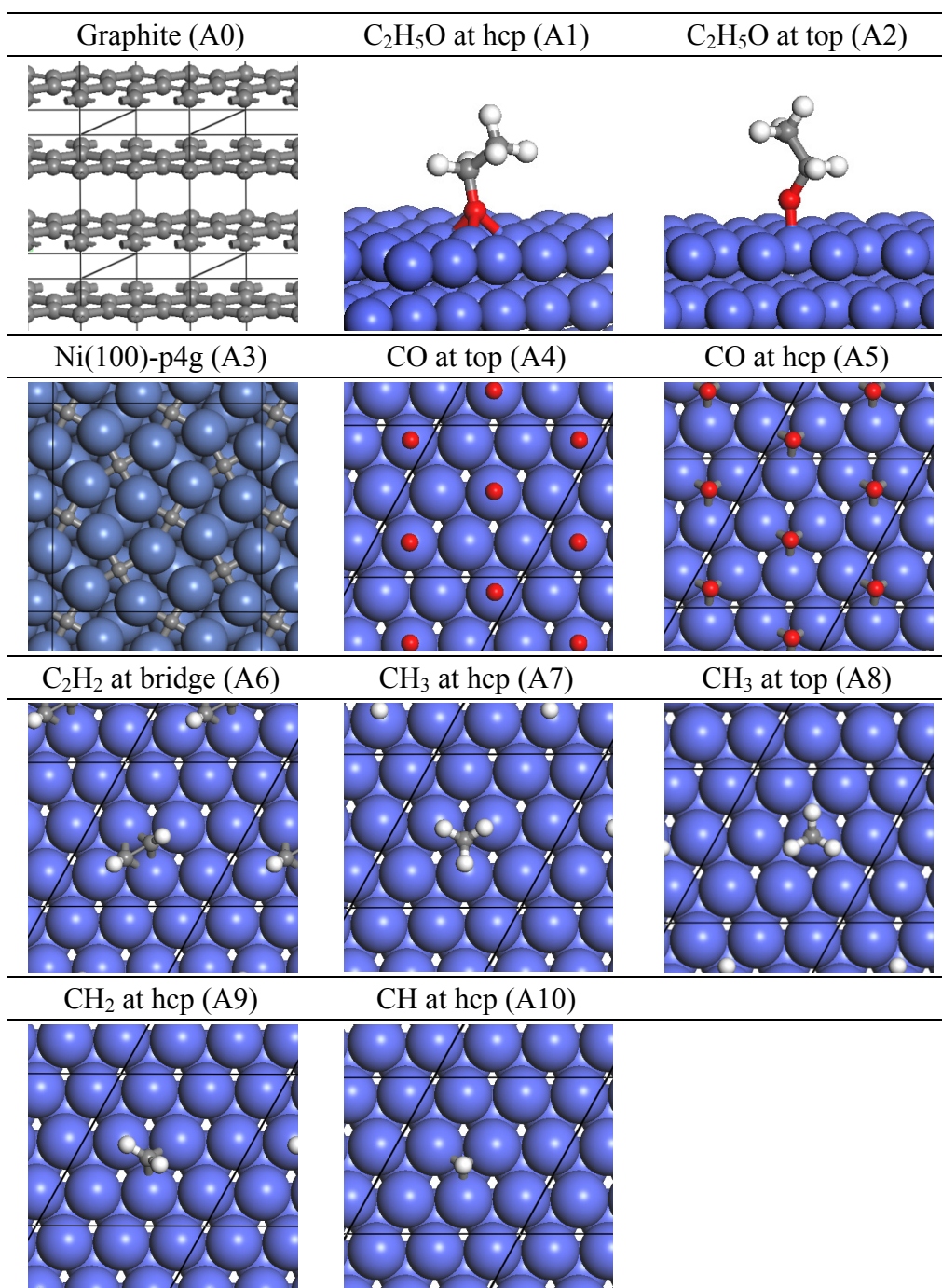
interactions were described by the projector-augmented wave (PAW) method [40,41]. The structures were optimized using a conjugate-gradient method until the atomic forces were less than 0.01 eV/Å. A second-order Methfessel-Paxton scheme with a 0.2 eV smearing width was used to facilitate the convergence of the electronic structure, and the energy convergence for the electronic structure was set to  $10^{-4}$  eV. Those parameters were chosen to ensure the optimized compromise between the accuracy and computational. All the optimized structures are shown in the Table 3.1, Table 3.2 and Table 3.3 for C1s B.E calculations on Co(0001), Pt(111) and B1s B.E calculations, respectively.

We focused our study on closed-packed Pt(111) and Co(0001) surfaces because they are the dominant facets for catalyst particles, and because most experimental XPS literature is available for closed-packed surfaces. On Co(0001), the following species were considered for a 1/9 ML coverage (the experimental references are indicated for each structure): CH<sub>3</sub>CH<sub>2</sub>O at the hcp hollow site (Structure A1 in Table 3.1) [42] and, for comparison, at the less-preferred top site (A2), C<sub>2</sub>H<sub>2</sub> across the bridge site with C in neighboring hollow sites (A6) [43], CH at the hcp hollow site (A10) [44], CH<sub>2</sub> at the hcp hollow site (A9) [44], CH<sub>3</sub> at the hcp hollow (A7) [44] and at the less-preferred top site (A8), a graphene overlayer centered at the bridge sites, CCH<sub>3</sub> at the hcp hollow site, and carbon atoms at the subsurface octahedral sites, and CO at the top(A4) [45] and at the hcp hollow site for a 1/3 ML coverage (A5). In addition, carbon adsorption at the B5 step sites, and a surface p4g clock carbide growing from the step edge [33] were calculated. To

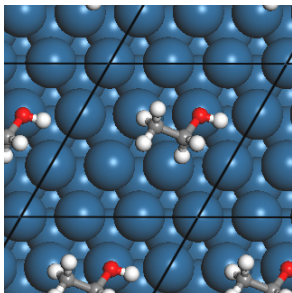
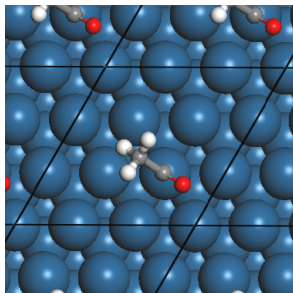
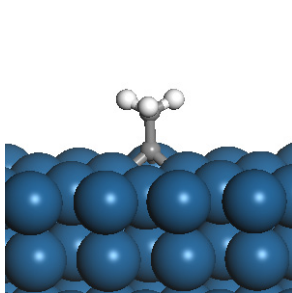
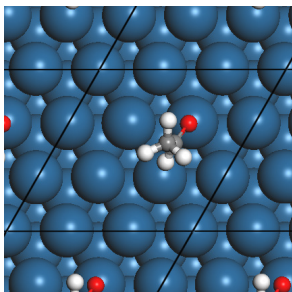
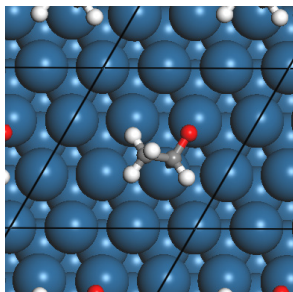
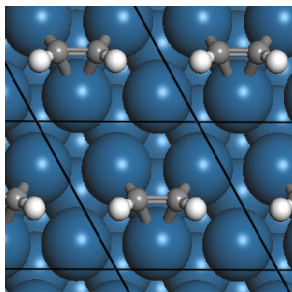
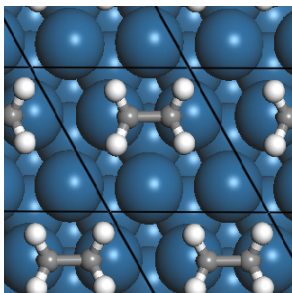
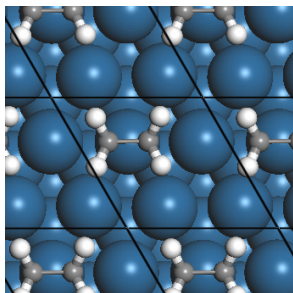
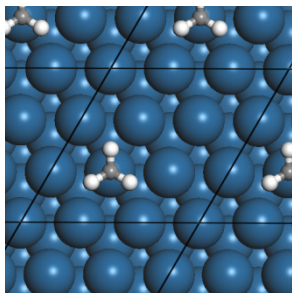
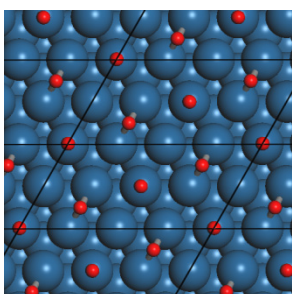
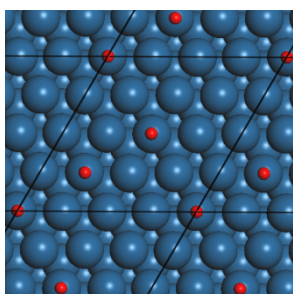


include a C 1s core-level BE for a surface p4g carbide in the test set, the p4g clock reconstruction induced by carbon on Ni(100) (A3) [13] was included. Orthorhombic bulk cobalt carbide ( $\text{Co}_2\text{C}$ ) with optimized lattice parameters of 2.92, 4.48 and 4.42 Å was also evaluated. Graphite was modeled using the experimental lattice (A0) [46].

**Table 3.1.** Optimized structures for various well-characterized species on Co(0001) and Ni(100).



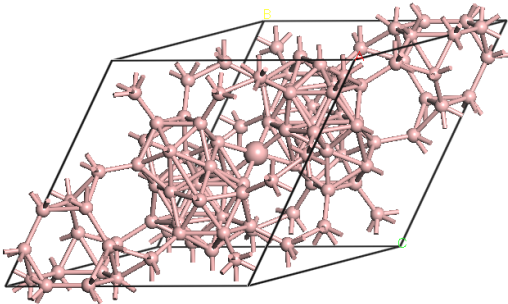
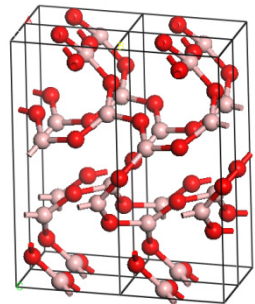
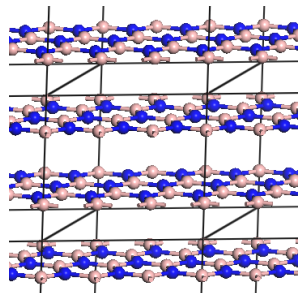
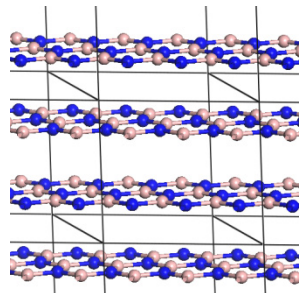
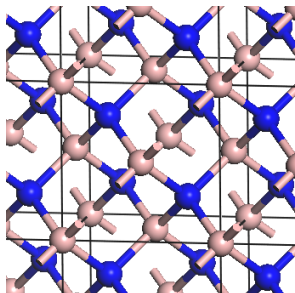
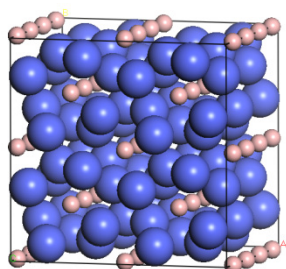
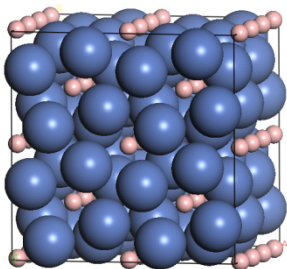
**Table 3.2.** Optimized structures and calculated C 1s binding energies for various well-characterized species on on Pt(111).

$C_2H_5OH$ at top (P1)	$CH_3CO$ at top (P2)	$CCH_3$ at hcp (P3)
		
$CH_3CHO - \eta^1(O)$ (atop) (P4)	$CH_3CHO - \eta^2(C,O)$ (di- $\sigma$ ) (P5)	Di- $\sigma$ - $\pi$ $C_2H_2$ (P6)
		
Di- $\sigma$ $C_2H_4$ (P7)	$\pi$ $C_2H_4$ (P8)	$CH_3$ at top (P9)
		
$1/2$ ML CO - $p(4 \times 2)$ (P10)	$3/16$ ML CO - $p(4 \times 4)$ (P11)	
		

On Pt(111), C 1s BEs were calculated for the following species for a coverage of 1/9 ML:  $CH_3CH_2OH$  (Structure P1 in Table 3.2) and  $CH_3CO$  (P2), both at the top site [47], two configurations of  $CH_3CHO$  ( $\eta^1(O)$  with O at a top site

(P4), and  $\eta^2(\text{C},\text{O})$  with  $\text{C}=\text{O}$  over a bridge site (P5) [48]), and  $\text{CH}_3$  at the top site (P9) [49]. Di- $\sigma$ - $\pi$  adsorbed  $\text{C}_2\text{H}_2$  (P6) [50], di- $\sigma$  adsorbed (P7) and  $\pi$ -adsorbed  $\text{C}_2\text{H}_4$  (P8) [50,51] and  $\text{CCH}_3$  at the fcc hollow site (P3) [51,52] were considered for a 1/4 ML saturation coverage. Two structures were considered for CO: 1/2 ML with CO at both top and bridge sites in a  $p(4\times 2)$  unit cell (P10) [52,53] and a lower 3/16 ML coverage with CO at the top sites in a  $p(4\times 4)$  unit cell. (P11) [52]

**Table 3.3.** Optimized structures and calculated B 1s binding energies for various well-characterized boron species

$\beta$ -rhombohedral Boron <sup>a</sup> (T0)		Trigonal $\text{B}_2\text{O}_3$ (T1)
		
Rhombohedral-BN (T2)	Hexagonal-BN (T3)	Cubic-BN (T4)
		
Cobalt Boride $\text{Co}_2\text{B}$ (T5)	Nickel Boride $\text{Ni}_2\text{B}$ (T6)	
		

<sup>a</sup>The B atom was chosen for calculated is indicated in bigger size in the center of the box. Noted that different B atoms at different positions might have the calculated B1s core-level binding energy differ of about 0.1 eV.

For the B 1s BEs, the following structures were considered:  $\beta$ -rhombohedral boron (Structure T0 in Table 3.3) [54] with an experimental lattice parameter of 10.13 Å and angle of 65.2°, tetragonal Co<sub>2</sub>B (T5) [55] with optimized lattice parameters of 4.98 and 4.28 Å, tetragonal Ni<sub>2</sub>B (T6) [56] with optimized lattice parameters of 4.99 and 4.28 Å, rhombohedral-BN (T2) [57] with experimental lattice parameters of 2.50 and 9.99 Å, hexagonal-BN (T3) [58] with experimental lattice parameters of 2.50 and 6.66 Å, cubic-BN (T4) [58] with an optimized lattice parameter of 3.58 Å, and B<sub>2</sub>O<sub>3</sub> (T1) [54] with optimized lattice parameters of 4.36 and 8.39 Å. In addition, a surface Co p4g clock boride growing from the step edges, boron at the B5 step sites, subsurface boron, and adsorbed BH with coverage of 1/9 ML at the hcp hollow site were included.

Hcp Co(0001), fcc Pt(111), and fcc Ni(100) surfaces were modeled as 3-layer slabs, where the bottom layer was fixed at the optimized bulk lattice parameters of 2.49, 3.98, and 3.52 Å, respectively. Co step sites were created by removing two rows of Co atoms from the top layer of a  $p(2 \times 8)$  hcp Co(0001) slab [33]. A (5x5x1) Monkhorst-Pack k-point grid was used to sample the Brillouin zone for  $p(3 \times 3)$  unit cells, while a (5x2x1) grid was used for larger  $p(2 \times 8)$  unit cells, and a (3x3x1) grid for  $p(4 \times 4)$  unit cells. Repeated slabs were separated by 12 Å to minimize interactions between slabs. Adsorption energies were converged within 5 kJ/mol with respect to the vacuum spacing and the k-point sampling. Increasing the slab thickness from 3 to 5 layers reduced the carbon adsorption energy at the hollow site on Co(0001) by 7 kJ/mol and the boron adsorption energy by 5 kJ/mol, while the

C 1s and B 1s BEs changed by less than 60 meV for adsorbed  $\text{CH}_x$  and BH species. Also for Pt(111), increasing the slab thickness to 5 layers changed C 1s BEs for  $\text{C}_2\text{H}_5\text{OH}$ ,  $\text{CH}_3\text{CO}$ ,  $\text{C}_2\text{H}_2$ ,  $\text{C}_2\text{H}_4$ , and  $\text{CCH}_3$  by less than 100 meV. Therefore, we only report results for the 3-layer calculations.

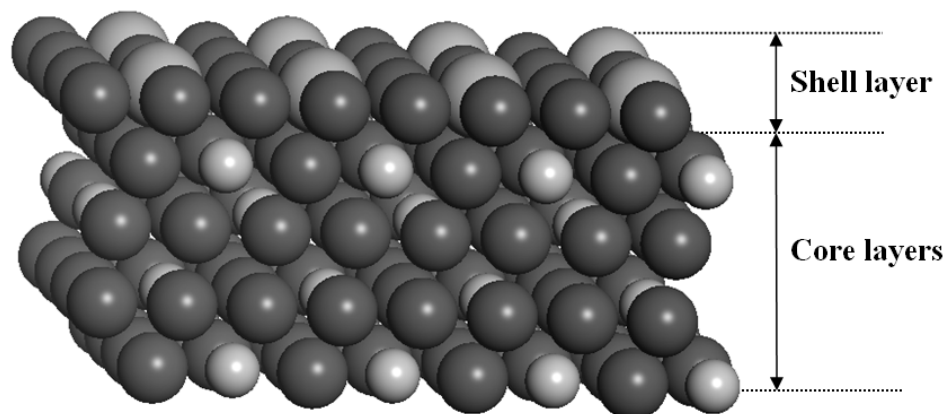


**Figure 3.1.** Model structure to simulate  $\text{Pd}_3\text{M}@Pd_3\text{Pt}$  core-shell electrocatalysts. The dark spheres represent Pd atoms, the large grey spheres are surface Pt atoms, and the small grey spheres correspond to core 3d transition metal atoms, M.

$\text{Pd}_3\text{M}@Pd_3\text{Pt}$  core-shell particles were modeled as a  $p(2 \times 2)$   $\text{Pd}_3\text{Pt}(111)$  shell on a fcc  $\text{Pd}_3\text{M}(111)$  core, where M is a 3d transition metal (M=Co, Fe, Ni, or Cr) [18,36]. An example of the core-shell model is shown in Figure 3.1. The lattice parameters for the  $\text{Pd}_3\text{M}@Pd_3\text{Pt}$  structures were obtained by minimizing the total energy of a fully relaxed  $\text{Pd}_3\text{M}@Pd_3\text{Pt}$  structure as a function of the lattice parameter. A  $(5 \times 5 \times 1)$  Monkhorst-Pack k-point grid was used for the Brillouin zone integration, and an interslab spacing of 12 Å was used to minimize interactions between repeated slabs. To test the convergence of the surface core-level shifts, the number of core layers was increased up to six. To evaluate the effect of the shell thickness on the surface core-level shift, structures with one, two, and three shell layers were considered.

### 3.2.2. *Core-level Binding Energy Calculations.*

In XPS, a core electron is excited by a beam of X-ray photons to create a core hole. The measured core-level BE is the energy difference between the initial, unexcited ground-state and the final, core-excited state. Several schemes have been developed to calculate core-level BEs using DFT [e.g., see 26,27 for a detailed discussion], and include the initial-state approximation where screening of the core hole in the core-excited state is neglected, the final-state approximation where the core hole is completely screened, and the transition-state model where partial orbital occupation numbers are introduced to describe the excitation process [26,27,59]. In this work, core-level BEs were calculated with the final-state approximation as implemented in VASP. For comparison, core-level BEs were also computed with the computationally more efficient initial-state approximation. In the initial-state approximation, the core-level BE corresponds to the energy eigenvalue of the core orbital relative to the Fermi level. Practically, the Kohn-Sham equations are solved inside the PAW sphere for the core electrons, after self-consistency with a frozen core has been reached [11]. In the final-state approximation, core-level BEs are calculated as the energy difference between an unexcited ground-state calculation and a core-excited-state calculation in which a specified core electron is removed and an electron is added to the lowest unoccupied valence state to completely screen the localized core hole and preserve the charge neutrality of the system. In the final-state approximation, the resulting core hole is hence completely screened, as indicated by the extra charge in the local valence density of states of the core-excited atom. It should be noted that in

the complete-screening scheme, the core levels can also shift to screen the core hole.

Since relative energies are calculated more accurately than absolute BEs, chemical shifts are calculated rather than absolute core-level BEs. Core-level BEs are then obtained using an experimental reference value. Hence, C 1s BEs are calculated using the C 1s BE of graphite, 284.4 eV, [46] as the reference, while the B 1s BE of bulk  $\beta$ -rhombohedral boron, 187.9 eV, [54] was used as the reference for the B 1s BEs. Pt 4f<sub>7/2</sub> SCLSs are calculated as the difference between the Pt 4f<sub>7/2</sub> core-level BE of shell Pt atoms in the Pd<sub>3</sub>M@Pd<sub>3</sub>Pt core-shell structures, and of Pt atoms in bulk Pt. With those settings, the calculated core-level BEs are expected to be numerically converged within 20 to 50 meV [11]. It has been reported that sufficiently large unit cells are required to avoid interactions between localized core-excited ions [60,61]. To evaluate the effect of the unit cell size on the calculated core-level BE, we calculated the C 1s core-level BE for 1 ML atop CO on Pt(111) by exciting one C 1s electron in a  $p(2 \times 2)$  and in a  $p(3 \times 3)$  unit cell. The calculated C 1s BE was found to increase by less than 20 meV when the unit cell size was increased. A similar small increase in the Pt 4f<sub>7/2</sub> SCLS was calculated when the Pt(111) unit cell was increased from  $p(2 \times 2)$  to  $p(3 \times 3)$ . Finally, since charge effects are reported to have an important effect on the core-level BEs [19,20] and are easy to evaluate, Bader charges [62,63] were computed to analyze the chemical shifts.

### 3.2.3. *Experimental Methods.*

Co/ $\gamma$ -Al<sub>2</sub>O<sub>3</sub> catalysts were prepared by slurry impregnation of a  $\gamma$ -Al<sub>2</sub>O<sub>3</sub> support with an aqueous Co nitrate solution, Co(NO<sub>3</sub>)<sub>2</sub>.6H<sub>2</sub>O, as described by Tan et al. [33]. The Co catalysts were tested during FTS, the conversion of synthesis gas to long chain hydrocarbons, for 200 hours in a fixed bed micro-reactor [33]. After 200 hours, the reactor temperature was reduced, and the catalyst was removed for characterization without exposure to air. The nature of the resilient carbon species remaining on the Co catalyst after careful wax extraction with hexane was studied with XPS. XPS spectra were obtained using a Thermo ESCALAB 250 spectrometer with a monochromatic aluminum anode (Al K $\alpha$  = 1487 eV). Measurements were recorded for a 20 eV pass energy, a 0.1 eV kinetic energy step and a 0.1 s dwelling time. Energy corrections used the Al 2*p* peak of the  $\gamma$ -Al<sub>2</sub>O<sub>3</sub> support at 74.3 eV. Promotion with small amounts of boron was found to increase stability of Co catalyst during FTS [34,35]. To improve the B 1s signal-to-noise ratio in XPS, 2.0 wt% boron was introduced to the Co/ $\gamma$ -Al<sub>2</sub>O<sub>3</sub> in second slurry impregnation step using aqueous boric acid (H<sub>3</sub>BO<sub>3</sub>) [35]. After reduction in flowing H<sub>2</sub> at 500 °C for 2 hours, the catalysts were purged with Ar and cooled to room temperature. Then, the catalysts were characterized by XPS using the equipment and procedure described above.

Pd<sub>3</sub>M@Pd<sub>3</sub>Pt core-shell catalysts were prepared by a galvanic replacement reaction between Pd<sub>3</sub>M alloy particles and an aqueous solution of PtCl<sub>4</sub><sup>2-</sup>, as described by Trinh et al. [18] and Yang et al. [64]. XPS spectra were obtained using a Thermo ESCALAB MKII spectrometer with a monochromatic



aluminum anode (Al  $K\alpha$  = 1487 eV), a 20 eV pass energy, a 0.05 eV kinetic energy step, and a 0.1 s dwelling time. Energy corrections were performed using the C 1s peak of the support at 284.5 eV. Pt 4f<sub>7/2</sub> binding energies were converted to SCLS using the binding energy of Pt atoms in bulk Pt, 71.1 eV. [65]. Both XPS instruments used a focused monochromatic Al X-ray gun, and utilize a 500 mm Rowland circle monochromator to produce a small X-ray spot with a minimum energy spread. The resolution observed using the full width at half-maximum intensity (FWHM) of the Ag 3d<sub>5/2</sub> peak from sputter-cleaned silver is 0.42 eV. However, the instruments have demonstrated higher resolutions for XPS peaks whose natural line width is smaller. When the microfocus monochromator of the Thermo ESCALAB 250 spectrometer was operated at a spot size of 500  $\mu$ m and for a 2.0 eV pass energy, the W 4f<sub>7/2</sub> FWHM of a WSe<sub>2</sub> single crystal was 0.29 eV, from which a peak natural line width of 0.13 eV could be obtained.

### **3.3. Results and Discussion.**

First, C 1s and B 1s BE calculations are evaluated for a range of well-characterized materials using both the initial-state and final-state approximation. Next, core-level BE calculations are used to help identify resilient carbon species formed during FTS, and the location and nature of the boron promoter introduced to enhance the stability of Co catalysts during FTS. Finally, we evaluate the effect of the shell thickness on the calculated Pt 4f<sub>7/2</sub> SCLSs of Pt<sub>3</sub>Pd@Pd<sub>3</sub>M core-shell catalysts, and compare the calculated values with experimental data.

3.3.1. C 1s core-level binding energies on Co(0001).

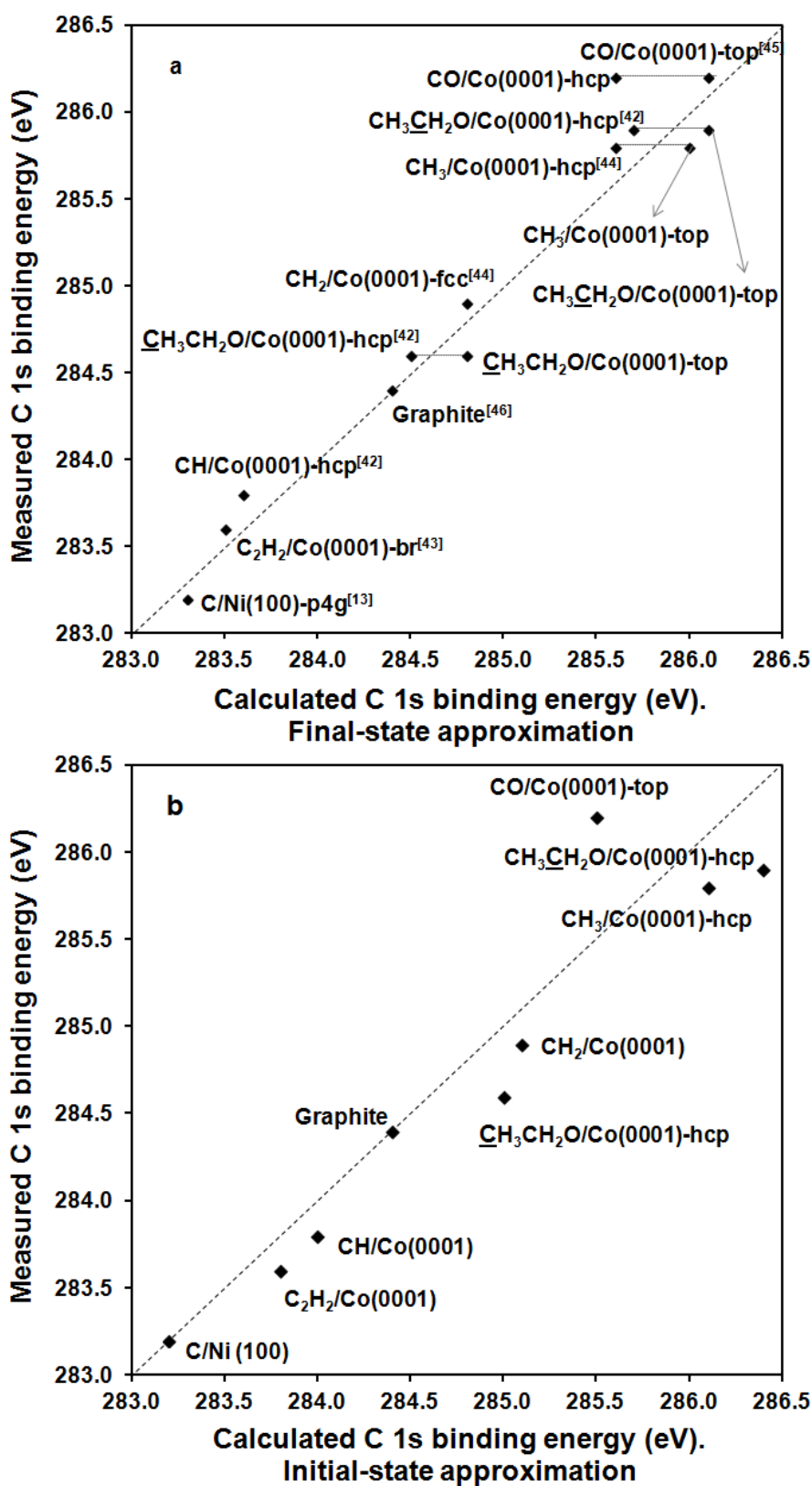


**Figure 3.2.** Calculated and experimental C 1s binding energies for various well-characterized carbon species on Co(0001) and Ni(100), using the final-state approximation (a) and the initial-state approximation (b). The adsorption site and the experimental reference are indicated.

Experimental C 1s XPS BEs are compared with calculated core-level BEs in Figure 3.2. The final-state approximation was used for the results in Figure 3.2a, while the computationally more efficient initial-state approximation was used for the results in Figure 3.2b. In general, the final-state DFT-PBE calculations capture the 2.8 eV variation in the experimental BEs well when going from a p4g clock carbide on Ni(100) to CO at a top site of the Co(0001) surface. Deviations between experimental C 1s XPS positions and calculated core-level BEs are typically smaller than 0.1 eV, and the average deviation is 85 meV. The largest deviation is found with the synchrotron-based XPS data for CH<sub>3</sub>CH<sub>2</sub>O on Co(0001), however, the difference between the calculated CH<sub>2</sub> and CH<sub>3</sub> C 1s BEs of 285.72 and 284.50 eV, respectively, corresponds well with the difference between the experimental peaks at 285.9 and 284.6 eV. These deviations should be compared with a typical energy resolution of about 0.5 eV in standard XPS and of about 0.1 eV in synchrotron-based XPS [6].

The average deviation between the experimental C 1s XPS positions and the calculated C 1s BEs are somewhat larger at 310 meV for the initial-state approximation. Though the initial-state calculations capture the variation in the C 1s BEs, the agreement with the experimental data improves significantly when final-state screening of the C 1s core hole is taken into account. Screening of the core hole depends on the valence band structure, and can have both a negative and a positive effect on the calculated chemical shift relative to graphite. For most systems in the test set, screening reduces the C 1s BE more than in graphite, e.g., leading to a negative chemical shift of 0.7

eV for  $\text{CH}_3\text{CH}_2\text{O}/\text{Co}(0001)\text{-hcp}$ . The effect of core-hole screening in  $\text{C}/\text{Ni}(100)\text{-p4g}$  and graphite are similar, leading to a change in the chemical shift of less than +0.1 eV in the final-state approximation. The only system in our test set where the C 1s core hole is significantly less screened than in graphite is  $\text{CO}/\text{Co}(0001)\text{-top}$  with a positive shift in the C 1s BE of +0.8 eV.

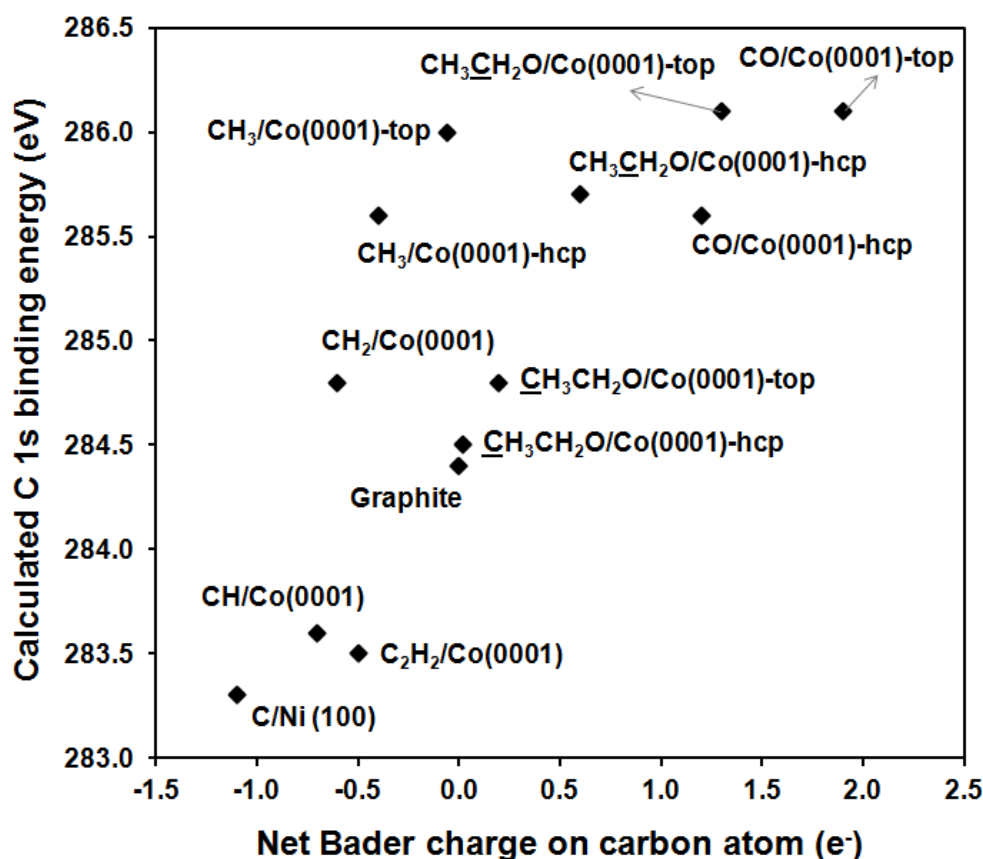


**Figure 3.3.** Correlation between the net Bader charge on the carbon atom and the calculated C 1s binding energy.

To analyze the effect of charge transfer on the variation in the core-level BEs over the test set, the net Bader charges on the carbon atoms are plotted against the calculated C 1s BEs in Figure 3.3. As discussed in the literature, charge transfer is often invoked to analyze chemical shifts. [11-16] Withdrawal of valence electrons reduces the screening of the nuclear charge by the valence electrons and hence increases the core-level BEs. However, other factors such as hybridization and local dipole moments also affect the chemical shift, [12-

14] and the correlation in Figure 3.3 seems valid only within homologous series at similar sites. Indeed, the correlation in Figure 1b is at best qualitative with a  $R^2$  value of 0.59. In particular when moving from one adsorption site to another, the change in core-level BE is often smaller than expected from the change in the Bader charge, suggesting that the change in hybridization is an important factor as well.

The low C 1s BE for p4g carbon on Ni(100) is found to correspond with the transfer of nearly one electron from the surrounding Ni atoms to the p4g clock carbon atom, as also discussed by Martensson and Nilsson [13]. A similar charge transfer was calculated for a p4g clock carbide formed near the edge sites of Co terraces [33]. Also for  $C_2H_2$ , the low C 1s BE correlates with strong backdonation from Co(0001) to adsorbed ethyne. Within the  $CH_x$  series, the variation in the core-level BE correlates with the carbon charge, though the variation in the BEs is somewhat larger than expected from the overall correlation. Among the  $CH_x$  species, the CH has the most negative charge due to the charge transfer to the anti-bonding C-H orbital is limited, and backdonation occurs to the non-hybridized C 2p orbitals instead, as also reported by Zuo et al. [66]. This results in a most negative net charge on the C atom for the CH adsorbate, and correlates with the lower C 1s BE.

To evaluate the sensitivity of the calculated C 1s BEs to the adsorption site, CO at the hcp hollow site,  $CH_3$  at the top site, and  $CH_3CH_2O$  at the top site were also considered. Though experiments show that CO adsorbs at the top sites on Co(0001) at low coverage [45], CO is calculated to be 18 kJ/mol more

stable at the hcp hollow site by DFT-PBE. The preference for CO adsorption at the hollow sites in DFT is well documented [e.g., 67] and is mainly attributed to the overestimated stability of the  $2\pi^*$  LUMO by DFT. Since backdonation to the empty  $2\pi^*$  orbitals is stronger at the hollow site, the stability at the hollow site is overestimated [67]. The calculated C 1s BE decreases from 286.1 to 285.6 eV when CO is moved from the top to the hcp site, and the calculated C 1s BE for CO at the hollow site does not agree with the experimental value of 286.2 eV for a low CO coverage. The decrease in core-level BE correlates with the lower positive Bader charge on the carbon atom, which is in turn consistent with the enhanced backdonation from the Co d-band to the CO  $2\pi^*$  orbitals at the hollow site. CH<sub>3</sub> is 46 kJ/mol less stable at the top site than at the hcp site on Co(0001), in agreement with other theoretical studies. [68,69] The calculated C 1s BE increases from 285.6 to 286.0 eV when CH<sub>3</sub> is moved from the hcp site to the top site. The increase in core-level BE correlates with a decrease in the charge density on the carbon atom. CH<sub>3</sub>CH<sub>2</sub>O binds 71 kJ/mol stronger at the hcp site than at the top site. The change in adsorption site increases the C 1s BE of the CH<sub>2</sub> group by 0.5 eV and of the CH<sub>3</sub> group slightly less by 0.3 eV. In particular for the CH<sub>3</sub> group, the agreement with the experimental value worsens. The increase in the core-level BE is correlated with a decrease in the Bader charge. However, for the CH<sub>2</sub> group the decrease in the Bader charge, 0.7 e, is larger than expected from the increase in the C 1s BE, and other factors again affect the shift in the CH<sub>2</sub> C 1s BE.



To confirm the accuracy of the C 1s BE calculations for other surfaces, we considered several well-characterized hydrocarbon species on a closed-packed Pt(111) surface with the final-state calculations only. C 1s BE calculations for nine structures are compared with experimental data in Figure 3.4a. The final-state DFT calculations capture the 4.2 eV variation in the C 1s BEs for the test set, ranging from CH<sub>3</sub> at the top site to CO at top sites, with an average deviation of 73 meV. The largest deviation is for CH<sub>3</sub> at the top site, where the calculations underestimate the BE by 270 meV, to be compared with a typical conventional XPS resolution of about 0.5 eV [6].

When there are multiple carbon atoms in the structure, they can be difficult to distinguish by conventional XPS. For a low ethanol coverage on Pt(111), synchrotron-based XPS was able to distinguish the CH<sub>2</sub> and CH<sub>3</sub> groups, with peaks at 284.8 and 283.7 eV, respectively, [47] while a single peak was reported in an earlier conventional XPS study. [48] Both the position and the difference in the measured BEs are in good agreement with the calculated values of 284.7 and 283.5 eV, respectively. Also for CH<sub>3</sub>CO, two peaks at 285.2 and 283.5 eV are separated by synchrotron-based XPS, [47] and both compare well with the calculated values, 285.1 and 283.3 eV. In a conventional XPS study, only a single C 1s peak at 283.9 eV was observed for acetaldehyde on Pt(111), and this peak was assigned to CH<sub>3</sub> [48]. Two stable configurations are found for acetaldehyde on Pt(111):  $\eta^1(\text{O})$  (top) and  $\eta^2(\text{C},\text{O})$  (di- $\sigma$ ), (Table 3.2) with a DFT-PBE adsorption energy difference of only 4 kJ/mol. The calculated C 1s BEs for the CHO and CH<sub>3</sub> group in the  $\eta^2(\text{C},\text{O})$  configuration are 284.5 and 283.2 eV, respectively, and 286.1 and 284.0 eV,



respectively, in the  $\eta^1(\text{O})$  configuration. The calculated  $\text{CH}_3$  C 1s BE for the  $\eta^1(\text{O})$  configuration agrees with the experimental value of 283.9 eV, while the calculated BEs for the  $\eta^2(\text{C},\text{O})$  configuration differ somewhat more. This is consistent with the dominant  $\eta^1(\text{O})$  configuration that has been observed in surface science studies. [70] An important species during hydrogenation and dehydrogenation reactions on Pt is  $\text{CCH}_3$ . Both synchrotron-based and conventional XPS studies find a single C 1s peak at 284.1 eV for  $\text{CCH}_3$  on Pt(111), and the two carbon atoms could not be distinguished [51,52]. This is consistent with the very small difference in the calculated C 1s BEs of 284.27 and 284.13 eV. Note that for  $\text{CCH}_3$  on Co(0001), the difference in the C 1s BEs is much larger at 1.0 eV (Table 3.4).

Also on Pt(111), the calculated C 1s BEs are sensitive to the adsorption site. For a high  $\frac{1}{2}$  ML coverage, CO occupies both the top and the bridge sites in a  $p(4 \times 2)$  unit cell (Table 3.2), as shown by low-energy electron diffraction (LEED) [52] and by photoelectron diffraction (PED) studies [53]. In synchrotron-based XPS, two C 1s peaks are distinguished at 286.8 and 286.1 eV for this structure. The calculated C 1s BEs of 286.74 eV for CO-top and 285.96 eV for CO-bridge agree well with the experimental values. At a lower coverage, CO occupies only top sites on Pt(111). In particular for a  $\frac{3}{16}$  ML coverage, a C 1s BE of 286.8 eV was measured by conventional XPS [52], in reasonable agreement with the calculated value of 287.03 eV. Two adsorption geometries have been reported for  $\text{C}_2\text{H}_4$  on Pt(111), di- $\sigma$  and  $\pi$ . Though di- $\sigma$  adsorption is the most stable structure in the DFT-PBE calculations, both structures have been identified by high-resolution electron energy loss

spectroscopy (HREELS) and temperature programmed desorption (TPD) studies [71]. The calculated C 1s BE for di- $\sigma$  C<sub>2</sub>H<sub>4</sub>, 283.38 eV, matches both the 283.2 eV peak determined by synchrotron-based XPS [51] and the 283.4 eV peak determined by conventional XPS for a 1/4 ML C<sub>2</sub>H<sub>4</sub> coverage [50]. The calculated C 1s BE for  $\pi$ -adsorbed C<sub>2</sub>H<sub>4</sub>, 284.24 eV, does not agree well with those experimental values.

The Bader charges on the carbon atoms are plotted against the calculated C 1s BEs in Figure 3.4b. The chemical shifts and the charges show similar trends, and the correlation is somewhat better than for hydrocarbon species on Co(0001), with a R<sup>2</sup> value of 0.83 (Figure 3.4b). The lowest C 1s BE in the test set, CH<sub>3</sub> on Pt(111), corresponds with the most negative charge of -0.3. Similarly to Co(0001), there is significant backdonation to the CH<sub>3</sub> group, but most charge remains on the carbon atom rather than flow to the C-H antibonding orbital. Therefore, the carbon atom is more negative for CH<sub>3</sub> on Pt(111) than for CH<sub>3</sub> on Co(0001). For unsaturated hydrocarbons such as C<sub>2</sub>H<sub>4</sub> and C<sub>2</sub>H<sub>2</sub> there is net charge transfer to Pt(111), as also reported by Toulhoat et al. [72], but charge transfer from the H atoms to the C atoms still results in a slightly negative charge on the C atoms. For CCH<sub>3</sub>, the charges on the C atoms are quite different (0.3 e), yet the two C 1s BEs are very similar, again illustrating that charge transfer is not the only factor determining the core-level shift, and detailed calculations are needed to correctly interpret measured chemical shifts.

3.3.3. B 1s core-level binding energies.

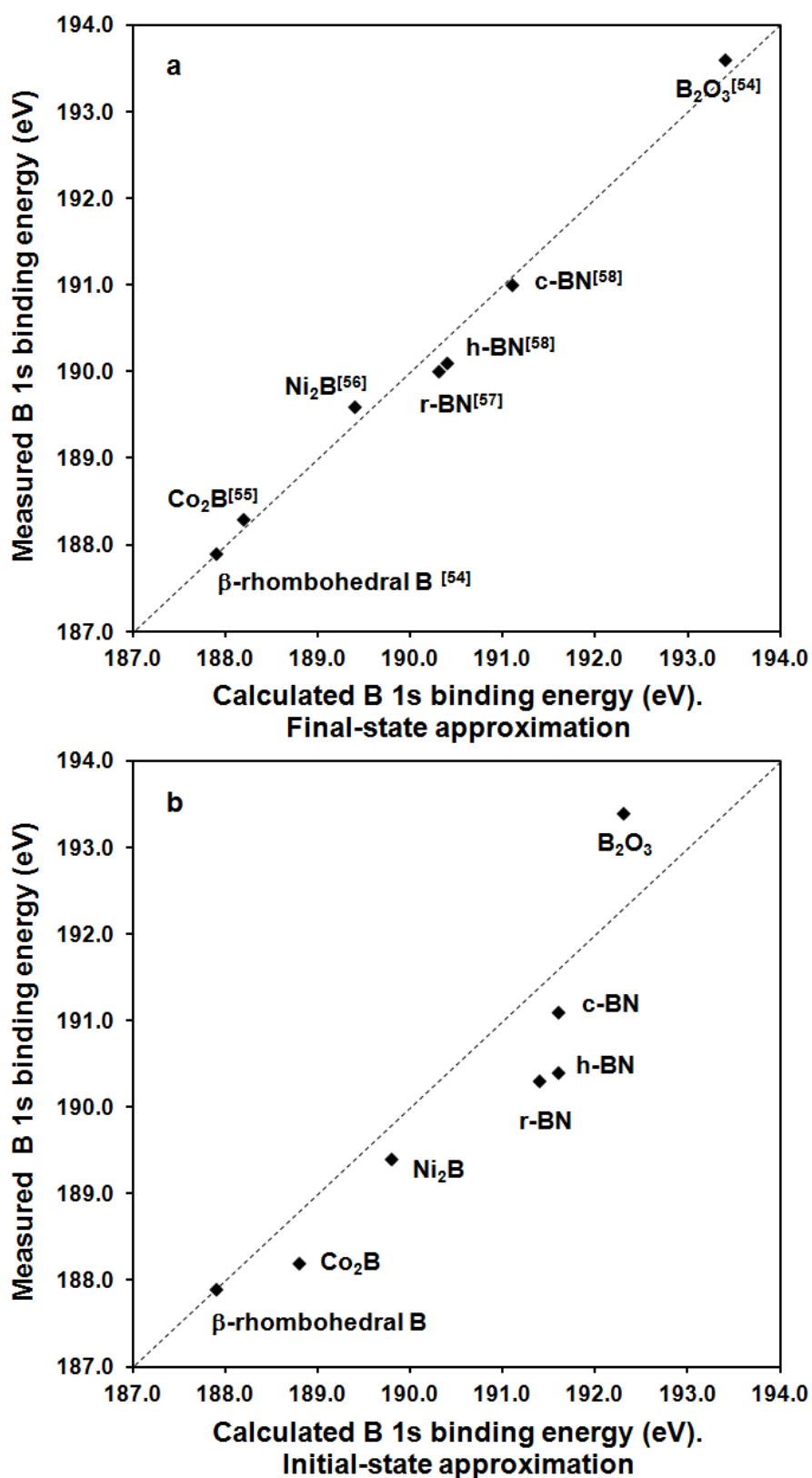


**Figure 3.5.** Calculated and experimental B 1s binding energies for various well-characterized bulk boride structure, using the final-state approximation (a) and the initial-state approximation (b). Experimental references are indicated.

B 1s BEs were calculated for B<sub>2</sub>O<sub>3</sub>, hexagonal-BN, cubic-BN, rhombohedral-BN, Ni<sub>2</sub>B, and Co<sub>2</sub>B. Final-state calculations are compared with experimental values in Figure 3.5a, while initial-state calculations are shown in Figure 3.5b. Experimental XPS data for boron compounds are somewhat scarcer than for carbon species and our test set is more varied than for carbon. In addition, the range in the experimental data for each structure can be rather larger, e.g., reported B 1s XPS peak positions for B<sub>2</sub>O<sub>3</sub> range from 192.0 [73] to 193.6 eV [54]. We have selected the experimental values that best agree with our calculated B 1s BEs for Figure 3.5a.

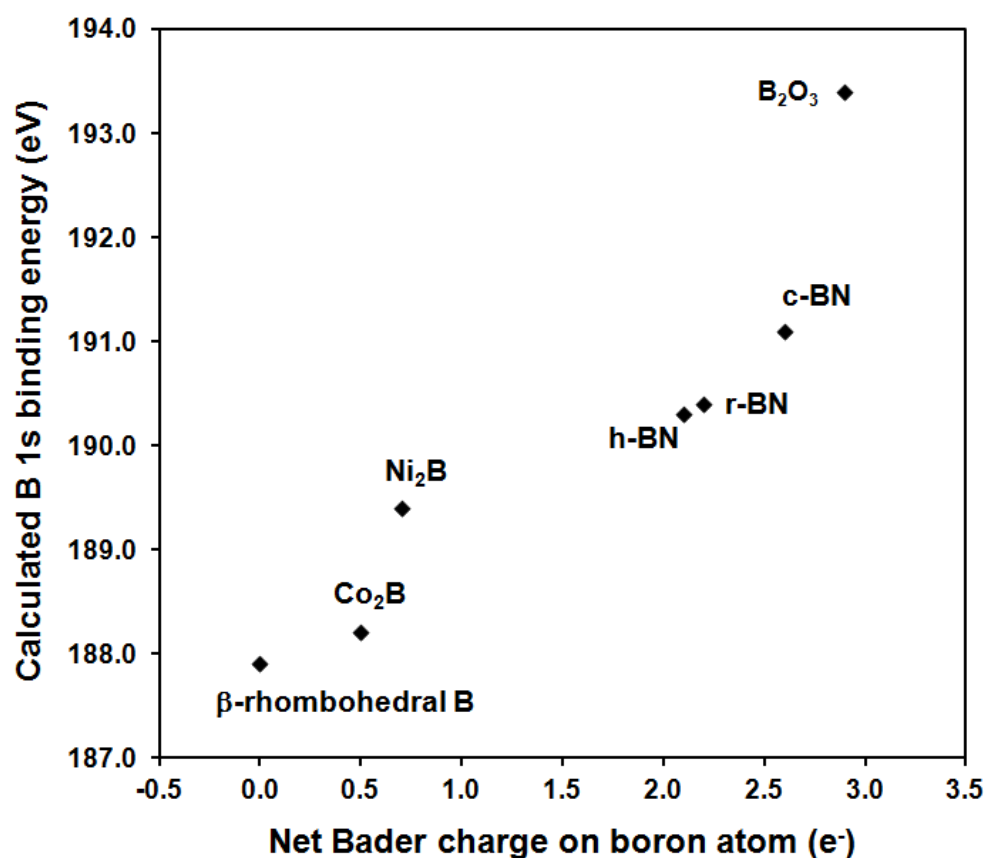


**Figure 3.6.** Correlation between the net Bader charge on the boron atom and the calculated B 1s binding energy.

With those data, the final-state DFT-PBE calculations describe the 6.0 eV variation in the experimental data with an average deviation of less than 50 meV. The initial-state calculations again show a larger average deviation of

820 meV, illustrating that final-state screening effects influence the calculated B 1s chemical shifts. The initial-state B 1s BEs are generally stronger than the final-state BEs, indicating that screening stabilizes the B 1s core hole more in the test set structures than in  $\beta$ -rhombohedral boron, the reference structure. The only exception is  $B_2O_3$ , where the final-state approximation predicts a lower BE than the initial-state approximation. The strongest B 1s BE is calculated for  $B_2O_3$ , consistent with strong electron withdrawal from the  $sp_2$  boron atoms by the three surrounding oxygen atoms. Boron nitride exists in different crystal structures. The most stable form is hexagonal-BN. It has a layered structure similar to graphite, and the boron atoms are  $sp_2$  hybridized. Rhombohedral-BN is also a layered structure, but with a three-layer stacking sequence. It is calculated to be 12 kJ/mol BN less stable than the hexagonal form. The cubic phase has a structure similar to diamond, with  $sp_3$  boron atoms. It is calculated to be 38 kJ/mol BN less stable than h-BN. The relative B 1s BEs for r-BN and h-BN are correctly predicted, and the slightly lower core-level BE for the more stable r-BN correlates with the more positive Bader charge on the boron atom (Figure 3.6). The higher BE in c-BN follows from the  $sp_3$  hybridization of the boron atom. Indeed,  $sp_3$  hybridization moves the valence electrons slightly further from the nucleus, leading to reduced screening of the nuclear charge [20]. Finally, two metal borides were considered;  $Ni_2B$  and  $Co_2B$ . Both display a positive chemical shift relative to bulk boron, as already reported in early XPS studies [55]. The positive shift in tetragonal transition-metal semi-borides has been attributed to charge transfer from boron to the transition metal [74], and is opposite to the charge transfer in transition-metal carbides (Figure 3.3). The charge transfer is larger for  $Ni_2B$

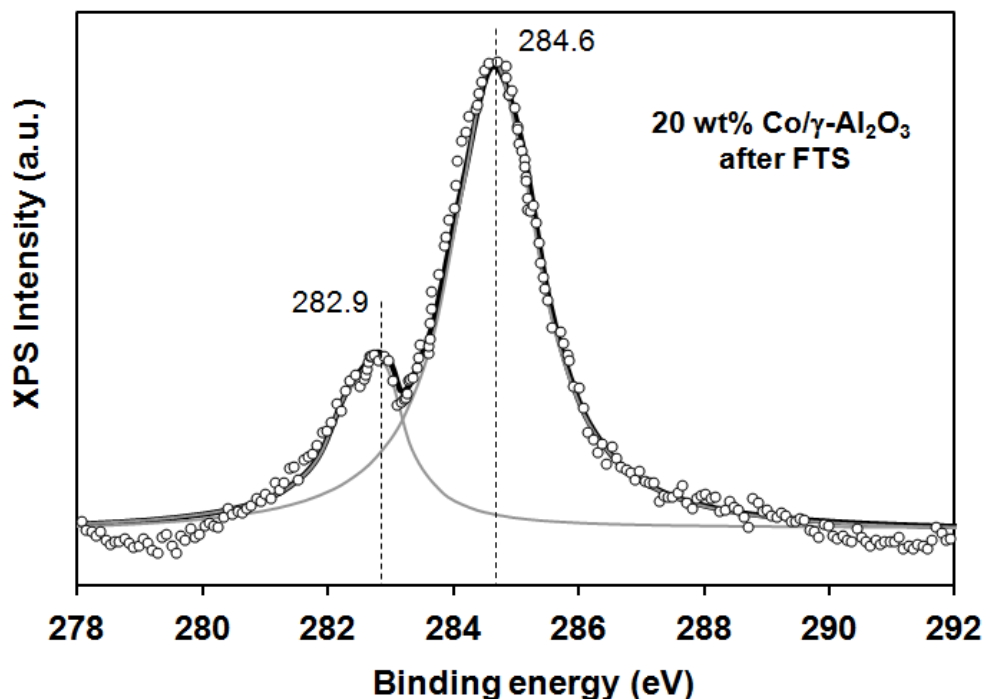
than for  $\text{Co}_2\text{B}$ , consistent with the higher electronegativity of Ni. Again, the net Bader charges on the boron atoms correlate with the calculated B 1s chemical shifts, as shown in Figure 3.6.

The higher BE in c-BN follows from the  $\text{sp}_3$  hybridization of the boron atom. Indeed,  $\text{sp}_3$  hybridization moves the valence electrons slightly further from the nucleus, leading to reduced screening of the nuclear charge [20]. Finally, two metal borides were considered;  $\text{Ni}_2\text{B}$  and  $\text{Co}_2\text{B}$ . Both display a positive chemical shift relative to bulk boron, as already reported in early XPS studies [55]. The positive shift in tetragonal transition-metal semi-borides has been attributed to charge transfer from boron to the transition metal [74], and is opposite to the charge transfer in transition-metal carbides (Figure 3.3). The charge transfer is larger for  $\text{Ni}_2\text{B}$  than for  $\text{Co}_2\text{B}$ , consistent with the higher electronegativity of Ni. Again, the net Bader charges on the boron atoms correlate with the calculated B 1s chemical shifts, as shown in Figure 3.6.

#### *3.3.4. Identification of carbon and boron species on supported Co catalysts by core-level BE calculations.*

The results in the previous sections suggest that final-state DFT-PBE calculations can predict C 1s and B 1s BEs with an accuracy of better than 100 meV. Moreover, the calculated chemical shifts are sensitive to the chemical state and adsorption site of the boron and carbon species, and can hence be used to help identify surface species. Next, we illustrate how such calculations, in combination with stability calculations and additional characterization techniques [33-35], can help identify the nature of the

resilient carbon species formed on a supported Co catalyst during FTS, and the nature of the boron promoter introduced to Co catalysts to improve their long-term stability during FTS.

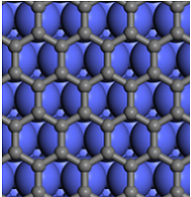
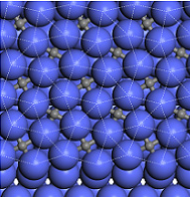
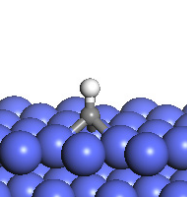
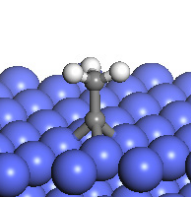
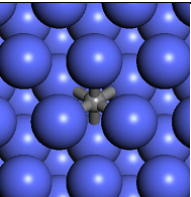
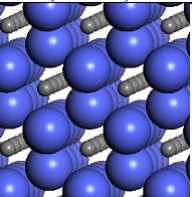
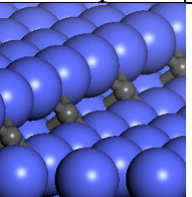
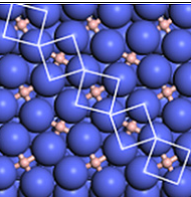
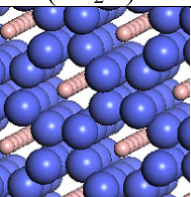
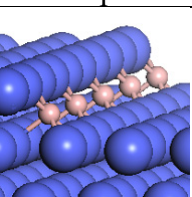
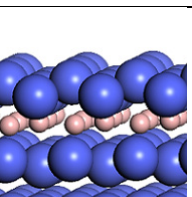
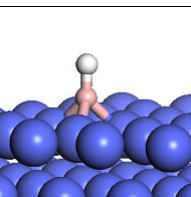


**Figure 3.7.** C 1s XPS spectra for a 20 wt% Co/ $\gamma$ -Al<sub>2</sub>O<sub>3</sub> catalyst after 200 hours of FTS at 20 bar and 240 °C

Supported Co/ $\gamma$ -Al<sub>2</sub>O<sub>3</sub> catalysts were tested for 200 hours during FTS at 240 °C [33]. Over this period, the catalyst activity decreased by 30 %. Based on Temperature-Programmed Hydrogenation (TPH) and Transmission Electron Microscopy (TEM) analysis of the spent Co catalysts after 200 hours of reaction, the deactivation is attributed, at least in part, to the formation of resilient carbon deposits [33]. The C 1s XPS spectrum for the catalyst after 200 hours of reaction and after wax extraction is shown in Figure 4a. Deconvolution suggests the presence of at least two types of resilient carbon species, with C 1s BEs of 283.0 and 284.6 eV, respectively.

To help identify those carbon deposits, the thermodynamic stability under FTS conditions and the C 1s BE were calculated for various possible carbon species (Table 3.4).

**Table 3.4.** Calculated stability under Fischer-Tropsch conditions,  $\Delta G_r$  (500 K, 20 bar), and C 1s and B 1s binding energy for various carbon and boron species on Co surfaces.

	Graphene	p4g carbide	CH at hcp	CCH <sub>3</sub> at hcp
Structure				
Calculated C 1s BE	284.5	283.3	283.6	284.1 (C) 285.1 (CH <sub>3</sub> )
Stability <sup>a</sup>	-116	-98	-72	-90
	Subsurface carbon	Bulk carbide (Co <sub>2</sub> C)	Carbon at B5 step	p4g boride
Structure				
Calculated C(B) 1s BE	283.9	283.2	284.0	187.9
Stability	-15 <sup>a</sup>	+16 <sup>a</sup>	-95 <sup>a</sup>	-59 <sup>b</sup>
	Bulk boride (Co <sub>2</sub> B)	Boron at B5 step	Monolayer of subsurface B	BH at hcp
Structure				
Calculated B 1s BE	188.2	186.5	187.0	186.8
Stability <sup>b</sup>	-29	-27	-53	-24

<sup>a</sup>Gibbs free energy for  $\text{CO (g)} + (n/2+1) \text{H}_2 \text{(g)} \leftrightarrow \text{C}_1\text{H}_n^* + \text{H}_2\text{O (g)}$  at typical FTS conditions, 500 K,  $p_{\text{CO}} = 4.4$  bar;  $p_{\text{H}_2} = 8.9$  bar;  $p_{\text{H}_2\text{O}} = 6.7$  bar; <sup>b</sup>Gibbs free energy for  $1/2 \text{B}_2\text{H}_6 \text{(g)} \leftrightarrow \text{B}^* + 3/2 \text{H}_2 \text{(g)}$  at 500 K,  $p_{\text{B}_2\text{H}_6} = 1.0$  bar;  $p_{\text{H}_2} = 8.9$  bar. [33-35]

The most stable carbon species are an extended poly-aromatic graphene overlayer and a p4g surface carbide. Surface hydrocarbon species such as CH<sub>2</sub>



and  $\text{CH}_3\text{CH}_2$  are also found to be thermodynamically stable, consistent with the Gibbs free energy of reaction of about  $\pm 55$  kJ/mol converted CO for the formation of long chain alkanes from a synthesis gas reservoir during FTS. The formation of subsurface carbon and of bulk Co carbide ( $\text{Co}_2\text{C}$ ) are less favorable. Based on the calculated C 1s BEs, the peak at 284.6 eV likely corresponds with poly-aromatic carbon deposits, though hydrocarbon waxes remaining after careful wax extraction might also contribute to this XPS peak. This assignment is consistent with the TPH profile and the TEM images [33]. The peak at 283.0 eV is attributed to a carbide phase, either a p4g surface carbide or a bulk carbide  $\text{Co}_2\text{C}$ . Since thermodynamic calculations show that the formation of a p4g surface carbide is significantly more favorable, the p4g surface carbide structure is the most likely candidate for the peak at 283.0 eV.

The addition 0.5 wt% boron to a 20 wt% Co/ $\gamma$ - $\text{Al}_2\text{O}_3$  was reported to enhance the catalyst stability during FTS without affecting the maximum activity or selectivity [34,35]. Indeed, after 200 hours of reaction, the boron promoted catalyst retained 95 % of its activity, while the activity of the unpromoted catalyst decreased by 30 %. To investigate the nature of the boron species on the supported Co catalyst, B 1s XPS spectra were used. The B 1s XPS profile for a Co catalyst promoted with 2.0 wt% boron is shown in Figure 3.8. A higher boron loading was used to improve the XPS signal to noise ratio. However, the XPS profile for a Co catalyst promoted with 0.5 wt% boron is qualitatively similar [35]. Deconvolution of the B 1s spectrum suggest the presence of two boron species, a boron oxide with a core-level BE around 191.6 eV and a reduced form of boron with a core-level BE around 188.1 eV.

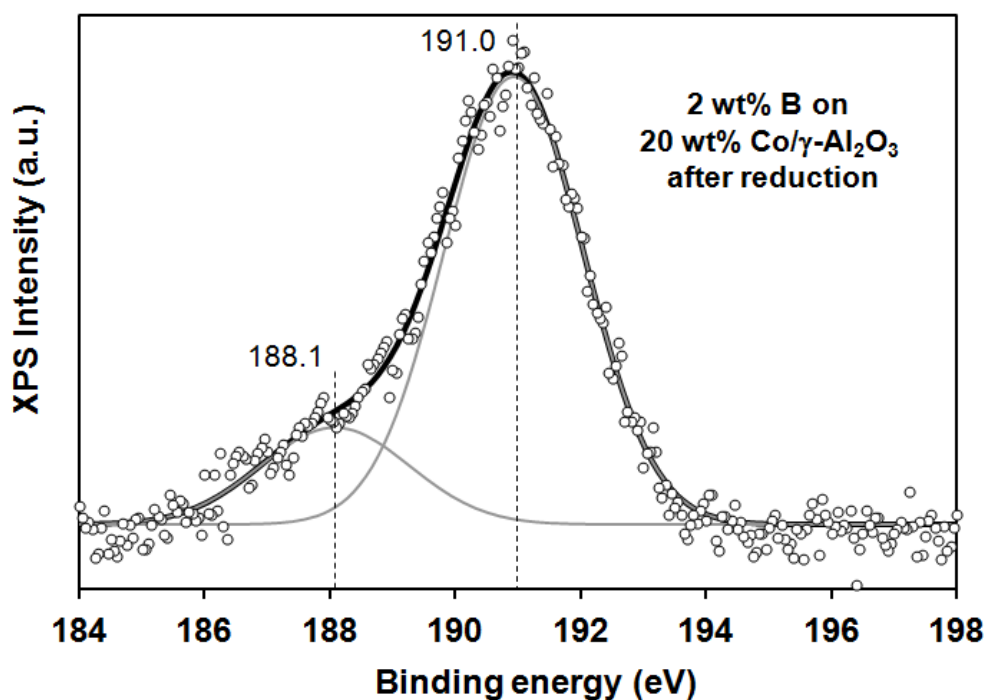
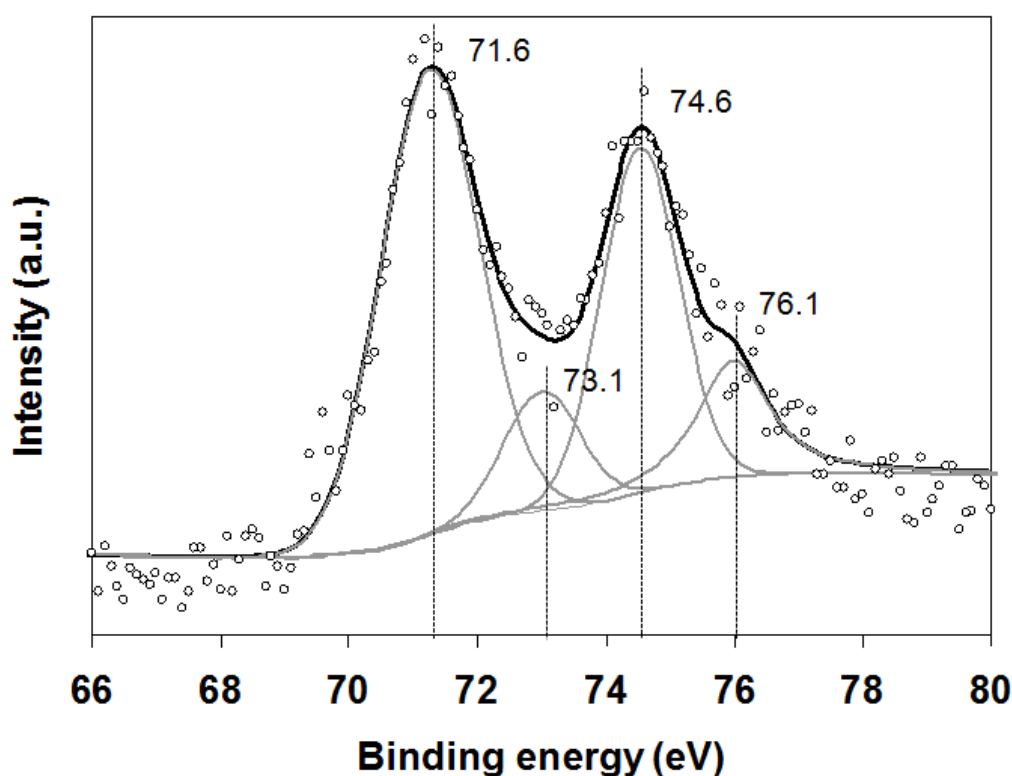


**Figure 3.8.** B 1s XPS spectra for a 20 wt% Co/ $\gamma$ -Al<sub>2</sub>O<sub>3</sub> catalyst promoted with 2 wt% boron, after reduction for 12 hours in 50 Nml/min H<sub>2</sub> at 500 °C and at atmospheric pressure.

The boron oxide species is likely associated with the  $\gamma$ -Al<sub>2</sub>O<sub>3</sub> support, since a similar peak was observed when 2.0 wt% boron was introduced to a  $\gamma$ -Al<sub>2</sub>O<sub>3</sub> support without Co [35]. Several candidates were considered for the reduced boron species (Table 3.4). Based on thermodynamic stability calculations, a p4g surface boride and a monolayer of subsurface boron are the most likely candidates. Several BH<sub>x</sub> surface species were also considered. BH is the most stable surface species in this family, and BH is 22 kJ/mol more stable than adsorbed BH<sub>3</sub>. Surface BH<sub>2</sub> decomposes to BH and surface H during the optimization. A surface boron atom is also thermodynamically unstable under FTS conditions [35]. Since the amount of introduced boron is rather small, and a sequential impregnation procedure was followed, the formation of a bulk Co boride (Co<sub>2</sub>B) seems unlikely. The calculated B 1s BE for subsurface boron, 187.0 eV, seems too low to correspond with the XPS peak at 188.1 eV. Based

on the XPS peak position and the thermodynamic stability, a surface p4g boride is therefore the most likely candidate for the reduced boron species present on the Co/ $\gamma$ -Al<sub>2</sub>O<sub>3</sub> catalyst.

### 3.3.5. Structural study of Pd<sub>3</sub>M@Pd<sub>3</sub>Pt core-shell particles using Pt 4f<sub>7/2</sub> BE calculations.

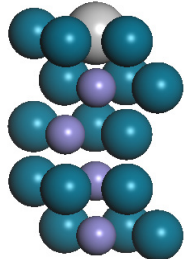
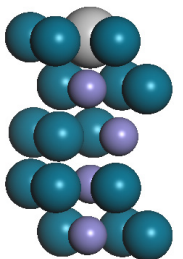
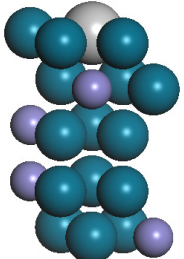
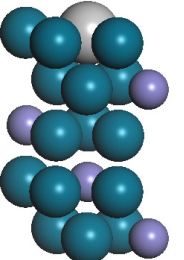


**Figure 3.9.** Pt 4f XPS spectrum for Pd<sub>3</sub>Fe@Pd<sub>3</sub>Pt/C, as synthesized. The Pt 4f<sub>7/2</sub> peak is indicated.

Core-shell particles have been proposed to improve the activity of oxygen reduction catalysts in fuel cells [e.g., 18,75]. We have reported the synthesis of a series of Pd<sub>3</sub>M@Pd<sub>3</sub>Pt (M= Co, Fe, Ni, and Cr) core-shell electrocatalysts, and found that the CO and oxygen adsorption energy on those catalysts decreases gradually from a Pd<sub>3</sub>Pt to a Pd<sub>3</sub>Cr core [18,36]. The change in oxygen adsorption energy leads to a volcano-like change in the oxygen reduction activity, with a maximum activity for the Pd<sub>3</sub>Fe@Pd<sub>3</sub>Pt catalysts

[18,36]. The core-shell particles were characterized using a combination of Energy-Dispersive X-ray spectroscopy (EDX), X-ray Diffraction (XRD), and TEM, as well as XPS [18].

**Table 3.5.** Relative stability for different possible Pd<sub>3</sub>M@Pd<sub>3</sub>Pt core-shell structures.

		Structure A	Structure B	Structure C	Structure D
Structure <sup>a</sup>					
Relative energy per unit cell (eV)	Pt	0.13	0.15	0.29	0
	Ni	0.26	0.29	0.65	0
	Co	0.40	0.44	1.67	0
	Fe	0.51	0.53	2.86	0
	Cr	0.59	0.62	3.78	0

<sup>a</sup>The blue spheres represent Pd atoms, the large grey spheres are surface Pt atoms, and the small purple spheres correspond to 3d transition metal atoms M

Various atomic arrangements are possible for the M atoms in a  $p(2 \times 2)$  Pd<sub>3</sub>M@Pd<sub>3</sub>Pt core-shell slab (Table 3.5). The most stable structure for all five Pd<sub>3</sub>M@Pd<sub>3</sub>Pt structures corresponds to the regular fcc unit cell (structure D), where the distance between M atoms is maximized. Indeed, the fcc unit cell contains four atoms, corresponding with the Pd<sub>3</sub>M stoichiometry. In structure D, each fcc unit cell contains one M atom. A similar stable structure was reported by Ramírez-Caballero et al. for Pd<sub>3</sub>M alloys [76]. Some of the fcc units cells that can be drawn for the other structures contain either no or two M atoms. Some of the M atoms hence share the same unit cell, leading to a less stable structure. Average magnetic moments for the 3d transition metal atoms M in the Pd<sub>3</sub>M@Pd<sub>3</sub>Pt core-shell structures are reported in Table 3.6. The magnetic moments are somewhat larger than in the corresponding pure 3d

metals, consistent with the larger separation between the M atoms in the Pd<sub>3</sub>M alloy. The calculated magnetic moments of the surface Pt atoms are small.

**Table 3.6.** Average magnetic moments ( $\mu_B$ /atom) of the 3d transition metal atoms, M, and of the surface Pt atoms in a Pd<sub>3</sub>M@Pd<sub>3</sub>Pt core-shell slab with a four-layer core and a monolayer shell (Figure 3.1).

	Pd <sub>3</sub> Fe@Pd <sub>3</sub> Pt	Pd <sub>3</sub> Cr@Pd <sub>3</sub> Pt	Pd <sub>3</sub> Co@Pd <sub>3</sub> Pt	Pd <sub>3</sub> Ni@Pd <sub>3</sub> Pt
M	3.22	2.44	2.14	0.98
Pt	0.29	0.32	0.33	0.33

Assuming cuboctahedral catalyst particles, and combining the average particle diameter obtained from XRD with the Pt weight-fraction from point-resolved EDX, a Pd<sub>3</sub>Pt shell thickness of one to two monolayers is estimated [18]. To provide additional support for the core-shell structure and for the shell thickness, final-state Pt 4f<sub>7/2</sub> BEs were calculated for different possible shell structures, and compared with the experimentally measured chemical shifts for the different core-shell particles (Figures 3.10 and 3.11). To evaluate the importance of final-state screening effects for Pd<sub>3</sub>M@Pd<sub>3</sub>Pt core-shell structures, initial-state calculations are reported as well. An illustrative Pt 4f XPS spectrum is shown in Figure 3.9 for the most active Pd<sub>3</sub>Fe@Pd<sub>3</sub>Pt catalyst.

The calculated Pt 4f<sub>7/2</sub> SCLS depends on the number of layers used to model the Pd<sub>3</sub>M core (Figure 3.10a). For a monolayer shell, at least four layers are required to converge the calculated Pt 4f<sub>7/2</sub> BE. Also the Bader charge on the surface Pt atoms was found to be converged within 0.05 electrons for a four-layer core. The calculated Pt 4f<sub>7/2</sub> chemical shift depends strongly on the shell thickness in the model (Figure 3.10b).

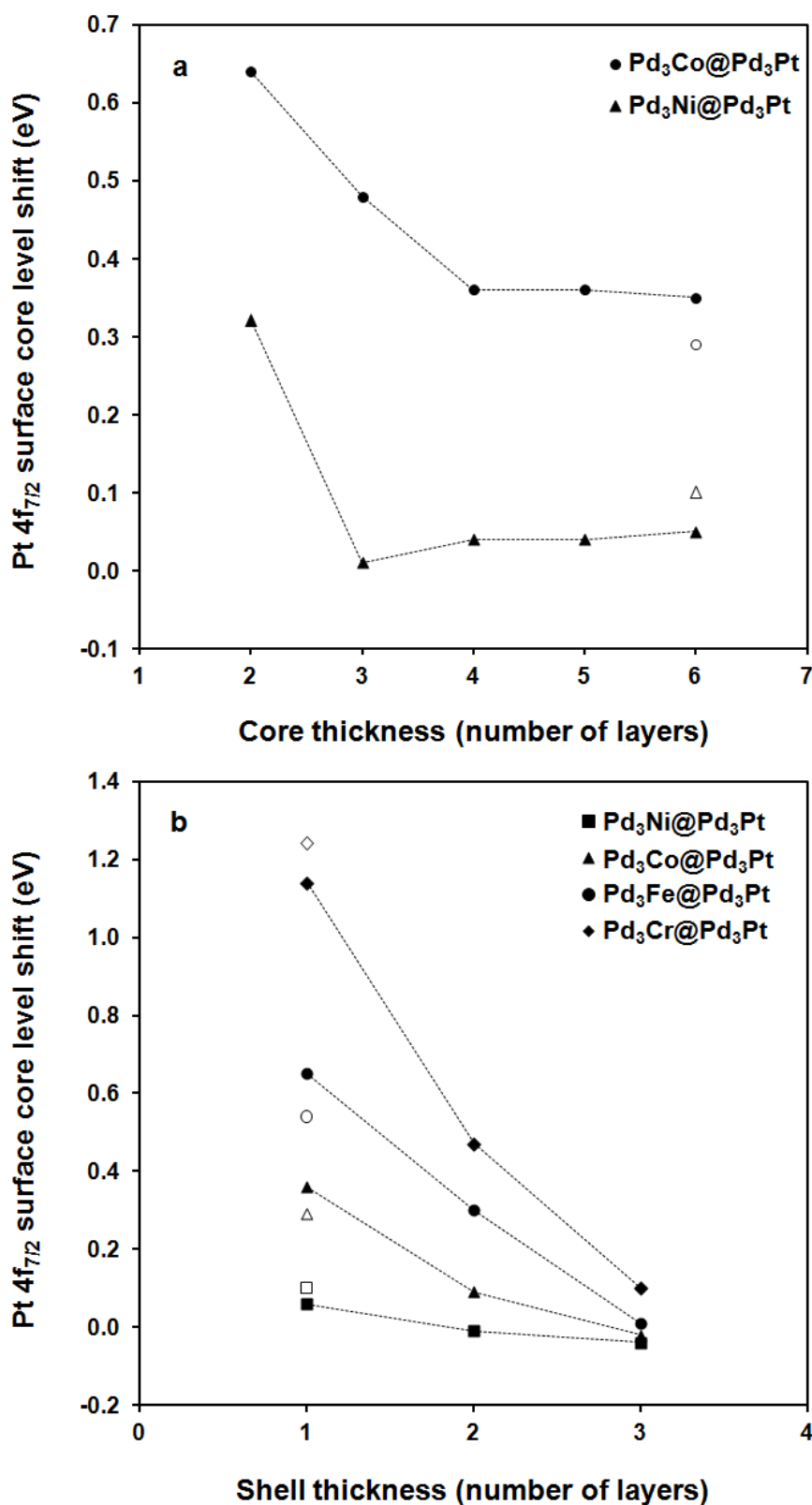


**Figure 3.10.** (a) Calculated Pt 4f<sub>7/2</sub> surface core-level shift as a function of the core thickness in the model (Fig. 3.1), and for a shell thickness of one layer; (b) Calculated Pt 4f<sub>7/2</sub> surface core-level shift for the surface Pt atoms as a function of the shell thickness for a core thickness of four layers. Filled symbols represent calculated values, while open symbols represent measured Pt 4f<sub>7/2</sub> surface core-level shifts for the corresponding core-shell particles.

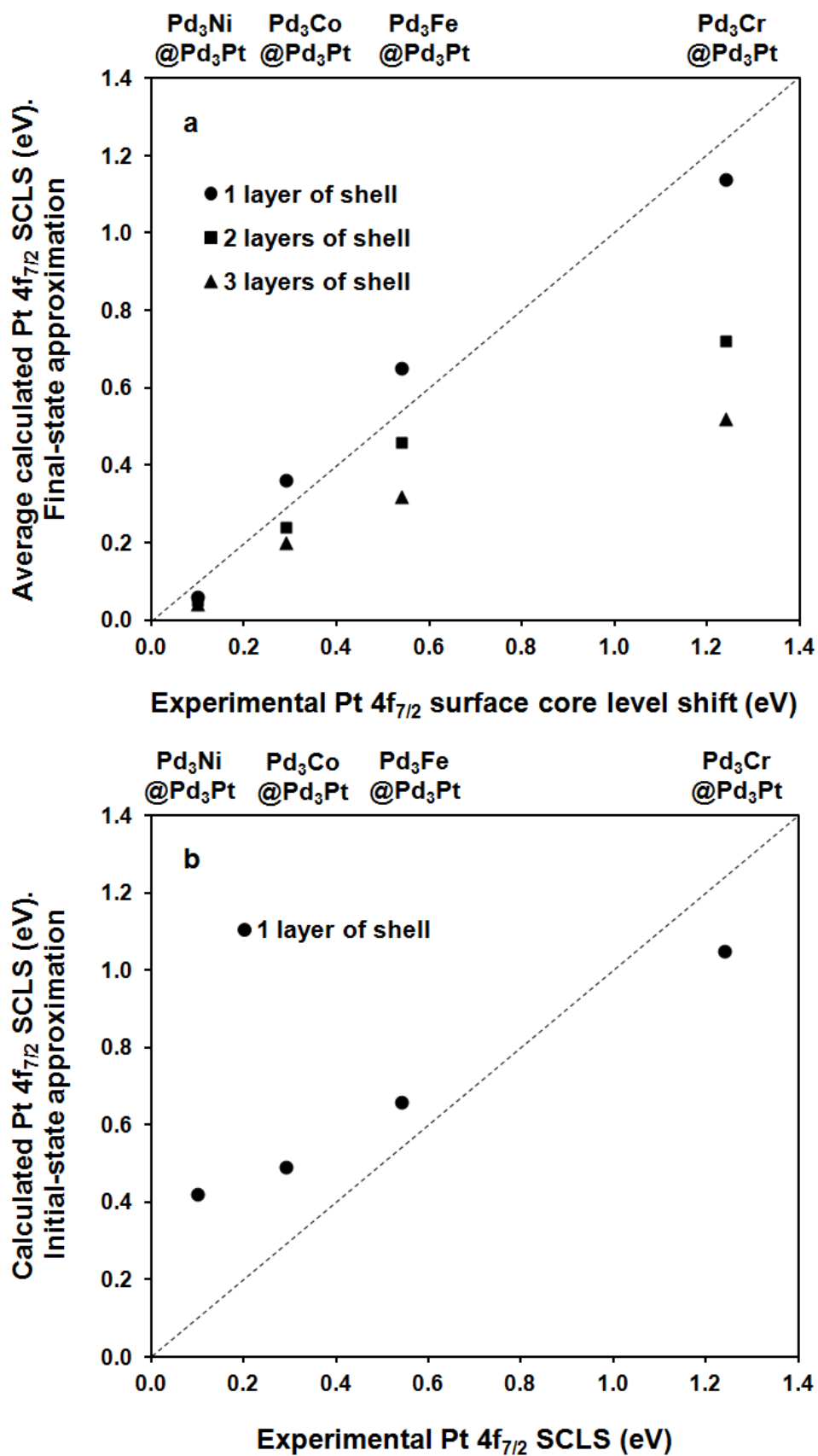


**Figure 3.11.** Average calculated and experimental Pt 4f<sub>7/2</sub> surface core-level shifts (SCLS) for different shell thicknesses, using the final-state approximation (a), and the initial-state approximation (b).

As the shell becomes thicker, the calculated chemical shift of the surface Pt atoms rapidly decreases, and the Pt 4f<sub>7/2</sub> BE converges to the Pt(111) surface value when the shell is about four layers thick. In Figure 3.11a, the final-state SCLSs are compared with the experimental XPS values for the different core-shell catalysts. The best agreement with the experimental data is obtained for the models with a monolayer-thick Pd<sub>3</sub>Pt shell, with an average deviation of 80 meV. The Pt 4f<sub>7/2</sub> BE calculations hence suggest that a monolayer Pd<sub>3</sub>Pt shell is formed on the Pd<sub>3</sub>M cores. This is consistent with the shell thickness estimated using the average particle size and the Pt content.

To evaluate the importance of core-hole screening, SCLSs were also calculated using the initial-state approximation for core-shell structures with a four-layer Pd<sub>3</sub>M core and a monolayer Pd<sub>3</sub>Pt shell (Figure 3.11b). The initial-state calculations show an average deviation of 260 meV with the experimental data. For the core-shell systems studied here, final-state core-hole screening increases the Pt 4f<sub>7/2</sub> BEs more than in bulk Pt and leads to an increase in the SCLS, except for the Pd<sub>3</sub>Cr@Pd<sub>3</sub>Pt catalysts. The importance of screening effects for core-shell catalysts is consistent with the results of Wertheim for small metal clusters [77].



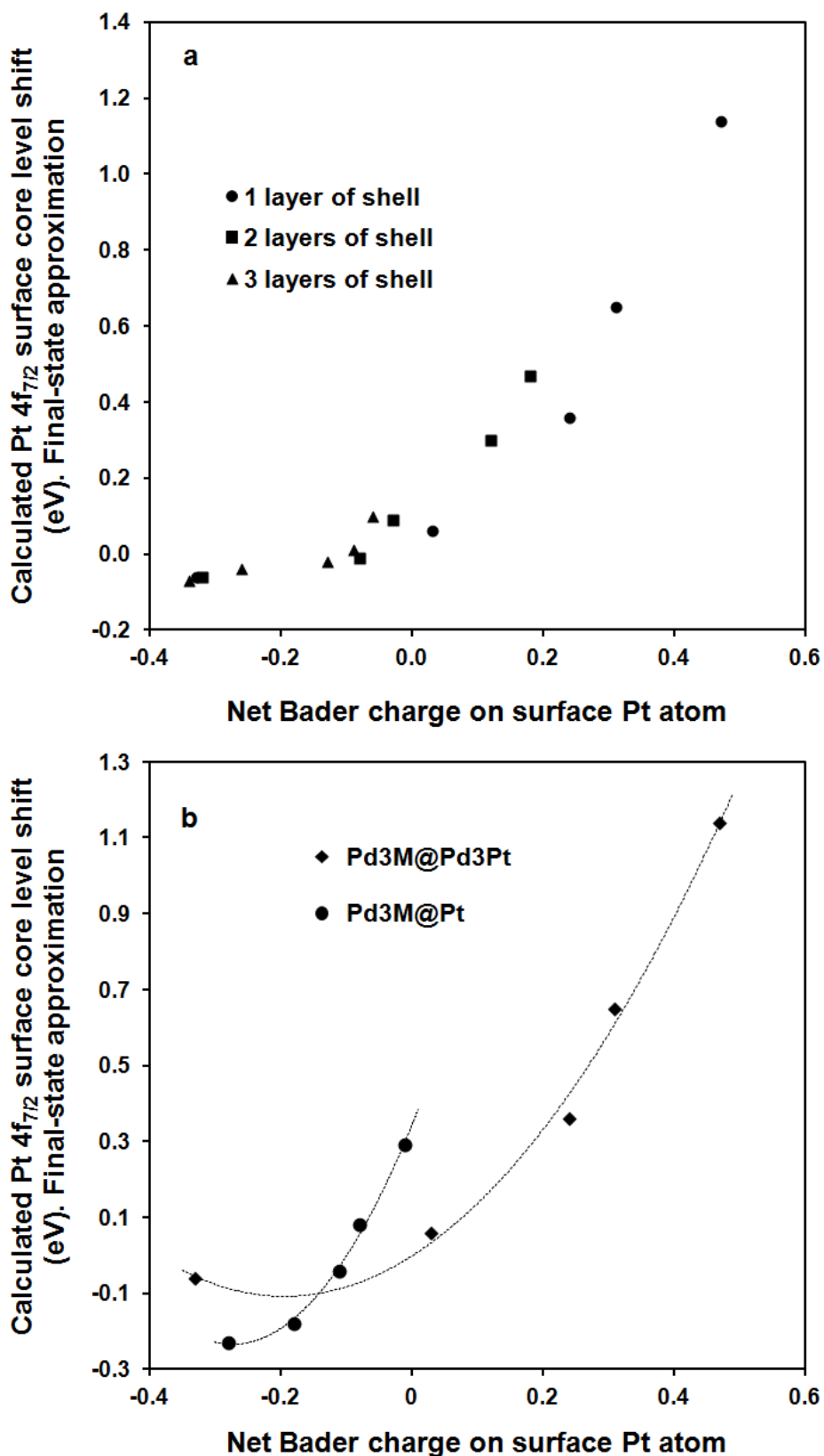


**Figure 3.12.** (a) Correlation between the net Bader charge on the surface Pt atoms and the calculated Pt 4f<sub>7/2</sub> SCLS for the surface Pt atom for different shell thicknesses and (b) Correlation between the net Bader charge on the surface Pt atoms and the calculated Pt 4f<sub>7/2</sub> SCLS for a series of Pd<sub>3</sub>M@Pt core-shell catalysts with a monolayer Pt shell and a four-layer Pd<sub>3</sub>M core.

To further analyze the variation of the calculated chemical shifts in the five core-shell catalysts, Bader charges on the surface Pt atoms (Figure 3.12a) and surface Pt d-band densities of state (Figure 3.13) were calculated. As suggested by Rodriguez and Goodman [19] and by Egelhoff [78], charge transfer between the surface and substrate is an important factor in the SCLSs of bimetallic core-shell systems. Indeed, as also observed for the C 1s and B 1s chemical shifts, the calculated Pt surface core-level shifts are correlated with the Bader charges on the surface Pt atoms in this family of Pd<sub>3</sub>M@Pd<sub>3</sub>Pt core-shell structure. The more positive the charge on the surface Pt atoms, the stronger the core-level BE. One should however note that this particular correlation only holds for similar structures. E.g., for a series of Pd<sub>3</sub>M@Pt core-shell catalysts with a monolayer Pt shell and a four-layer Pd<sub>3</sub>M core, the calculated Pt 4f<sub>7/2</sub> SCLSs also correlate with the Bader charges on the surface Pt atoms, but the correlation is different from the correlation of the Pd<sub>3</sub>M@Pd<sub>3</sub>Pt test set (Figure 3.12b).

To further elucidate the correlation between the Pt Bader charges and the chemical shifts, the DOS projected on the d-band of the surface Pt atoms are shown in Figure 3.13. Substitution of a subsurface Pt atom in Pd<sub>3</sub>Pt with a 3d transition metal causes a downward shift in the Pt d-band center [18,36]. The downward shift in the Pt d-band center relative to the Fermi level correlates with the calculated increase in the Pt 4f<sub>7/2</sub> BEs, however, the shifts in the d-band center are smaller than the core-level shifts [18]. In addition to a downward shift of the d-band center, more Pt d-states are pushed above the

Fermi level and the occupancy of the Pt d-band decreases from 89 % in Pd<sub>3</sub>Pt to 83 % in Pd<sub>3</sub>Cr@Pd<sub>3</sub>Pt (Figure 3.13).

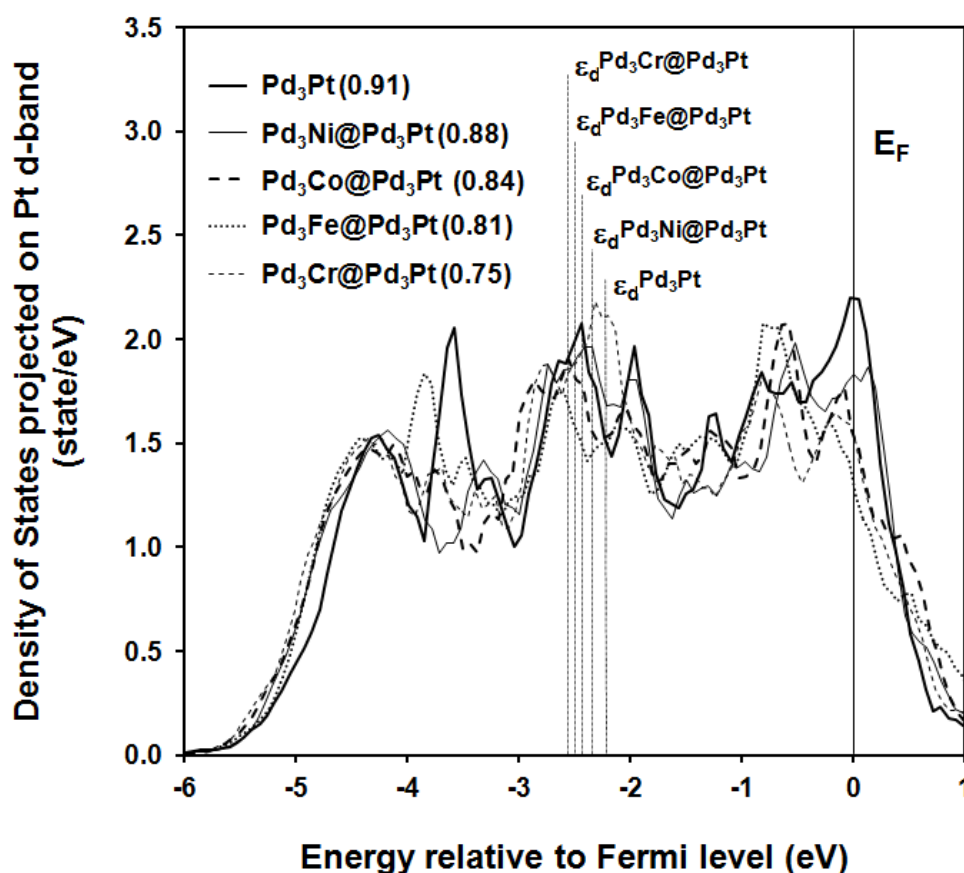


**Figure 3.13.** Total density of states (DOS) projected on the d-band of the surface Pt atoms in Pd<sub>3</sub>Pt@Pd<sub>3</sub>M. The d-band centers are indicated. Note that a downward shift in d-band correlates with a stronger core-level BEs is Figure 6a. The occupancy of the Pt d-band is shown in the legend. The decreased occupancy, from 0.89 to 0.83, correlates roughly with an increased Pt Bader charge (Figure 3.12a).

The decreased occupancy in turn correlates with the increased Bader charge (Figure 3.12a). Though both observations might seem contradictory, they can be explained by the broadening of the d-band due to compressive strain (Figure 3.13). Indeed, the optimized lattice constant decreases from 3.88 Å in Pd<sub>3</sub>Pt to 3.83 Å in Pd<sub>3</sub>Cr@Pd<sub>3</sub>Pt, leading to a wider d-band, and a downward shift of the d-band center. Charge transfer from the Pd<sub>3</sub>Pt shell to the Pd<sub>3</sub>M core in turn reduces the d-band occupancy and slightly reduces the downward shift in the d-band center. The influence of strain and ligand effects on the d-

band DOS in core-shell structures has been studied in detail by Kitchin et al. [79].

### 3.4. Conclusions.

X-ray Photoelectron Spectroscopy (XPS) is a popular surface characterization technique in heterogeneous catalysis. With the development of fast, high-resolution synchrotron-based XPS with *in situ* capabilities, the importance of XPS is expected to increase. In this work, we illustrate how DFT-PBE calculations can help analyze and interpret XPS data. First, final-state DFT-PBE calculations are shown to predict C 1s BEs for eight well-characterized surface carbon species with deviations smaller than 100 meV, and B 1s BEs with deviations smaller than 50 meV. To illustrate our approach, the nature of the resilient carbon deposits formed on a Co/ $\gamma$ -Al<sub>2</sub>O<sub>3</sub> catalyst during FTS was analyzed by computing C 1s BEs and thermodynamic stabilities for various possible carbon species. The calculations suggest that poly-aromatic carbon islands and a p4g surface carbide are the most likely candidates for the deposits with XPS peaks at 284.6 and 283.0 eV, respectively. The formation of these resilient carbon species is likely responsible for the observed loss in catalyst activity. Promotion with small amounts of boron was found to enhance the stability of Co FTS catalysts. To investigate the nature of the boron promoter on Co catalysts, calculated B 1s BEs for different possible boron species were compared with the observed B 1s XPS peak. A p4g surface cobalt boride is the most likely candidate for the XPS peak at 188.1 eV. Core-level BE calculations can also help determine the structure of core-shell catalysts. Indeed, the calculated chemical shifts depend strongly on the shell

thickness. For a series of Pd<sub>3</sub>M@Pd<sub>3</sub>Pt (M= Co, Fe, Ni, and Cr) core-shell electrocatalysts, the measured Pt 4f<sub>7/2</sub> chemical shift is best described by a structure with a monolayer Pd<sub>3</sub>Pt shell. This is consistent with the shell thickness estimated independently from the particle diameter and the Pt content.

### 3.5.References.

1. E. Sokolowski, C. Nordling, K. Siegbahn, *Phys. Rev.*, **110**, 776 (1958).
2. A. Knop-Gericke, E. Kleimenov, M. Havecker, R. Blume, D. Teschner, S. Zafeiratos, R. Schlögl, V.I. Bukhtiyarov, V.V. Kaichev, I.P. Prosvirin, A.I. Nizovskii, H. Bluhm, A. Barinov, P. Dudin, M. Kiskinova, *Adv. Catal.*, **52**, 213 (2009).
3. A.M. Venezia, *Catal. Today*, **77**, 359 (2003).
4. S. Tougaard, *X-Ray Photoelectron Spectroscopy*, in P. Worsfold, A. Townshend, C. Poole (eds.), *Encyclopedia of Analytical Science*, 2<sup>nd</sup> edition, Elsevier Ltd, pg. 446-456, (2005).
5. C. J. Powell, A. Jablonski, I. S. Tilinin, S. Tanuma, D. R. Penn, *J. Elec. Spec. Relat. Phenom.*, **98-99**, 1 (1999).
6. A. Baraldi, *J. Phys.: Condens. Matter*, **20**, 093001 (2008).
7. D. Teschner, J. Borsodi, A. Wootsch, Z. Revay, M. Havecker, A. Knop-Gericke, S.D. Jackson, R. Schlögl, *Science*, **320**, 86 (2008).
8. E.M. Vass, M. Havecker, S. Zafeiratos, D. Teschner, A. Knop-Gericke, R. Schlögl, *J. Phys.: Condens. Matter*, **20**, 184016 (2008).
9. M.A. Bañares, *Top. Catal.*, **52**, 1301 (2009).

10. F.G. Requejo, E.L.D. Hebenstreit, D.F. Ogletree, M. Salmeron, *J. Catal.*, **226**, 83 (2004).
11. L. Kohler, G. Kresse, *Phys. Rev. B*, **70**, 165405 (2004).
12. K. Siegbahn, C. Nordling, G. Johansson, J. Hedman, P.F. Heden, K. Hamrin, U. Gelius, T. Bergmark, L.O. Werme, R. Manne, Y. Baer, *ESCA applied to free molecules*, North-Holland, Amsterdam-London, (1969).
13. N. Martensson, A. Nilsson, *J. Elec. Spec. Relat. Phenom.*, **75**, 209 (1995).
14. S. Linic, H. Piao, K. Adib, M.A. Barteau, *Angew. Chem. Int. Ed.*, **43**, 2918 (2004).
15. M.T. Schaal, M.P. Hyman, M. Rangan, S. Ma, C.T. Williams, J.R. Monnier, J.W. Medlin, *Surf. Sci.*, **603**, 690 (2009).
16. M. Methfessel, V. Fiorentini, S. Oppo, *Phys. Rev. B*, **61**, 5229 (2000).
17. M. Weinert, R.E. Watson, *Phys. Rev. B*, **51**, 17168 (1995).
18. Q.T. Trinh, J.H. Yang, J.Y. Lee, M. Saeys, *J. Catal.*, **291**, 26 (2012).
19. J.A. Rodriguez, D.W. Goodman, *Science*, **257**, 897 (1992).
20. P.S. Bagus, F. Illas, G. Pacchioni, F. Parmigiani, *J. Elec. Spec. Relat. Phenom.*, **100**, 215 (1999).
21. R.A. van Santen, M. Neurock, *Molecular heterogeneous catalysis: a conceptual and computational approach*, VCH-Wiley, Weinheim, (2006).
22. J.K. Nørskov, T. Bligaard, J. Rossmeisl, C.H. Christensen, *Nat. Chem.*, **1**, 37 (2009).
23. F. Tielens, M. Saeys, E. Tourwe, G.B. Marin, A. Hubin, P. Geerlings, *J. Phys. Chem. A*, **106**, 1450 (2002).
24. M. Saeys, M.F. Reyniers, G.B. Marin, M. Neurock, *J. Phys. Chem. B*, **106**, 7489 (2002).

25. C. Morin, D. Simon, P. Sautet, *J. Phys. Chem. B*, **107**, 2995 (2003).
26. W. Olovsson, T. Marten, E. Holmstrom, B. Johansson, I.A. Abrikosov, *J. Elec. Spec. Relat. Phenom.*, **178-179**, 88, (2010).
27. W. Olovsson, C. Göransson, T. Marten, I.A. Abrikosov, *Phys. Stat. Sol. (b)*, **243**, 2447 (2006).
28. Y. Takahata, D.P. Chong, *J. Elec. Spec. Relat. Phenom.*, **133**, 69 (2003).
29. M. Todorova, E. Lundgren, V. Blum, A. Mikkelsen, S. Gray, J. Gustafson, M. Borg, J. Rogal, K. Reuter, J.N. Andersen, M. Scheffler, *Surf. Sci.*, **541**, 101 (2003).
30. L. Bianchettin, A. Baraldi, S. de Gironcoli, E. Vesselli, S. Lizzit, G. Comelli, R. Rosei, *J. Phys. Chem. C*, **113**, 13192 (2009).
31. A.D. Gandubert, E. Krebs, C. Legens, D. Costa, D. Guillaume, P. Raybaud, *Catal. Today*, **130**, 149 (2008).
32. T.K. Todorova, M. Sierka, J. Sauer, S. Kaya, J. Weissenrieder, J.-L. Lu, H.-J. Gao, S. Shaikhutdinov, H.-J. Freund, *Phys. Rev. B*, **73**, 165414 (2006).
33. K.F. Tan, J. Xu, J. Chang, A. Borgna, M. Saeys, *J. Catal.*, **274**, 121 (2010).
34. M. Saeys, K.F. Tan, J. Chang, A. Borgna, *Ind. Eng. Chem. Res.*, **49**, 11098 (2010).
35. K.F. Tan, J. Chang, A. Borgna, M. Saeys, *J. Catal.*, **280**, 50 (2011).
36. J. Xu, J.H. Yang, J.Y. Lee, M. Saeys, *Ind. Eng. Chem. Res.*, **49**, 10251 (2010).
37. J.P. Perdew, K. Burke, M. Ernzerhof, *Phys. Rev. Lett.*, **77**, 3865 (1996).
38. G. Kresse, J. Hafner, *J. Phys. Rev. B*, **47**, 558 (1993).

39. G. Kresse, J. Futhmuller, *Comput. Mater. Sci.*, **6**, 15 (1996).
40. P.E. Blochl, *Phys. Rev. B*, **50**, 17953 (1994).
41. G. Kresse, D. Joubert, *Phys. Rev. B*, **59**, 1758 (1999).
42. C.J. Weststrate, H.J. Gericke, M.W.G.M. Verhoeven, I.M. Ciobã A.M. Saib, J.W. Niemantsverdriet, *J. Phys. Chem. Lett.*, **1**, 1767 (2010).
43. J. Vaari, J. Lahtinen, P. Hautajarvi, *Catal. Lett.*, **44**, 43 (1997).
44. F. Steinbach, J. Kiss, R. Krall, *Surf. Sci.*, **157**, 401 (1985).
45. J. Lahtinen, J. Vaari, K. Kauraala, *Surf. Sci.*, **418**, 502 (1998).
46. P. Bennich, C. Puglia, P.A. Bruhwiler, A. Nilsson, A.J. Maxwell, A. Sandell, N. Martensson, *Phys. Rev. B*, **59**, 8292 (1999).
47. Lee, A.F.; Gawthrope, D.E.; Hart, N.J.; Wilson, K. *Surf. Sci.*, **548**, 200 (2004).
48. M.K. Rajumon, M.W. Roberts, F. Wang, P.B. Wells, *J. Chem. Soc., Faraday Trans.*, **94**, 3699 (1998).
49. Y. Matsumoto, Y.A. Gruzdkov, K. Watanabe, K. Sawabe, *J. Chem. Phys.*, **105**, 4775 (1996).
50. N. Freyer, G. Pirug, H.P. Bonzel, *Surf. Sci.*, **126**, 487 (1983).
51. A.F. Lee, K. Wilson, *J. Vac. Sci. Technol. A*, **21**, 563 (2003).
52. O. Bjorneholm, A. Nilsson, H. Tillborg, P. Bennich, A. Sandell, B. Hernnk, C. Puglia, N. Martensson, *Surf. Sci.*, **315**, L983 (1994).
53. F. Bondino, G. Comelli, F. Esch, A. Locatelli, A. Baraldi, S. Lizzit, G. Paolucci, R. Rosei, *Surf. Sci.*, **459**, L467 (2000).
54. C.W. Ong, H. Huang, B. Zheng, R.W.M. Kwok, Y.Y. Hui, W.M. Lau, *J. Appl. Phys.*, **95**, 3527 (2004).
55. G. Mavel, J. Escard, P. Costa, J. Castaing, *Surf. Sci.*, **35**, 109 (1973).



56. X. Feng, Y.J. Bai, B. Lu, Y.R. Zhao, J. Yang, J.R. Chi, *Inorg. Chem. Commun.*, **7**, 189 (2004).
57. K. Bao, F. Yu, L. Shi, S. Liu, X. Hu, J. Cao, Y. Qian, *J. Solid State Chem.*, **182**, 925 (2009).
58. D.H. Berns, M.A. Cappelli, *J. Mater. Res.*, **12**, 2014 (1997).
59. F. Janak, *Phys. Rev. B*, **18**, 7165 (1978).
60. S. Lizzit, A. Baraldi, A. Groso, K. Reuter, M. V. Ganduglia-Pirovano, C. Stampfl, M. Scheffler, M. Stichler, C. Keller, W. Wurth, D. Menzel, *Phys. Rev. B*, **63**, 205419 (2001).
61. M. Borg, M. Birgersson, M. Smedh, A. Mikkelsen, D.L. Adams, R. Nyholm, C-O. Almbladh, J.N. Andersen, *Phys. Rev. B*, **69**, 235418 (2004).
62. R.F.W. Bader, *Atoms in Molecules - A quantum theory*, Oxford University Press, New York, (1990).
63. G. Henkelman, A. Arnaldsson, H. Jonsson, *Comput. Mater. Sci.*, **36**, 254 (2006).
64. J.H. Yang, W.J. Zhou, C.H. Cheng, J.Y. Lee, Z.L. Liu, *ACS Appl. Mater. Interfaces*, **2**, 119 (2010).
65. A.V. Kalinkin, M.Y. Smirnov, A.I. Nizovskii, V.I. Bukhtiyarov, *J. Elec. Spec. Relat. Phenom.*, **177**, 15 (2010).
66. Z.J. Zuo, W. Huang, P.D. Han, Z.H. Li, *Appl. Surf. Sci.*, **256**, 5929 (2010).
67. P.J. Feibelman, B. Hammer, J.K. Nørskov, F. Wagner, M. Scheffler, R. Stumpf, R. Watwe, J. Dumesic, *J. Phys. Chem. B*, **105**, 4018 (2001).
68. M.K. Zhuo, K.F. Tan, A. Borgna, M. Saeys, *J. Phys. Chem. C*, **113**, 8357 (2009).

69. Q.Y. Yang, K.J. Maynard, A.D. Johnson, S.T. Ceyer, *J. Chem. Phys.*, **102**, 7734 (1995).
70. H.B. Zhao, J. Kim, B.E. Koel, *Surf. Sci.*, **538**, 147 (2003).
71. J.M. Essen, J. Haubrich, C. Becker, K. Wandelt, *Surf. Sci.*, **601**, 3472 (2007).
72. F. Mittendorfer, C. Thomazeau, P. Raybaud, H. Toulhoat, *J. Phys. Chem. B*, **107**, 12287 (2003).
73. W.A. Brainard, D.R. Wheeler, *J. Vac. Sci. Technol.*, **15**, 1801 (1978).
74. P. Mohn, *J. Phys. C: Solid State Phys.*, **21**, 2841 (1988).
75. R.R. Adzic, J. Zhang, K. Sasaki, M.B. Vukmirovic, M. Shao, J.X. Wang, A.U. Nilekar, M. Mavrikakis, J.A. Valerio, F. Uribe, *Top. Catal.*, **46**, 249 (2007).
76. G.E. Ramírez-Caballero, Y. Ma, R. Callejas-Tovar, P.B. Balbuena, *Phys. Chem. Chem. Phys.*, **12**, 2209 (2010).
77. G.K. Wertheim, *Z. Phys. B - Condensed Matter*, **66**, 53 (1987).
78. W.F. Egelhoff, Jr., *Surf. Sci. Rep.*, **6**, 253 (1987).
79. J.R. Kitchin, J.K. Nørskov, M.A. Barteau, J.G. Chen, *Phys. Rev. Lett.*, **93**, 156801 (2004).

## CHAPTER 4

# Computational and Experimental Study of the Volcano Behavior of the Oxygen Reduction Activity of PdM@PdPt/C (M=Pt, Ni, Co, Fe and Cr) Core-Shell Electrocatalysts.

### 4.1. Introduction

The Sabatier principle states that an optimal catalyst must have an intermediate affinity for the reactants. [1] Therefore, when the activity of catalysts is compared as a function their affinity, a Volcano-shaped curve is obtained. [2-5] Volcano behavior has been demonstrated for several reactions, e.g., hydrodesulfurisation [2], ammonia synthesis [3] and oxygen reduction [4]. Different descriptors have been proposed to measure the affinity, including the heat of formation of oxides, nitrides and sulfides [5] and the d-band occupancy [6]. The development of computational catalysis has facilitated the calculation of adsorption energies for a wide range of catalyst materials, and the calculated adsorption energies can serve as reactivity descriptors. [7] As reviewed by Nørskov et al., this approach can be used to guide the design of optimal catalysts. [7]

The oxygen reduction reaction (ORR) is often used to illustrate the Sabatier principle. [4] Electrocatalytic oxygen reduction involves the activation of O<sub>2</sub>, followed by the removal of surface oxygen species as water. Catalysts with a high affinity for oxygen facilitate O<sub>2</sub> activation, but complicate the removal of

the reaction intermediates. Pt has an intermediate affinity for oxygen and is therefore the best pure metal ORR catalyst. [4] The development of more economical and more active oxygen electrode catalysts has been identified as an important challenge for the introduction of fuel cell technology. [8] In direct methanol fuel cells, the sluggish nature of the ORR is further exacerbated by methanol crossover through the polymer electrolyte membrane. [9] Alloying Pt with Pd improves the methanol tolerance of the cathode ORR catalyst in methanol fuel cells, but unfortunately further decreases the ORR activity. [10,11]

Early studies report that alloying Pt electrocatalysts with 3d transition metals such as Ni, Co and Cr enhances the ORR activity by a factor 2 to 3. [6,12] The enhanced activity was attributed to a decrease in the surface Pt d-band occupancy. [6] Cyclic voltammetry further demonstrated that alloying Pt with 3d metals reduces the stability of chemisorbed O or OH groups, [6] while calculations on small Pt clusters highlighted the relationship between the ORR activity and the calculated O and OH binding strength. [13] A detailed relationship between the calculated oxygen binding energy and the ORR activity was introduced by Nørskov et al. [4]. In a schematic kinetic analysis, the ORR activity is governed by the O-O dissociation rate, either via direct O<sub>2</sub> dissociation or via the formation of OOH, and by the proton/electron transfer rates to the adsorbed oxygen or hydroxide species for a given potential and pH. Both rates depend differently on the oxygen binding energy, leading to the Volcano behavior. The model developed by Nørskov et al. further suggests that the ORR activity of Pt can be improved by slightly reducing the oxygen

binding energy. Following this prediction, different approaches have been followed to improve the ORR activity of Pt. Using the calculated oxygen binding energy as a descriptor, Greeley et al. screened Pt-based alloys and reported that alloying Pt with Y improves the ORR activity by a factor 6 to 10. [14] Tuning the Core-shell particles provide an alternative approach to tune the oxygen binding energy, [15,16] and various core-shell electrocatalysts with improved ORR activity and reduced Pt content have been reported. [15-20] Recently, volcano behavior of the ORR activity was nicely demonstrated for a series of model Cu/Pt(111) near-surface alloys with a varying subsurface Cu coverage. An 8-fold variation in ORR activity was reported when the submonolayer concentration of Cu in Pt(111) was changed. [19]

To improve the activity of PdPt-based ORR catalysts for direct methanol fuel cells, we proposed to substitute the subsurface Pt atoms by 3d transition metal atoms and create core-shell structures. [20,21] DFT calculations show that the oxygen binding energy for Pd<sub>3</sub>M@Pd<sub>3</sub>Pt core-shell structures can be tuned, [20] which is expected to enhance the ORR activity. A series of carbon supported PdM@PdPt (M=Pt, Ni, Co, Fe and Cr) core-shell electrocatalysts was therefore prepared by a replacement reaction between PdM nanoparticles and an aqueous solution of PtCl<sub>4</sub><sup>2-</sup> and tested for their ORR activity. Optimal activity and high methanol tolerance were observed for PdFe@PdPt/C [20]. In this work, we provide a detailed analysis of the Volcano behavior of the PdM@PdPt/C (M= Pt, Ni, Co, Fe and Cr) core-shell electrocatalysts. In section 2, we summarize the computational and experimental procedures. In section 3, we report a detailed characterization of the core-shell structures,

using energy-dispersive X-ray spectroscopy (EDX), X-ray photoelectron spectroscopy (XPS), X-ray diffraction (XRD), electrochemical active surface area (ECASA) measurements and CO stripping voltammetry, supported by DFT calculations. Next, DFT calculations demonstrate the variation in ORR activity for the series of core-shell catalysts and the Volcano behavior is confirmed experimentally. In addition, the methanol tolerance and the stability of the proposed catalysts are discussed briefly. The entire content of this Chapter was published in Trinh et al., *Journal of Catalysis*, 291 (2012), 26.

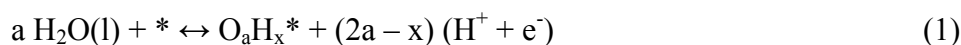
## **4.2. Computational and Experimental Methods.**

### *4.2.1. Computational Methods.*

To evaluate the ORR activity of the various PdM@PdPt/C core-shell catalysts, adsorption energies and activation barriers were calculated on Pd<sub>3</sub>M@Pd<sub>3</sub>Pt slabs using spin-polarized periodic DFT with the Perdew-Burke-Ernzerhof functional (DFT-PBE), [25] as implemented in the Vienna Ab initio Simulation Package (VASP) [26,27]. The calculations were performed using a plane-wave basis with a cut-off kinetic energy of 450 eV. Electron-ion interactions were described by the projector-augmented wave (PAW) method [28,29]. The catalysts were modeled as 5-layer, *p*(2x2) slabs, consisting of a single Pd<sub>3</sub>Pt(111) surface layer and four Pd<sub>3</sub>M core layers, where M is Co, Fe, Ni, Mn, or Cr. Selected calculations with a thicker, 2-layer Pd<sub>3</sub>Pt shell were also performed to compare with the characterization data. Optimal lattice constants for the Pd<sub>3</sub>M@Pd<sub>3</sub>Pt structures were obtained by minimizing the total energy as a function of the lattice parameter for the 5-layer slabs. The bottom two Pd<sub>3</sub>M layers were constrained at these optimized positions, while

the other layers and the adsorbed species were fully relaxed. A 5x5x1 Monkhorst-Pack grid was used to sample the Brillouin zone and an inter-slab spacing of 12 Å was found to sufficiently reduce interactions between repeated slabs. To analyze the reactivity trends, the Pt d-band center was calculated by projecting the d-band density of states (DOS) onto the surface Pt atoms.

Both the dissociative and the associative ORR mechanism [4] were evaluated. Following the approach by Nørskov et al., the proton/electron transfer rate to O\*, OH\*, O<sub>2</sub>\*, and OOH\* was determined from the reaction free energy,  $\Delta G_{\text{rxn}}$ , including a fitted pre-exponential factor. [4] The Gibbs free energy to form the reaction intermediates, i.e., OH\*, O\*, OOH\*, O<sub>2</sub>\* and the O<sub>2</sub> dissociation transition state, O<sub>2</sub><sup>TS</sup>, were calculated relative to liquid H<sub>2</sub>O(l) at 300 K for a potential U of 0.8 V and a pH of 1.0, using the following reaction:



where a is 1 or 2 and x is 0 or 1. The effect of pH and potential U were included using the Gibbs free reaction energy of reaction (2), as proposed by Nørskov [4]:



Zero point energies (ZPE) were calculated for all species. For the adsorbed species, the ZPE was calculated on a Pd<sub>3</sub>Pt slab and assumed to remain similar on the other surfaces. Entropy and enthalpy corrections were obtained from the NIST-JANAF tables [30] for the gas-phase species and calculated on a Pd<sub>3</sub>Pt slab for the adsorbed species. The effect of the water environment on the

stability of the surface species was not included, as it is expected to have a minor influence on the *variation* in the stability of a specific intermediate from one Pd<sub>3</sub>M@Pd<sub>3</sub>Pt surface to the next. The Gibbs free energy of O<sub>2</sub>(g) relative to H<sub>2</sub>O(l) was obtained from the experimental standard potential of water, +1.23 eV [4]. The oxygen affinity, ΔE<sub>O</sub>, was used as the descriptor for the ORR activity. ΔE<sub>O</sub> is calculated as the DFT electronic reaction energy for reaction (3):



The O<sub>2</sub> dissociation transition state was determined with the climbing-image Nudged Elastic Band (NEB) method [31]. Climbing-image NEB calculations were performed for all reactant and product configurations within 10 kJ/mol of the most stable co-adsorbed configuration within the *p*(2x2) unit cell. The transition states were fully optimized and vibration frequencies were calculated to confirm the nature of the transition state. Though several reaction paths were considered for all systems, only the lowest O<sub>2</sub> activation energies are reported.

Pt 4f<sub>7/2</sub> surface core-level shifts were calculated for the various core-shell Pd<sub>3</sub>M@Pd<sub>3</sub>Pt structures using the final-state approximation procedure as implemented in VASP. [32] Briefly, core-level binding energies were obtained as the energy difference between an unexcited ground-state calculation and a calculation where a specified core electron is shifted to the valence band. In the final-state approximation, screening of the localized core-hole is taken into account by allowing the electrons to relax after shifting the core electron. Pt



$4f_{7/2}$  surface core-level shifts are then calculated as the difference between the Pt  $4f_{7/2}$  core-level binding energy of shell Pt atoms in the  $\text{Pd}_3\text{M}@\text{Pd}_3\text{Pt}$  core-shell structure and the Pt  $4f_{7/2}$  core-level binding energy of Pt atoms in bulk Pt. Absolute core-level binding energies for the core-shell structures were obtained using the bulk Pt  $4f_{7/2}$  binding energy of 71.1 eV. [33]

#### 4.2.2. *Experimental methods.*

Experiments were carried out to validate the theoretical prediction.  $\text{Pd}_3\text{M}@\text{Pd}_3\text{Pt}$  core-shell catalysts were prepared by a galvanic replacement reaction between  $\text{Pd}_3\text{M}$  alloy particles and an aqueous solution of  $\text{PtCl}_4^{2-}$ , as described by Trinh et al. [18] and Yang et al. [64]. In the first step,  $\text{PdM}/\text{C}$  ( $\text{M}=\text{Pt}, \text{Ni}, \text{Co}, \text{Fe}$  and  $\text{Cr}$ ) alloy particles with an optimized  $\text{Pd}:\text{M}$  atomic ratio of 70:30 were prepared by a liquid salt precursor impregnation method [22]. Unfortunately, the synthesis of  $\text{PdMn}/\text{C}$  alloy particles following the same procedure was unsuccessful and the XRD spectra showed separate Pd and Mn phases. This could be due to the high Nernst potential for Mn ( $\text{Mn}^{2+}/\text{Mn}$  is -1.19 V, while  $\text{Co}^{2+}/\text{Co}$  is -0.28 V and  $\text{Cr}^{3+}/\text{Cr}$  is -0.74 V [23]) which complicates the reduction of the  $\text{Mn}^{2+}$  salt to a  $\text{PdMn}$  alloy. Next, core-shell  $\text{PdM}@\text{PdPt}/\text{C}$  nanoparticles were prepared by a replacement reaction, [21,24].

The  $\text{PdM}@\text{PdPt}/\text{C}$  core-shell catalysts were characterized with point-resolved EDX, XPS, XRD and Transmission Electron Microscopy (TEM). TEM images were collected with a JEOL JEM2010 field emission transmission electron microscope. The catalyst composition was determined by an EDX attachment to the electron microscope. Powder XRD patterns were recorded

on a Rigaku D/Max-3B diffractometer, using Cu K $\alpha$  radiation ( $\lambda=1.54056 \text{ \AA}$ ). XPS spectra were measured with a Thermo ESCALAB MKII spectrometer with a monochromatic aluminum anode (Al K $\alpha$  = 1487 eV), a 20 eV pass energy, a 0.05 eV kinetic energy step and a 0.1 s dwelling time. Energy corrections were performed using the C 1s peak of the carbon support at 284.5 eV. The peak resolution of the spectrometer for the Ag 3d $_{5/2}$  peak from sputter-cleaned silver is 0.42 eV. The ECASA for the different catalysts was determined from the hydrogen adsorption/desorption region in cyclic voltammograms recorded between 0.014 and 1.2 V at 20 mV/s in an Ar-purged 0.1 M HClO $_4$  solution. Electrochemical measurements were performed using an Autolab PGSTAT12 potentiostat/galvanostat and a standard three-electrode cell. The evaluation of ORR activities were carried out in a 0.1 M HClO $_4$  aqueous solution (Merck). To test the methanol tolerance of the ORR catalysts, an aqueous solution of 0.1 M methanol (Fisher Scientific) and 0.1 M HClO $_4$  was used.

### **4.3. Results and Discussion.**

First principle calculations indicate that the oxygen binding energy changes gradually for a series of Pd $_3$ M@Pd $_3$ Pt core-shell electrocatalysts, leading to Volcano-like behavior in the calculated ORR activity. First, characterization data are reported to illustrate that the surface electronic structure changes gradually for the series of core-shell electrocatalysts, while the surface area remains similar. Next, this gradual variation in chemical affinity is shown to cause a gradual variation in the ORR activity. Finally, we briefly discuss the methanol tolerance and the stability of the core-shell electrocatalysts.

### 4.3.1. Catalyst characterization.

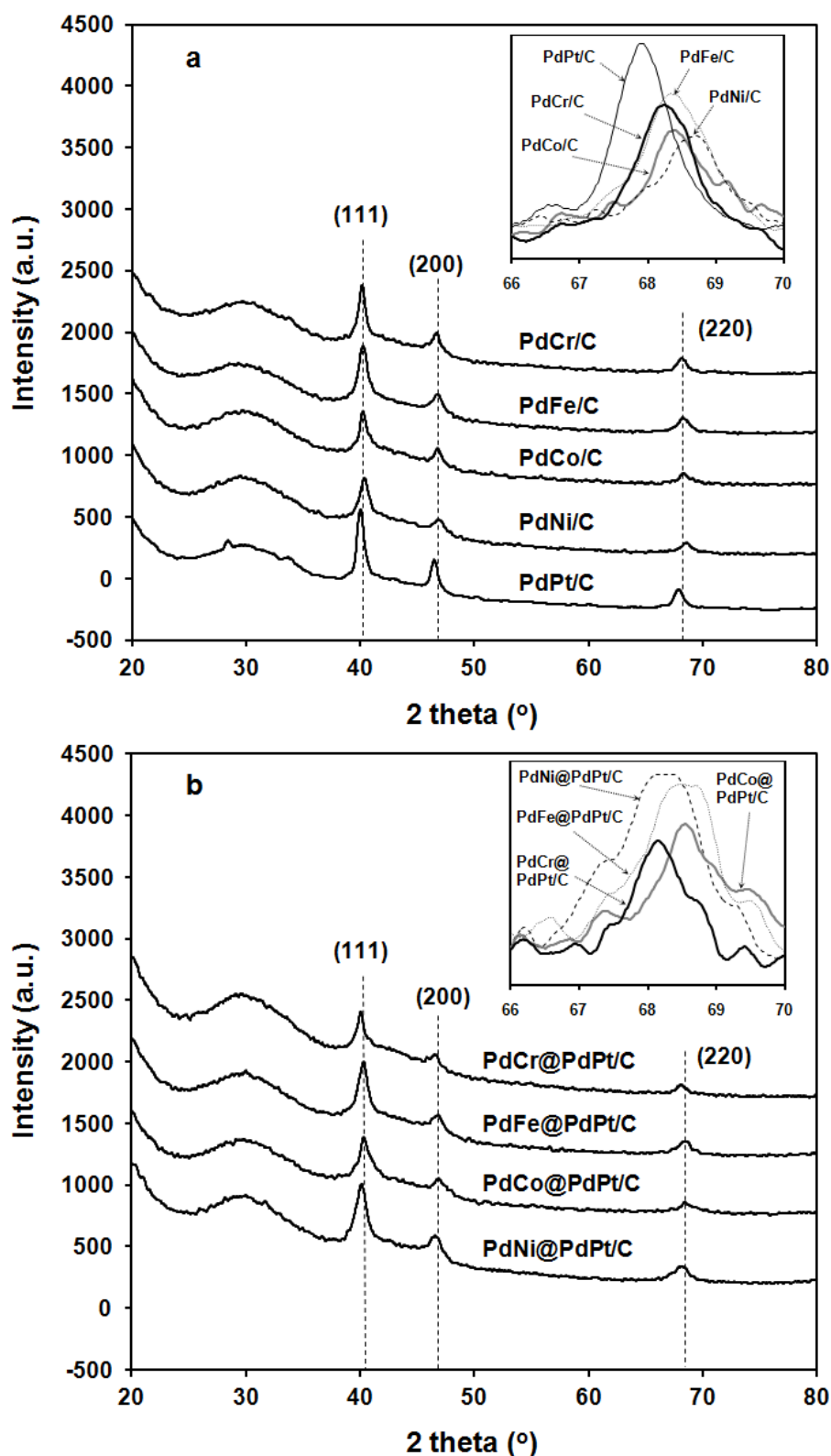


**Figure 4.1.** XRD patterns for the PdM/C catalysts with a Pd:M ratio of 70:30 (a) and for the core-shell PdM@PdPt/C (M=Ni, Co, Fe and Cr) catalysts (b). The dotted lines indicate the fcc (111), (200) and (220) peaks positions for PdFe/C and PdFe@PdPt/C. The insert shows the (220) peak that was used to determine the average crystallite sizes in Table 4.1.

Uniform PdM alloy particles with a Pd:M ratio of 70:30 were synthesized by a liquid salt precursor impregnation method, described in Section 2. XRD spectra for the carbon supported PdM particles are shown in Figure 4.1a. The absence of diffraction peaks corresponding to the 3d transition metals suggests that the M precursors are fully incorporated into the Pd lattice, forming a PdM alloy. The XRD spectra for the PdM@PdPt/C core-shell particles in Figure 4.1b are similar to the spectra for the PdM/C precursors, suggesting that replacement reaction did not affect the PdM core structure. Particle sizes of around 8.0 nm were estimated from the width of the (220) XRD peak at  $68.1^\circ$  using Scherrer's formula [34] (Table 4.1). The (220) peak was used because the (111) peak is affected by the carbon support. [35] Similar average particle sizes were also determined independently electrochemically (Table 4.1) and from the TEM images [18]. The core-shell structure of the PdM@PdPt/C particles is further supported by comparing the Pt:Pd:M atomic ratios determined by point-resolved EDX with XPS values (Table 4.1).

**Table 4.1.** PdM@PdPt/C sizes determined from the width of the (220) XRD peak (Figure 4.2b), the electrochemically active surface area (ECASA) and corresponding size and the Pd:Pt:M atomic ratios obtained from point-resolved EDX and XPS measurements. The lattice parameters were determined by DFT.

Catalyst	Pd:Pt:M atomic ratios from EDX / XPS	Average size XRD (nm)	ECASA/size ( $\text{m}^2 \text{g}_{\text{Pd+Pt}}^{-1} / \text{nm}$ )	Lattice parameter ( $\text{\AA}$ )
PdPt/C	69:31:0 / 73:27:0	8.3	57 / 7.6	3.88
PdNi@PdPt/C	70:11:19 / 67:21:12	8.0	70 / 8.6	3.83
PdCo@PdPt/C	71:11:18 / 67:22:11	8.0	73 / 8.2	3.83
PdFe@PdPt/C	68:13:19 / 66:21:13	8.1	70 / 8.5	3.83
PdCr@PdPt/C	70:11:19 / 68:22:10	7.9	70 / 8.6	3.84

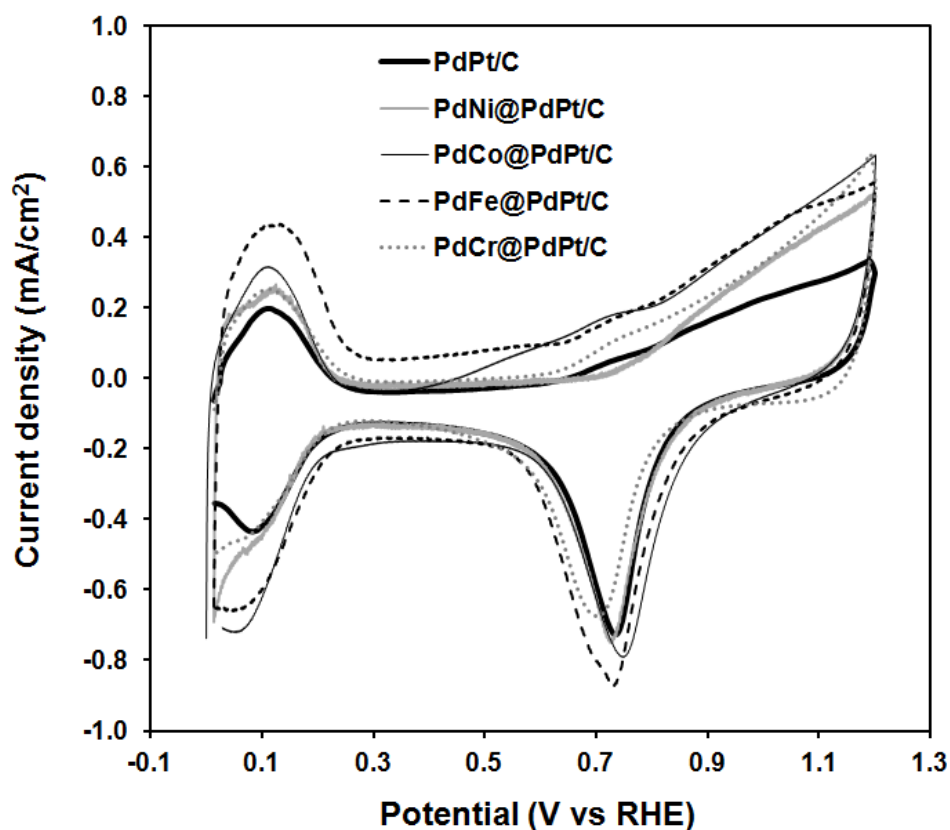


**Figure 4.2.** Cyclic voltammograms of core-shell catalyst PdM@PdPt/C (M=Pt, Ni, Co, Fe and Cr) in argon purged 0.1 M HClO<sub>4</sub>. Sweep rate 20 mV s<sup>-1</sup>; room temperature.

While EDX measures the overall particle composition, XPS is more sensitive to the surface composition of the 8 nm particles. EDX shows that the M content in the PdM@PdPt/C particles is significantly lower than the 30% in the original PdM/C alloy particles, while the Pd content remains close to 70%. This suggests that M atoms in the PdM particles have been selectively etched during the replacement reaction and replaced by Pt atoms. Furthermore, XPS shows an enhanced Pt signal and a reduced M signal compared to EDX, suggesting that Pt has replaced M in the shell region of the particles. Since replacement reaction involves a one-to-one exchange of M by Pt, the change in particle size as determined from the ECASA is small (Table 4.1). The Cyclic voltammograms of core-shell catalyst PdM@PdPt/C is shown in Figure 4.2. Combining the point-resolved EDX composition with the average

particle size, a PdPt shell thickness of 1 or 2 monolayers can be estimated, assuming cuboctahedral particles.

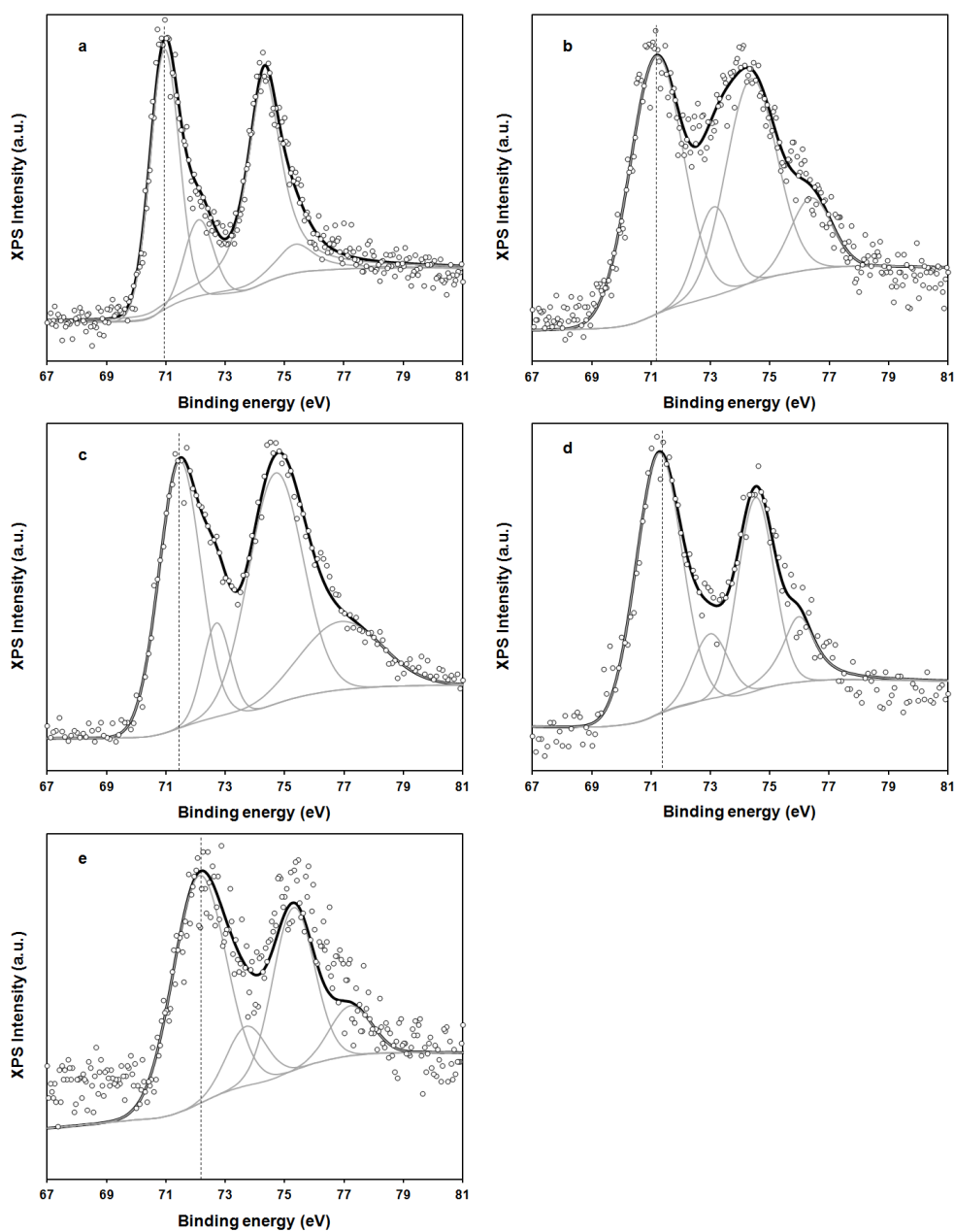


**Figure 4.3:** Pt 4f XPS spectra of PdPt/C (a) and PdM@PdPt/C [M = Ni (b), Co(c), Fe (d) and Cr (e)]. Dot lines indicate the Pt 4f<sub>7/2</sub> peaks deconvoluted with Gaussian-Lorentzian peak fit using XPSpeak software.

The influence of the PdM-core composition on the surface Pt electronic structure of the PdM@PdPt/C catalysts was first evaluated with Pt 4f<sub>7/2</sub> XPS.

To provide support for the Pd<sub>3</sub>M@Pd<sub>3</sub>Pt slab catalyst model used in the first

principle calculations, Pt  $4f_{7/2}$  binding energies were also calculated with DFT-PBE and the final-state approximation as described in Chapter 3.

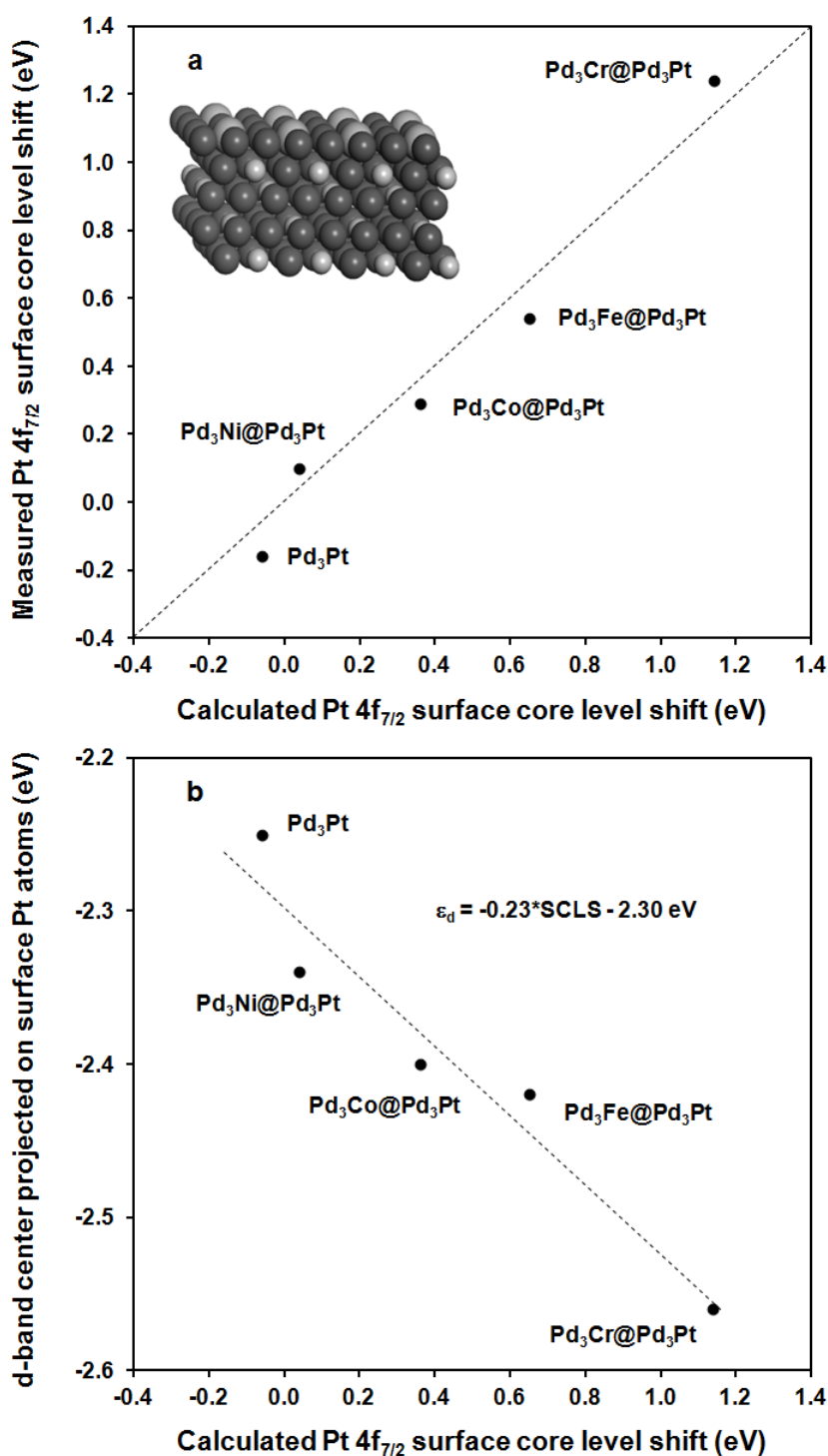


**Figure 4.4.** (a) Parity diagram comparing the calculated Pt  $4f_{7/2}$  surface core-level shift for a slab with a monolayer Pd<sub>3</sub>Pt placed on four layers Pd<sub>3</sub>M (shown in insert), with the chemical shift measured by XPS for the PdM@PdPt/C catalysts. (b) Correlation between the calculated Pt  $4f_{7/2}$  surface core-level shift and the Pt d-band center projected on the surface Pt atoms relative to the Fermi level for this family of Pd<sub>3</sub>M@Pd<sub>3</sub>Pt core-shell structures.

In short, Final-state DFT calculations provide an accurate description of the chemical shifts measured by XPS, with typical deviations of less than 50 meV [32,36]. The Pt  $4f_{7/2}$  XPS spectra are shown in Figure 4.3, while the experimental Pt  $4f_{7/2}$  chemical shifts are compared with calculated shifts in Figure 4.4a. Substitution of subsurface Pt atoms by 3d transition metal atoms increases the Pt 4f binding energy, with the largest shift for PdCr@PdPt/C. The calculated chemical shifts accurately describe the 1.3 eV variation in the measured values with an average deviation of 80 meV. When a 2-layer Pd<sub>3</sub>Pt shell is used in the DFT-PBE calculations, much smaller surface chemical shifts are computed and the average deviation with the experimental data increase to 200 meV (Figure 3.11a). As mentioned in Chapter 3, two important factors contribute to the Pt  $4f_{7/2}$  surface core-level shifts in core-shell particles: charge transfer and lattice strain [37,38]. As discussed by Rodriguez and Goodman [37], charge transfer between the surface and substrate is an important factor determining the surface core-level shift of core-shell systems. The increased Pt  $4f_{7/2}$  binding energy in the PdM@PdPt core-shell particles can be indeed correlated with the reduced charge on the surface Pt atoms [36]. Withdrawal of valence electrons reduces screening of the nuclear charge by the valence electrons and increases the core-level binding energies. A decrease in the lattice constant (Table 4.1) also increases the Pt  $4f_{7/2}$  core-level binding energy. The effect of strain on the Pt core-level binding energy was analyzed in detail by Lewara et al. [38] and the increase in the Pt core-level binding energy was attributed to the increased participation of the d-electrons in the metal-metal bonding, thereby reducing the nuclear screening.



While XPS measures shifts in the core-level binding energies, reactivity trends for transition metals are typically governed by changes in the valence d-band structure [39]. In particular for the ORR, the relation between the d-band center, the oxygen binding energy and the activity was discussed by Stamenkovic et al. [40]. Therefore, the d-band center projected on the surface Pt atoms relative to the Fermi level was also calculated for the Pd<sub>3</sub>M@Pd<sub>3</sub>Pt structures (Figure 4.4b). Changes in the Pt d-band center are found to correlate with the Pt 4f<sub>7/2</sub> core-level shifts for this family of core-shell structures. Similar correlations have for example been reported by Rigsby et al. [41]. However, the variation in the d-band center is smaller than the variation in the core-level binding energies and a 1.0 eV increase in the Pt 4f<sub>7/2</sub> core-level binding energy correlates with a smaller 0.23 eV downward shift in the Pt d-band center relative to the Fermi level. Similar to the core-level binding energies, the position of the d-band center in core-shell structures is influenced by both lattice strain and charge transfer [42,43]. Compressive strain (Table 4.1) shifts the d-band center away from the Fermi level [42] and increases the Pt core-level binding energy. Calculations on a Pd<sub>3</sub>Pt monolayer show that both the d-band center and the core-level binding energy shift by about 0.5 eV when the lattice constant is reduced from 3.96 to 3.72 Å. Charge transfer induced by placing the monolayer of Pd<sub>3</sub>Pt on a Pd<sub>3</sub>M core has a limited effect on the d-band center (smaller than 0.1 eV), but has a large effect on the calculated core-level binding energy (more than 1.0 eV). Since charge transfer has a smaller effect on the position of d-band center, the variation in the d-band center is smaller than the variation in the core-level binding energy for this family of core-shell structures, as shown in Figure 4.4b.

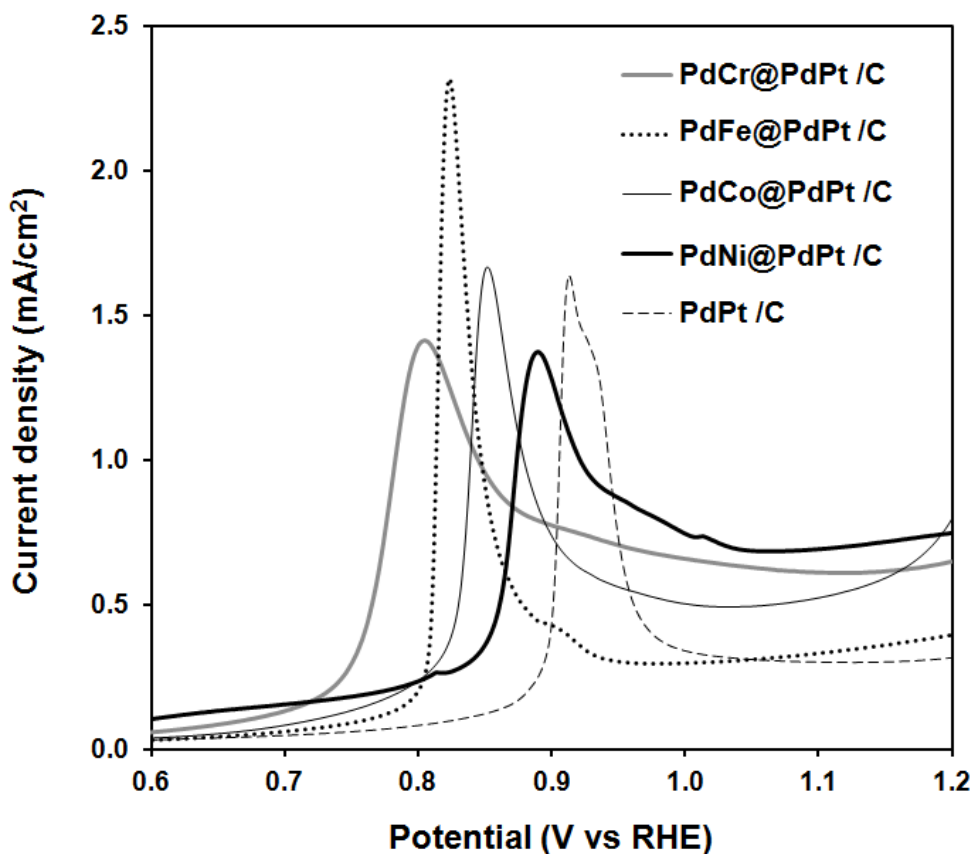


**Figure 4.5.** CO-stripping voltammograms for the PdM@PdPt/C catalysts in 0.1 M HClO<sub>4</sub> after saturation with CO for 900 s. Scan rate: 20 mV/s.

To confirm the variation in the surface electronic structure for the family of PdPt@PdM/C core-shell electrocatalysts, anodic CO-stripping voltammetry was used. The CO-stripping voltammograms in Figure 4.5 show a 0.15 V variation in the CO peak position. In voltammetric CO stripping, pre-adsorbed CO is oxidized by surface OH groups, generated by the activation of water [44]. Therefore the rate of oxidation depends on the CO binding energy and the activation of water. In Figure 4.6a, we show that also in our system, the stripping peak position correlates with the calculated CO binding energy at the Pt atop sites of the Pd<sub>3</sub>M@Pd<sub>3</sub>Pt slabs. As expected, a stronger CO binding energy correlates with a more anodic peak position. In addition, a stronger CO binding energy also correlates with a higher oxygen affinity (Figures 4.6b and 4.9), which facilitates H<sub>2</sub>O activation.

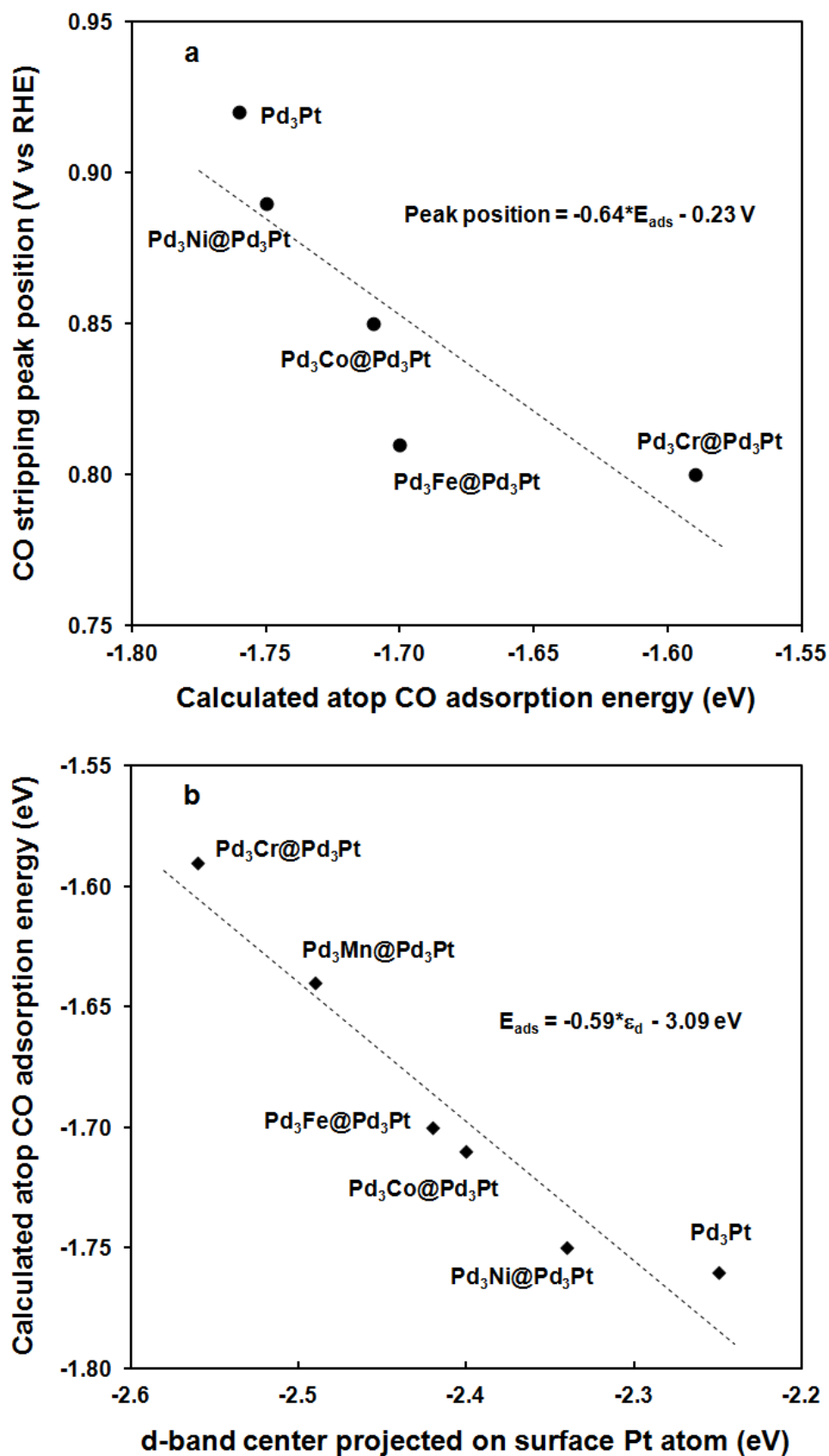


**Figure 4.6.** (a) Correlation between the experimental CO stripping peak and the calculated CO adsorption energy at the Pt top site. (b) Correlation between the calculated CO adsorption energy and d-band center projected on the surface Pt atoms.

The CO binding energy is also a sensitive probe for the surface electronic structure and the CO binding energy correlates well with the d-band center [43,45], as illustrated in Figure 4.6b. Within the Blyholder model [46], the CO binding energy is determined by a balance between donation from the CO  $5\sigma$  orbital to the empty d-states and backdonation from the filled d-states to the CO  $2\pi^*$  orbital. As reported by Norskov et al. [45], changes in backdonation to the CO  $2\pi^*$  orbital dominate the variation in the CO binding energy on transition metals. A downward shift in the d-band center decreases backdonation and reduces the CO binding energy. Similarly, the variation in the oxygen binding energy is governed by changes in the d-states [39]. Therefore, a similar variation in the oxygen binding energy is expected, as shown in the next section. According to the model proposed by Nørskov et al. [4], such a variation in the oxygen binding energies should lead to Volcano-like behavior in the ORR activity. Anodic CO-stripping voltammetry can furthermore be used to determine the surface area [47] by integrating the peak in Figure 4.5. Though the surface area determined by anodic CO-stripping voltammetry is less reliable than the ECASA, similar average particle sizes could again be determined for the five core-shell structures.

Summarizing, the characterization data indicate that 8.0 nm PdM@PdPt/C (M=Pt, Ni, Co, Fe and Cr) core-shell particles with a 70:30 Pd:M core composition and a 1-2 monolayer PdPt shell were synthesized by a liquid salt precursor impregnation method, followed by a replacement reaction. Pt  $4f_{7/2}$  XPS chemical shifts in combination with Pt  $4f_{7/2}$  core-level binding energy calculations support the structural characterization data and show that the

surface electronic structure changes gradually in this family of core-shell catalysts. The gradual variation in the core-level binding energies correlates with a variation in the valence d-band center for this family of core-shell catalysts and with the variation in the CO adsorption energy, as shown by CO-stripping voltammetry. The surface area determined by hydrogen adsorption/desorption cyclic voltammetry indicates that the particle sizes are similar in this family, in agreement with the XRD and CO stripping data.

#### 4.3.2. Volcano-like variation in the ORR activity.

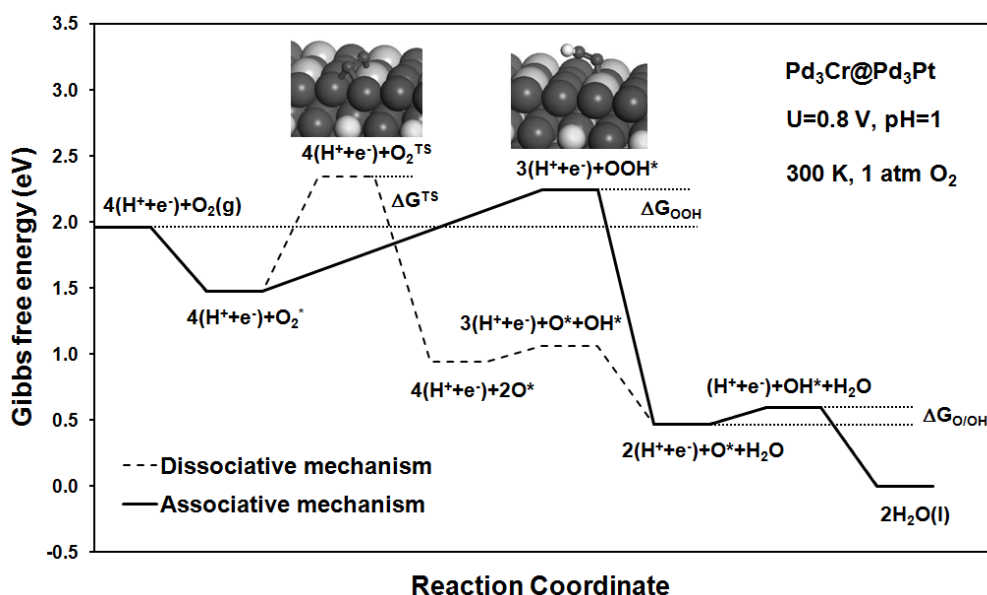


**Figure 4.7.** Free-energy diagram for the associative and the dissociative ORR mechanism, calculated on a  $p(2 \times 2)$   $\text{Pd}_3\text{Cr}@Pd_3\text{Pt}$  core-shell structure, for a potential  $U$  of 0.8 V, a pH of 1, 300 K and 1 atm  $\text{O}_2$ . Inserts show the optimized  $\text{O}_2$  dissociation transition state and the adsorbed  $\text{OOH}^*$  geometry. All free energies were calculated relative to  $\text{H}_2\text{O}(l)$ .

To evaluate the effect of the core-shell structure on the ORR activity, free energy diagrams were calculated for the family of  $\text{Pd}_3\text{M}@Pd_3\text{Pt}$  structures. Two mechanisms were considered [4]. In the dissociative mechanism, O-O scission occurs by dissociation of  $\text{O}_2$ , while in the associative mechanism, O-O scission takes place by protonation of  $\text{OOH}^*$ , formed by protonation of one

of the oxygen atoms in adsorbed  $O_2^*$ . The relative importance of both mechanisms has been discussed in the literature, [4] and depends on the catalyst, the oxygen coverage, the potential and the pH. In both mechanisms, surface  $O^*$  and  $OH^*$  groups are removed through protonation to form  $H_2O$ . Depending on the oxygen affinity of the catalyst, either O-O scission or  $O^*/OH^*$  removal can become rate-limiting [4].

The calculated ORR free energy diagram for  $Pd_3Cr@Pd_3Pt$  is shown in Figure 4.7, for a potential of 0.8 V, a pH of 1, 300 K and an  $O_2$  pressure of 1 atm.  $Pd_3Cr@Pd_3Pt$  has the weakest oxygen affinity in our family of  $Pd_3M@Pd_3Pt$  catalysts, with a calculated oxygen binding energy,  $\Delta E_O$ , of +1.93 eV. For this catalyst, direct O-O scission has an effective free energy barrier of +0.38 eV, while protonation of  $O_2^*$  to  $OOH^*$  has an effective free energy barrier of +0.28 eV. This suggests that the associative mechanism is preferred on  $Pd_3Cr@Pd_3Pt$ .  $O^*$  protonation is endothermic with a free energy of reaction of +0.12 eV, while  $OH^*$  protonation is highly favorable under those conditions. Note, however, that the presence of a water layer might affect the calculated stability of  $OH^*$  and  $O^*$  *differently*, thereby influencing the calculated  $O^*$  protonation reaction energy. The lower barrier for  $O^*$  removal suggests that O-O scission, likely via the associative mechanism, is rate limiting on the  $Pd_3Cr@Pd_3Pt$  catalyst.

Similar calculations were performed for all the catalysts in our family and are summarized in Figure 4.8. For each structure, three effective free energy barriers are shown,  $\Delta G_{OOH}$  for the formation of  $OOH^*$  from  $O_2(g)$ ,  $\Delta G_{TS}$  for

the direct dissociation of  $O_2(g)$  and  $\Delta G_{O/OH}$  for the protonation of  $O^*$  or  $OH^*$ . All three effective barriers correlate with the oxygen affinity of the catalysts, represented by  $\Delta E_O$ .

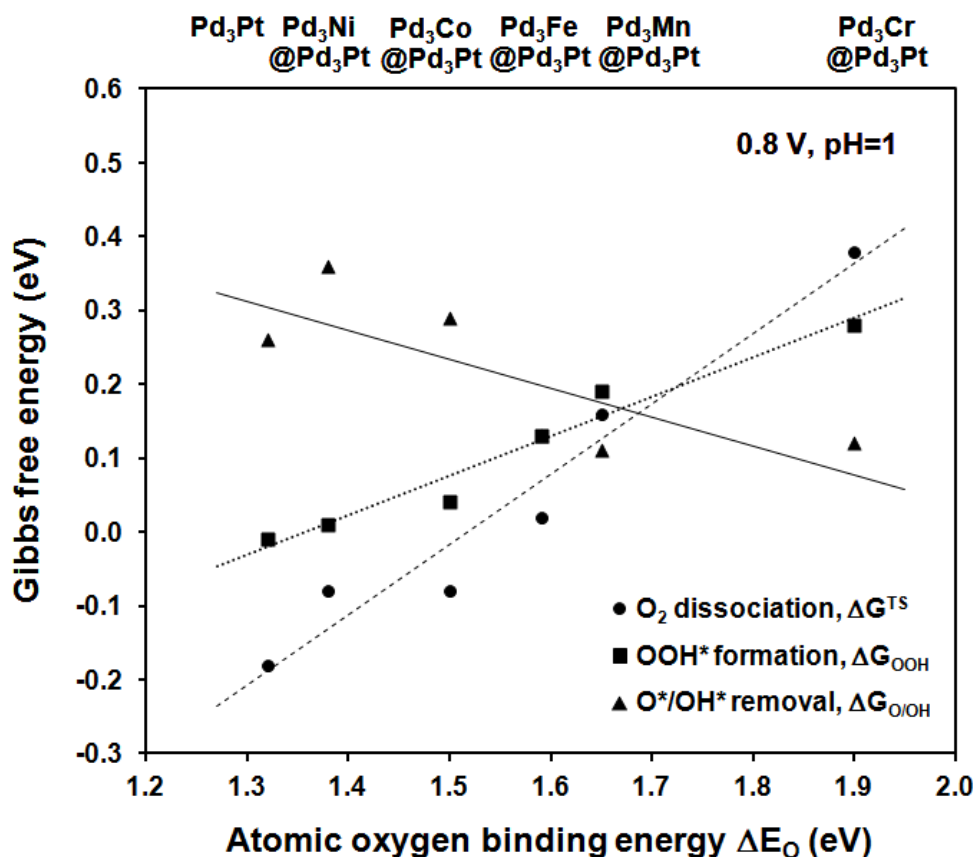


**Figure 4.8.** Calculated Gibbs free reaction energy to form  $OOH^*$  from  $O_2(g)$  ( $\Delta G_{OOH}$ ), to protonate  $O^*$  ( $\Delta G_{O/OH}$ ) and to dissociate  $O_2$  ( $\Delta G^{TS}$ ), as illustrated in (a), for a potential  $U$  of 0.8 V and pH of 1, as a function of the oxygen affinity,  $\Delta E_O$  (equation (3));

The  $O_2$  dissociation barrier,  $\Delta G_{TS}$  and the  $OOH^*$  formation energy,  $\Delta G_{OOH}$ , both increase as the oxygen affinity reduces. However, the  $O_2$  dissociation barrier,  $\Delta G_{TS}$ , is more sensitive to the oxygen affinity of the catalyst. For catalysts with a high oxygen affinity, such as  $Pd_3Pt$ ,  $Pd_3Ni@Pd_3Pt$ ,  $Pd_3Co@Pd_3Pt$  and  $Pd_3Fe@Pd_3Pt$ , the direct dissociation mechanism is calculated to be preferred over the associative mechanism, while the reverse is calculated for  $Pd_3Cr@Pd_3Pt$ . However, the switch between the mechanisms

depends on the reaction conditions and on the presence of water in the computational model [4] because the stability of OOH\* and of the O<sub>2</sub> dissociation transition state (O<sub>2</sub><sup>TS</sup>) are affected differently by the presence of water in the model.

The correlations of  $\Delta G_{TS}$  and  $\Delta G_{OOH}$  with  $\Delta E_O$  are well-known, [4] and form the basis of the Volcano-behavior. The free energy barrier for O\* removal,  $\Delta G_{O/OH}$ , depends on the relative stability of O\*, OH\* and H<sub>2</sub>O(l), and also correlates with the oxygen affinity. High reaction free energies of +0.26 and +0.36 eV are calculated for catalysts with a high oxygen affinity such as Pd<sub>3</sub>Pt and Pd<sub>3</sub>Ni@Pd<sub>3</sub>Pt, while low values of +0.12 and +0.11 eV are calculated for Pd<sub>3</sub>Cr@Pd<sub>3</sub>Pt and Pd<sub>3</sub>Mn@Pd<sub>3</sub>Pt, respectively. Following the kinetic analysis of Nørskov et al., [4] O\* removal limits the ORR rate for catalysts with a high oxygen affinity, such as Pd<sub>3</sub>Pt, Pd<sub>3</sub>Ni@Pd<sub>3</sub>Pt and Pd<sub>3</sub>Ni@Pd<sub>3</sub>Pt. For Pd<sub>3</sub>Mn@Pd<sub>3</sub>Pt the calculated barrier for O<sub>2</sub> dissociation, +0.16 eV in the direct mechanism, is very close to the calculated reaction free energy for O\* removal, +0.11 eV. For Pd<sub>3</sub>Cr@Pd<sub>3</sub>Pt, O\* removal with a  $\Delta G_{O/OH}$  of +0.12 eV becomes easier than O<sub>2</sub> activation via the associative mechanism, +0.28 eV and O<sub>2</sub> scission is predicted to become rate-limiting, as shown in Figure 4.8. Since  $\Delta G_{O/OH}$  depends on the relative stability of O\*, OH\* and H<sub>2</sub>O(l), both the O\* coverage and solvation effects are known to affect this correlation by 0.1 to 0.2 eV. [4] Typically, OH\* is more stabilized than O\* by including a water overlayer in the model and O\* removal hence becomes easier. This would shift the predicted crossing point for the correlations in Figure 4.8 from Pd<sub>3</sub>Mn@Pd<sub>3</sub>Pt towards Pd<sub>3</sub>Fe@Pd<sub>3</sub>Pt.



Since the atomic oxygen binding energy,  $\Delta E_{\text{O}}$ , describes the variation in ORR activity for our family of core-shell catalysts, we also evaluated the relation between the oxygen affinity and the surface electronic structure through the center of the Pt d-band. Figure 4.9 illustrates that the  $\Delta E_{\text{O}}$  descriptor changes gradually in steps of about 0.1 eV and correlates well with the Pt d-band center, in agreement with other reports. [4,20,39,40,43]

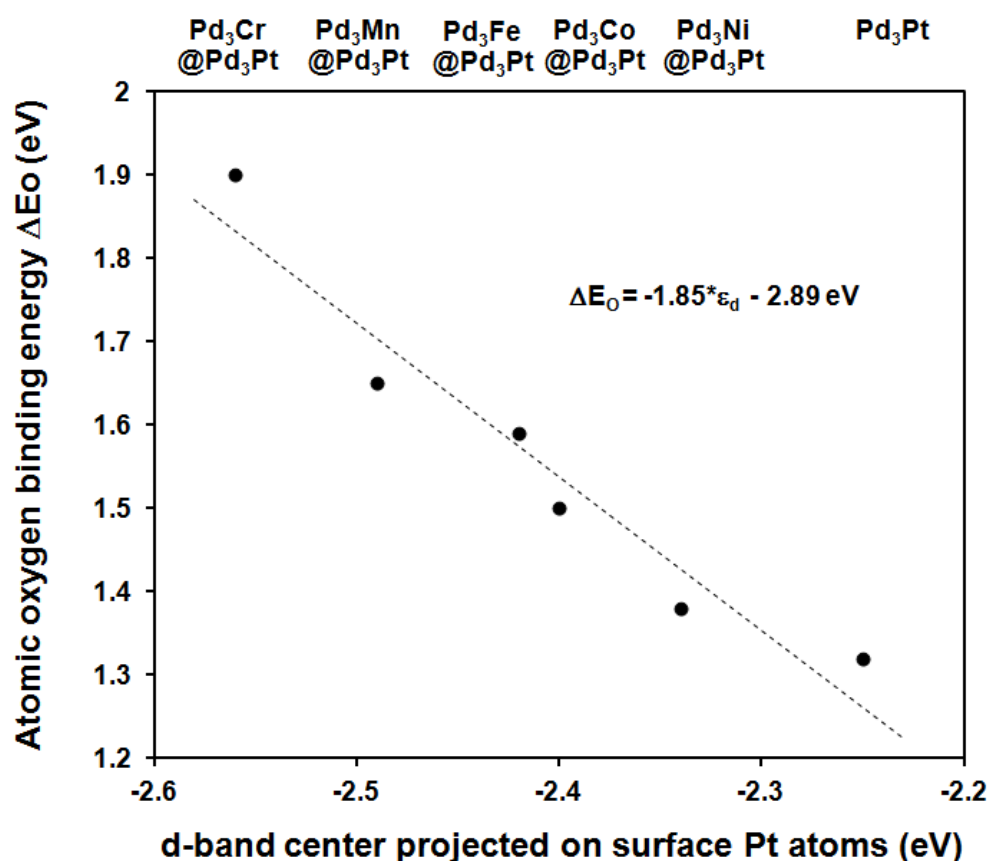


**Figure 4.9.** Oxygen binding energy,  $\Delta E_{\text{O}}$ , as a function of center of the d-band projected on surface Pt atoms,  $\epsilon_d$ .

To confirm the predicted variation in the ORR activity, polarization curves were measured for the family of PdM@PdPt/C electrocatalysts in an oxygen-saturated solution (Figure 4.10). Since the catalysts have a similar PdPt surface composition (Table 4.1) and a similar electrochemical surface area (Table 4.1), the variation in the kinetic mass activity is attributed to changes in the PtPd surface electronic structure induced by the PdM core. Note that the

polarization curve for PdCr@PdPt/C crosses the other curves around 0.8 V, and the relative kinetic mass activity of PdCo@PdPt and PdCr@PdPt/C switches at 0.8 V (Figure 4.11).

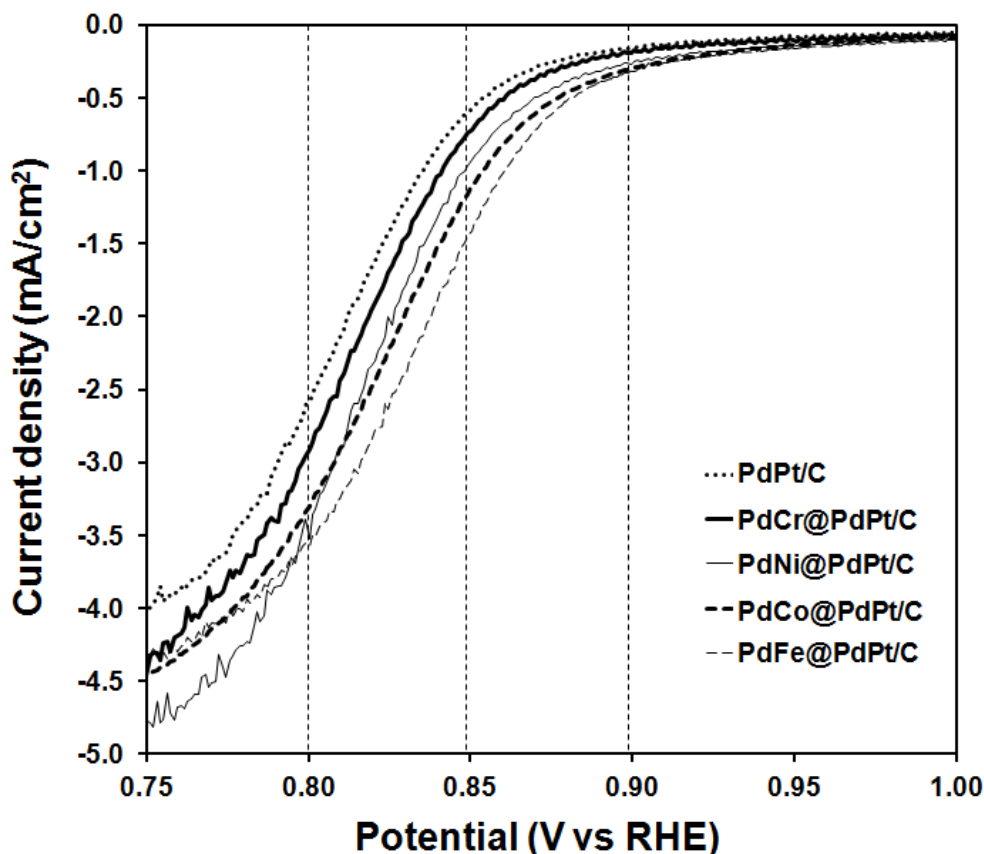


**Figure 4.10.** ORR linear-sweep voltammograms for the PdM@PdPt/C (M=Pt, Ni, Co, Fe and Cr) electrocatalysts in an oxygen-saturated, 0.1M HClO<sub>4</sub> solution. Standard three-electrode cell with a sweep rate of 20 mV/s, rotation speed of 1600 rpm and at room temperature.

The different behavior of the PdCr@PdPt/C catalyst might be related to the predicted change in the rate-limiting step from O removal to O-O activation (Figure 4.8). However, as the measured current density begins to be affected by O<sub>2</sub> diffusion at 0.8 V, differences in the diffusion rate near the carbon-supported catalysts might also contribute to the crossing.

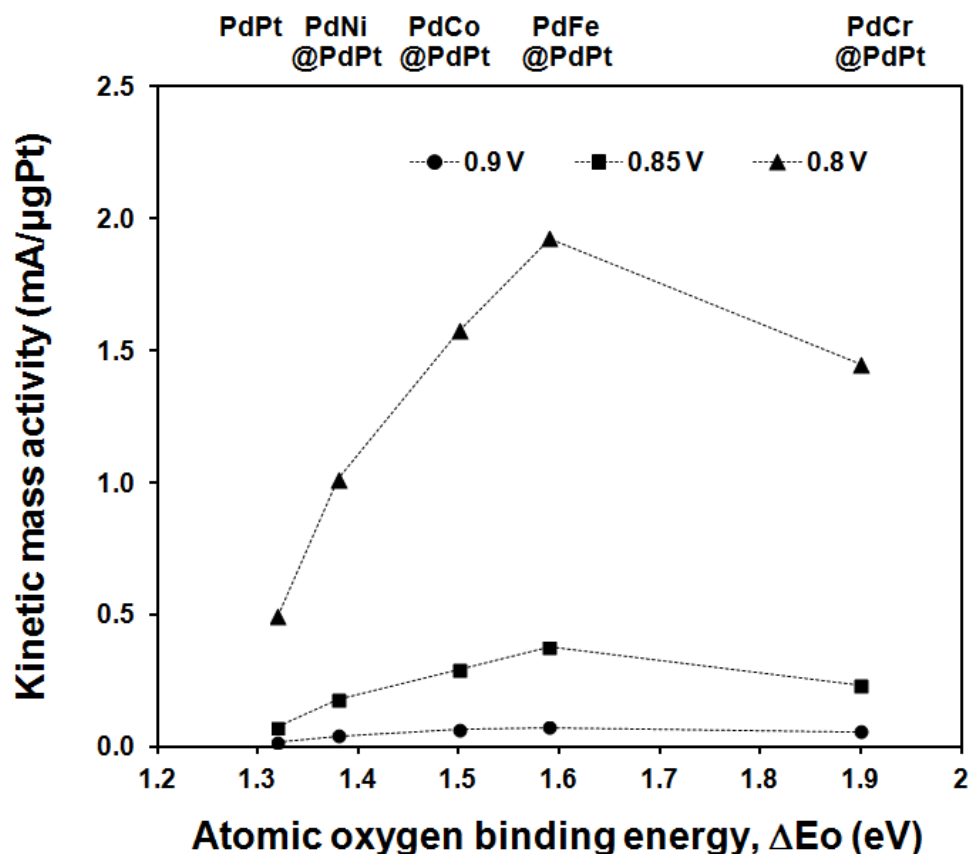


**Figure 4.11:** Kinetic mass activities at 0.8, 0.85 and 0.9 V RHE as a function of calculated oxygen binding energy.

When the measured kinetic Koutecký-Levich current densities per  $\mu$ g Pt are plotted as a function of the calculated oxygen binding energies,  $\Delta E_o$ , a Volcano-like variation in the activity is obtained, with a maximum activity for the PdFe@PdPt/C catalysts (Figure 4.11). Both the variation in ORR activity and the location of the Volcano-optimal catalyst agree with the first principle calculations summarized in Figure 4.8. Alternatively, to find an experimental descriptor for the activity, the measured activity can be plotted as a function of the measured CO affinity as determined by CO-stripping voltammetry (Figure 4.12a), or as a function of the experimental XPS Pt 4f<sub>7/2</sub> core-level shifts (Figure 4.12b). Again, Volcano-like behavior is observed.

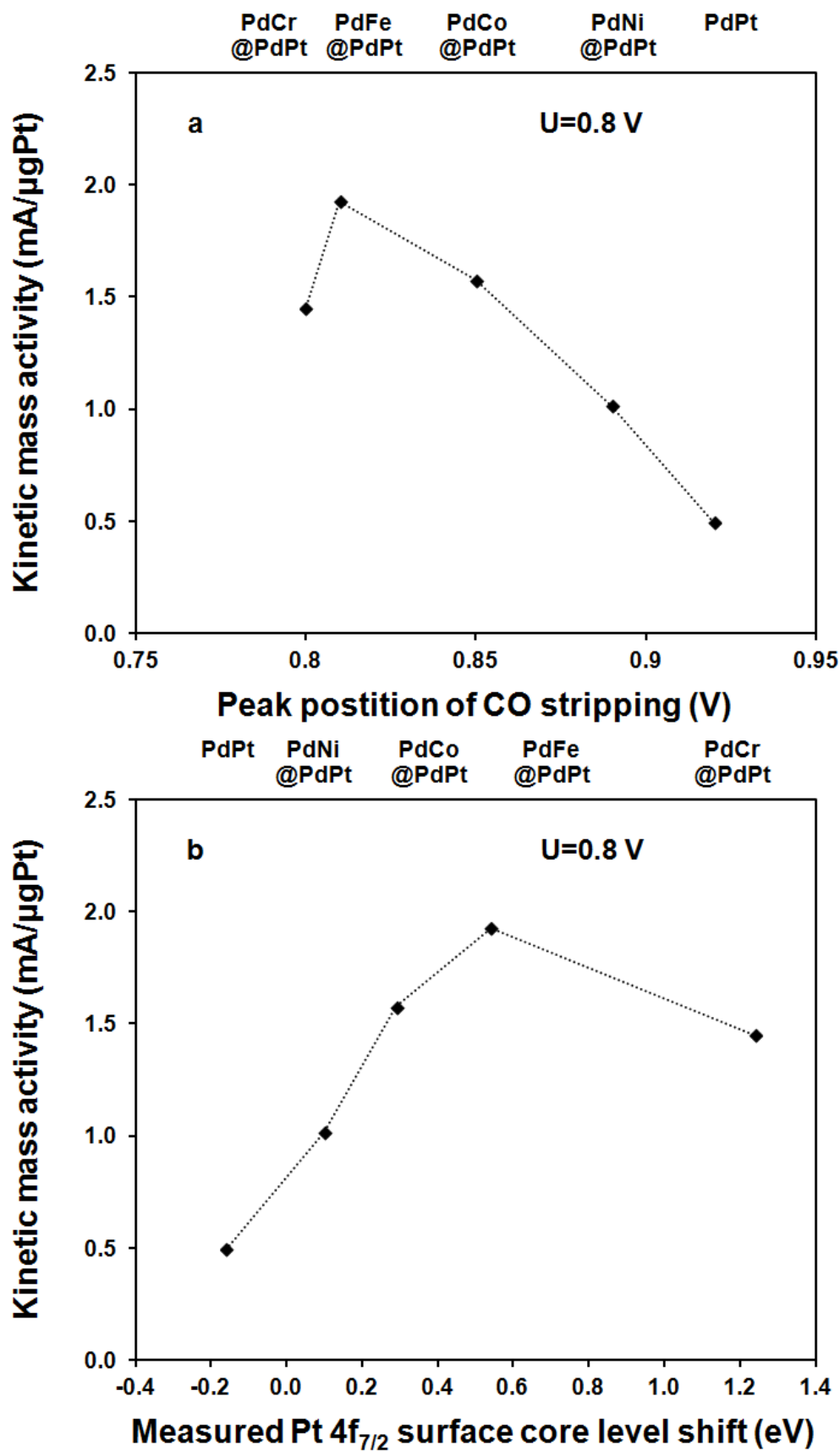


**Figure 4.12:** (a) Kinetic mass activity at 0.8 V RHE as a function of CO stripping peak position and (b) Kinetic mass activity at 0.8 V RHE as a function of XPS Pt 4f<sub>7/2</sub> surface core-level shifts

### 4.3.3. Methanol tolerance and stability.

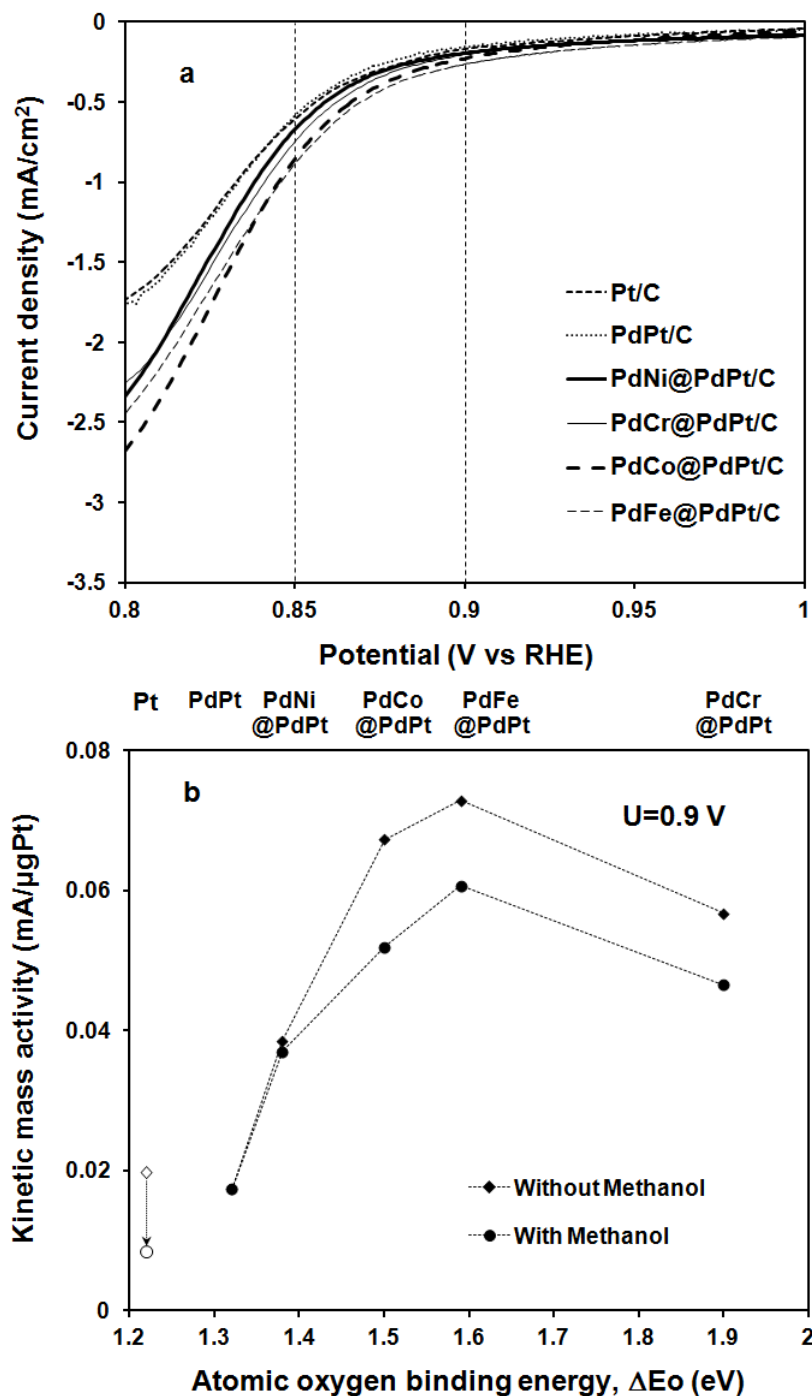


**Figure 4.13.** (a) ORR linear-sweep voltammograms for the PdM@PdPt/C (M=Pt, Ni, Co, Fe and Cr) electrocatalysts and for a commercial 3.0 nm Pt/C reference catalyst in an oxygen-saturated, 0.1M HClO<sub>4</sub> solution **in the presence of 0.1 M methanol**. Standard three-electrode cell with a sweep rate of 20 mV/s, rotation speed of 1600 rpm and at room temperature. (b) Kinetic mass activities at 0.9 V RHE without and with 0.1 M methanol as a function of calculated oxygen binding energy,  $\Delta E_o$ . The kinetic mass activity of a commercial 3.0 nm Pt/C catalyst without and with 0.1 M methanol (open symbols) is included for comparison.

To evaluate the methanol tolerance of the core-shell catalysts, ORR linear-sweep voltammograms were measured in an oxygen-saturated 0.1 M HClO<sub>4</sub> solution in the presence of 0.1 M methanol (Figure 4.13a). The catalysts were also compared with a commercial 3.0 nm Pt/C direct methanol fuel cell cathode catalyst under the same experimental conditions. All core-shell catalysts displayed higher current densities in the presence of methanol than the reference Pt/C catalyst. Figure 4.13b shows the variation in the kinetic mass activity at 0.9 V RHE as a function of the calculated oxygen binding energy,  $\Delta E_{\text{O}}$ . Again, a Volcano-like variation in the activity is obtained, with a maximum activity for PdFe@PdPt/C.

It is interesting to note that methanol only reduces the ORR activity of the PdM@PdPt/C catalysts at 0.9 V by 25%, while the activity of the commercial Pt/C catalyst is reduced by more than 50%. This suggests that alloying the surface with Pd improves the selectivity between methanol oxidation and ORR. Based on the Pt mass, the activity of the Volcano-optimal PdFe@PdPt/C catalyst at 0.9 V and in the presence of 0.1 M methanol is 7 times higher than for Pt/C (Figure 4.13b).

One of the challenges for core-shell catalysts is their stability during ORR [48,49]. To computationally evaluate the possible stability of the Pd<sub>3</sub>M@Pd<sub>3</sub>Pt structures in the presence of various adsorbates, the energy difference between the original structure and the structure where subsurface M and surface Pt are exchanged was calculated (Table 4.2).

**Table 4.2.** Calculated surface segregation energies for M-Pt exchange (indicated by arrow) in the Pd<sub>3</sub>M@Pd<sub>3</sub>Pt core-shell structures for the clean surface, and with 0.25 ML CO\*, OOH\*, OH\* and O\*. Positive values correspond to a stable Pd<sub>3</sub>M@Pd<sub>3</sub>Pt core-shell configuration.

Catalyst structure	Surface segregation energy (eV)				
	Clean surface	CO	OOH	OH	O
Pd <sub>3</sub> Co@Pd <sub>3</sub> Pt	0.48	0.54	-0.22	-0.31	-0.44
Pd <sub>3</sub> Cr@Pd <sub>3</sub> Pt	0.56	0.59	-0.32	-0.51	-0.82
Pd <sub>3</sub> Fe@Pd <sub>3</sub> Pt	0.70	0.76	0.21	0.13	0.05
Pd <sub>3</sub> Ni@Pd <sub>3</sub> Pt	0.28	0.33	0.06	-0.21	-0.32

In a direct methanol fuel cell, the ORR cathode catalyst is exposed to various possible species which could affect surface segregation. We therefore considered the effect of adsorbed CO\*, OOH\*, OH\* and O\* on the stability of the core-shell structures. The results in Table 4.2 show that the clean Pd<sub>3</sub>M@Pd<sub>3</sub>Pt core-shell structures are significantly thermodynamically stable, and M segregation to the surface is a least 0.28 eV unfavorable. This is consistent with the XPS data which show the surface is enriched in Pt, even after thermal treatment (Table 4.1). In the presence of CO, the stability is further enhanced, consistent with the higher CO binding energy on Pt, compared to M. However, oxygen-containing adsorbates bind stronger on M surfaces and favor the exchange of subsurface M with surface Pt, as also discussed by Ma and Balbuena [50]. However, the volcano-optimal

Pd<sub>3</sub>Fe@Pd<sub>3</sub>Pt core-shell structure is calculated to remain stable, even in the presence of 0.25 ML of O\*. The calculated resistance to surface segregation is higher for Pd<sub>3</sub>Fe@Pd<sub>3</sub>Pt for all considered adsorbates. It seems that two factors contribute to the stability of the Pd<sub>3</sub>Fe@Pd<sub>3</sub>Pt structure. First, oxygen species bind significantly stronger on a Pd<sub>3</sub>M surface than on Pd<sub>3</sub>Pt. For Pd<sub>3</sub>Fe, this difference is about 0.65 eV. However, Fe is more stable in the PdM core than on the surface by 0.70 eV for the clean surface and the stronger O\* binding energy cannot overcome the strong anti-segregation tendency of the Pd<sub>3</sub>Fe@Pd<sub>3</sub>Pt core-shell structure. Experimental long-term ORR stability tests will however need to confirm this predicted stability.

#### **4.4. Conclusions.**

The activity of many catalytic systems is governed by Sabatier's principle, which states that the most active catalysts have an intermediate chemical affinity. In this work, a series of core-shell PdM@PdPt/C (M=Pt, Ni, Co, Fe and Cr) oxygen reduction reaction (ORR) catalysts was prepared by replacement reaction, and characterized by XPS, EDX, XRD, electrochemical hydrogen adsorption/desorption and CO-stripping voltammetry. XRD and electrochemical hydrogen adsorption/desorption indicate that the core-shell catalysts have comparable average sizes and dispersions. XPS and EDX provide evidence for the core-shell structure. The gradual change in the Pt 4f<sub>7/2</sub> surface core-level shift over the family of catalysts was well-described by final-state DFT-PBE calculations for a slab with a Pd<sub>3</sub>M core and a monolayer Pd<sub>3</sub>Pt shell. The CO-peak position measured by CO-stripping voltammetry for the family of catalysts gradually shifts in steps of about 0.03 V, corresponding



with a gradual change in the CO affinity, again consistent with the DFT calculations. The gradual shift in the CO affinity is calculated to correlate with a gradual change in the oxygen binding energy,  $\Delta E_{\text{O}}$ , a reactivity descriptor for the ORR activity. DFT calculations suggest that the ORR activity for  $\text{Pd}_3\text{M}@\text{Pd}_3\text{Pt}$  catalysts increases as  $\text{Pd}_3\text{Pt} < \text{Pd}_3\text{Ni}@\text{Pd}_3\text{Pt} < \text{Pd}_3\text{Co}@\text{Pd}_3\text{Pt} < \text{Pd}_3\text{Fe}@\text{Pd}_3\text{Pt}$  because the oxygen affinity reduces and oxygen removal becomes faster. For  $\text{Pd}_3\text{Mn}@\text{Pd}_3\text{Pt}$  and  $\text{Pd}_3\text{Cr}@\text{Pd}_3\text{Pt}$ , the ORR activity is predicted to decrease because slow  $\text{O}_2$  activation begins to limit the activity. This trend was confirmed experimentally, and optimal ORR activity was observed for  $\text{PdFe}@\text{PdPt}/\text{C}$ .

The activity of the ORR catalysts was also evaluated in the presence of methanol to test their selectivity for use in direct methanol fuel cells. While commercial Pt/C catalysts lose more than 50% of their activity in the presence of 0.1 M methanol at 0.9 V because of their high methanol oxidation activity, the  $\text{PdM}@\text{PdPt}/\text{C}$  catalysts retain more than 75% of their activity. Long-term catalyst stability is an important concern for core-shell catalysts. DFT-PBE calculations suggest that the Volcano-optimal  $\text{PdFe}@\text{PdPt}/\text{C}$  remains stable in the presence of a high coverage of oxygen species. However, this would need to be confirmed experimentally by long-term stability tests.

#### 4.5. References.

1. P. Sabatier, *Berichte der Deutschen Chem. Gesellschaft*, **44**, 1984 (1911).
2. R.R. Chianelli, G. Berhault, P. Raybaud, S. Kasztelan, J. Hafner, H. Toulhoat, *Appl. Catal. A Gen.*, **227**, 83 (2002).

3. S. Dahl, A. Logadottir, C.J.H. Jacobsen, J.K. Nørskov, *Appl. Catal. A Gen.*, **222**, 19 (2001).
4. J.K. Nørskov, J. Rossmeisl, A. Logadottir, L. Lindqvist, J.R. Kitchin, T. Bligaard, H. Jónsson, *J. Phys. Chem. B*, **108**, 17886 (2004).
5. H. Knözinger, K. Kochloefl, *Heterogeneous Catalysis and Solid Catalysts*, Ullmann's Encyclopedia of Industrial Chemistry, Wiley-VCH Verlag, (2003).
6. S. Mukerjee, S. Srinivasan, M.P. Soriaga, J. McBreen, *J. Electrochem. Soc.*, **142**, 1409 (1995).
7. J.K. Nørskov, T. Bligaard, J. Rossmeisl, C.H. Christensen, *Nat. Chem.*, **1**, 37 (2009).
8. G.M. Whitesides, G.W. Crabtree, *Science*, **315**, 796 (2007).
9. A.S. Arico, S. Srinivasan, V. Antonucci, *Fuel Cells*, **1**, 133 (2001).
10. H.C. Ye, R.M. Crooks, *J. Am. Chem. Soc.*, **129**, 3627 (2007).
11. H.Q. Li, *Chem. Commun.*, **23**, 2776 (2004).
12. S. Mukerjee, S. Srinivasan, *J. Electroanal. Chem.*, **357**, 201 (1993).
13. A.B. Anderson, *Electrochimica Acta*, **47**, 3759 (2002).
14. J. Greeley, I.E.L. Stephens, A.S. Bondarenko, T.P. Johansson, H.A. Hansen, T.F. Jaramillo, J. Rossmeisl, I. Chorkendorff, J.K. Nørskov, *Nat. Chem.*, **1**, 552 (2009).
15. R.R. Adzic, J. Zhang, K. Sasaki, M.B. Vukmirovic, M. Shao, J.X. Wang, A.U. Nilekar, M. Mavrikakis, J.A. Valerio, F. Uribe, *Top. Catal.*, **46**, 249 (2007).
16. W.P. Zhou, X.F. Yang, M.B. Vukmirovic, B.E. Koel, J. Jiao, G. Peng, M. Mavrikakis, R.R. Adzic, *J. Am. Chem. Soc.*, **131**, 12755 (2009).

17. J.H. Yang, J.Y. Lee, Q.B Zhang, W.J Zhou, Z.L. Liu, *J. Electrochem. Soc.*, **155**, B776 (2008).
18. K. Sasaki, J.X. Wang, H. Naohara, N. Marinkovic, K. More, H. Inada, R.R. Adzic, *Electrochimica Acta*, **55**, 2645 (2010).
19. I.E.L. Stephens, A.S. Bondarenko, F.J. Perez-Alonso, F. Calle-Vallejo, L. Bech, T.P. Johansson, A.K. Jepsen, R. Frydendal, B.P. Knudsen, J. Rossmeisl, I. Chorkendorff, *J. Am. Chem. Soc.*, **133**, 5485 (2011).
20. J. Xu, J.H. Yang, J.Y. Lee, M. Saeys, *Ind. Eng. Chem. Res.*, **49**, 10251 (2010).
21. J.H. Yang, W.J. Zhou, C.H. Cheng, J.Y. Lee, Z.L. Liu, *ACS Appl. Mater. Interfaces*, **2**, 119 (2010).
22. M.H. Shao, K. Sasaki, R.R. Adzic, *J. Am. Chem. Soc.*, **128**, 3526 (2006).
23. A.J. Bard, R. Parsons, J. Jordan, *Standard Potentials in Aqueous Solutions*, Marcel Dekker, New York, (1985).
24. Y.G. Sun, Y.N. Xia, *Science*, **298**, 2176 (2002).
25. J.P. Perdew, K. Burke, M. Ernzerhof, *Phys. Rev. Lett.*, **77**, 3865 (1996).
26. G. Kresse, J. Hafner, *Phys. Rev. B*, **47**, 558 (1993).
27. G. Kresse, J. Futhmuller, *Comput. Mater. Sci.*, **6**, 15 (1996).
28. J. Hafner, *J. Comput. Chem.*, **29**, 2044 (2008).
29. P.E. Blochl, *Phys. Rev. B*, **50**, 17953 (1994).
30. M.W. Chase, *NIST-JANAF Thermodynamical Tables, Fourth Edition*, J. Phys. Chem. Ref. Data, Monograph 9, (1998).
31. G. Henkelman, B.P. Uberuaga, H. Jónsson, *J. Chem. Phys.*, **113**, 9901 (2000).
32. L. Kohler, G. Kresse, *Phys. Rev. B*, **70**, 165405 (2004).

33. C.D. Wagner, W.M. Riggs, L.E. Davis, J.F. Moulder, G.E. Muilenberg, *Handbook of X-Ray Photoelectron Spectroscopy*, Perkin-Elmer Corporation, Physical Electronics Division, Eden Prairie, Minnesota 55344, USA, (1979).
34. J.L. Lemaitre, P.G. Menon, F. Delannay, F. Delannay, (Ed), *Characterization of Heterogeneous Catalysts*, Vol. 15, Dekker, New York, pg. 325, (1984).
35. V. Radmilovic, H. A. Gasteiger, P. N. Ross, Jr., *J. Catal.*, **154**, 98 (1995).
36. Q.T. Trinh, K.F. Tan, A. Borgna, M. Saeys, *Journal of Physical Chemistry C*, **117**, 1684 (2013).
37. J.A. Rodriguez, D.W. Goodman, *Science*, **257**, 897 (1992).
38. A. Lewera, W.P. Zhou, R. Hunger, W. Jaegermann, A. Wieckowski, S. Yockel, P.S. Bagus, *Chem. Phys. Lett.*, **447**, 39 (2007).
39. B. Hammer, J.K. Nørskov, *Adv. Catal.*, **45**, 71 (2000).
40. V.R. Stamenkovic, B.S. Mun, K.J.J. Mayrhofer, P.N. Ross, N.M. Markovic, J. Rossmeisl, J. Greeley, J.K. Nørskov, *Angew. Chem. Int. Edit.*, **45**, 2897 (2006).
41. M.A. Rigsby, W.P. Zhou, A. Lewera, H.T. Duong, P.S. Bagus, W. Jaegermann, R. Hunger, A. Wieckowski, *J. Phys. Chem. C*, **112**, 15595 (2008).
42. J.R. Kitchin, J.K. Nørskov, M.A. Barteau, J.G. Chen, *J. Chem. Phys.*, **120**, 10240 (2004).
43. J.G. Chen, C.A. Menning, M.B. Zellner, *Surf. Sci. Rep.*, **63**, 201 (2008).
44. M.T.M. Koper, S.C.S. Lai, E. Herrero, *Mechanism of the oxidation of Carbon monoxide and small organic molecules at metal electrodes*, in

- M.T.M. Koper (Edt), *Fuel Cell Catalysis: A Surface Science Approach*, John Wiley & Sons, Inc., Hoboken, New Jersey, pg. 159 – 207, (2009).
45. B. Hammer, Y. Morikawa, J.K. Nørskov, *Phys. Rev. Lett.*, **76**, 2141 (1996).
46. G. Blyholder, *J. Phys. Chem.*, **68**, 2772 (1964).
47. K.J.J. Mayrhofer, D. Strmcnik, B.B. Blizanac, V. Stamenkovic, M. Arenz, N.M. Markovic, *Electrochimica Acta*, **53**, 3181 (2008).
48. J. Greeley, J.K. Nørskov, *J. Phys. Chem. C*, **113**, 4932 (2009).
49. A.V. Ruban, H.L. Skriver, J.K. Nørskov, *Phys. Rev. B*, **59**, 15990 (1999).
50. Y.G. Ma, P.B. Balbuena, *Surf. Sci.*, **603**, 349 (2009).

## CHAPTER 5

# **DFT study on the reversal of the CH/OH selectivity in the activation of methanol over platinum by the presence of water**

### **5.1. Introduction**

The catalytic activation of alcohols plays an important role in direct alcohol fuel cells and in the conversion of biomass-derived feedstock [1-3]. The presence of both OH and CH bonds in alcohols leads to interesting selectivity patterns and challenges. The mechanism and selectivity in methanol activation has been studied extensively, in particular over Pt catalysts [4-16]. Some studies indicate that the initial step in methanol electro-oxidation involves C-H activation [10-13], while others suggest that the electro-oxidation starts with O-H activation [14-16]. Often a dual pathway mechanism with two parallel paths is proposed: an indirect pathway involving OH activation leading to CO, and a direct pathway involving CH activation and leading to formaldehyde and formic acid which are subsequently oxidized to CO<sub>2</sub> [5-9]. However, overall, the selectivity between initial C-H versus O-H activation is still not clarified.

The apparent rate of methanol electro-oxidation depends significantly on the Pt surface structure [6,7,11,13,17,18], however, the mechanism was believed to be similar on different facets due to the similar current efficiency of CO<sub>2</sub> detected by on-line differential electrochemical mass spectrometry (DEMS)

study [17]. Several reaction intermediates have been detected during the electro-oxidation of methanol over Pt(111). Using *in situ* IR reflection-absorption spectroscopy (IRRAS) at low electrode potentials, CH<sub>2</sub>OH, CHOH, and COH were detected, suggesting the reaction starts by C-H activation [10,11]. However, the detection of HCO by electrochemically modulated IR reflectance spectroscopy (EMIRS) [15], and HCOO by *in situ* surface-enhanced IR absorption spectroscopy (SEIRAS) [19] at higher potentials indicates an initial O-H activation mechanism [13-15]. Isotope labeling studies show that methanol forms methoxy by O-H activation under UHV conditions, but CH<sub>2</sub>OH by C-H activation under electrochemical conditions. [12] The change in selectivity was attributed to the presence of water and the local electric field. Using chronoamperometry (CA) and cyclic voltammetry (CV), Cao et al. [13] reported a switch from a C-H activation mechanism to an O-H activation mechanism when the potential was increased above 0.4 V during the electro-oxidation of methanol.

Methanol electro-oxidation has also been studied by density functional theory (DFT) [13,20-25]. On clean Pt(111) surfaces, the lowest barrier is calculated for CH activation [21-23]. However, water can have a significant effect on the selectivity and recent studies show that the presence of a single water molecule lowers the O-H activation barrier in isopropanol oxidation by 8 kJ/mol and reverses the CH/OH selectivity in ethanol oxidation on Pt(111) [26]. The same observation was reported for Ethanol oxidation on Rh(111) by Sautet et al [27]. Experimental study showed that even a small amount of water greatly enhanced the initial reaction rate in 1-octanol oxidation [26]. The

mechanism of the methanol oxidation reaction was also suggested to be different when changing from using a gas-fed electrode to the electrolyte-fed electrode [28]. The effect of the water has been addressed in several studies [13,24-29]. Okamoto et al. reported a 70 kJ/mol increase in the CH activation barrier in methanol on Pt(111) when 21 water molecules were included in the model [24]. Hartnig using Ab initio molecular dynamic simulations to study the solvent effect of water during the Methanol oxidation on Pt(111), and reported the initial step of the reaction is the cleavage of a C-H bond which points towards the platinum surface [25]. The effect of the potential and the aqueous environment on the stability of the reaction intermediates during the electro-oxidation of methanol on Pt(111) was studied by Neurock et al. [13,29]. These calculations showed a gradual shift from C-H activation to O-H activation with increasing potential.

Water not only affects the activity and selectivity through changes in the interactions with reactants and transition states, it can also acts as the source of active hydroxyl groups and open another reaction pathway. Surface hydroxyl groups can play an active role through hydrogen abstractions [26,30-32]. In the oxidation of alcohols to acids on Pt and Au, isotope labeling experiments demonstrated that hydroxyl species are the real active oxidizing species instead of molecular oxygen in air [30] Recently, the importance of a hydrogen abstraction pathway in the O-H activation of methanol has been demonstrated [26,30,31]. On Au, hydroxyl groups were proposed to also facilitate CH activation in methoxy during methanol electro-oxidation [32]. Besides, formate adsorbate was identified as an active intermediate during the



methanol electro-oxidation by Osawa et al, but its formation only could be observed at applied potential higher than 0.5V (which is the condition for surface OH starts to form). The presence of active surface oxygen source (adsorbed O\* or OH\* on the surface) was claimed to be the prerequisites for the oxidation of methanol to formate [19]. All of those results emphasize the importance of considering water and surface OH\* into studying mechanism of alcohol decomposition under fuel cell conditions.

In this study, the effect of water on the activity and selectivity of activation methanol on Pt(111) was studied using density functional theory (DFT) with the revPBE-VdW functional [33,34]. The calculations show that the presence of water increases the activation barriers for both C-H and O-H activation because water molecules stabilize the reactants more than the transition states. Hydrogen bonding has a larger effect for the O-H pathway than for the C-H pathway, and reverses the selectivity observed on clean surfaces. The presence of surface hydroxyl groups opens a new hydrogen-abstraction pathway with a very low O-H activation barrier and again reverses the selectivity.

## **5.2. Computational Methods.**

All calculations were performed using spin-polarized periodic DFT with the revised Perdew-Burke-Ernzerhof functional [33] including non-local vdW-DF correlation (revPBE-VdW) [34], a plane-wave basis set with a cut-off kinetic energy of 450 eV, and the projector-augmented wave (PAW) method [35,36] as implemented in the Vienna Ab-initio Simulation Package (VASP) [37,38]. The Pt(111) surface was modeled as a 3-layer  $p(3 \times 3)$  slab, with an optimized

lattice constant of 4.04 Å. The Brillouin zone was sampled with a 3x3x1 Monkhorst-Pack grid, and repeated slabs were separated by 12 Å to minimize interactions. Geometries were fully relaxed until the energy changes by less than 0.1 kJ/mol.

Transition states were located using the climbing-image Nudged Elastic Band (ci-NEB) method [39]. In the NEB method, a series of intermediate states distributed along the initial reaction path connecting a reactant and a product state are simultaneously optimized while restricting atomic motions to hyperplanes perpendicular to the reaction path. Generally, six to ten intermediate states were used and forces minimized to 0.05 eV/Å with the quasi-Newton algorithm. The NEB intermediate structure with the highest energy was further optimized to the transition state structure. Frequency calculations confirmed the nature of the transition states with have exactly one imaginary degree of freedom which corresponds to the mode that takes reactants to products. NEB calculations were performed for all reactant and product configurations within 10 kJ/mol of the most stable co-adsorbed configuration within the unit cell, and only the lowest energy transition states are included. The methanol coverage in a  $p(3\times 3)$  unit cell, 0.11 ML, is also close to methanol coverage of the 0.09 ML determined under working conditions by on-line differential electrochemical mass spectrometry on a Pt(111) electrode [17]. Bader charges [40,41] were computed to analyze the nature of the transferred hydrogen atom in the hydrogen abstraction reactions.

### 5.3. Results and Discussion.

To evaluate the effect of water, we studied 3 cases: on a clean Pt(111) surface, representing UHV conditions; activation in the presence of a single water molecule (i.e., a single hydrogen bond with the methanol OH group), and in the presence of a water overlayer (i.e., two hydrogen bonds with the OH group). Several reactant structures were considered in the  $p(3\times 3)$  unit cell for the methanol + water overlayer, but the structure where methanol replaces two water molecules in an ice-like 6-membered ring represents the starting point for the most favorable pathway (section 5.3.2). To evaluate reaction paths where hydroxyl groups abstract a hydrogen atom from methanol, one of the four water molecules in the unit cell was replaced by hydroxyl.

#### 5.3.1. Adsorption of methanol, methoxy and hydroxyl groups on Pt(111)

The adsorption of methanol and water on the Pt(111) surface was studied first (Table 2.1). On a clean surface, methanol adsorbs at a top site with a calculated adsorption energy of -44 kJ/mol, slightly weaker than the value measured by Karp et al. using calorimetry, -59 kJ/mol [42]. The important role of van der Waals (vdW) forces in the weak interaction between water molecules with metal surfaces has been reinforced [43,44] when evaluating the relative stability, adsorption sites, and adsorption geometries of competing water ad-structures. VdW correlation significantly improves the adsorption energy from -38 kJ/mol for revPBE to -44 kJ/mol with revPBE-VdW. Also the reaction energy for the decomposition of water to OH\* and H\*, +48 kJ/mol, and for the transfer of a H atom from methanol to O\*, -69 kJ/mol, agree well with the measurements by Campbell et al. [45,46] (Table 2.1).

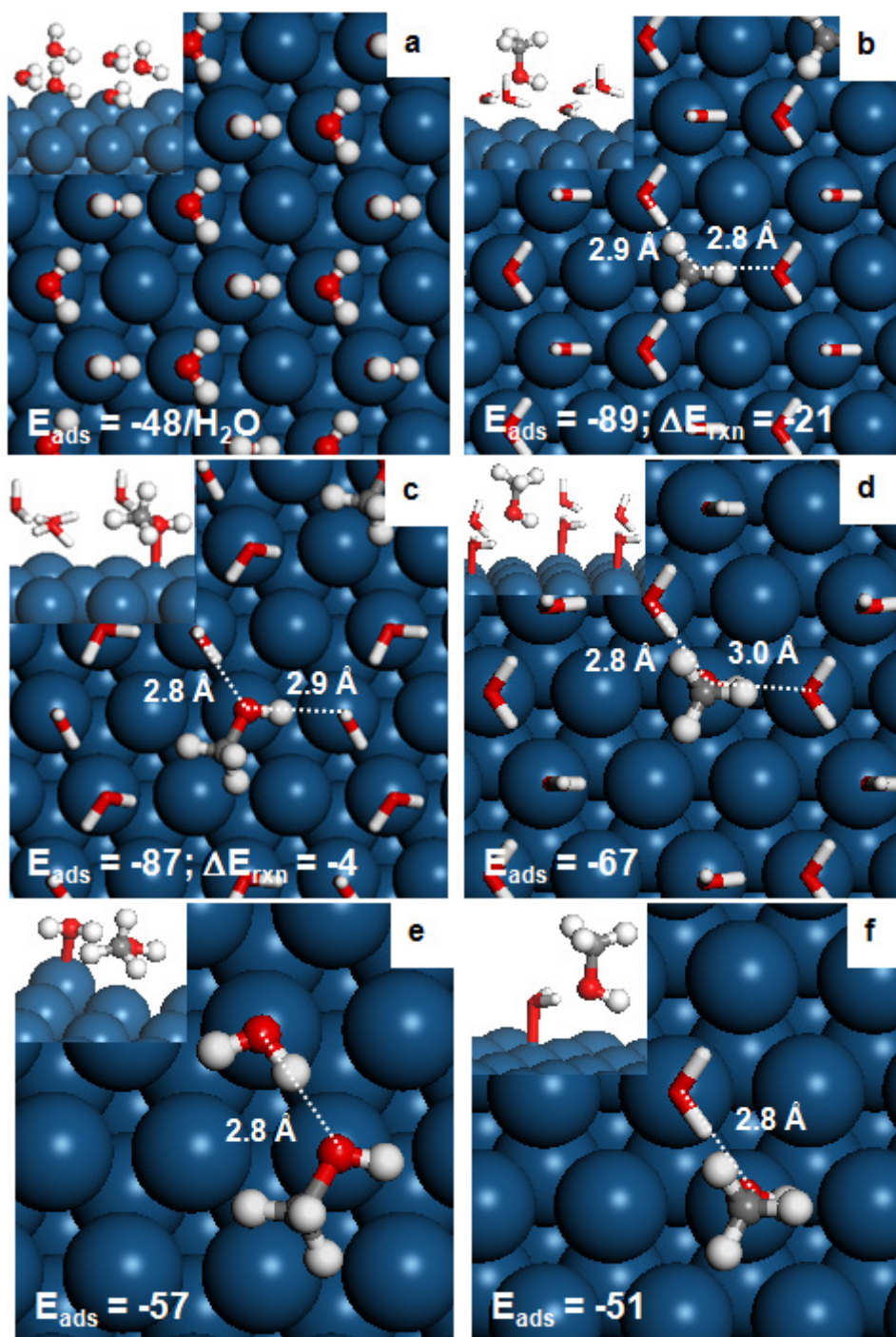


**Figure 5.1.** (a) Ice-like structure of water layer on Pt(111); (b) Adsorption of Methanol on pre-covered water layer on Pt(111); (c),(d) Two configurations of the adsorption of Methanol with 4 water on Pt(111). Adsorption energy  $E_{\text{ads}} = E_{\text{Methanol-water/Pt}} - E_{\text{water/Pt}} - E_{\text{Methanol(gas)}}$ . The reaction energy  $\Delta E_{\text{rxn}}$  is calculated for the reaction:  $\text{CH}_3\text{OH}_{(l)} + 6 \text{H}_2\text{O}^* \rightarrow \text{CH}_3\text{OH-nH}_2\text{O}^* + (6-n) \text{H}_2\text{O}_{(l)}$ ; (e),(f) two configurations of Methanol coadsorbed with a single water on Pt(111).

The calculated adsorption energy of an ice-like water layer (2/3 ML, Fig. 5.1a), -48 kJ/mol, is comparable to the experimental value of  $-46.2 \pm 7$  [45],

and much stronger than for the revPBE functional without VdW correlation, -39 kJ/mol. Next, the adsorption of methanol on the ice-like water-covered surface is investigated. The desorption of a water molecule and the subsequent adsorption of methanol is 21 kJ/mol favorable, forming a structure with 5 water molecules (5/9 ML) and 1 methanol molecule per ring (Fig. 5.1b). The hydrogen-bonds significantly stabilize methanol on the Pt(111) surface from -44 kJ/mol on the clean surface to -89 kJ/mol in the presence of water. The O-O distances of  $\sim 2.8$  Å are indeed representative of H-bonding interactions [47,48]. The 43 kJ/mol increase in the adsorption energy in the presence of water is consistent with a typical hydrogen bond strength of about 20 kJ/mol per hydrogen bond [49]. In this structure, the methyl group points away from the surface and only OH activation is possible. To allow CH activation, methanol needs to adsorb parallel to the surface and a second water molecule needs to desorb (Fig. 5.1c). This step costs 17 kJ/mol. Note that the entropy and stability gained by the water molecule in the liquid phase makes this step somewhat more favorable (26.4 kJ/mol). The methanol adsorption energy on the structure with 4/9 ML water, -87 kJ/mol, is similar to the value reported by Błonski et al. using PBE with dispersion corrections [50]. Also in this structure, methanol has two hydrogen bonds with water (Fig. 5.1c). A second structure where methanol co-adsorbs with 4 water molecules is shown in Fig 5.1d, in which methanol is perpendicular to the surface. This structure is 20 kJ/mol less stable than the structure in Fig 5.1c.

The adsorption energy of methanol next to a single water molecule (Fig. 5.1e) is 57 kJ/mol. The increment of 13 kJ/mol is contributed by one Hydrogen

bond formed between methanol and water. Note that the co-adsorption of methanol with water gain around 20 kJ/mol from forming a Hydrogen bond, but also lost 7 kJ/mol from the weaker binding of Methanol with Pt(111) surface, reflect from the longer distance of C-Pt bond compare to the clean surface. There are few alternative structures, and the most next stable is shown in Fig 5.1f, with methanol perpendicular to the surface and is 6 kJ/mol less stable.

### 5.3.2. *Methanol activation on a clean surface.*

To establish a reference point, the activation of methanol was studied on a clean Pt(111) surface. Transition states for the different reaction pathways for the first and second dehydrogenation step are shown in Fig. 5.2. The calculated C-H activation barrier of 88 kJ/mol is comparable to the values of 92 kJ/mol reported for the PW91 functional [23] and 101 kJ/mol for the PBE functional [20] and higher than the barrier of 65 kJ/mol reported using a fixed Pt(111) slab by Greeley et al. [22]. C-H activation is 15 kJ/mol exothermic. O-H activation has a slightly lower barrier of 82 kJ/mol, again consistent with the 78 kJ/mol barrier reported for PW91 [21] and 82 kJ/mol for PBE [20]. O-H activation is 51 kJ/mol endothermic, close to the experimental value of  $57 \pm 10$  kJ/mol [42] measured by calorimetry. Our calculations indicate that the C-H and O-H pathway are competitive under UHV conditions with a slight preference for O-H activation, consistent with labeling experiments and with the detection of a methoxy intermediate under UHV conditions [12].

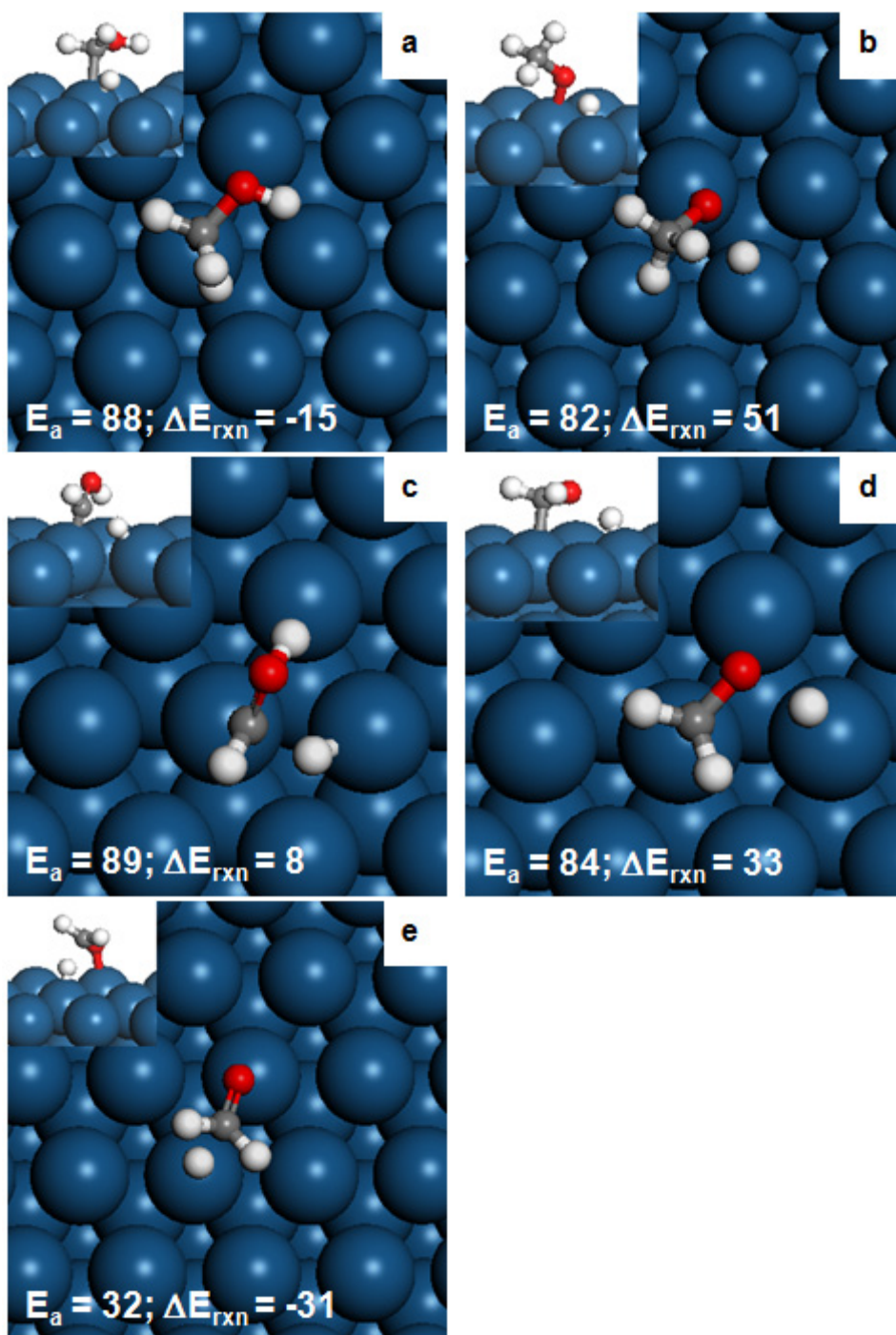


**Figure 5.2.** Transition states of C-H (a) and O-H (b) activation from  $\text{CH}_3\text{OH}$ , Transition states of C-H (c) and O-H (d) activation from  $\text{CH}_2\text{OH}$  and C-H activation from  $\text{CH}_3\text{O}$  (e) on clean Pt(111) surface. Reaction energy  $\Delta E$  is calculated for the reaction:  $\text{A-H}^* + * \rightarrow \text{A}^* + \text{H}^*$  ( $\text{H}^*$  and  $\text{A}^*$  are on separate unit cells).

The second dehydrogenation step was considered for  $\text{CH}_3\text{O}$  and  $\text{CH}_2\text{OH}$ . Both the CH and the OH activation barriers in  $\text{CH}_2\text{OH}$ , 89 and 84 kJ/mol, respectively, are very similar to the barriers in methanol and the CH and OH

pathway are again competitive. Our barrier for OH pathway is slightly higher than the barrier calculated with PW91 on a frozen slab, 73 kJ/mol [22,23]. Our barrier for CH pathway is much higher than the barrier calculated with PW91 on a frozen slab, 62 kJ/mol [22,23], and the reason might be due to the Pt surface was fixed in that study, while the reconstruction of surface active site in the Transition state might require extra energy. Indeed, in the Transition state of CH activation, the surface active Pt atom is pushed 0.16 Å above the surface when the surface was allowed to relax, and the energy cost to push that Pt atom can explain the difference of around 27 kJ/mol among those calculations.

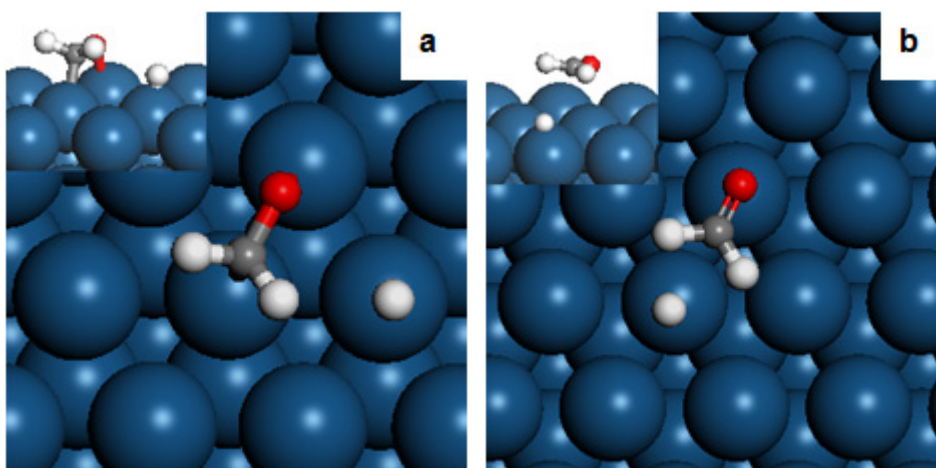


**Figure 5.3.** Two configurations of adsorbed CH<sub>2</sub>O on Pt(111): di- $\sigma$   $\eta$ (C,O) structure (a) and  $\eta$ (O) atop structure (b)

The OH activation in CH<sub>2</sub>OH forms CH<sub>2</sub>O. It is important to note that formaldehyde (CH<sub>2</sub>O) can adopt 2 conformations: a di- $\sigma$   $\eta$ (C,O) structure which is 15 kJ/mol more stable than an atop  $\eta$ (O) structure [52,53] (Figure 5.3). Transition states were optimized for both final geometries, and the lowest energy pathway was found to form the stable di- $\sigma$  product. Methoxy is significantly more reactive and the C-H activation barrier is only 33 kJ/mol, similar to barriers calculated with PW91, 24 kJ/mol, [22] and with PBE, 26



kJ/mol [20,53]. However for CH<sub>3</sub>O, the lowest energy pathway forms the less stable  $\eta(\text{O})$  CH<sub>2</sub>O product, which then relaxes to the more stable di- $\sigma$  structure. Note that DFT might under-estimate the binding energy of the atop  $\eta(\text{O})$  structure for the aldehydes. For example, acetaldehyde was predicted to be more stable in the di- $\sigma$   $\eta(\text{C},\text{O})$  structure with a DFT-PBE adsorption energy difference of only 4 kJ/mol [54], but surface science study could detect the dominant  $\eta(\text{O})$  configuration of Acetaldehyde on Pt(111) [55] and consistent with the DFT-XPS resolved C1s core-level binding energy calculations [54].

### 5.3.3. Effect of water on methanol activation.

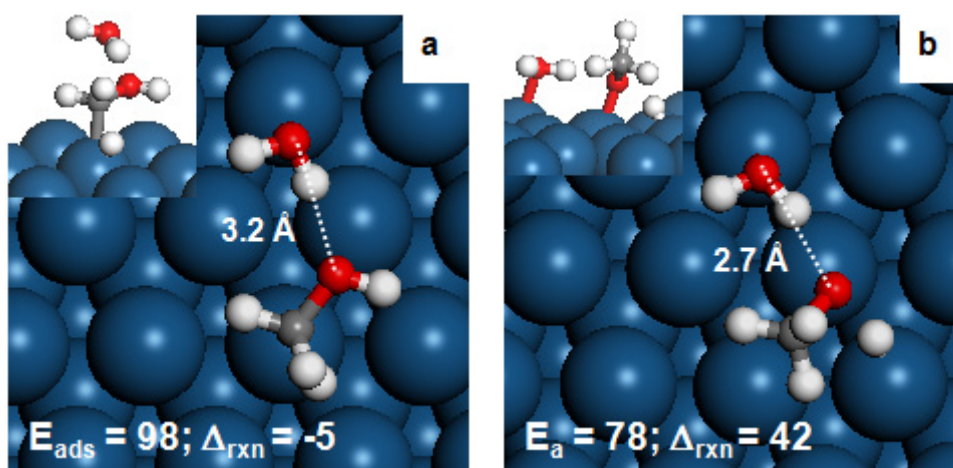


**Figure 5.4.** Transition states of C-H (a) and O-H (b) activation from CH<sub>3</sub>OH on surface with single water co-adsorbed.

The effect of a single water molecule (i.e., a single hydrogen bond) on the reaction pathway is studied first (Figure 5.4). The presence of a single hydrogen bond strengthens methanol adsorption by 13 kJ/mol to -57 kJ/mol. Note that the 13 kJ/mol interaction energy might not be sufficient to overcome the entropy cost to form a water-methanol complexes under UHV conditions, except at sufficiently low temperatures.

The increased stability of methanol increases the C-H activation barrier by 10 kJ/mol to 98 kJ/mol (Fig. 5.4a), close to the sum of the barrier without water, 88 kJ/mol and the water-methanol interaction energy, 13 kJ/mol. In the transition state, the O...O distance increases to 3.3 Å consistent with absence of a hydrogen bond. The reaction energy is 10 kJ/mol less exothermic, because there is no H-bond in the product while the Initial state is stabilize by 13 kJ/mol. Interestingly, the presence of a single water molecule decreases the O-H activation barrier slightly by 4 kJ/mol to 78 kJ/mol and makes the O-H pathway selective. There is still a H-bond in the Transition state, which stabilize it and reduce the activation barrier. The increase in O-H selectivity by a single water molecule was also found for ethanol decomposition on Rh(111) [27] and on Pt(111) [26].

When the water coverage increases to 5/9 ML (5 water molecules for every methanol), methanol forms two hydrogen bonds (Fig. 5.1b). O-H activation for this water coverage has a barrier of 132 kJ/mol (Fig. 5.5a) and is 75 kJ/mol endothermic. The 50 kJ/mol higher activation barrier than on clean surface results from the broken of two H-bonds. As the methyl group points away from the surface, no reaction path for C-H activation was found for this water coverage. Desorption of a water molecule provides space for the parallel adsorption of methanol (Fig. 5.1c). This step is 17 kJ/mol endothermic. However the total reaction energy of this structure reference to the starting point of 2/3ML ice-like structure of water on Pt(111) is still 4 kJ/mol feasible.

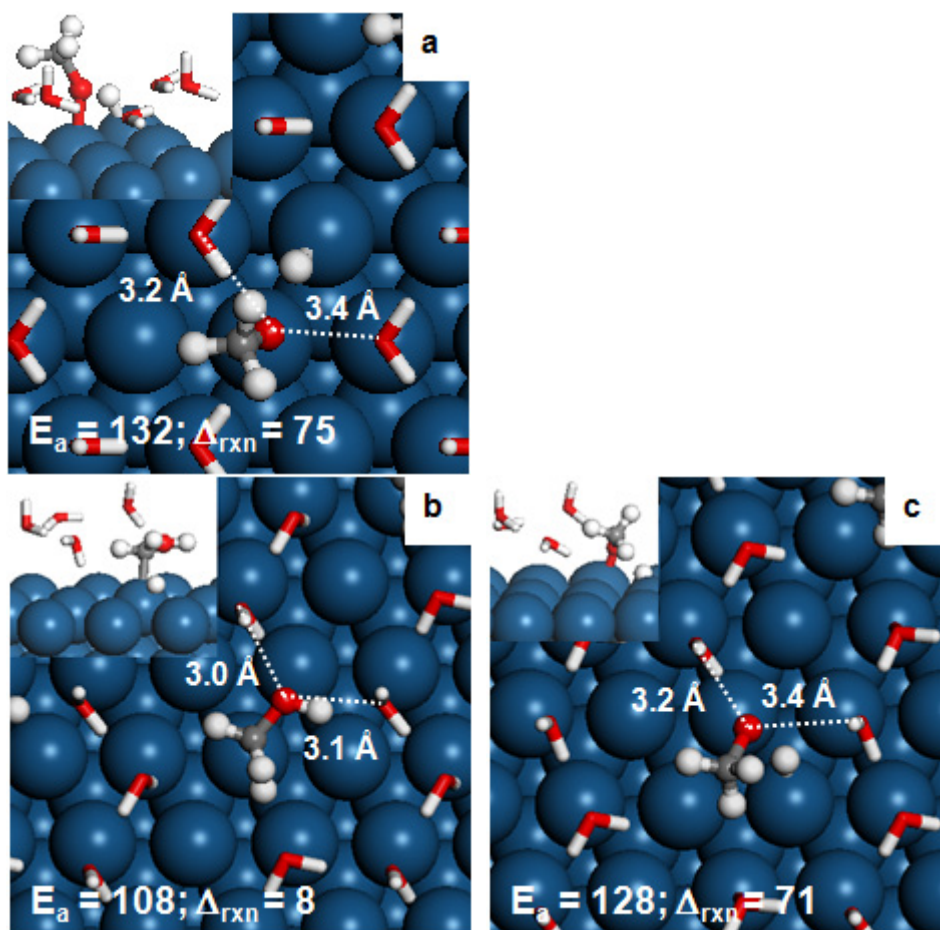
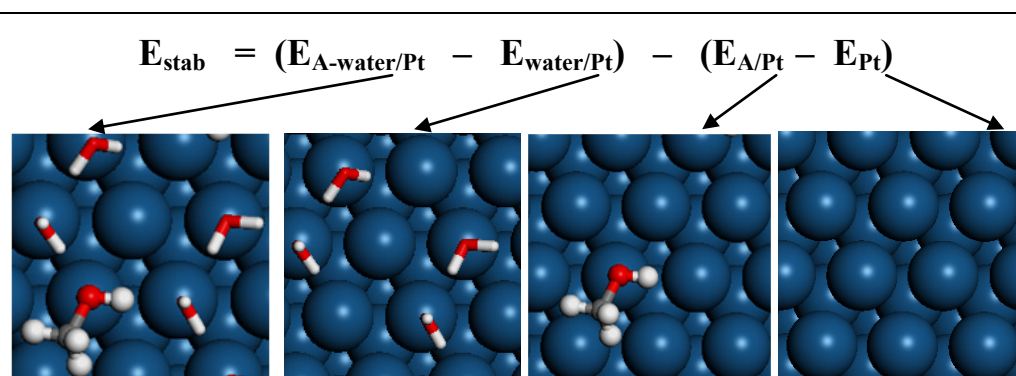


**Figure 5.5.** (a) OH activation in Methanol on Pt(111) with 5/9 ML coverage of water; (b) and (c) CH and O-H activation in Methanol on Pt(111) with 4/9 ML coverage of water.

The presence of a second hydrogen bond increases the C-H activation barrier by another 10 kJ/mol to 108 kJ/mol. In the transition state, the O-O distances increase from  $\sim 2.8$  Å in the reactant to  $\sim 3.0$  Å in the transition state. Because the hydrogen bonds are broken in the  $\text{CH}_2\text{OH}$  product, dehydrogenation also becomes significantly less favorable at +8 kJ/mol. The presence of an additional hydrogen bond has a more dramatic effect on the barrier for O-H activation, which increases by nearly 50 kJ/mol to 128 kJ/mol in the presence of a water overlayer and C-H activation becomes the dominant path, in agreement with experiments at low potentials [12,13]. The increase by 46 kJ/mol on the 4/9ML water coverage surface is consistent with the increase of

50 kJ/mol on the 5/9ML water coverage surface for the activation of OH due to both of two cases all involves the breaking of two H-bonds. At typical fuel cell conditions, the 128 kJ/mol barrier makes this reaction very sluggish.

**Table 5.1.** Stabilization energy  $E_{\text{stab}}$  of water towards the C-H and O-H activation from  $\text{CH}_3\text{OH}$  and  $\text{CH}_2\text{OH}$  on Pt(111)



	$\text{CH}_3\text{OH}$	$\text{TS}_{\text{CH}_3\text{O}-\text{H}}$	$\text{TS}_{\text{H}-\text{CH}_2\text{OH}}$
Single water	-14	-14	-2
Water layer	-43	+6	-27
	$\text{CH}_2\text{OH}$	$\text{TS}_{\text{CH}_2\text{O}-\text{H}}$	$\text{TS}_{\text{H}-\text{CHOH}}$
Water layer	-7	+3	-2
	$\text{CH}_3\text{O}$		$\text{TS}_{\text{H}-\text{CH}_2\text{O}}$
Water layer	-4		-5

While a single hydrogen bond slightly activates the OH group, the presence of two hydrogen bonds to the OH group significantly deactivates this path. To quantify the effect of the hydrogen bonds, we decomposed the adsorption energy of the reactant and of the C-H and O-H transition states as illustrated in Table 5.1. While a single water molecule increase the adsorption energy of methanol by 14 kJ/mol, a higher water coverage has a much stronger effect. In the O-H transition state for the water overlayer both hydrogen bonds are essentially broken and the “stabilization” becomes 6 kJ/mol repulsive. The

effect for a single water molecule is very different and the hydrogen bond remains essentially intact. The behavior is very different for the C-H path. For a single water molecule, the hydrogen bond is broken in the transition state while they remain intact (though somewhat weakened) for the water overlayer.

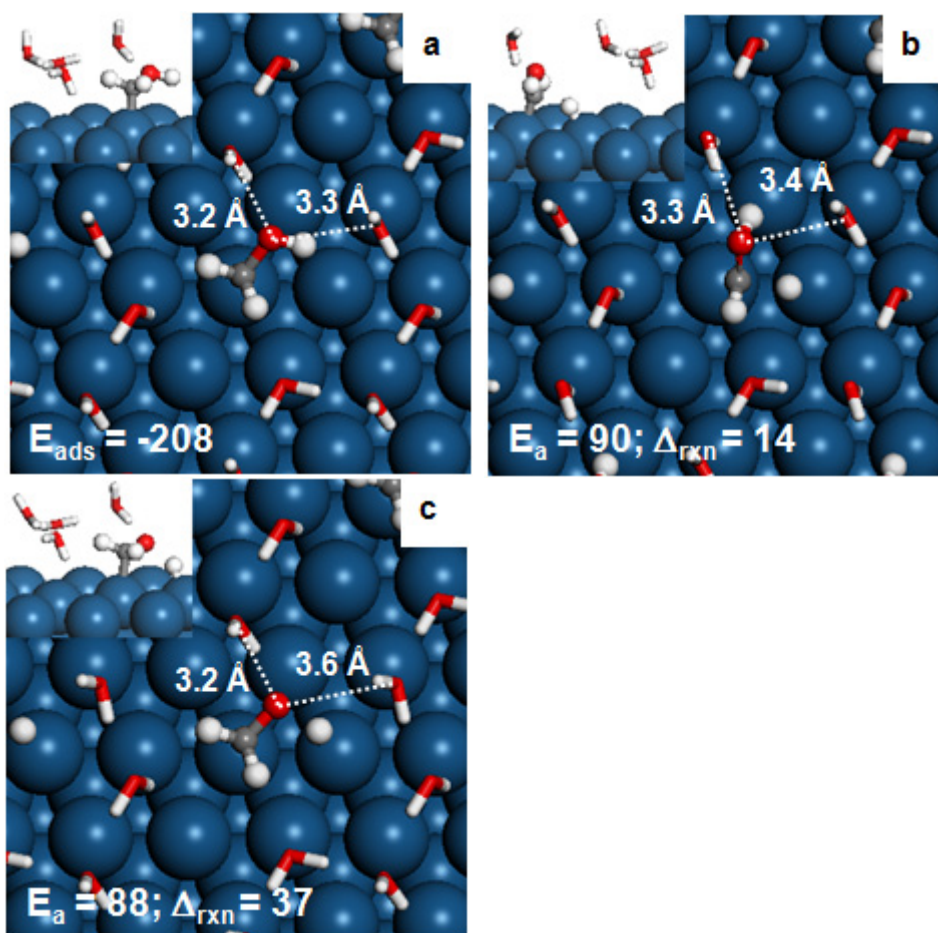


**Figure 5.6.** Adsorption of  $\text{CH}_2\text{OH}$  (a); and the activation of C-H (b) and O-H (c) from  $\text{CH}_2\text{OH}$  on water covered Pt(111) surface;

Next we briefly consider the effect of a water layer for the second dehydrogenation step, starting from  $\text{CH}_3\text{O}$  and  $\text{CH}_2\text{OH}$ . Both  $\text{CH}_3\text{O}$  and  $\text{CH}_2\text{OH}$  are not stabilized by the water overlayer with stabilization energies of only 7 and 4 kJ/mol (Table 5.1). On bare surface,  $\text{CH}_2\text{OH}$  adsorbed on Pt(111) surface with the adsorption energy of -201 kJ/mol, which is very consistent with earlier computation results using PW91 functional of -1.98 eV [22] and -209 kJ/mol [23]. On water covered Pt surface, the adsorption energy of

CH<sub>2</sub>OH is -208 kJ/mol, and the stabilization energy of water to CH<sub>2</sub>OH is only -7 kJ/mol, much lower than the stabilization effect -43 kJ/mol of water to CH<sub>3</sub>OH due to the poor Hydrogen bonding between CH<sub>2</sub>OH and surrounding water molecules (Figure 5.6a).

Because of the short C-Pt distance of 2.1 Å for CH<sub>2</sub>OH, the O-O distances become too long (~3.3 Å) to form strong hydrogen bonds (the hydrogen bond is considered to be broken if the bond length is greater than 3.20 Å [48,56]) and the CH and OH activation barriers are essentially identical to the values on a bare surface (Figure 5.6b and 5.6c). Indeed, the activation barrier of both the C-H and O-H scission on water covered surface are only slightly higher than those values on bare surface (90 and 88 kJ/mol for C-H and O-H scission on water covered surface compared to 88 and 84 kJ/mol on bare surface, respectively). The stabilization energies in Table 5.1 confirm this observation.

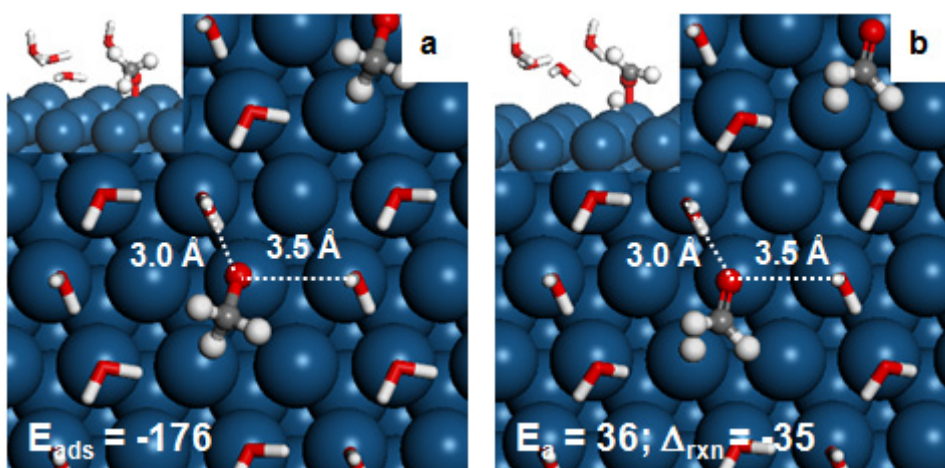


**Figure 5.7.** Adsorption of CH<sub>3</sub>O (a) and the transition state of CH activation from CH<sub>3</sub>O (b) on water covered Pt(111) surface

Also for C-H activation in CH<sub>3</sub>O, the effect of water is minimal with only a small increase in the activation barrier. The computed activation barrier is 36 kJ/mol, while its value on bare surface is 32 kJ/mol. Though water has a

dramatic effect on the selectivity determining first dehydrogenation step, its effect on the second step is minimal because the strong interaction of  $\text{CH}_2\text{OH}$  and  $\text{CH}_3\text{O}$  with the surface prevent the flexibility to interact with the water overlayer. The structures of the Transition states are also not much different from those structures on bare surfaces. For example, the distances of C-H and O-H in the Transition states of CH and OH activation from  $\text{CH}_2\text{OH}$  are 1.58 Å and 1.63 Å on water covered surface (Figure 5.6b,c), which are very close to the values of 1.55 Å and 1.70 Å on bare surface. For the CH activation in  $\text{CH}_3\text{O}$ , the C-H distance in the Transition state on water covered surface is 1.60 Å (Figure 5.7b), which is also close to the distance in the transition state on the bare surface (1.55 Å).

#### 5.3.4. Effect of surface hydroxyl species on methanol activation.

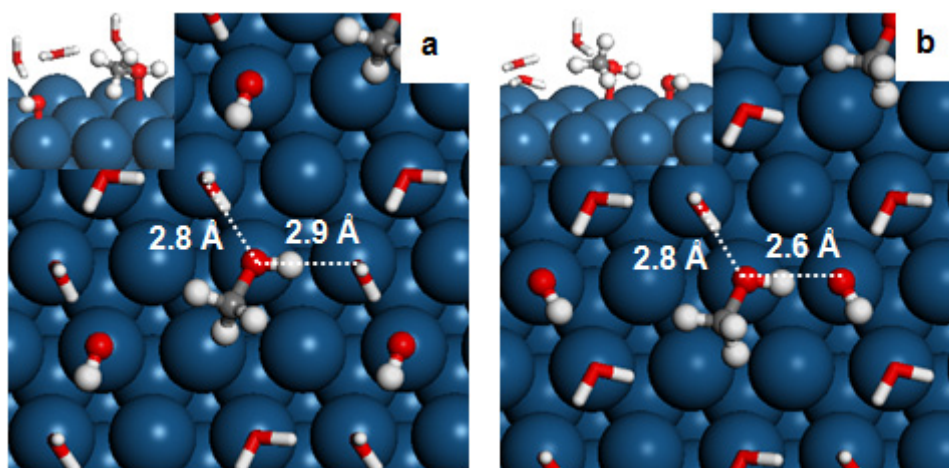


**Figure 5.8.** Replacement of one water by surface Hydroxyl group in (a) C-H activation and (b) O-H activation from  $\text{CH}_3\text{OH}$  on water covered Pt(111)

At potential of 0.5 V, hydroxyl groups start to form on Pt(111) [57]. The Gibbs free energy of reaction to form  $\text{OH}^* + \text{H}^+$  from a water overlayer becomes favorable for a potential of 0.66 V using revPBE-vdW. Interestingly, a structure with 3  $\text{OH}^*$  groups per water ring is 8 kJ/mol more stable than a

structure with isolated OH\* groups. This value is close to the potential of 0.63 V calculated by Rossmeisl et al. [58] and 0.59 V reported by Taylor et al. [59].

The presence of hydroxyl group opens a hydrogen abstraction pathways [26,30,31]. In our calculations, one of the four water molecules in the ring structure was replaced by a hydroxyl group and the hydrogen abstraction reaction paths were calculated for methanol, methoxy and CH<sub>2</sub>OH (Figure 5.8). The strong H-O bond in the water product makes CH activation 42 kJ/mol exothermic and OH activation in methanol nearly thermoneutral.

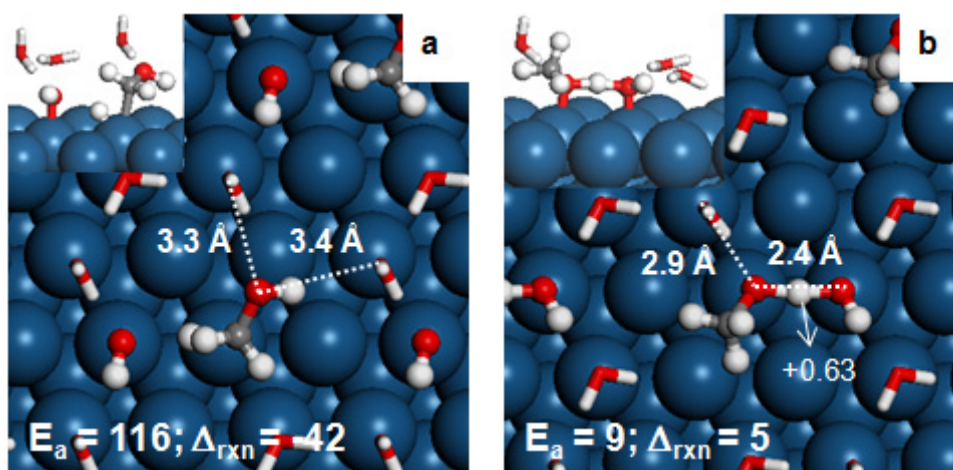


**Figure 5.9.** Surface OH assistance reactions on Pt(111): (a) Activation of C-H and (b) activation of OH from CH<sub>3</sub>OH

H abstraction from the CH<sub>3</sub> group has a barrier of 116 kJ/mol (Figure 5.9a), 8 kJ/mol higher than the unimolecular direct CH activation on a water-covered surface (108 kJ/mol). Clearly, CH activation follows a direct pathway on Pt(111). The presence of a surface hydroxyl group opens a O-H activation pathway with a very low barrier of 9 kJ/mol, typical for such a reaction [26,30,31]. The transition state is best described as proton shuttling as indicated by a Bader charge of +0.6 on the transferred H (Figure 5.9b). In the



presence of surface hydroxyl group, O-H activation is clearly the preferred path, in agreement with the interpretation from experimental results [30].

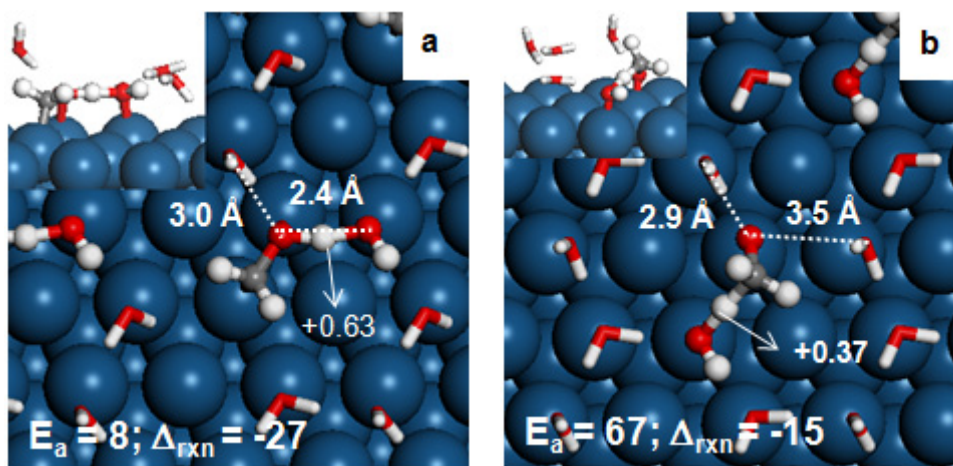


**Figure 5.10.** Surface OH assistance reaction on Pt(111): (a) OH activation in  $\text{CH}_2\text{OH}$  and (b) CH activation in  $\text{CH}_3\text{O}$

Finally, the effect of hydroxyl groups on the second dehydrogenation step was evaluated as well. (Figure 5.10). Proton transfer from  $\text{CH}_2\text{O-H}$  to  $\text{OH}^*$  is again easy with a barrier of 8 kJ/mol, however, the formation of  $\text{CH}_2\text{OH}$  through initial C-H activation is kinetically slow in the presence of  $\text{OH}^*$ . Hydrogen abstraction from  $\text{CH}_3\text{O}$  has a barrier of 67 kJ/mol. The charge on the transferring H is +0.37 and this hydrogen abstraction is better described as a radical reaction. The 67 kJ/mol barrier is however 31 kJ/mol higher than the direct dehydrogenation barrier on Pt(111), and the direct pathway is found to dominate on Pt(111).

### 5.3.5. Activation of CH in $\text{CH}_3\text{O}$ on other transition metals: competition between direct dehydrogenation versus H-abstraction pathway

Pt(111) was reported to be the best catalyst for Methoxy decomposition [52,53] among other transition metals due to the largest exothermic behavior of the reaction. Previous section has demonstrated that the activation of CH in

Methoxy could be processed via two different pathways: the direct dehydrogenation catalyzed by metal surface, and the Hydrogen abstraction pathway assisted by surface Hydroxyl group. On Pt(111) the prefer pathway is the direct dehydrogenation. In this section, we expand this study to evaluate the competition between those two reaction pathways on other transition metal. The considered candidates are Au(111), Pd(111), Rh(111) and Ag(111) surfaces.

Au is receiving much attention as an interesting catalyst for alcohol oxidation [30,32]. Recently, Koper et al. reported the enhancement of methanol oxidation activity by CO pre-adsorption [32]. In that study, adsorption of CO enhanced OH adsorption on Au, and consequently enhanced the C-H activation in methanol electro-oxidation. Similar to the study on Pt(111), OH activation assisted by surface Hydroxyl is very feasible with the low activation barrier of 9 kJ/mol and is likely the initial step for the Methanol oxidation on Au(111). The transition state structure is shown in Figure 5.11. The Bader charge on transferred H atom is 0.64, demonstrate again this is a Proton transferred reaction.

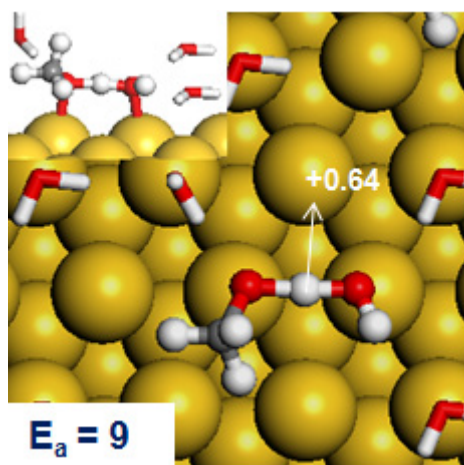


**Figure 5.11.** OH activation in CH<sub>3</sub>O assisted by surface Hydroxyl group on water covered Au(111)

Therefore under fuel cell conditions, the initial products will be dominated by Methoxy. In the next step, the direct dehydrogenation occurs with the activation barrier of 67 kJ/mol (Figure 5.12a). This value is in good agreement with the value reported earlier [53]. However the H-abstraction pathway is even more feasible with the activation barrier of only 47 kJ/mol, 20 kJ/mol lower than the dehydrogenation pathway (Figure 5.12b). The computed Bader charge on transferred H atom is +0.25, smaller than the value on Pt(111) surface, +0.35. The appearance of surface OH facilitates the C-H activation by open the lower activation barrier pathway, which could explain the experimental observation by Koper et al. [32]

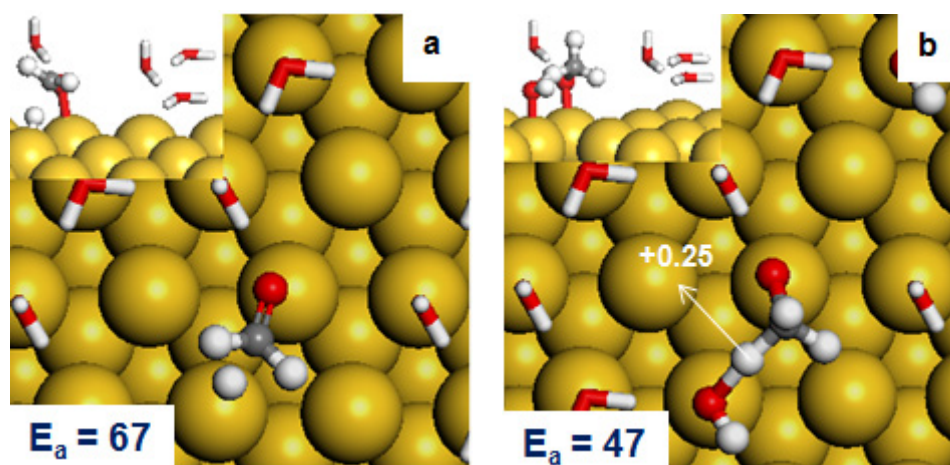


**Figure 5.12.** Decomposition of Methoxy on Au(111): the direct dehydrogenation pathway (a), and the H-abstraction by surface Hydroxyl pathway (b)

From Pt(111) to Au(111), the preferred reaction pathway of  $\text{CH}_3\text{O}$  decomposition has switched from direct dehydrogenation to H-abstraction. We have conducted the evaluation on another metal which is less active than Pt but more active than Au, which is Pd. On Pd(111), the activation barriers for the dehydrogenation pathway and the H-abstraction pathways are 66 and 72 kJ/mol, respectively (Figure 5.13). The difference between those activation

barriers is only +6 kJ/mol, compare with the value of +31 kJ/mol on Pt(111) and -20 kJ/mol on Au(111). The less active the transition metal, the more feasible the H-abstraction pathway. The Bader charge calculated on transferred H-atom in the H-abstraction pathway on Pd(111) is +0.35.

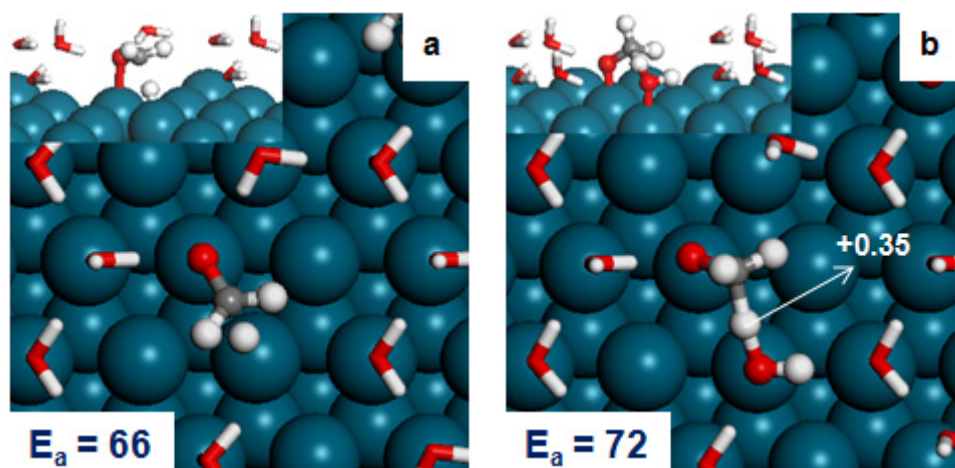


**Figure 5.13.** Decomposition of Methoxy on Pd(111): the direct dehydrogenation pathway (a), and the H-abstraction by surface Hydroxyl pathway (b)

Finally, we expanded the study on study on Rh(111) and Ag(111). The results are summarized in Table 5.2.

**Table 5.2.** Activation barriers for two pathway of Methoxy decomposition on transition metals (kJ/mol)

	Rh	Pt	Pd	Ag	Au
Direct dehydrogenation	66	36	66	103	67
H-abstraction	102	67	72	88	47
$\Delta E_a$	+36	+31	+6	-14	-20
Charge on transferred H in H-abstraction pathway	+0.42	+0.37	+0.35	+0.28	+0.25

On Rh(111), the H-abstraction pathway is inhibited by the much higher activation barrier than the direct dehydrogenation pathway, +36 kJ/mol, and correlates well with the highest charge on transferred H atom in the H-abstraction pathway. In contrast, the H-abstraction pathway is preferred on

Ag(111) with 14 kJ/mol lower activation barrier than the direct dehydrogenation pathway. Plot the difference in the activation barriers between the direct dehydrogenation and the H-abstraction pathways as a function of the charge on transferred H atom in the H-abstraction pathway, a nice correlation is observed, as shown in Figure 5.14.

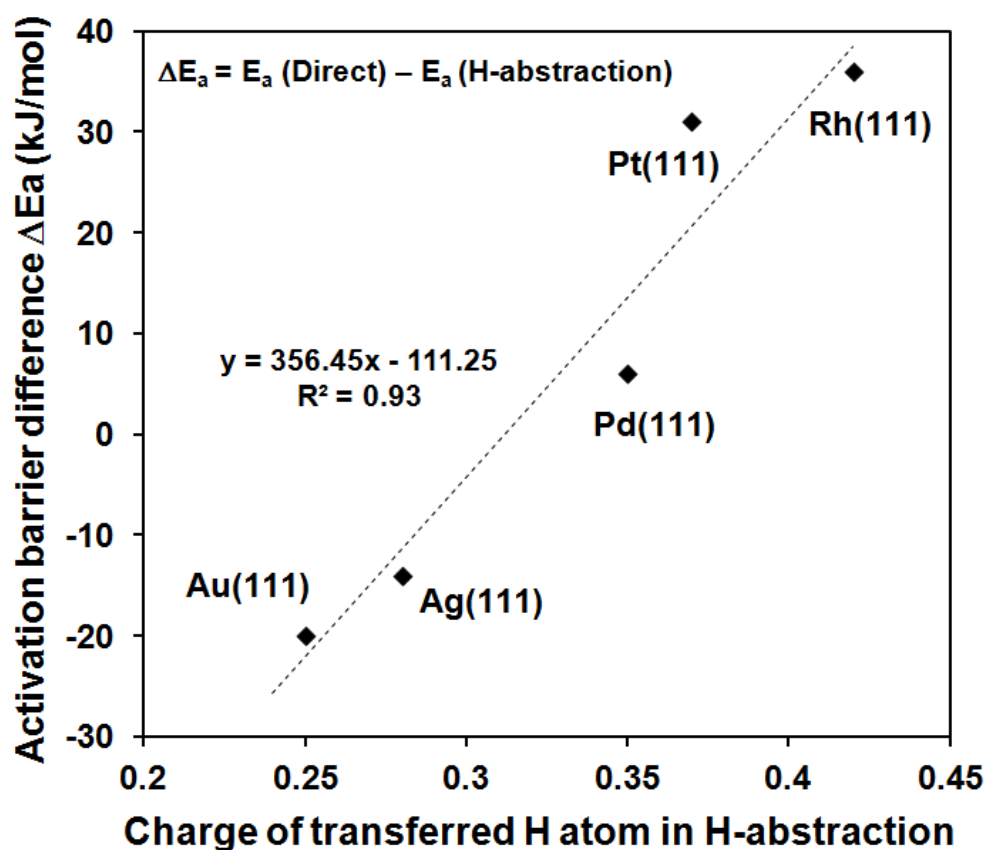


**Figure 5.14.** Correlation between the activation barriers difference of the two pathways versus the charge of transferred H atom in the H-abstraction pathway

From Figure 5.14, the higher charge of transferred H atom in the H-abstraction pathway, the more difficult the reaction. Clearly surface OH group also acts as active agent in abstraction H from the C-H bonds in  $\text{CH}_3\text{O}$ , however the C-H abstraction reaction only preferred on less active surfaces, e.g. Ag(111) and Au(111). The detail explanation on this correlation is beyond the scope of this study and will be the subject for future study.

5.3.6. Energy Profile for the dehydrogenation of methanol.

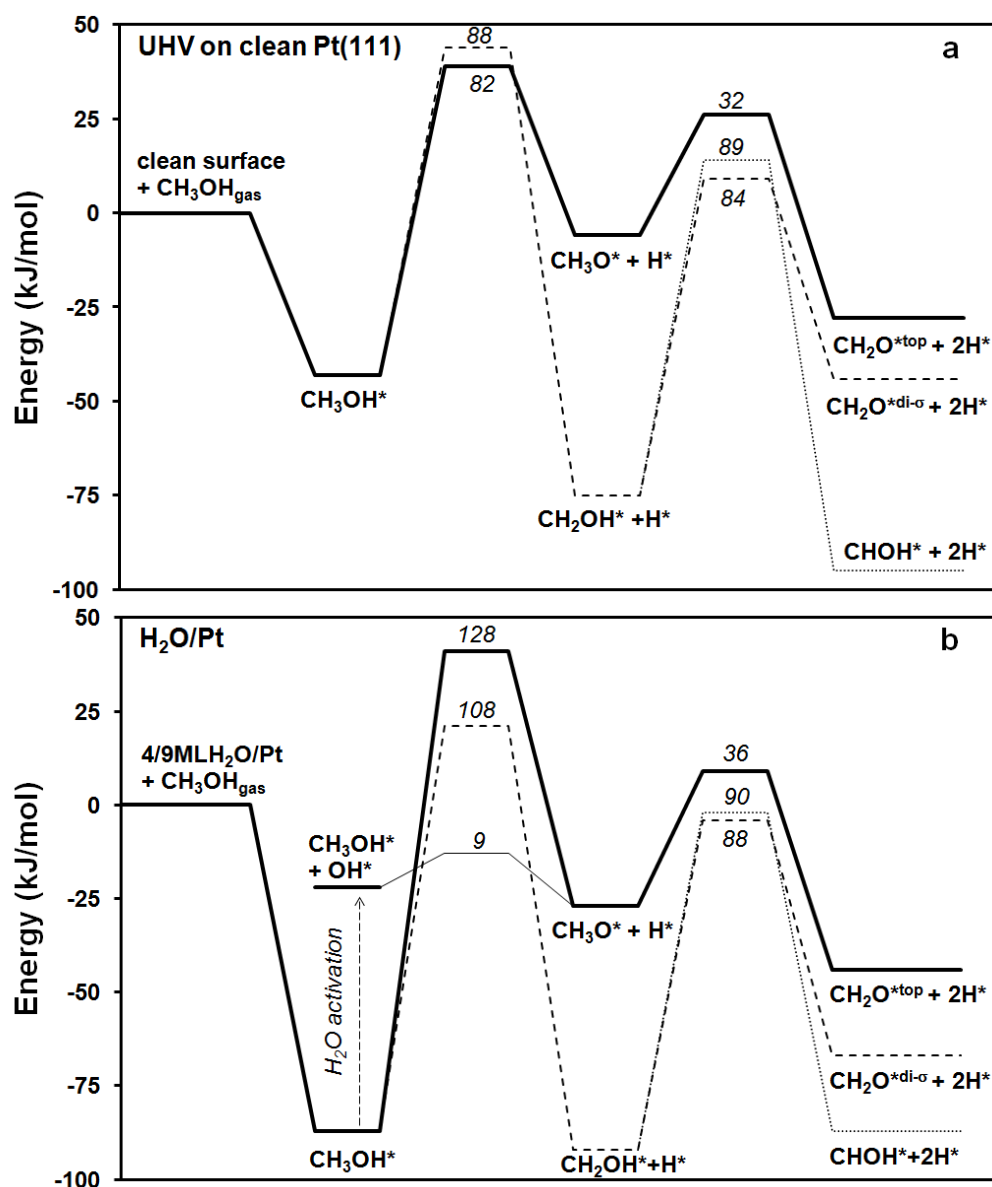


**Figure 5.15.** The reaction Energy Profile for the Deprotonation of Methanol on Pt(111). (a) Reactions under UHV on clean surface; (b) Reactions in aqueous media on water covered surface. The reaction on clean surface and in water on Pt(111) can be expressed by the reaction:  $A-H \rightarrow A + H$ , while the reaction in the surface OH assisted pathways can be expressed by the reaction:  $A-H + OH \rightarrow A + H_2O$ .

Figure 5.15 summarizes the energy profile for methanol dehydrogenation. Under UHV conditions, the barrier for O-H activation is slightly lower than the barrier for C-H activation (Figure 5.15a). The effective barrier for the dehydrogenation of CH<sub>3</sub>O\*, 103 kJ/mol (71 + 32 kJ/mol) is comparable to the

first dehydrogenation barrier. For the C-H pathway, the barriers for the second dehydrogenation step, 88 kJ/mol for C-H and 84 kJ/mol for O-H, are similar to the barrier for the first step. On a water-covered surface, dehydrogenation of methanol becomes more difficult due to the strong hydrogen bonding with methanol (Figure 5.15b). The hydrogen bonding affects the O-H pathway much more than the C-H pathway and C-H activation becomes preferred. Therefore C-H activation is the initial step in the electro-oxidation of methanol over Pt at low potentials, consistent with experiments [11,12] Since the  $\text{CH}_2\text{OH}$  and  $\text{CH}_3\text{O}$  products form only very weak hydrogen bonds with the water layer, the second dehydrogenation step is not affected by the water overlayer and is hence easier than the first step.

When the applied potential is sufficient to facilitate the formation of surface  $\text{OH}^*$  groups, a proton shuttling pathway opens (Figure 5.15b). Deprotonation of the methanol O-H group by  $\text{OH}^*$  has a very low barrier and is nearly thermoneutral. Even at zero potential, where the formation of  $\text{OH}^*$  is 65 kJ/mol endothermic, the effective barrier for the proton shuttling pathway, 74 kJ/mol, is still lower than the direct dehydrogenation pathways. Dehydrogenation of  $\text{CH}_3\text{O}^*$  is however not facilitated by  $\text{OH}^*$  and the direct pathway has the lower barrier. Combining the  $\text{CH}_3\text{O}^*$  barrier, 32 kJ/mol, with the endothermicity of the deprotonation of adsorbed methanol at zero bias, 68 kJ/mol, leads to an effective barrier of 100 kJ/mol, very close to the direct C-H activation barrier in methanol, 108 kJ/mol. Clearly both pathways are competitive and their selectivity depends strongly on the potential and on the rate of formation of surface  $\text{OH}^*$  groups.

#### 5.4. Conclusions.

DFT studies showed that water significantly affect to the reactions that involve the alcohol reactants via forming the Hydrogen bonding. Therefore in more polar solvent this should be the very important factor. On bare surface, the barrier of O-H activation is 6 kJ/mol lower than the C-H activation. Stabilization of Methanol by water increases activation barriers for C-H and O-H activation by 20 and 44 kJ/mol compare to the values on bare surfaces, respectively, and switches the selectivity from O-H to C-H activation. The reverse selectivity on water covered surface was explained due to the stronger stabilization effect of water towards the Transition state of C-H activation than O-H activation. Therefore in aqueous media, at low potential the decomposition of Methanol should be initiated by C-H scission. When the potential is high enough to generate surface OH, the abstraction of Hydrogen in Hydroxyl group becomes very feasible to switch the mechanism towards initial O-H activation follow the “proton shuttling” mechanism. Therefore the first step of alcohol electro-oxidation in fuel cell condition is likely the O-H activation. After the removal of O-H bond in alcohol (losing hydrogen bonding with environment), consequence steps is much less affected by the solvent effect. Surface OH group also acting as active agent in abstraction H from the C-H bonds in CH<sub>3</sub>O, however on Pt(111) it is more difficult than the Direct dehydrogenation pathway with the activation barrier is 31 kJ/mol higher. The competition between the direct C-H dissociation pathway and the C-H abstraction pathway on different transition metal surfaces [64] are also evaluated, and the more active the surface, the easier the direct pathway and



vice versa. The C-H abstraction reaction only becomes more feasible for much less active surface, e.g. Ag(111) and Au(111).

## 5.5. References.

1. A.S. Aricò, V. Baglio, and V. Antonucci, *Direct Methanol Fuel Cells: History, Status and Perspectives*, in H. Liu and J. Zhang (Edt), *Electrocatalysis of Direct Methanol Fuel Cells: From Fundamentals to Applications*, WILEY-VCH Verlag GmbH & Co. KGaA, Weinheim, pg. 1 – 78, (2009).
2. J.N Beltramini and C.-H. Zhou, *Catalytic Conversion of Glycerol to Valuable Commodity Chemicals*, in M. Crocker (Edt), *Thermochemical Conversion of Biomass to Liquid Fuels and Chemicals*, The Royal Society of Chemistry, Cambridge, pg. 435-467, (2010).
3. E.H. Yu, X. Wang, X.T. Liu and L. Li, *Challenges and Perspectives of Nanocatalysts in Alcohol-Fuelled Direct Oxidation Fuel Cells*, in Z.-X. Liang and T.S. Zhao (Edts), *Catalysts for Alcohol-Fuelled Direct Oxidation Fuel Cells*, The Royal Society of Chemistry, Cambridge, pg. 227-249, (2012).
4. A. Hamnett, *Catalysis Today*, **38**, 445 (1997)
5. R. Parsons and T. VanderNoot, *J. Electroanal. Chem.*, 257, 9, (1988).
6. C. Lamy and C. Coutanceau, *Electrocatalysis of Alcohol Oxidation Reactions at Platinum Group Metals*, in Z.-X. Liang and T.S. Zhao (Edts), *Catalysts for Alcohol-Fuelled Direct Oxidation Fuel Cells*, Royal Society of Chemistry, Cambridge, pg. 1-70, (2012).

7. M.T.M. Koper, S.C.S. Lai, E. Herrero, *Mechanism of the oxidation of Carbon monoxide and small organic molecules at metal electrodes*, in M.T.M. Koper (Edt), *Fuel Cell Catalysis: A Surface Science Approach*, John Wiley & Sons, Inc., Hoboken, New Jersey, pg. 159 – 207, (2009).
8. E. Gyenge, *Electrocatalytic Oxidation of Methanol, Ethanol and Formic Acid*, in H. Liu and J. Zhang (Edt), *Electrocatalysis of Direct Methanol Fuel Cells: From Fundamentals to Applications*, WILEY-VCH Verlag GmbH & Co. KGaA, Weinheim, pg. 165 – 287, (2009).
9. S.C.S. Lai, N.P. Lebedeva, T.H.M. Housmans, M.T.M. Koper, *Top. Catal.*, **46**, 320 (2007).
10. V.S. Bagotzky, Y.B. Vassiliev, O. Khazova, *J. Electroanal. Chem.*, **81**, 229 (1977).
11. X.H. Xia, T. Iwasita, F. Ge and W. Vielstich, *Electrochimica Acta*, **41**, 711 (1996).
12. K. Franaszczuk, E. Herrero, P. Zelenay, A. Wieckowski, J. Wang, R.I. Masel, *J. Phys. Chem.*, **96**, 8509 (1992).
13. D. Cao, G.-Q. Lu, A. Wieckowski, S. A. Wasileski and M. Neurock, *J. Phys. Chem. B*, **109**, 11622 (2005).
14. J.L. Davis, M.A. Barteau, *Surf. Sci.*, **187**, 387 (1987).
15. B. Beden, J.M. Leger, C. Lamy, In *Modern Aspects of Electrochemistry*; J.O.M Bockris (Edt), Plenum Press: New York, Vol. 22, pg. 97–264, (1992).
16. M.S. Brogan, J.A. Cairns, T.J. Dines, C.H. Rochester, *Spectrochim. Acta A*, **53**, 943 (1997).
17. H. Wang and H. Baltruschat, *J. Phys. Chem. C*, **111**, 7038 (2007).

18. L.P. Ford, P. Blowers, and R.I. Masel, *J. Vac. Sci. Technol. A*, **17**, 1705 (1999)
19. Y.X. Chen, A. Miki, S. Ye, H. Sakai, and M. Osawa, *J. Am. Chem. Soc.*, **125**, 3680 (2003).
20. C.-Y. Niu, J. Jiao, B. Xing, G.-C. Wang and X.-H. Bu, *J. Comput. Chem.*, **31**, 2023 (2010).
21. J. Greeley, M. Mavrikakis, *J. Am. Chem. Soc.*, **124**, 7193 (2002).
22. J. Greeley, M. Mavrikakis, *J. Am. Chem. Soc.*, **126**, 3910 (2004).
23. S.K. Desai, M. Neurock, K. Kourtakis, *J. Phys. Chem. B*, **106**, 2559 (2002).
24. Y. Okamoto, O. Sugino, Y. Mochizuki, T. Ikeshoji, Y. Morikawa, *Chem. Phys. Lett.*, **377**, 236 (2003).
25. C. Hartnig and E. Spohr, *Chem. Physics*, **319**, 185 (2005).
26. S. Chibani, C. Michel, F. Delbecq, C. Pinel and M. Besson, *Catal. Sci. Technol.*, **3**, 339 (2013).
27. C. Michel, F. Auneau, F. Delbecq, and P. Sautet, *ACS Catal.*, **1**, 1430 (2011).
28. A.S. Lin, A.D. Kowalak, W.E. O'Grady, *J. Power Sources*, **58**, 67 (1996).
29. M.J. Janik, C.D. Taylor, M. Neurock, *Top. Catal.*, **46**, 306 (2007).
30. B.N. Zope, D.D. Hibbitts, M. Neurock, R.J. Davis, *Science*, **330**, 74 (2010)
31. R. Kavanagh, X. Cao, W.-F. Lin, C. Hardacre and P. Hu, *J. Phys. Chem. C*, **116**, 7185 (2012).
32. P. Rodriguez, Y. Kwon and M.T.M. Koper, *Nat. Chem.*, **4**, 177 (2012).
33. M. Dion, H. Rydberg, E. Schröder, D.C. Langreth, and B.I. Lundqvist, *Phys. Rev. Lett.*, **92**, 246401 (2004).

34. J. Klimes, D.R. Bowler, A. Michaelides, *Phys. Rev. B*, **83**, 195131 (2011).
35. J. Hafner, *J. Comput. Chem.*, **29**, 2044 (2008).
36. P.E. Blochl, *Phys. Rev. B*, **50**, 17953 (1994).
37. G. Kresse, J. Hafner, *Phys. Rev. B*, **47**, 558 (1993).
38. G. Kresse, J. Futhmuller, *Comput. Mater. Sci.*, **6**, 15 (1996).
39. G. Henkelman, B.P. Uberuaga, H. Jónsson, *J. Chem. Phys.*, **113**, 9901 (2000).
40. R.F.W. Bader, *Atoms in Molecules - A quantum theory*, Oxford University Press, New York, (1990).
41. G. Henkelman, A. Arnaldsson, H. Jonsson, *Comput. Mater. Sci.*, **36**, 254 (2006).
42. E.M. Karp, T.L. Silbaugh, M.C. Crowe, C.T. Campbell, *J. Am. Chem. Soc.*, **134**, 20388 (2012).
43. J. Carrasco, J. Klimes, A. Michaelides, *J. Chem. Phys.*, **138**, 024708 (2013)
44. I. Hamada, K. Lee and Y. Morikawa, *Phys. Rev. B*, **81**, 115452 (2010)
45. E.M. Karp, C.T. Campbell, F. Studt, F. Abild-Pedersen and J.K. Nørskov, *J. Phys. Chem. C*, **116**, 25772 (2012).
46. W. Lew, M.C. Crowe, C.T. Campbell, J. Carrasco, and A. Michaelides, *J. Phys. Chem. C*, **115**, 23008 (2011).
47. R.N. Karingithi, C.L. Shaw, E.W. Roberts, P.A. Molina, *Journal of Molecular Structure: THEOCHEM*, **851**, 92 (2008).
48. G.A. Jeffrey, *An Introduction to Hydrogen Bonding*, Oxford University Press, (1997).
49. S.J. Suresh and V.M. Naik, *J. Chem. Phys.*, **113**, 9727 (2000).

50. P. Błonski and N. Lopez, *J. Phys. Chem. C*, **116**, 1548 (2012).
51. X.H. Xia, T. Iwasita, *J. Electroanal. Chem.*, **411**, 95 (1996).
52. M. Mavrikakis, M.A. Barteau, *J. Mol. Catal. A*, **131**, 135 (1998).
53. R. Ren, C. Niu, S. Bu, Y. Zhou, Y. Lu and G. Wang, *J. Nat. Gas Chem.*, **20**, 90 (2011).
54. Q.T. Trinh, K.F. Tan, A. Borgna and M. Saeys, *J. Phys. Chem. C*, **117**, 1684 (2013).
55. H.B. Zhao, J. Kim, B.E. Koel, *Surf. Sci.*, **538**, 147 (2003).
56. A. Khan, *J. Phys. Chem.*, **104**, 11268 (2000).
57. X.H. Xia, T. Iwasita, *J. Electroanal. Chem.*, **411**, 95 (1996).
58. J. Rossmeisl, J.K. Norskov, C.D. Taylor, M.J. Janik and M. Neurock, *J. Phys. Chem. B*, **110**, 21833 (2006)
59. C.D. Taylor, R.G. Kelly and M. Neurock, *J. Electrochem. Soc.*, **154**, F217 (2007).

## CHAPTER 6

# **Reaction path analysis to identify selectivity determining steps for the complete oxidation of Ethanol and guided design of an EOR catalyst: Preliminary results**

### **6.1. Introduction**

The direct ethanol fuel cells (DEFCs) are a strong emerging alternative to the direct methanol fuel cells (DMFCs) [1-5]. The benefits, besides the obvious advantage of being a room temperature liquid fuel cell, are reduced fuel toxicity and the possibility of using a fuel that can be produced abundantly from renewable resources (i.e. bio-ethanol) [1-3]. Except for the anode catalyst, the DEFC technology shares many common features with the DMFC technology, and hence can benefit from years of developmental efforts in the latter. However, DEFCs are presently beset with very slow anode kinetics associated with the difficulty in activating the C-C bond in the ethanol molecule under the (mild) reaction conditions, and an effective low temperature catalyst has yet to be found. The current development of DEFCs is therefore constrained by the lack of good catalysts for ethanol electrooxidation [3-5]. Pt is the most common catalyst component for electrochemical reactions such as electro-reduction of oxygen and electro-oxidation of alcohols, especially for fuel cell applications [3,6-8]. Until now, Pt is still the best pure catalyst for ethanol electro-oxidation [3,7]. Since the development of new catalyst is usually based on existing design,

understanding reaction mechanisms on Pt is not only of fundamental interest, but also important for the design of new catalysts.

The mechanism of ethanol electro-oxidation on a Pt surface has been studied extensively both experimentally and theoretically [8-15]. By combining electrochemical analytical methods and modern experimental techniques such as differential electrochemical mass spectrometry (DEMS) and in-situ infrared spectroscopy (FTIR), products and intermediates during the oxidation of ethanol were identified [8-11]. While there are still different opinions about the detailed mechanism of the decomposition of ethanol, the main products are those of partial oxidation: acetaldehyde and acetic acid form with high yields [2,8-10], reflecting the lack or limits of C-C cleavage on the Pt surface. The complete oxidation product, CO<sub>2</sub> is usually formed in very small amounts. Some hydrocarbons such as CH<sub>4</sub>, C<sub>2</sub>H<sub>6</sub> are also observed in traces [9]. The intermediates that have also been detected during the oxidation of ethanol include CH<sub>3</sub>CO, CH<sub>3</sub>COH, CH<sub>x</sub>, CO... The yields of main products in the EOR are summarized in Table 6.1 [2].

**Table 6.1.** Chemical yield of main products in the EOR on different electrocatalyst

Electrocatalyst	Acetic acid yield, %	Acetaldehyde yield, %	CO <sub>2</sub> yield, %
60% wt Pt/C	33	47	20
60% wt Pt-Sn (9:1)/C	77	15	8

From the experimental results, the electro-oxidation of ethanol on platinum electrodes is proposed to follow the mechanism shown in Figure 6.1 [9].

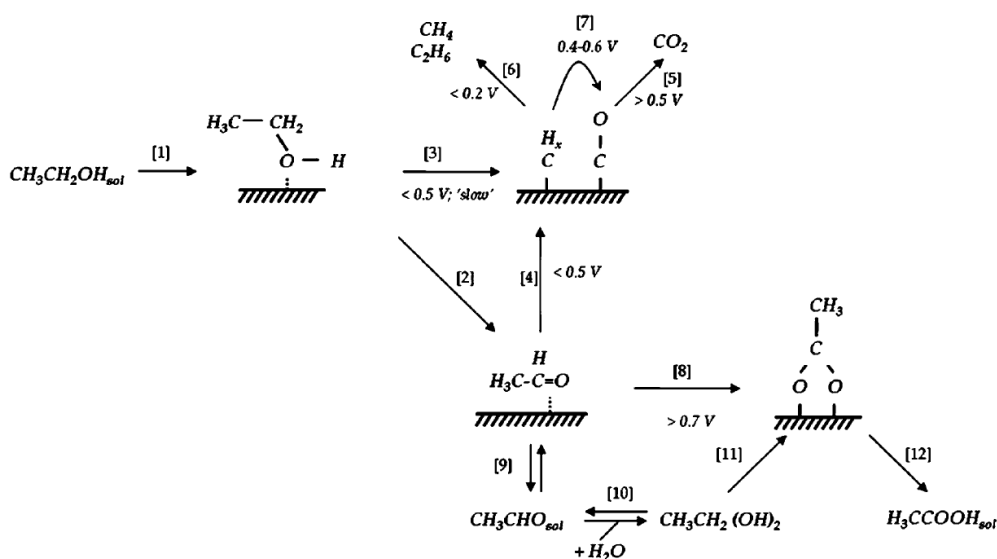


**Figure 6.1.** Mechanism of the electro-oxidation of ethanol on platinum electrodes (extracted from Ref. 9)

According to this mechanism, the adsorption of ethanol (step [1]) produces acetaldehyde and releases 2 electrons (step [2]). From theoretical studies,  $\text{CH}_3\text{CHO}$  could be formed by the deprotonation from  $\text{CH}_3\text{CHOH}$  [12-15]. Acetaldehyde can be further oxidized either to acetic acid at higher potentials (step [8]), or undergo C-C cleavage to form carbon monoxide and  $\text{CH}_x$  fragments (step [4]). However, the calculated activation barrier of the C-C dissociation in  $\text{CH}_3\text{CHO}$  has been reported to be very high, which makes this step infeasible at room temperature [15]. The CO and  $\text{CH}_x$  can be fully oxidized to carbon dioxide by extra oxygen/hydroxyl from the activation of water on the catalyst surface. The further oxidation of acetic acid on Pt surface is very difficult to occur at room temperature [11,14,15].

Therefore the problem hindering the EOR on Pt catalyst might be the high selectivity towards acetaldehyde.  $\text{CH}_3\text{CHO}$  can easily convert to the intermediate  $\text{CH}_3\text{CO}$ , and the difficulty in the decomposition of  $\text{CH}_3\text{CO}$  will



then terminate the EOR [14,15].  $\text{CH}_3\text{CO}$  can be oxidized to acetic acid by surface  $\text{OH}^*$ , which is formed by water splitting at a sufficient potential.  $\text{CH}_3\text{COOH}$  converts to adsorbed acetate  $\text{CH}_3\text{COO}^*$ , which is considered as the most stable product of the EOR on Pt(111) and block the surface [14,15].

The selectivity towards  $\text{CO}_2$  is improved when the formation of  $\text{CH}_3\text{CHO}$  is inhibited in the EOR on Rh(111) [16-18]. Similarly to the EOR on Pt(111), the mechanism of ethanol decomposition on Rh(111) is proposed to follow a stepwise dehydrogenation and the reaction map is shown in Figure 6.2. [16]

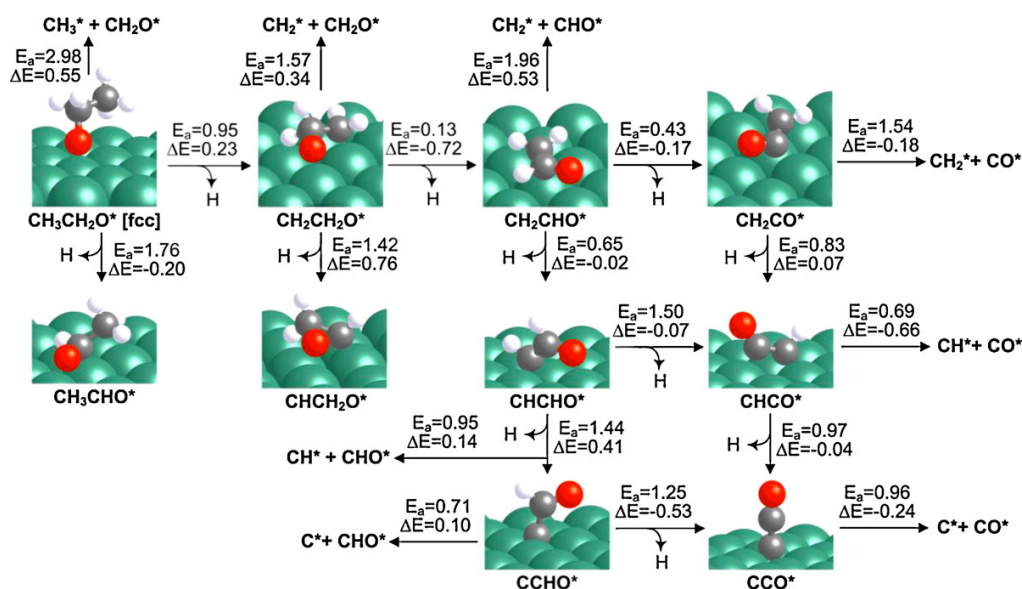


**Figure 6.2.** Reaction map for the ethanol decomposition on Rh(111) (extracted from Ref. 16)

On Rh(111), the formation of the intermediate oxametallacycle  $^*\text{CH}_2\text{CH}_2\text{O}^*$  is much easier than the formation of acetaldehyde due to its barrier energy is 0.81 eV lower [16]. The further decomposition of  $^*\text{CH}_2\text{CH}_2\text{O}^*$  is facile, and the C-C bond is broken in  $\text{CHCO}$  with the activation barriers of 0.69 eV. During the oxidation of ethanol on Rh surfaces,  $^*\text{CH}_2\text{CH}_2\text{O}^*$  was also detected by high resolution electron energy-loss spectroscopy (HREELS) [19]. The formation of  $^*\text{CH}_2\text{CH}_2\text{O}^*$  recently has been highlighted by Adzic and

collaborators as the key step to fully oxidize ethanol to CO<sub>2</sub> [20]. In their study, the ternary PtRhSnO<sub>2</sub>/C electro-catalyst was synthesized by the cation-adsorption-reduction-galvanic displacement method, and showed high activity in the ethanol oxidation. Rh played the important role to direct the formation of CH<sub>2</sub>CH<sub>2</sub>O and inhibit the formation of CH<sub>3</sub>CHO. The experimental activity and the calculated reaction pathway are shown in Figure 6.3. [20].

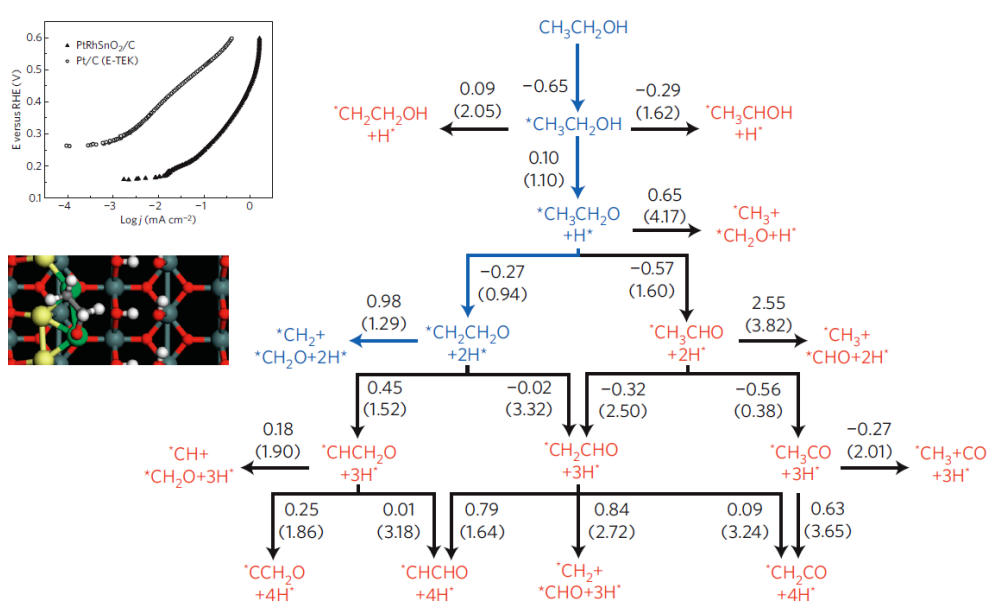


**Figure 6.3.** Possible pathways for the C–C bond breaking of ethanol on the ternary RhPt/SnO<sub>2</sub>(110) catalyst. (extracted from Ref. 20)

Therefore good catalyst for EOR should inhibit the CH<sub>2</sub> activation (C<sub>α</sub>) in the first step, and favor the formation of \*CH<sub>2</sub>CH<sub>2</sub>O\* in the second step. Although the EOR on Rh has high selectivity towards CO<sub>2</sub>, it encounters the difficulty in activating ethanol in the initial step and adsorbed ethoxy CH<sub>3</sub>CH<sub>2</sub>O in the next step with the activation barrier of 0.85 eV and 0.95 eV, respectively [17]. Conversely, those steps on Pt(111) are much more facile with the corresponding activation barriers of 0.46 eV and 0.53 eV. As a result, the activity of Pt in the EOR is much better than Rh, though the selectivity towards CO<sub>2</sub> is much lower.

The most popular method to improve the cell activity is the synthesis of binary, or even ternary electro-catalysts based on combining Pt with other transition metals, such as Sn [4,21], Ru [4,22], Rh [20,23], W [24], Ir [25], Pd [26], ... Alloying Pt could combine the advantage of each component, and can change the selectivity of reaction pathways. For example, the PtRh/SnO<sub>2</sub> catalyst from Adzic's group [20] has changed the facile formation of CH<sub>3</sub>CHO on Pt to the favorable formation of CH<sub>2</sub>CH<sub>2</sub>O (Figure 8). Whereas Rh directs the formation of CH<sub>2</sub>CH<sub>2</sub>O and facilitates the C-C bond breaking, and Pt plays the important role in activating ethanol in the initial steps [20,23]. The activity of Pt-Rh only is still poor, but it also can be improved by adding another component. Recently, the study by Lee's group demonstrated that Ir has promotional effect for the EOR on Pt-Rh at room temperature, and Ir was proposed to help in activating C-H bonds [25]. The activity of Pt-Rh-Ru in the EOR is also remarkable improved, and Ru facilitates the water activation to remove strongly bound intermediates [22].

This Chapter will show some preliminary results on how DFT calculations could help to guide the catalyst design for the EOR. Firstly, the reaction energy profile of Ethanol decomposition on Pt(111) will be analyzed to identify the selectivity determining steps during the electro-oxidation of ethanol. Next, the screening over a series of transition metals for a competition between the O-H, C<sub>β</sub>-H and the C<sub>α</sub>-H activation for the first two deprotonation steps will guide the selection of promising candidates for catalyst alloying.

## 6.2. Computational Methods.

All calculations (including adsorption energies and activation barriers) are done using spin-polarized periodic DFT with the Perdew-Burke-Ernzerhof functional (DFT-PBE) [27] as implemented in the Vienna Ab initio Simulation Package (VASP) [28,29]. The calculations are performed using a plane-wave basis with a cut-off kinetic energy of 450 eV. Electron-ion interactions are described by the projector-augmented wave (PAW) method [30,31].

The transition states and activation barriers are determined using the climbing-image Nudged Elastic Band (NEB) method [32]. Climbing-image NEB calculations will be performed for all reactant and product configurations within 10 kJ/mol of the most stable co-adsorbed configuration within the  $p(3 \times 3)$  unit cell. Vibration frequencies confirm the nature of the transition states. Though several reaction paths were considered for all systems, only the lowest activation energies are reported.

For studying ethanol oxidation on transition metallic surfaces, metal surfaces (including Pt(111), Rh(111), Pd(111), Ir(111), Ru(0001) and Co(0001)) are modeled as 3-layer,  $p(3 \times 3)$  slabs. Optimal bulk lattice constants are obtained by minimizing the total energy as a function of the lattice parameter. The bottom layer is constrained at these optimized positions, while the two top layers and the adsorbed species are fully relaxed. A  $(3 \times 3 \times 1)$  Monkhorst-Pack grid was used to sample the Brillouin zone, and an inter-slab spacing of 12 Å is found to sufficiently reduce interactions between repeated slabs. Convergence tests were performed to confirm that the structure is sufficient to

model the metal surfaces. Increasing the number of layer to 4 layers, expanding the vacuum thickness to 15 Å or using larger Monkhorst-Pack grid of (5x5x1) changed the calculated total energy by less than 5 kJ/mol.

### 6.3. Results and Discussion.

#### 6.3.1. Energy profile of the ethanol decomposition on Pt(111)

Based on DFT calculations, the energy profile of ethanol decomposition catalyzed by the Pt(111) surface was investigated (Figure 6.4). All the energies were calculated relative to gas phase ethanol and liquid water. Several groups have since published computational studies of the ethanol decomposition reaction on Pt(111) at the same time [14,15], and our results agree well with the literature.

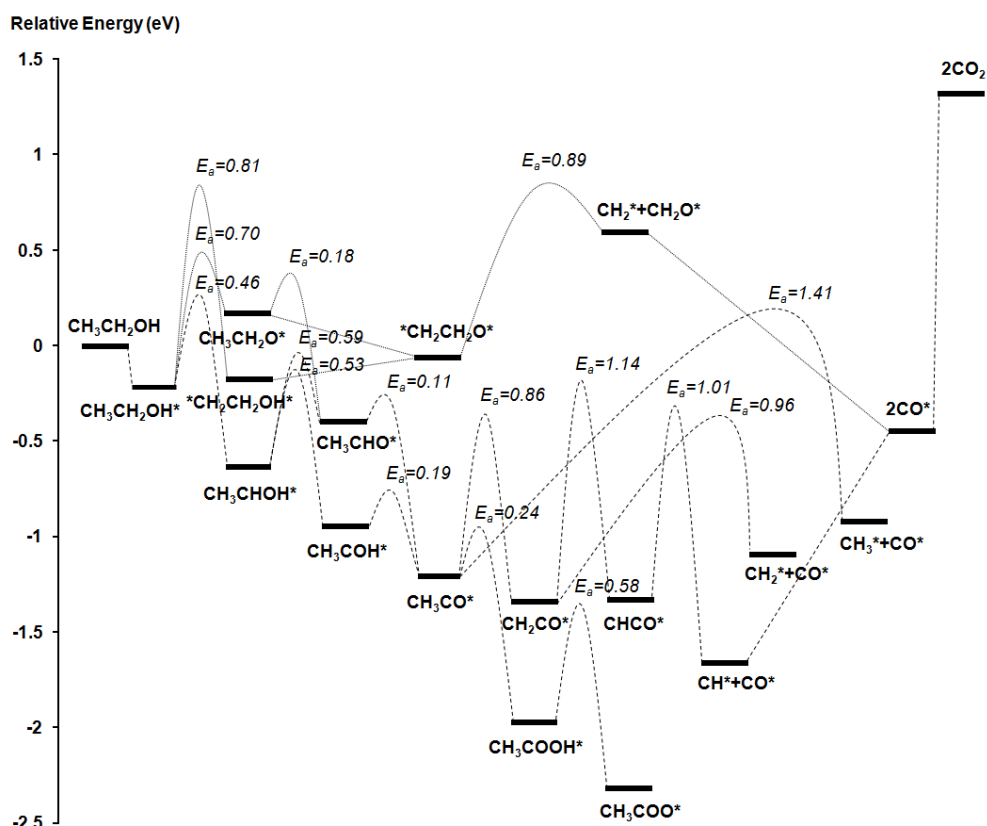


Figure 6.4: Energy profile of ethanol decomposition on Pt(111)

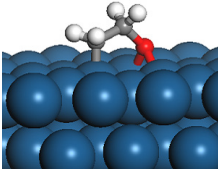
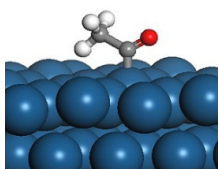
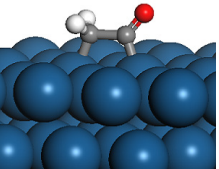
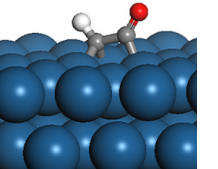
From this energy profile, it follows that ethanol is decomposed from  $\text{CH}_3\text{CH}_2\text{OH}$  to  $\text{CH}_3\text{CHOH}$  (the most favorable pathway). From this point, there are two parallel pathways to form  $\text{CH}_3\text{COH}$  or  $\text{CH}_3\text{CHO}$  with nearly identical activation barriers. However, even if  $\text{CH}_3\text{CHO}$  can be formed it will decompose easily to  $\text{CH}_3\text{CO}$  with a low activation barrier of 0.11 eV. The dehydrogenation from  $\text{CH}_3\text{CO}$  to  $\text{CH}_2\text{CO}$  is unfortunately impeded by high activation energy of 0.86 eV. Further decomposition seems more challenging due to the very high activation energy of 1.14 eV for  $\text{CHCO}$  formation, or 0.96 eV for the C-C cleavage into  $\text{CH}_2 + \text{CO}$ . The  $\text{CH}_3\text{CHO}$  formation pathway prevails over the C-C bond cleavage pathway because of the higher activation energy of the latter ( $\sim 1$  eV) than the former (0.59 eV).  $\text{CH}_3\text{CO}$  is hence an endpoint in the dehydrogenation of ethanol on Pt, and can either leave the surface by protonation to  $\text{CH}_3\text{CHO}$ , or by oxidation to  $\text{CH}_3\text{COOH}$  and formation of the very stable  $\text{CH}_3\text{COO}^{**}$  species which poisons the Pt catalyst.

Clearly, the reaction pathway via  $\text{C}_\alpha\text{-H}$  activation and leading to  $\text{CH}_3\text{CO}^*$  is not an effective EOR pathway. It involves exothermic reactions and the intermediates become more stable as the reaction proceeds. Further decomposition of  $\text{CH}_3\text{CO}^*$ , eventually to  $\text{CO}$  and  $\text{CO}_2$ , is kinetically and thermodynamically hindered on Pt. A high applied potential is therefore required to overcome the energy difference with  $\text{CO}^*$  and  $\text{CO}_2$ . As shown in Figure 6.4, reaction pathways via the formation of  $^*\text{CH}_2\text{CH}_2\text{O}^*$ , either through  $^*\text{CH}_2\text{CH}_2\text{OH}$  or through  $\text{CH}_3\text{CH}_2\text{O}^*$ , result in a smoother pathway towards  $\text{CO}_2$  and should be facilitated.

### 6.3.2. Study C-C cleavage in different intermediates on Pt(111):

The C-H activations are likely the initial steps for the Ethanol decomposition. However, to facilitate the complete oxidation of ethanol oxidation towards CO<sub>2</sub>, the C-C bond will need to be dissociated, either at earlier or later steps. Evaluations of the C-C cleavage in the stepwise dehydrogenation on Pt(111) have been done. The precursors for the C-C cleavage are considered include CH<sub>3</sub>CO, CH<sub>2</sub>CO, CHCO (generated during the initial C $\alpha$ -H activation pathway in Ethanol) and CH<sub>2</sub>CH<sub>2</sub>O (generated during the initial C $\beta$ -H activation or O-H activation pathway) (Figure 6.4). The structure of those precursors and the calculated activation barriers are summarized in Table 6.2.

**Table 6.2.** Calculated activation barrier for the C-C cleavage in some intermediates on Pt(111)

	CH <sub>2</sub> CH <sub>2</sub> O	CH <sub>3</sub> CO	CH <sub>2</sub> CO	CHCO
Precursor				
C-C bond length (Å)	1.55	1.49	1.50	1.46
C-C cleavage barrier (eV)	0.89	1.41	0.96	1.01

From Table 6.2, the activation barriers to break the C-C bond in CH<sub>2</sub>CO and CHCO are lower than in CH<sub>3</sub>CO, refers that the C-C dissociation might be easier after the C $\beta$ -H activation occurs. However, the C-C cleavage for all precursors generated during the initial C $\alpha$ -H activation pathway in Ethanol is still difficult due to high barrier, but it is more feasible in another precursor, CH<sub>2</sub>CH<sub>2</sub>O. The computed activation barrier for the C-C cleavage in CH<sub>2</sub>CH<sub>2</sub>O

is 0.86 eV, which is the lowest value compared to other precursors. The C-C bond length in CH<sub>2</sub>CH<sub>2</sub>O is the largest among all intermediate. CH<sub>2</sub>CH<sub>2</sub>O binds on the surface by the C-Pt and O-Pt bonds, stretches the C-C bond and make it easier to be broken. However the activation barrier of the C-C cleavage in CH<sub>2</sub>CH<sub>2</sub>O on Pt(111) is still high, as the activation barrier should be lower than 0.8 eV for the reaction occurs at room temperature [15]. The breaking of C-C bond in CH<sub>2</sub>CH<sub>2</sub>O or its derivatives (CHCH<sub>2</sub>O, CH<sub>2</sub>CHO ...) was reported to be more feasible on other transition metals or Pt-based alloys [33]. This observation again demonstrates the role of C $\beta$ -H activation during the oxidation of ethanol in order to facilitate the C-C cleavage.

*6.3.3. Screening the selectivity of the initial deprotonation step on different transition metals.*

**Table 6.3.** Calculated activation barriers for the first dehydrogenation steps in ethanol (eV)

Surfaces	E <sub>a</sub> -OH (eV)	E <sub>a</sub> -CH <sub>2</sub> (eV)	E <sub>a</sub> -CH <sub>3</sub> (eV)
<b>Ir(111)</b>	<b>0.75</b>	1.13	0.86
Pd(111)	1.06	0.85	0.89
<b>Rh(111)</b>	0.88	0.90	<b>0.75</b>
Pt(111)	0.7	<b>0.59</b>	0.81
Pt@Pd (111)	0.81	0.75	0.86
Pt@Ir (111)	0.99	0.98	1.03
Pt@Rh(111)	1.1	1.09	1.36
Co(0001)	0.84	1.02	0.95
<b>Ru(0001)</b>	0.80	0.87	<b>0.56</b>

Since the first deprotonation steps determine the dominant reaction pathway, we have evaluated the selectivity on a series of catalysts include Pt(111),



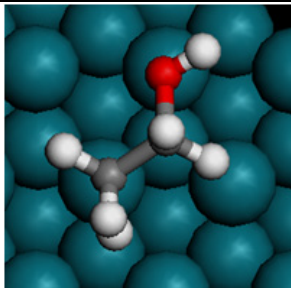
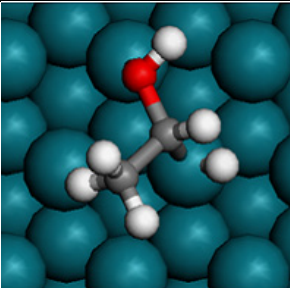
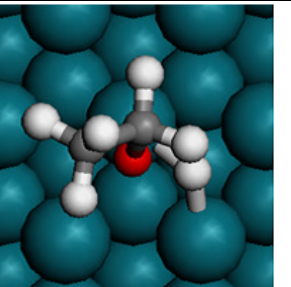
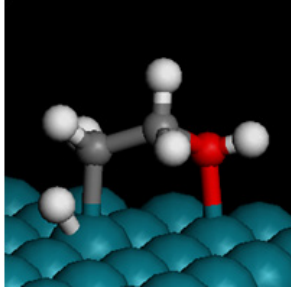
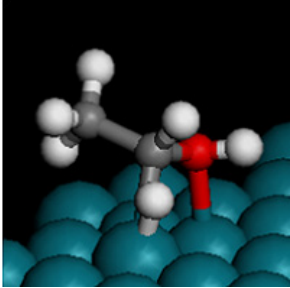
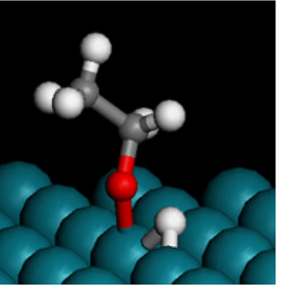
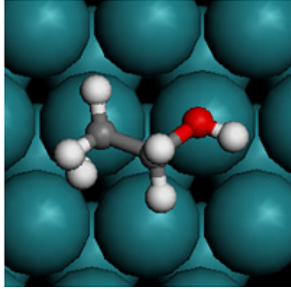
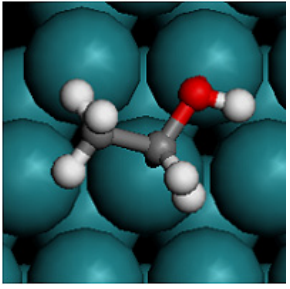
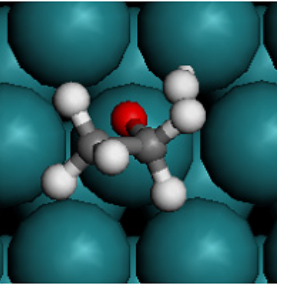
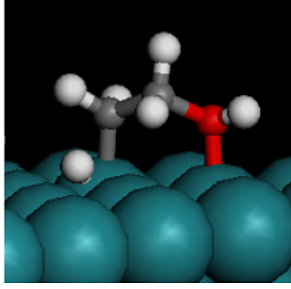
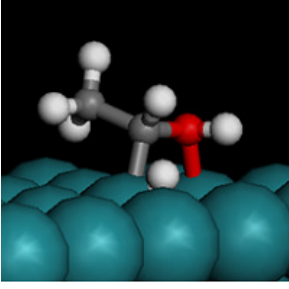
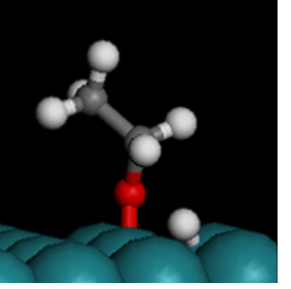
Pd(111), Ir(111), Rh(111), Ru(0001) and Co(0001) for the activations of O-H (OH pathway), C<sub>β</sub>-H (CH<sub>3</sub> pathway) and C<sub>α</sub>-H (CH<sub>2</sub> pathway). We also expanded the evaluation of those steps on other structures include monolayer of Pt(111) on Rh, Ir and Pd. Reported activation barriers are relative to the adsorption state of ethanol on clean surfaces and displayed in Table 6.3.

From the previous section, it follows that promising catalysts should inhibit the C<sub>α</sub>H<sub>2</sub> activation pathway and favor either the C<sub>β</sub>H<sub>3</sub> or the OH activation pathway with reasonable activation barriers of less than 0.8 eV in order to have reasonable room temperature activity. Pt favor CH<sub>2</sub> activation, in agreement with literature [12-15]. The same trend is found on Pd, but with higher activation barriers, agrees with another theoretical study [24]. Co is inactive for the EOR at room temperature due to the high activation barriers for all three pathways. Co activates ethanol via the OH pathway, but could only occur at high temperature, which is consistent with surface science studies by Weststrate et al. [25]. Core-shell catalysts with a monolayer Pt shell on another transition metal (Rh, Ir and Pd) still favor the CH<sub>2</sub> pathway and moreover the calculated barriers are slightly higher than for pure Pt.

Interesting candidates seem to be Ir, Rh and Ru, which are highlighted in Table 6.3. Those catalysts inhibit the C<sub>α</sub>H<sub>2</sub> activation pathway in Ethanol. Ir favors the OH pathway with the feasible activation barrier of 0.75 eV, while Rh and Ru favor the CH<sub>3</sub> pathway, all with reasonable barriers of 0.75 eV and 0.56 eV, respectively. In particularly, the activation barrier of C<sub>β</sub>H<sub>3</sub> on Ru is quite low and makes Ru a very promising candidate. This is consistent with

the experimental activity improvement of Ethanol oxidation on Pt-Ru binary alloy [22]. Further studies need to evaluate the selectivity of the second deprotonation steps. The structure of the transition states (top view and side view) for the different first dehydrogenation steps on Rh and Ru are shown in Table 6.4.

**Table 6.4.** Structures of transition states of first dehydrogenation steps from ethanol on Rh and Ru

	CH <sub>3</sub> pathway	CH <sub>2</sub> pathway	OH pathway
Rh			
			
Ru			
			

#### 6.3.4. Screening the selectivity of the second deprotonation step.

From the first screening, Ir, Rh and Ru have been detected as promising candidate for Pt alloying. The next step will be the evaluation of second Deprotonation on those candidates.

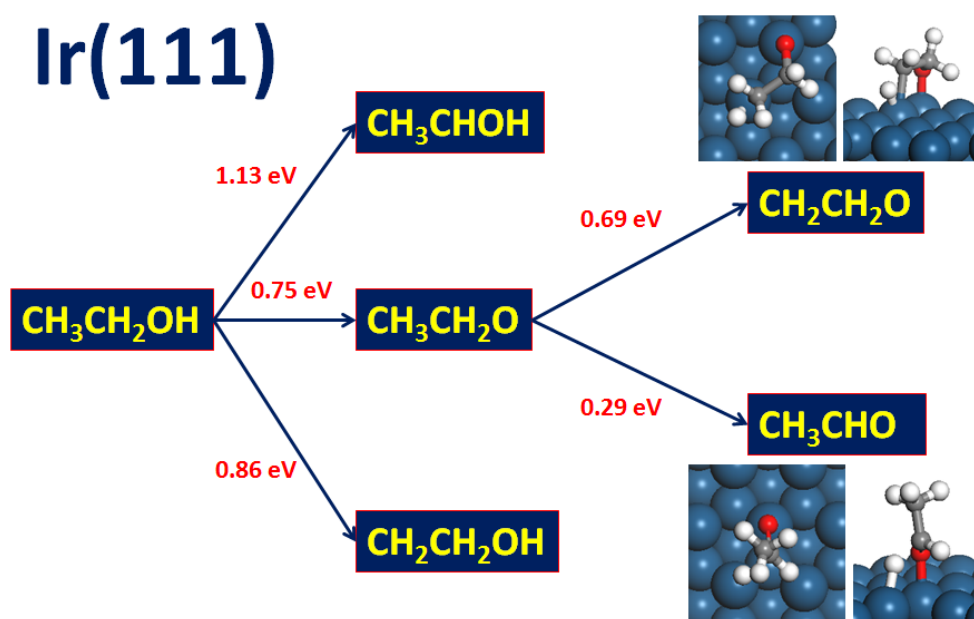


**Figure 6.5.** Two first Deprotonation step of Ethanol decomposition on Ir(111)

Ir(111) prefers the formation of Ethoxy  $\text{CH}_3\text{CH}_2\text{O}$  in the first step (Table 6.4 and Figure 6.5). In the second step on Ir(111), there are two possible pathways:  $\text{C}\alpha\text{-H}$  activation to form acetaldehyde, and  $\text{C}\beta\text{-H}$  activation to form epoxy. The former pathway is much more preferred with very low activation barrier, 0.29 eV, which is 0.4 eV lower than the later pathway. The formation of stable acetaldehyde will likely be the end product for the ethanol oxidation on Ir(111). However, the Ir(111) could easily activation the C-H bonds, with both the activation barriers of  $\text{C}\alpha\text{-H}$  and  $\text{C}\beta\text{-H}$  scission are quite low. It is consistent with the claim that Ir helps facilitate the C-H dissociation by Lee at al. [25].

The preferred product from the initial deprotonation step on Rh(111) is  $\text{CH}_2\text{CH}_2\text{OH}$  (Table 6.3 and Table 6.4). There is again the competition between three reaction routes:  $\text{C}\alpha\text{-H}$  activation generates  $\text{CH}_2\text{CHOH}$ ,  $\text{C}\beta\text{-H}$  activation generates  $\text{CHCH}_2\text{OH}$ , and OH activation generates  $\text{CH}_2\text{CH}_2\text{O}$ . The calculated activation barriers and structures of transition states are shown in Figure 6.6.

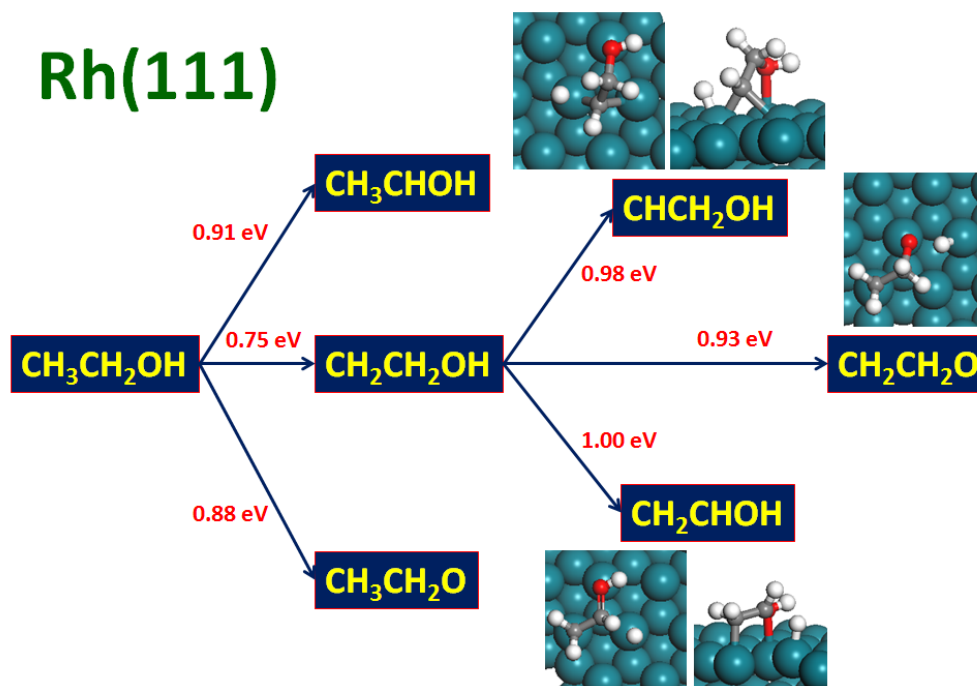


**Figure 6.6.** Two first Deprotonation steps of Ethanol decomposition on Rh(111)

All the activation barriers for three pathways are quite high, and the OH activation is the most preferred with the computed barrier of 0.93 eV, 0.05 eV lower than the  $\text{C}\beta\text{-H}$  activation. The higher selectivity towards the formation of  $\text{CH}_2\text{CH}_2\text{O}$  in this study is consistent with the detection of  $\text{CH}_2\text{CH}_2\text{O}$  during the oxidation of Ethanol on Rh by high resolution electron energy-loss spectroscopy [19] and by X-ray Photoelectron Spectroscopy [18]. The high activation barrier also reflects the low activity of Rh(111) catalyst towards the EOR, but it could be improved by combining Rh with Pt and other promoters [20,23,33].

Finally, the second deprotonation steps on Ru(0001) are considered. Similar to Rh(111), Ru(0001) favors the formation of CH<sub>2</sub>CH<sub>2</sub>OH in the first deprotonation step, which is very consistent with another literature study [36]. There is also the competition between three reaction pathways, and the next favorable step will be the formation of CH<sub>2</sub>CHOH via the C $\alpha$ -H activation with the reasonable activation barrier of 0.69 eV (Figure 6.7). The C $\beta$ -H and OH activation are inhibited in the second deprotonation with much higher barrier, 0.97 and 0.85 eV, respectively. The high selectivity towards the formation of CH<sub>2</sub>CHOH will need further study to evaluate how it will influence to the total EOR efficiency on Ru(0001).

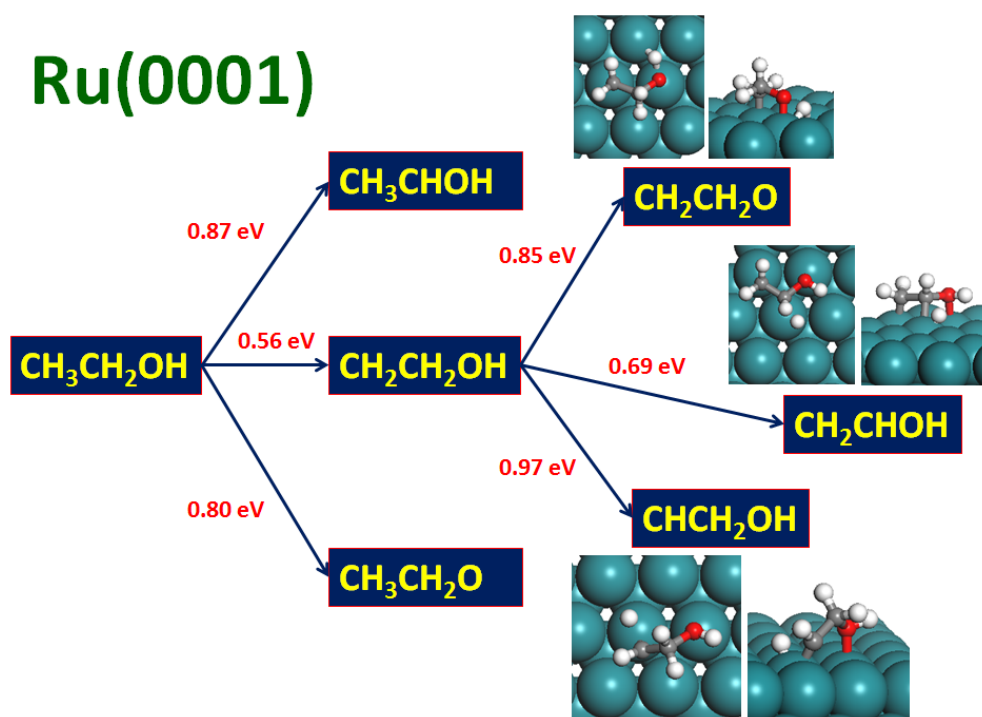


**Figure 6.7.** Two first Deprotonation step of Ethanol decomposition on Ru(0001)

#### 6.4. Conclusions.

This Chapter illustrates how to use the mechanistic insight obtained from first principle modeling to help guide our catalyst design, screening and optimization efforts. Using a Density Functional Theory-based reaction path

analysis, the ethanol electro-oxidation reaction (EOR) mechanism was studied on a model Pt(111) surface. The subsequent reaction path analysis provided insight in the low CO<sub>2</sub> selectivity of Pt catalysts, identified activity and selectivity determining steps and provided suggestions to improve the EOR activity. The low activity/selectivity of pure Pt EOR catalysts can be understood from the selectivity of the first two dehydrogenation steps, leading to CH<sub>3</sub>CHO and CH<sub>3</sub>COOH. These intermediates can block the catalyst surface and poison the catalyst. Effective EOR catalysts should inhibit the formation of CH<sub>3</sub>C\*OH species, and facilitate the formation of \*CH<sub>2</sub>CH<sub>2</sub>O\* instead. Computational screening efforts helped identify Rh, Ru and Ir as potentially selective catalysts. Unfortunately, their activity is calculated to be lower than Pt because of their higher C-H activation barriers, which is a challenge for all proposed non-Pt catalysts.

The theoretical study in this Chapter was conducted without considering the influence of aqueous environment to the reactions. Actually, oxidation of ethanol requires electro-activation of water and hence a fairly high potential on Pt catalysts. As investigated from previous Chapter, the presence of water could change the selectivity of CH/OH activation, and surface OH also opens up new reaction pathways, i.e., dehydrogenation steps via hydrogen abstraction and unwanted steps leading to CH<sub>3</sub>COO\*\*. Particularly, Ru are famously reported to facilitate the activation of water, so these steps need to be considered in the selection of novel catalyst structures and is the subject for future studies.

## 6.5. References.

1. W. Vielstich, H.A. Gasteiger, A. Lamm (Edt), Handbook of Fuel Cells – Fundamentals, Technology and Applications, John Wiley & Sons, Ltd, (2010).
2. F. Vigier, S. Rousseau, C. Coutanceau, J.-M. Leger, C. Lamy, *Top. Catal.*, **40**, 111 (2006)
3. E.H. Yu, X. Wang, X.T. Liu and L. Li, *Challenges and Perspectives of Nanocatalysts in Alcohol-Fuelled Direct Oxidation Fuel Cells*, in Z.-X. Liang and T.S. Zhao (Edts), *Catalysts for Alcohol-Fuelled Direct Oxidation Fuel Cells*, Royal Society of Chemistry, Cambridge, pp. 227-249 (2012).
4. E. Antolini, *J. Power Sources*, **170**, 1 (2007).
5. S. Song, P. Tsiakaras, *App. Catal. B: Environ.*, **63**, 187 (2006).
6. Q. Wang, G.Q. Sun, L.H. Jiang, Q. Xin, S.G. Sun, Y.X. Jiang, S.P. Chen, Z. Jusys, R. Behm, *Phys. Chem. Chem. Phys.*, **9**, 2686 (2007).
7. J.K. Nørskov, J. Rossmeisl, A. Logadottir, L. Lindqvist, J.R. Kitchin, T. Bligaard, H. Jónsson, *J. Phys. Chem. B*, **108**, 17886 (2004).
8. T. Iwasita, E. Pastor, *Electrochim. Acta*, **39**, 531 (1994).
9. S.C.S. Lai, M.T.M. Koper, *Faraday Discuss.*, **140**, 399 (2008).
10. S. Rousseau, C. Coutanceau, C. Lamy, J.-M. Leger, *J. Power Sources*, **158**, 18 (2006).
11. M. Heinen, Z. Jusys, R.J. Behm, *J. Phys. Chem. C*, **114**, 9850 (2010).
12. R. Alcalá, M. Mavrikakis, J.A. Dumesic, *J. Catal.*, **218**, 178 (2003).
13. E. Vesselli, G. Coslovich, G. Comelli, R. Rosei, *J. Phys.: Condens. Matter.*, **17**, 6139 (2005).

14. H.F. Wang, Z.P. Liu, *J. Phys. Chem. C*, **111**, 12157 (2007).
15. H.F. Wang, Z.P. Liu, *J. Am. Chem. Soc.*, **130**, 10996 (2008).
16. Y.M. Choi, P. Liu, *Catal. Today*, **165**, 64 (2011).
17. M. Li, W.Y. Guo, R.B. Jiang, L.M. Zhao, X.Q. Lu, H.Y. Zhu, D.L. Fu, H.H. Shan, *J. Phys. Chem. C*, **114**, 21493 (2010).
18. E. Vesselli, A. Baraldi, G. Comelli, S. Lizzit, R. Rosei, *Chem. Phys. Chem.*, **5**, 1133 (2004).
19. C.J. Houtman, M.A. Barteau, *J. Catal.*, **130**, 528 (1991).
20. A. Kowal, M. Li, M. Shao, K. Sasaki, M.B. Vukmirovic, J. Zhang, N.S. Marinkovic, P. Liu, A.I. Frenkel, R.R. Adzic, *Nat. Mat.*, **8**, 325 (2009).
21. G. Wu, R. Swaidan, G.F. Cui, *J. Power Sources*, **172**, 180 (2007).
22. J. Melke, A. Schoekel, D. Dixon, C. Cremers, D.E. Ramaker, C. Roth, *J. Phys. Chem. C*, **114**, 5914 (2010).
23. A. Kowal, S.L. Gojkovic, K.S. Lee, P. Olszewski, Y.E. Sung, *Elec. Commun.*, **11**, 724 (2009).
24. E. Antolini, E.R. Gonzalez, *Appl. Catal. B: Environ.*, **96**, 245 (2010).
25. B. Liu, Z.W. Chia, C.H. Cheng, J.Y. Lee, *Energy Fuels*, **25**, 3135 (2011).
26. E. Antolini, *Energy Environ. Sci.*, **2**, 915 (2009).
27. J.P. Perdew, K. Burke, M. Ernzerhof, *Phys. Rev. Lett.*, **77**, 3865 (1996).
28. G. Kresse, J. Hafner, *J. Phys. Rev. B*, **47**, 558 (1993).
29. G. Kresse, J. Futhmuller, *Comput. Mater. Sci.*, **6**, 15 (1996).
30. J. Hafner, *J. Comput. Chem.*, **29**, 2044 (2008).
31. P.E. Blochl, *Phys. Rev. B*, **50**, 17953 (1994).
32. G. Henkelman, B.P. Uberuaga, H. Jónsson, *J. Chem. Phys.*, **113**, 9901 (2000).



33. T. Sheng, W.-F. Lin, C. Hardacre, P. Hu, *Phys. Chem. Chem. Phys.*, **16**, 13248 (2014).
34. M. Li, W.Y Guo, R.B Jiang, L.M. Zhao, H.H. Shan, *Langmuir*, **26**, 1879 (2010).
35. C.J. Weststrate, H.J. Gericke, M.W.G.M. Verhoeven, I.M. Ciobã; A.M. Saib, J.W. Niemantsverdriet, *J. Phys. Chem. Lett.*, **1**, 1767 (2010).
36. R. Jiang, W. Guo, M. Li, D. Fu, H. Shan, *J. Phys. Chem. C*, **113**, 4188 (2009).

## CHAPTER 7

### Conclusion and Suggestion for Future works

This PhD study aims to use first principle calculations to guide design of catalyst for Alcohol fuel cell devices. In essence, this thesis addresses modeling of heterogeneous catalyst for electrochemical reactions in Direct Alcohol fuel cell at four aspects include structural characterization, mechanistic study, catalytic activity and selectivity evaluation. This was accomplished by analyzing all the elementary steps during the reaction on atomic level by Density functional theory calculations within the developed thermodynamics model to identify the key determining steps for improvement suggestion. The summarization on major findings and some suggestions for future works will be described below.

#### 7.1. Summary of major findings.

Characterization of catalyst, especially for multi-component electro-catalysts is quite challenging due to small particle size and complicated composition. In this PhD study, the method to evaluate the structure of catalysts using Core-Level binding energies calculated from First Principles combine with XPS experiment is developed. DFT calculations describe the 2.8 eV variation in the C 1s binding energies on Co surfaces, the 4.2 eV variation in the C 1s binding energies on Pt surfaces, and the 5.5 eV variation in the B1s binding energies in the test sets with average deviations of 85, 73, and 53 meV, respectively. To illustrate how binding energy calculations can help elucidate catalyst structures, the nature of the resilient carbon species deposited during

Fischer–Tropsch synthesis (FTS) over  $\text{Co}/\gamma\text{-Al}_2\text{O}_3$  catalysts was studied. The catalysts were investigated using XPS after reaction, and the measured C 1s binding energies were compared with DFT calculations for various stable structures. The XPS peak at 283.0 eV is attributed to a surface carbide, while the peak at 284.6 eV is proposed to correspond to remaining waxes or polyaromatic carbon species. Boron promotion has been reported to enhance the stability of Co FTS catalysts. Again, the combination of XPS with DFT B 1s binding energy calculations helped identify the nature and location of the boron promoter on the  $\text{Co}/\gamma\text{-Al}_2\text{O}_3$  catalyst. Core-shell catalysts are popular in low temperature fuel cell applications. Core-level BE calculations can also help determine the structure of core-shell catalysts. To evaluate the structure of a series of  $\text{Pd}_3\text{M}@\text{Pd}_3\text{Pt}$  ( $\text{M} = \text{Co}, \text{Fe}, \text{Ni}, \text{and Cr}$ ) core-shell catalysts, Pt  $4f_{7/2}$  surface binding energies were calculated and compared with XPS data. When the core is changed in steps from  $\text{Pd}_3\text{Cr}$  to  $\text{Pd}_3\text{Fe}$ ,  $\text{Pd}_3\text{Co}$  and  $\text{Pd}_3\text{Ni}$ , the experimental Pt  $4f_{7/2}$  binding energies decrease by 1.4 eV. DFT calculations accurately describe this variation for a model structure with a monolayer  $\text{Pd}_3\text{Pt}$  shell. This is consistent with the shell thickness estimated independently from the particle diameter and the Pt content. DFT XPS calculation does not only help in characterization of catalyst, it also helps to identify the adsorption configurations, adsorption sites, and resolving identity for reaction intermediates during the decomposition of ethanol on transition metals, and can be used to support mechanistic study.

Another aspect of alcohol fuel cell catalyst that need to be addressed is the improvement the cathode activity, where the oxygen reduction reaction

occurs. The activity of oxygen reduction electrocatalysts is governed by the Sabatier principle and follows a Volcano curve as a function of the oxygen-binding energy. Density functional theory calculations show that the oxygen-binding energy decreases in steps of about 10 kJ/mol in a series of core-shell  $\text{Pd}_3\text{M}@\text{Pd}_3\text{Pt}$  ( $\text{M} = \text{Ni}, \text{Co}, \text{Fe}, \text{Mn}, \text{and Cr}$ ) electrocatalysts, leading to a gradual, Volcano-like variation in the oxygen reduction activity. A series of carbon-supported  $\text{PdM}@\text{PdPt}$  ( $\text{M} = \text{Ni}, \text{Co}, \text{Fe}, \text{and Cr}$ ) nanoparticles with similar particle sizes were prepared by an exchange reaction between PdM nanoparticles and an aqueous solution of  $\text{PtCl}_2^{-4}$ . The variation in the surface electronic structure of the core-shell structures was evaluated by Pt  $4f_{7/2}$  X-ray photo-electron spectroscopy and by CO-stripping voltammetry and agrees with the first principle calculations. At 0.85 V, the  $\text{PdM}@\text{PdPt}/\text{C}$  core-shell electrocatalysts show a 6-fold variation in activity, following the Volcano trend predicted by the calculations. The Pt mass activity of the Volcano-optimal  $\text{PdFe}@\text{PdPt}/\text{C}$  catalyst is an order of magnitude higher than the activity of commercial 3.0-nm Pt/C catalysts. The core-shell catalysts also display a high methanol tolerance, which is important for use in direct methanol fuel cells. Calculated Pt-M segregation energies suggest that the  $\text{Pd}_3\text{M}@\text{Pd}_3\text{Pt}$  core-shell structures are stable, in particular in the presence of 1/4 ML CO. Adsorption of oxygen-containing species may induce surface segregation of the 3d transition metal, except for the Volcano-optimal ORR catalyst,  $\text{Pd}_3\text{Fe}@\text{Pd}_3\text{Pt}$ .

To provide the comprehensive evaluation of the catalyst efficiency in aqueous phase catalytic reactions, the role of water is also studied. The presence of

water not only influences the activity and selectivity through specific hydrogen-bond interactions with reactants and transition states, it also supplies active surface hydroxyl groups. In this study, the effect of water on the activity and selectivity of CH/OH activation of methanol on Pt was studied using the RPBE-VdW functional. This functional accurately describes the hydrogen-bond interactions, which greatly affects the activity and selectivity. On clean terraces, C-H and O-H activation are competitive with barriers of 88 and 82 kJ/mol, respectively. The presence of a single water molecule increases the stability of the methanol reactant more than the transition states and increases the CH and OH barrier to 99 and 89 kJ/mol, increasing the selectivity of OH activation. The selectivity however reverses for a water monolayer and the presence of two hydrogen bonds increase the OH activation barrier to 128 kJ/mol. CH activation is found to be favorable with a barrier of 108 kJ/mol, in agreement with experiments at low potential. At higher potentials, the presence of surface hydroxyl groups opens a new hydrogen-abstraction pathway, with a very low barrier for OH activation by proton shuttling. C-H abstraction of the resulting methoxy group by surface hydroxyl species has a barrier of 67 kJ/mol, higher than the barrier for direct CH activation pathway on Pt, 36 kJ/mol. Extend the study on the competition between direct CH activation pathway and surface OH group assisted (C-H abstraction) pathway on a series of transitional metals (Rh, Pd, Au, Ag), C-H activation only can be facilitated by surface hydroxyl groups for less reactive surfaces, e.g Au, Ag...

Finally, DFT calculations are used to obtain mechanistic insight of the ethanol electro-oxidation reaction (EOR) to guide catalyst design. In particular, in a

first step, the electro-oxidation of ethanol will be studied theoretically on a model Pt(111) surface in order to (i) identify the *level of theory* required to obtain results that are sufficiently accurate to provide guidance to the later catalyst design steps. (ii) Once the level of theory has been established, the *selectivity and rate determining steps* will be identified for the electro-oxidation over Pt. The mechanistic insight obtained from this study will help guide the catalyst design efforts. The problem hindering the EOR on Pt catalyst might be the high selectivity towards acetaldehyde, and the selectivity determining steps are identified to be the first and second deprotonation, and the key intermediate for the C-C cleavage is  $^*CH_2CH_2O^*$ , either through  $^*CH_2CH_2OH$  or through  $CH_3CH_2O^*$ . The O-H, C $\alpha$ -H and C $\beta$ -H activations from Ethanol are evaluated on clean surface of a series of transition metals to guide the most promising component for catalyst modification. From those data, promising catalysts should inhibit the C $\alpha$ -H pathway and favor the O-H or C $\beta$ -H pathway with reasonable activation barriers, i.e, 0.8 eV for the feasible reaction at room temperature, and good candidates are Rh, Ru and Ir. The observed data opens some suggestions for future studies. This study is also a scientific effort directed at discovering new insights on ethanol electrooxidation mechanism and ethanol oxidation catalyst design to pave the way for a rational approach to catalyst design in the future.

## **7.2. Suggestion for future works.**

### *7.2.1. Study the C-C cleavage in the EOR via the decarboxylation pathways*

Ethanol is the smallest alcohol containing a C-C bond, and in order to fully oxidize ethanol to CO<sub>2</sub>, the catalyst will have to activate the C-C bond.

Although Pt is a good catalyst for the C-C cleavage in the steam reforming of C<sub>2</sub>-C<sub>4</sub> hydrocarbons [1], the performance of Pt for the C-C cleavage in the EOR is still very poor [2-4].

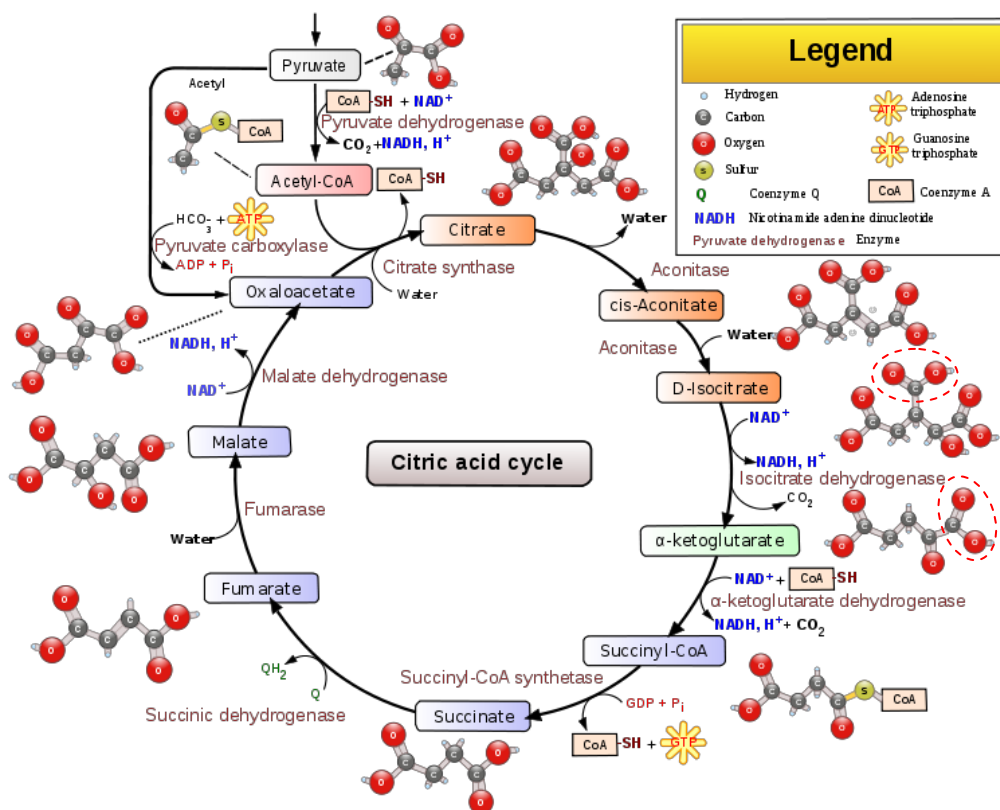


**Figure 7.1.** Diagram of the Krebs cycle (extracted from Ref. 6)

There are other pathways to break the C-C bond that have not been considered in the literature. The C-C bond has been reported to be easier broken in  $\alpha$ -keto-acid and dicarboxylic acids, e.g. oxalic acid decomposed into  $\text{CO}_2$  at moderate temperatures [5]. The electro-oxidation of acetyl  $\text{CH}_3\text{CO}$  to  $\text{CO}_2$  in the citric acid cycle (Krebs cycle) (Figure 7.1) [6] involves the formation of  $\alpha$  keto-acids catalyzed by enzymes, and the C-C cleavage occurs through the decarboxylation from the  $-\text{COOH}$  groups next to the carbonyl  $\text{C}=\text{O}$ . Clearly the C-C scission here is quite feasible; therefore we can try to design an EOR catalyst follow that nature does.

In the EOR on transition metals, the intermediate  $\text{CH}_2\text{CH}_2\text{O}$  could be converted to dicarbonyl species, such as glyoxal  $\text{CHO-CHO}$ , glyoxalic acid  $\text{CHO-COOH}$  or oxalic acid  $(\text{COOH})_2$  ... with the incorporation of surface  $\text{OH}^*$ . The C-C bond in those dicarbonyl species might be easier to be broken by decarboxylation produce  $\text{CO}_2$ . Therefore this reaction pathway of C-C cleavage should be studied to evaluate the fully oxidized ethanol towards  $\text{CO}_2$ .

### *7.2.2. Comprehensively evaluate EOR activity on alloys and core-shell catalysts.*

As mentioned in Chapter 6, the influence of water and the assistance of surface Hydroxyl group need to be integrated into reaction path analysis. This approach includes the study on competition between the direct versus surface OH assistance pathway at each step, similar to the study in Chapter 5. It will give a comprehensive evaluation on the activity of EOR catalyst. In the next step, the mechanistic understanding will be used to evaluate the effect of catalyst modifications on the relative stability of the key intermediates and transition states. Such modifications can be tested easily computationally, and provide input for the catalyst discovery efforts.

The similar procedure also will be applied for evaluate the activity of core-shell catalyst for the EOR. The core-shell catalyst that will be studied include the core-shell  $\text{Pd}_3\text{Pt}@Pd_3\text{M}$  ( $\text{M} = \text{Pt}, \text{Ni}, \text{Co}, \text{Fe}$  and  $\text{Cr}$ ), which was reported to be good catalyst for the Oxygen reduction reaction, and turns out to be a promising candidate for EOR too. Another core-shell structure will be also studied include the  $\text{Pt}_3\text{Rh}@Pt_3\text{Sn}$  structure, which is expected to combine the



advantage of both the components. Pt<sub>3</sub>Rh could facilitate the C-C bond cleavage in ethanol molecules, while Pt<sub>3</sub>Sn could provide activated –OH groups to remove the adsorbed reaction intermediates. The more complicated combination such as Pt-Rh-Ru-Sn could also be considered.

### 7.2.3. Study the water activation on metal oxide:

To design an effective ethanol oxidation electrocatalyst, both selectivity (C-C activation vs. C-O activation) and activity (in particular CO oxidation) need to be considered. The catalyst has to be able to first activate the C-C bond and then oxidize the resulting C<sub>1</sub> species, CH<sub>x</sub> and CO, to CO<sub>2</sub>. In order to achieve this, the catalyst has to show optimal activities for the different reaction steps, dehydrogenation, C-C activation, and oxidation, leading to a constrained optimization problem.

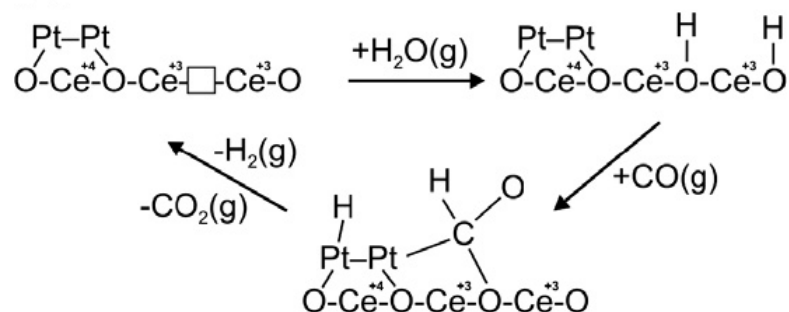


**Figure 7.2.** Mechanisms operated in the WGS reaction over ceria-supported platinum catalysts, surface oxygen vacancy is indicated by the blank square (extracted from Ref. 9)

The activation of water is a critical step for the DEFCs. Metal oxides have been studied as potential catalysts to solve the CO poisoning problem in EOR by facilitating the water splitting and improve the oxidation of CO by water [7]. Theoretical studies should be made to different metal oxides to explore the activity based on WGS. Research show the surface Oxygen-vacancy is the key

to this water-splitting reaction on metal oxides [8,9]. For example, in Figure 7.2., surface oxygen vacancies facilitate the water-splitting reaction to provide hydroxyl group OH\* to react with CO, which make metal oxides more active in water-gas-shift reaction (WGS).

Various metal oxides could be chosen to study the production and reformation of O-vacancy site through WGS cycle: the rock salt structures of MO (M=Fe, V, Co) and CeO<sub>2</sub>, rutile structures of MO<sub>2</sub> (M= Sn, Ti, Ru), rhombohedra structures of M<sub>2</sub>O<sub>3</sub> (M=Fe, V), spinel structure of M<sub>3</sub>O<sub>4</sub> (M=Co), and monoclinic or orthorhombic structure of MO<sub>3</sub> (M=W, Mo) [10]. The stable and easily-prepared surfaces should be used to study the activity of O-vacancy sites to WGS: the (111) surface for MO, the (110) surface for MO<sub>2</sub>, (1-102) for M<sub>2</sub>O<sub>3</sub>, and the (100) surface of MO<sub>3</sub> [11]. The database will set up to get the prototype reference to experiments. Furthermore, a kinetic model will be set up based on the calculations. This study will guide the selection of metal oxides as support/promoter for the EOR electro-catalysts.

### 7.3. References.

1. K. Liu, C. Song, V. Subramani, Hydrogen and Syngas Production and Purification Technologies, John Wiley & Sons, Inc., Hoboken, New Jersey, (2010).
2. T. Iwasita, E. Pastor, *Electrochim. Acta*, **39**, 532 (1994).
3. P. Ferrin, D. Simonetti, S. Kandoi, E. Kunkes, J.A. Dumesic, J.K. Norskov, M. Mavrikakis, *J. Am. Chem. Soc.*, **131**, 5809 (2009).
4. S.C.S. Lai, M.T.M. Koper, *Faraday Discuss.*, **140**, 399 (2008).

5. W. Riemenschneider, M. Tanifuji, Oxalic Acid, in Ullmann's Encyclopedia of Industrial Chemistry (6<sup>th</sup> ed.), Wiley-VCH, (2003).
6. J.M. Berg, J.L. Tymoczko, L. Stryer, Biochemistry (5th ed.), WH Freeman and Company, pp. 465–484, 498–501, (2002).
7. B. Qiao, A. Wang, X.F. Yang, L.F. Allard, Z. Jiang, Y. Cui, J.Y. Liu, J. Li, T. Zhang, *Nat. Chem.*, **3**, 634 (2011).
8. W. Zhang, A. Trunschke, R. Schlogl, D.S. Su, *Angew. Chem. Int. Ed.*, **49**, 6084 (2010).
9. C.M. Kalamaras, S. Americanou, A.M. Efstathiou, *J. Catal.*, **279**, 287 (2011).
10. R.W.G. Wyckoff, Crystal Structures, Interscience Publishers, New York, (1960).
11. H.T. Li, W.Q. Zhang, J.R. Smith, *Phys. Status Solidi A – Applications and Materials Science*, **208**, 1166 (2011).